LUMS
A Not-for-Profit University

DEVELOPMENT OF NANOCATALYSTS FOR WATER SPLITTING - A SUSTAINABLE SOURCE OF ENERGY

By

Akhtar Munir

A THESIS

Submitted in partial fulfillment of the requirements for the degree of PhD in Chemistry from Lahore University of Management Sciences (LUMS)

DHA, Lahore Cantonment. 54792
Lahore, Pakistan

June-18-2020

DEVELOPMENT OF NANOCATALYSTS FOR WATER SPLITTING - A SUSTAINABLE SOURCE OF ENERGY

A Dissertation Submitted to

Department of Chemistry and Chemical Engineering

Lahore University of Management Sciences

By

Akhtar Munir

2016-13-0031

In Partial Fulfillment of the Requirements for the Degree of

Doctor of Philosophy

June-18-2020

Lahore University of Management Sciences
D.H.A, Lahore Cantt. 54792
Lahore, Pakistan

Department of Chemistry and Chemical Engineering

Lahore University of Management Sciences

Lahore

Certificate

This is to certify that the thesis entitled **"DEVELOPMENT OF NANOCATALYSTS FOR WATER SPLITTING-A SUSTAINABLE SOURCE OF ENERGY"** is an authentic record of research work carried out by **Mr. Akhtar Munir,** Roll No. 2016-13-0031, under my supervision, in partial fulfilment of the requirements for the degree of PhD in Chemistry at Lahore University of Management Sciences, and that no part of this thesis has been presented for any other degree.

Dr. Irshad Hussain

Professor

(Supervisor)

Dated:

18-06-2020

Department of Chemistry and Chemical Engineering

Lahore University of Management Sciences

Lahore

DECLARATION

I hereby declare that the work presented in this thesis entitled ***"Development of Nanocatalysts for Water Splitting - A Sustainable Source of Energy"*** is entirely original and was carried out by me independently under the supervision of Dr. Irshad Hussain (Associate Professor, Department of Chemistry & Chemical Engineering, Lahore University of Management Sciences) and has not been included in any other thesis submitted for the award of any other degree.

Akhtar Munir

ID: 2016-13-0031

(Approved by the Thesis Evaluation Committee)

Title of the Thesis:	**Development of Nanocatalysts for Water Splitting - A Sustainable Source of Energy**
Name of the Student:	**Akhtar Munir**
Roll Number:	**2016-13-0031**

Thesis approved by the Department of Chemistry and Chemical Engineering, Lahore University of Management Sciences (LUMS), Lahore, for the partial fulfilment of the requirement for the Degree of Doctor of Philosophy in Chemistry.

THESIS EVALUATION COMMITTEE

Dr. Irshad Hussain (Supervisor) ____________________________

Dr. Falak Sher (Committee Member) ____________________________

Dr. Salman Noshear Arshad (Committee Member) _________________________

Dedicated to all Those Effected by

COVID-19

ACKNOWLEDGMENTS

I owe my profound thanks and deepest sense of gratitude to Almighty **ALLAH**, the Creator of the Universe, and Worthy of all praises, the Merciful, who blessed me with determination, potential, and ability to complete this research. I offer my humblest and sincere thanks to the **Holy Prophet Muhammad** (Sallallah-o-Alaih-e-Waalyh-e-Wasallum), who is the source of knowledge and guidance for the entire world forever and exhorted his followers to seek knowledge from cradle to grave.

I wish to express sincere thanks to my PhD supervisor, **Dr. Irshad Hussain,** for his enthusiastic support, scholastic guidance, invigorating encouragement, fruitful discussions, and providing me all the required laboratory facilities, the flexibility to explore various ideas that enabled me to complete the PhD research and thesis efficiently. Apart from the above all, I feel highly privileged in taking opportunity to express my deep sense of gratitude to my supervisor for his extreme humbleness, reassurance and way of counseling from time to time. It has been an honor to have such a cool supervisor for the rest of my life. I would also like to pay special regards to my thesis committee members i.e., **Dr. Falak Sher (Current Department Chair)** and **Dr. Salman Noshear Arshad** for their professional guidance and continuous encouragement. Special thanks to **Dr. Habib Ur Rehman (LUMS)** and **Tanveer Ul Haq (**PhD student, HBKU Qatar**)** for their tremendous support, valuable contributions, generous help, and friendly discussions that enabled me to complete my research work.

It is inevitable to thank **Dr. Ahsanulhaq Qurashi** (Khalifa University, Abu Dhabi), **Anwar Ul Hamid** (KFUPM, Saudi Arabia), **Asim Jilani** (KAU, Jeddah) for their humble support in sample analysis, professional guidance and continuous encouragement during my research. Their efforts and opinions are greatly appreciated.

A special thank goes to **Syed Baber Ali School of Science and Engineering** (SBASSE), Department of Chemistry and Chemical Engineering, for my PhD finance and exciting scientific environment at LUMS. I also extend my gratitude to **Higher Education Commission** (HEC) Pakistan for funding through an NRPU-Project-5918 awarded to Irshad Hussain, SBASSE.

I am really delighted to acknowledge **Syed Zajif Hussain (LUMS)** and **Dr**. **Murtaza Saleem** from SBASSE central lab for their help, useful suggestions and extensive SEM/EDX/STEM analysis, whenever I needed. A special word of gratitude to the group members i.e., **Irfanullah (PhD)**, **Ms. Zille Huma (PhD), Ms. Farwa Abbas (MS) and Muhammad Tariq (MS),** all my lab fellows (senior and junior) especially **Qasim Qayyum Kashif** and **Farhan Arshad**, my PhD fellows (**Iqra Azeem, Faryal Aftab, Bushra Iqbal and Asma Gilani**), staff members, my **senior-juniors colleagues** of department for their nice company, continued encouragement, moral support and necessary guidance during my stay at LUMS.

Many thanks to all of my sincere friends especially **Muhammad Javed Iqbal** (PhD, QAU Islamabad), **Muhammad Zubair** (PhD, QAU Islamabad), **Noor Ud din** (PhD, QAU Islamabad), and **Jamal Abdul Nasir** (PhD, UCL-UK), **Ubaidullah** (PhD, LUMS), **Tuheed Ullah** (PhD, China) and **Irshad Ullah** (PhD, UOP). I wish them very best of luck for their PhD’s and future ahead. I extend my appreciation to **Dr. Saqib Ali** (QAU Islamabad), **Dr. Ali Haider** (QAU Islamabad), **Dr. Zia-ur-Rehman** (QAU Islamabad), and **Dr. Amir Wasim** (QAU Islamabad) for their great contribution in my academic carrier.

I lack words to express my infinite gratitude, feelings, regards, love and respect to my **Parents**. Thanks much for your continuous prayers, love and care for me. My father, **Ubaidullah Jan,** is the head of our family, but the heart of our family is my Great Respectable Mother. May you both live long with sound health, peaceful and cheerful life ahead. My brothers **Khalid Usman, Arifullah, Hasibullah, Zakirullah, Wasimullah, and my sisters,** especially **Namra Gul,** always gave me support, love and kind words during my PhD project. **Ahya jan, Basrullah Jan, Kashif, Danish**, **Talha, Aimen**, Cute **Mowahid** and little **Mughera**, I love you all. I am also indebted to my uncle **“Sarwar Jan”** whose prays not only enabled me to achieve this target but also for his financial and moral support throughout my career. I am also grateful to my Cousins **Muhammad Amin** (PST), **Hazrat Amin** (SST), **Kalimullah** (SS), **Eng. Ikramullah** for their prayers, love and care.

I would like to express my thanks, regards and admiration to my Wife for her love, care and support, and for helping me and easing my life at home, especially when I was writing this thesis and Quarantined at home due to COVID-19 pandemic. Finally, I would like to thank everybody who contributed whatsoever towards the successful completion of my PhD thesis, directly or indirectly.

Akhtar Munir

ABSTRACT

The demand and consumption of energy is expected to be doubled in the coming 50 years and meanwhile the energy cost is also expected to rise significantly. Fossil fuels, currently the leading source of energy, subsidize a lot of CO_2 to the environment causing many environmental issues including greenhouse effect. To address these challenges, there is a dire need to develop alternative and renewable resources of energy. Water, being a renewable source, is a promising candidate in this regard because of its ability for the production of H_2 (HER) and O_2 (OER). OER is the $4e^-$ multistep process with a demand of 240-600 mV extra energy, which makes it more unfavorable both kinetically and thermodynamically. Intense research efforts have been made to accelerate the kinetics of water splitting process at the potential reasonably close to the thermodynamics limits (1.23 V). Until now, RuO_2 and IrO_2 are among the best electrocatalysts for OER, while Pt based materials for HER with minimum overpotential. However, their instability in wide pH range and high cost deteriorate their large scale applications. Therefore, the design and development of cost-effective and more efficient electrocatalysts is direly needed to make the water splitting process practically viable for the sustainable production of 'H_2'. In this regard, nanostructuring of the materials, especially those of supported transition metal oxides, has garnered much attention not only due to their natural abundance but also their tunable size dependent catalytic/electronic properties and high inherent redox potential for electrochemical water splitting. More promisingly, metal nanoclusters (NCs, size ≈ 2nm) are new emerging nanoscale materials for water redox reaction. The drastic decrease in their size and intriguing size dependent catalytic properties make them more fascinating due to their high surface to volume ratio and superatoms-like behavior unlike their bulk counterparts. This research work mainly focuses on the development the cost-effective transition metals (Co, Cu and Ni) based nanostructured materials (metal oxides and carbides) to control their size, shape, and chemistry of the underlying carbon based support as electrode materials for OER and overall water splitting process.

This dissertation is organized in the following manner. The first chapter deals with the background of the research topic, opportunities and resources of the energy conversion, potential of H_2 as a future energy carrier and chemistry of electrochemical water splitting. The 2nd chapter deals with experimental work/protocols for the synthesis of all the supported metal/metal oxides NCs and metal carbides reported in this thesis, their physicochemical and electrochemical characterization and very brief fundamental principles behind the analytical techniques used to better understand the results.

During this research work, we have initially developed the thiol functionalized graphene oxide (G-SH) nanosheets via selective epoxidation reaction. The surface modified and exfoliated 2D G-SH nanosheets were used as support materials for the immobilization of ultrasmall meta/metal oxides NCs, and their comparative evaluation and pre-/post spectroscopic investigation for water oxidation catalysis were made (chapter 4). Motivated by the remarkable performance of ultrasmall NCs, we extended this work to develop a facile solid-state strategy for the in-situ growth of $Co/Co(OH)_2$ NCs embedded in N-doped mesoporous carbon network (HCN) for OER (Chapter 5). These ultrasmall NCs have high electrochemical active surface area, maximum accessibility of active sites and high redox potential for OER while endorsing the fast heterogeneous electron transfer owing to the concerted synergistic effect. All the supported NCs have been found much more active than their bulk analogues and ligand stabilized NCs, and the $Co/Co(OH)_2$ NCs outperform all the NCs with low onset potential (1.44 V) and high stability (> 5 days).

We extended the above solid-state strategy for the synthesis of Ni/Ni_3C NPs catalyzed growth of NCNTs of different sizes as bifunctional electrocatalyst for water splitting in wide pH window (Chapter 6). It was found that the electrocatalytic performance of these catalysts depends on the size of Ni/Ni_3C NPs and thus also the size of NCNTs probably due to the internal structural strain and electronic modulation. We believe, that metal carbides have a great potential for overall water splitting owing to their appreciable mechanical strength, high conductivity, high stability in harsh condition and tunable electronic properties.

This thesis significantly contributes to the filed demonstrating novel findings at the interface of materials science and electrocatalysis through (1) the design of nanoscale materials (NCs) based electrocatalytic approaches (ii) spectroscopic investigation of structure-performance relationship (iii) and the structure and surface modification of carbon based supports for the redox reaction of water splitting in the wide pH range. These accomplishments may pave the way towards the development of more advanced materials with tunable structure-properties relationship in energy conversion science.

LIST OF JOURNAL PUBLICATIONS

Publications (as 1st Author)

1. **Akhtar Munir,** Tanveer ul Haq, Ahsanulhaq Qurashi, Habib ur Rehman, Anwar Ul-Hamid, and Irshad Hussain*. "Ultrasmall Ni/NiO Nanoclusters on Thiol-Functionalized and-Exfoliated Graphene Oxide Nanosheets for Durable Oxygen Evolution Reaction." ***ACS Applied Energy Materials***, 2018, 2, 363-371.
2. **Akhtar Munir**, Khurram Saleem Joya, Tanveer Ul Haq, Noor‐ Ul‐ Ain Babar, Syed Zajif Hussain, Ahsanulhaq Qurashi, Najeeb Ullah, and Irshad Hussain*. "Metal Nanoclusters: New Paradigm in Catalysis for Water Splitting, Solar and Chemical Energy Conversion." ***ChemSusChem***, 2019, 12, 1517-1548.
3. **Akhtar Munir**, Tanveer ul Haq, Iqtidar Hussain, Ahsanulhaq Qurashi, Ubaid Ullah, Muhammad Javed Iqbal, and Irshad Hussain*. "Ultrasmall $Co@Co(OH)_2$ Nanoclusters Embedded in N‐ Enriched Mesoporous Carbon Network as Efficient Electrocatalysts for Durable Water Oxidation." ***ChemSusChem***, 2019, 12, 5117-5125.
4. **Akhtar Munir**, Tanveer-ul-Haq, Iqtidar Hussain, Irfanullah, Syed Zajif Hussain, Ahsanulhaq Qurashi, Javed Iqbal, and Irshad Hussain*, Controlled Assembling of Nanoscale Cu/Co-oxide on Thiolated Graphene Oxide Nanosheets for Half-cell Oxygen Evolution Reaction *(revised manuscript submitted to* ***Chemistry-A European Journal, 2020 (in press)***
5. **Akhtar Munir**, Tanveer ul Haq, Murtaza Saleem, Ahsanulhaq Qurashi, Syed Zajif Hussain, Falak Sher, Anwar-Ul-Hamid, Asim Jilani, and Irshad Hussain*. Controlled Engineering of Nickel Carbide Induced N-Enriched Carbon Nanotubes for Hydrogen and Oxygen Evolution Reactions in Wide pH Range. ***Electrochimica Acta, 2020 (in Press)***.

Publications (as co-author)

6. Irfan Ullah, **Akhtar Munir**, Shoaib Muhammad, Saqib Ali,*, Nasir Khalid, Muhammad Zubair, Sajjad Ahmed, Yaqoob Khan, Irshad Hussain*, Ali Haider*. Influence of W-doping on the Optical and Electrical properties of SnO_2 towards Photodegradation and Electrochemical Water Splitting, "***Journal of Alloys and Compounds***, 2020, 154247.
7. Tanveer ul Haq, **Akhtar Munir**, Said A. Mansour, Yousef Haik*, Gold-Supported Gadolinium doped Co-B Amorphous Sheets: A new Benchmark Electrocatalyst for Water Oxidation with High TOF, ***Advanced Functional Materials,*** *2020,* 1910309 ***(In Press)***
8. Tanveer ul Haq, Yusuf Bicer, **Akhtar Munir**, Mansour Said, Yousef Haik*. Surface Assembling of Highly Interconnected and Vertically Aligned Porous Nanosheets of Gd-CoB on TiO_2 nanoflower for durable methanol oxidation reaction***, ChemCatChem, 2020 (In Press)***
9. Farhan Arshad, **Akhtar Munir**, Qasim Qayyum Kashif, Tanveer ul Haq, Javed Iqbal, Falak Sher, Irshad Hussain*. Controlled Development of Higher-Dimensional Nanostructured Copper Oxide Thin Films as Binder Free Electrocatalysts for Oxygen Evolution Reaction, ***International Journal of Hydrogen Energy***, ***2020 (In Press)***.

CONFERENCE PRESENTATIONS

- Oral Talk at **2nd International Conference on Nanoscience & Nanotechnology** (**ICONN-2019**), LUMS, Lahore.
- Oral Talk at a **Symposium on Advanced Energy Material,** PINSTECH, Islamabad.
- Poster presentation at **2nd Sustainable and Green Energy Technology 2019,** U.S. Pakistan Center for Advanced Studies in Energy (USPCASE), UET, Peshawar.
- Oral Talk at '**1st International Conference on Nanoscience & Nanotechnology** (**ICONN-2018**), NUST, Islamabad.
- Poster presentation at International workshop on **'Energy Materials and Nanotechnology-2019**, COMSATS University Islamabad, Abbottabad Campus, 2018.
- Poster Presentation at International workshop on the '**Advanced Characterization Techniques – 2019,** COMSATS University Islamabad, Abbottabad Campus.

TABLE OF CONTENTS

LIST OF ACRONYMS

OER	Oxygen Evolution Reaction
HER	Hydrogen Evolution Reaction
RHE	Reversible Hydrogen Electrode
CE	Counter Electrode
Ag/AgCl	Silver/Silver Chloride
Hg/HgO	Mercury/Mercury Oxide
FTO	Fluorinated Tin Oxide
GC	Glassy Carbon
CCE	Chronoamperometry
CPE	Chronopotentiometry
LSV	Linear Swap Voltammetry
CV	Cyclic Voltammetry
TOF	Turn Over Frequency
ECSA	Electrochemically Active Surface Area
Cdl	Double Layer Capacitance
FE	Faradaic Efficiency
EIS	Electrochemical Impedance Spectroscopy
Rct	Charge Transfer Resistance
Rs	Solution Resistance
IR	Infrared Spectroscopy
SEM	Scanning Electron Microscopy
STEM	Scanning Transmission Electron Microscopy
EDX	Energy Dispersive X-rays Spectroscopy
TEM	Transmission Electron Microscopy
HRTEM	High Resolution Transmission Electron Microscopy
XPS	X-ray Photoelectron Spectroscopy
PXRD	Powder X-ray Diffraction
PEC	Electron Conversion Efficiency
HET	Heterogeneous Electron Transfer
PMTs	Photomultiplier Tubes

PE	Primary Electron
SE	Secondary Electron
BSE	Back Scattered Electron
NPs	Nanoparticles
Hcp	Hexagonal Close Packing
SP	Sabatier principle
HOMO	Highest Occupied Molecular Orbital
LUMO	Lowest Unoccupied Molecular Orbital
PV	Photovoltaic
NCs	Nanoclusters
G-SH	Thiolated Graphene Oxide
BNCs	Beaded Nanoclusters
HCN	Honeycomb like N-doped Carbon
LDHs	Layered Double Hydroxides
NCNT	Nitrogen Doped Carbon Nanotubes
NSts	Nanosheets
MOFs	Metal Organic Frameworks
ORR	Oxygen Reduction Reaction
PEM	Proton Exchange Membrane
PVP	Polyvinyl
GO	Reduced Graphene Oxide
HET	Heterogeneous Electrons Transfer
NCNT	Nitrogen doped carbon nanotubes
PET	2-phenylethane thiol
THF	Tetrahydrofuran
RDM	Redox Mediator
TOC	Table of Content
NFs	Nanoflowers
RT	Room Temperature
KJ	Kilo Joule

LIST OF FIGURES

LIST OF SCHEMES

LIST OF TABLES

Chapter 1.

Introduction and Background

1.1. Scope of the Sustainable Energy Conversion and Storage

Decoupling of energy and its production from fossil fuels demands us to develop and install renewable energy plants to equilibrate its supply and demand.[1] But the worldwide distribution of renewable energy resources pose various challenges regarding the design and efficiency of power distribution systems. On the other hand, these resources provide an opportunity for the large production of energy on industrial scale. It is believed that chemical bond is the central fulcrum between energy and materials and this freedom has been taken seriously by chemical sector around the globe. There is, therefore, a need to store renewable energy in the form of chemical bonds and its controlled harnessing *via* energy transfer/storage processes. Some major energy renewable sources such as sun, wind, water, and biomass can be utilized for the production of chemicals and electrical energy especially with the technological utilization of ever green solar power for the energy conversion/storage processes.[2,3, 4,5] The stored energy, be it in the form of chemical species or electricity, can be a source of fuel as an alternative to fossil fuels which are continuously generating CO_2 - a major source of global warming and serious threat to nature and human beings.[6,7] However, this threat can be minimized by converting CO_2 into useful industrial products or exploration of renewable resources production/storage of fuel/electricity with zero carbon footprint. In this regards, many countries including UK, US, Japan, China, and Germany have invested a lot to decrease their reliance on fossils fuels.[8] For instance, in 2014-2015, the electricity production in UK was increased up to 25% from the renewable energy resources, and they are now expecting to pleasantly meet their target for 2020 in view point of their progress, budget/projects and Govt. policies.[8] Similarly, Germany has also taken serious steps and banned the deployment of new fossil fuel based power plants and is considered as a pioneer country to lead the world particularly in solar energy production/storage technology. The successful implementation is also evident from the consistently drastic decrease in the CO_2 emission (27 % reduction since 1990), however, still far away from the set target (40% decrease by 2020). In addition, being a major contributor of CO_2 to the environment, China has also taken huge steps to replace the existing fossil fuel based power plants. Including many energy production and storage plants, currently the world largest Si based solar plant was employed on the surface of sea with the capacity to produce 40 MJ of energy. Similarly, Japan has recently installed the world largest H_2 production plant expanded over several kilometers to empower the fuel cell technology with the objective to partially/completely replace the usage of fossils fuels. Keeping in view the world trend/curiosity and expected energy demand of 22 TW by 2030, the implementation of renewable energy resources and their effective storage in the form of electricity/chemical species have been envisioned the only solution at least to maintain the current level of CO_2 in the atmosphere (≈ 400 ppm).[9] Hence, much effort is needed to decrease the cost and decoupling of proper/mature technology/infrastructure to meet the energy/fuel demand in a stipulated timeframe for the sustainable future.

1.2. Water Splitting as Future Energy Carrier (H_2 Economy)

Currently, hydrogen (H_2) is a key component of many vital industrial processes. For example, ammonia, fertilizers, oil refineries and petrochemicals are among the few industries that consume over 25 million tons of hydrogen each year. Historically, 3.2 billion years ago, nature has launched ever green photosynthesis process in plants to use the solar driven chemistry for the sustainable H_2 production.[10] Motivated by the natural approach for the production of environmentally benign fuel and its realization as an appealing solution to the intermittency of solar/wind energy, scientists have turned their efforts to produce H_2 as an undisputed future energy carrier. It is one of the neat and clean sources of energy with inherently highest mass energy density (120-140 MJ/kg) and 100% efficiency that is three to four times higher than the corresponding energy capacity of traditional fossil fuels. However, currently, over 90% of H_2 is being produced through a steam reforming process (SRP) from the fossil fuels at high temperature (700 -1100 °C), which are subsidizing a huge amount of CO_2 and many unwanted gases to the environment that causes global warming and many environmental issues and thus becoming a serious threat to the humanity around the globe. Therefore, there is an urgent need to address these problems for the safe and sustainable future while exploiting the renewable energy resources (sun, water, wind and biomass) for environmentally benign H_2 production. Among the renewable energy resources, water is one of the most clean and abundant source of hydrogen available to the planet. Photo- and electro-induced water splitting, to release electrons, protons and oxygen molecules instigate the energy experts to adopt as a promising pathway for the production of 'H_2' - a way forward to the H_2 based economy.[11,12] Various types of water splitting modules can be deployed to store/utilize the produced H_2 in the same manner as fossil fuels.[13]

1.3. Energy Storage Technology and Water Splitting on the Move

Generally, there are various energy storage processes including mechanical, thermal, and storage in the form of electricity and chemical bonds which are functional to meet the energy demand.[14] Among the various approaches, the **mechanical storage** of energy is the ancient/oldest and an easy approach. In this technology, the water is pumped/stored in a large reservoir with high potential energy. The stored water can be periodically used to run the same or different turbine/generator, thereby converting the potential energy to electrical energy. Although, it is cost-effective and an easy approach, however it does not match much with the diurnal solar cycle. For instance, it is likely impossible to refill and utilize such a big reservoir on daily basis. However, it can be used when large amount of energy is needed for long-term purpose and may substitute to cover any mishap in the energy supply system.

While, thermal energy is referred to '**solar thermal technology'** where the solar energy is stored in the form of heat by heating the water or other small molecules.[14] The thermally treated water can be supplied to the houses, building and even industries, where many industrial process can be accelerated with vapor/steam. It is an easy and simple approach, and has great potential to replace the natural gas if integrated in an effective manner. Another option is the electricity storage devices known as '**batteries'**. Battery works on charging and discharging principle, where the charged species (ions and electrons) are stored on the corresponding electrodes (charging) to create electric potential. The created potential difference between the electrodes can be desirably utilized (discharging) by providing an external load. Currently, batteries are in use everywhere especially the Li-ions batteries, which are the leading commercial energy storage devices in various fields including portable devices. More promisingly, these energy storage devices can be coupled with solar/wind energy to store energy in the form of electricity. However, the large scale application of such devices are still limited due to the low energy density in term of both weight and volume. Moreover, the instability, low shelf life of electrode materials and continuous decrease in their charging capacity further hamper their commercial applications for the electric vehicles and grid level infrastructure.

Yet another option is the storage of energy in the form of **chemical bonds**. In this case, the energy is stored in the form of chemical bonds and can be harnessed on demand by the controlled breakage of chemical bonds. In this quest, water is very promising source of energy that is found everywhere in the world.[13] It can be splitted in to green protons, electrons and oxygen molecules, which can be used in a variety of redox reactions for the production of chemicals stock even on industrial level. More promisingly, the produced protons can be reduced to molecular H_2 – and is considered a promising chemical solution to meet the future energy demand. It can be conventionally splitted by various means, for example i) thermal splitting (at 2000 and 2500 °C), ii) thermochemical water splitting (based on the chemical cycle) and iii) photo-biological water splitting (with green algae and cyanobacteria). However, all the above methods are commercially less viable due to various reasons including the need of high temperature, less compatibility of electrode materials, and especially the less/slow conversion efficiency of biological water splitting process. Therefore, the electrochemical and photo-electrochemical water splitting is currently the well accepted and leading pathway towards the solar-assisted H_2 based economy. However, serious efforts are still needed for the deployment of large electrolyzers with high efficiency and significant drop in their cost is essentially required to compete the existing sources of energy.[13]

1.4. Water Splitting and Various Integrated Systems

Conventionally, water electrolysis takes place in two electrodes system, where oxygen evolution reaction (OER) and hydrogen evolution reaction (HER) take place at the anode and cathode respectively as shown in the **Fig. 1.1(Equation 1.1, 1.2)**.[11]

$$2\ H_2O_{(l)} \rightarrow 4e^- + 4H^+_{(aq)} + O_{2(g)} \text{ (Oxidation reaction at anode, OER)} \qquad 1.1$$

$$4e^- + 4H^+_{(aq)} \rightarrow 2H_{2(g)} \text{ (Reduction reaction at cathode, HER)} \qquad 1.2$$

Bothe OER and HER are energy intense processes with high thermodynamic demand, where the overall water splitting can be carried out by providing at least the thermodynamic potential of 1.23 V vs RHE. To provide a sufficient amount of energy, it can be carried out either electrochemically (electrocatalysis) or photochemically (photocatalysis). In case of photocatalysis, semiconducting materials, mimicking natural photosystem II, are used as light harvesters and energy converters. After irradiation, electron-hole pairs (excitons) are generated by the excitation of electrons from the valence band of photocatalysts to the conduction band. The production of H_2 *via* this energy conversion scheme is achieved by solar-fuel devices, which comprise of photovoltaic materials (PV), proton exchange membrane (PEM), oxidation and reduction catalysts.[14] However, architecturally it can be categorized as wireless and wired configuration (**Fig. 1.1**).[11] In wireless configuration, semiconducting materials (photovoltaic cells) are directly exposed to sunlight, the electrons and holes are trapped towards the respective/opposite poles for the oxidation and reduction processes at the interface of catalysts-electrolyte interface. However, in the wired configuration, the electrodes are externally connected thorough conducting wire and internally separated by PEM. After trapping the sunlight, the oxidation of water takes place at the hole, while electrons are transferred towards the cathode *via* external circuit to complete the cycle. In both configuration, the produced hydrogen can be stored from the respective electrodes while directly harvesting the sunlight.[11] Although, these are the desirable approaches having their own advantages and chemistry, but not the subject of this dissertation. We will, therefore, mainly focus the electrochemical water splitting module, their electrode chemistry and future perspectives.

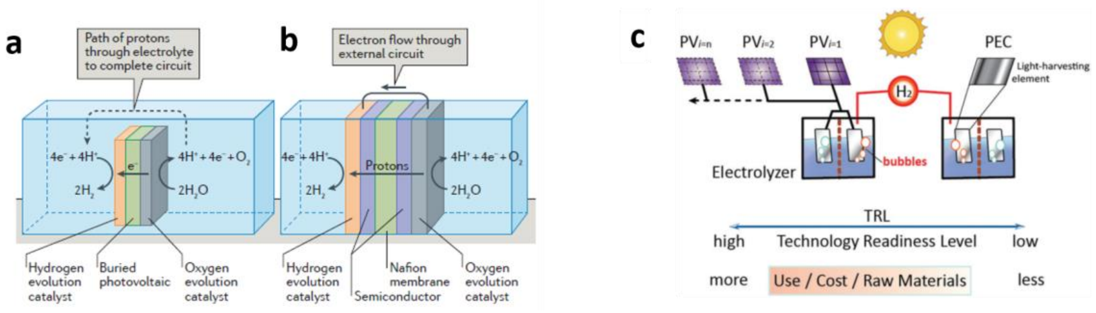

Figure 1.1 Schematic illustration of various water splitting modules (a) wireless configuration for photocatalytic water splitting assembled with PV cell in-between the electrodes (b) wired configuration for photocatalytic water splitting assembled with semiconductors based materials as light harvester (c) PV-cell electrolysis (left) and comparison with photocatalytic water splitting (right).

1.5. Electrochemical Water Splitting Module

Electrochemically, water can be heterogeneously splitted at the surface of electrodes by providing potential across the electrodes beyond the thermodynamic potential (1.23V). During oxidation of water, electrons, protons (H^+) and molecular oxygen are produced at the anode. These protons and electrons move towards the cathode *via* electrolyte and external circuit respectively to complete the cycle with the liberation of molecular H_2.[11] Generally, there are two different types of commercially available electrolyzers: i) alkaline electrolyzers and ii) proton exchange membrane (PEM) electrolyzers. The later one is highly efficient with the potential to deliver a current density of 1000-2000 mA/cm^2 while using highly expensive electrode materials. While, alkaline based electrolyzers are assembled with transition metal based electrode material (Ni based spinel family and perovskite) and produce comparatively low current density (20-30 mA/cm^2). Both these electrolyzers work in extremely alkaline conditions (high pH). Apart from these two electrolyzers, **solid oxide based electrolyzer**s have also been introduced to work at high temperature with high efficiency. However, due to the demand of high input potential at ambient conditions and less efficiency of overall water splitting process, the cost of hydrogen produced from water electrolysis currently stands at about 2-3 times of that produced from steam reforming process. Therefore, PV-cell electrolysis is an advanced version of water splitting process, where the electricity is provided by PV-cell by harvesting the sun light (**Fig 1.1c**).[15] Thus, solar-driven electrochemical water splitting process is the leading and burning area of research with comparatively low cost and high technology readiness level as compared to the traditional electrolyzers and simple photocatalysis (**Fig. 1.2**).[15] However, scientifically, it can be apprehended first by designing highly efficient PV material with high photon to electron conversion efficiency (PEC), which can be stored in batteries to drive a competent electrolyzer for overall water splitting process with high conversion efficiency.[16] The integration of these two modules (electrolyzer and PV) in a single assembly with proper storage of H_2 gas is the valuable pathway towards the electrochemical solar-driven technology for the sustainable hydrogen production. Although, the technical challenges, societal perception, political impact, and research opportunity are equally important to establish such an independent energy production grid. Currently, the penetration of PV cell in the market and continuous decrease in their cost is the positive indication of this technology.

However, it is equally important to improve the catalytic efficiency of electrolyzers to energetically accelerate the challenging redox reaction of water splitting process at low cost with high conversion efficiency. To address the associated problems with electrolyzers and the mediocre activity of the earth abundant materials, currently, various models have been introduced to somehow improve the water conversion efficiency. For instance, i) **overall water splitting process**, ii) **decoupled water splitting process** iii) **hybrid water splitting approach** and iv) **tandem water splitting approach** are the newly introduced models in this regard (**Fig 1.2**).[17]

Generally, the kinetics of OER and HER process can be improved by using basic and acidic medium respectively. However, the electrode set up becomes more complex while assembling an independent/separate compartment for the respective redox reactions. Therefore, it is highly desired to develop catalysts, which are bifunctional in nature and effective in a wide pH range or at least can catalyze both OER and HER at neutral pH (**Fig. 1.2a)**. The deployment of such a bifunctional catalysts are indeed fruitful not only to simplify the architecture of electrodes but also can significantly reduce the cost of overall water splitting process. However, among the two half-cell reactions, OER process is kinetically slow and, therefore, cannot meet the number of electrons needed for the reduction of protons on the counter electrode. To address this challenge, a new model with special separation of OER and HER compartment with redox mediator (RDM) has been introduced and is known as decoupled water electrolysis (**Fig. 1.2b**). The function of RDM is to stop the mixing of H_2/O_2 (reversible reaction) and meanwhile, partially prevent the formation of oxygen species by oxidizing itself in a solution instead of typical OER process. During the oxidation, RDM delivers electrons to the external circuit and back reduce on the same electrode coupled with OER. In this way, the chance of reversible reaction can be minimized while covering the deficiency of electron arising from the slow kinetics of OER. Similarly, the demand of high input potential for OER is also a daunting challenge that needs to be addressed for the efficient electrolyzers. In addition, the molecular O_2 produced during oxidation process is not a deemed product of water splitting process. In this regard, hybrid water electrolysis concept offers an alternative route, where the biomass derived small compounds/intermediates with high thermodynamic favorability, for example urea, thiourea, and HMF derived molecules etc., are used in electrolyzers which are oxidized at low overpotential compared to OER (**Fig. 1.2c)**.

Therefore, the easy oxidation of organic moieties at anode can possibly not only trim down the overpotential for overall water splitting process but also produce the valuable organic products. In addition, it can also prevent the mixing of H_2/O_2 and enhances the selectivity of proton reduction at cathode in the presence of other organic species.

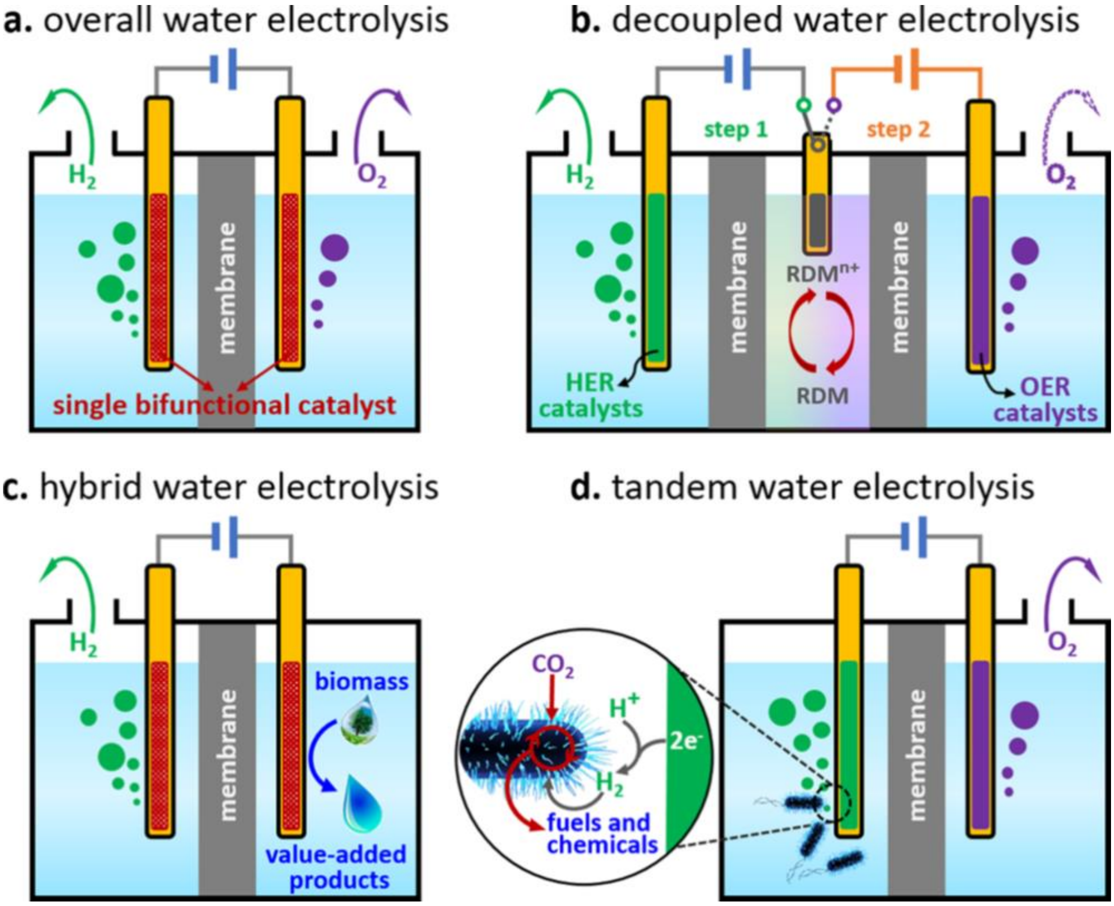

Figure 1.2 Schematic illustration of various electrochemical water splitting modules (a) overall water splitting catalysis using bifunctional electrode materials (b) decoupled water splitting scheme with redox mediator (RDM) (c) hybrid water splitting scheme with catalysis of biomass (d) tandem water splitting scheme for the direct utilization of H_2 with consumption of CO_2.

Once water is splitted, the next serious challenge is its cost-effective storage and transportation of H_2. To address this challenge, a new alternative scheme analogous to the natural photosystem II known as 'tandem water splitting' has been introduced. In this conversion scheme, the liberated H_2 can be directly utilized for the reduction of CO_2 on the cathode catalyzed by biological catalysts (enzymes) to produce the value-added products (CH_4 and NH_3 etc.). It has been considered an encouraging scheme if integrated on large scale for the perfect utilization of H_2, consumption of CO_2 gas, and production of value-added chemicals/fuels through water electrolysis (**Fig. 1.2d)**.

Taking into account the advantages of all the electrolyzers and various water splitting modules, the overall water splitting process by using bifunctional electrode material is of paramount importance and comparatively more mature. During the last few decades, a significant efforts have been directed to explore the nature of electrocatalysts, electrode chemistry, and mechanism to further enhance the efficiency of electrolyzers, and to increase the interest and achieve technology readiness level of solar-assisted water splitting pathway.

1.6. Thermodynamics and Chemistry of Electro-assisted Water Splitting

The overall water electrolysis reaction can be written as below:

$$H_2O_{(l)} \longrightarrow H_{2(g)} + \frac{1}{2}O_{2(g)} \qquad 1.3$$

Experimentally, it can be carried out in an electrochemical cell equipped with 2/3 electrodes set up. The electrodes are immersed in an appropriate electrolyte and are electronically wired with potential source (Potentiosat). The function of Potentiostate is to control/supply the potential across the electrodes.[11] The electrolysis process under specific conditions recognizes a set of thermodynamics values including cell potential, electrons transferred, and enthalpy change (heat transferred). Like many other reactions, water splitting is also an endothermic reaction at ambient conditions (STP). The **equation 1.3** indicates that the amount of released energy (enthalpy change, ΔH_{ws}) during electrolysis is equal to the heat of formation (enthalpy of formation, $-\Delta H_f$) of 1 mole of water. This absolute amount of energy (286 kj/mol or 2.96 eV) is equal to the highest amount of heat (H_{HH}) released by burning 1 mole of H_2.[18]

However, the minimum required potential (equilibrium potential) for the reversible electrolysis is 1.23 V, which depends upon the Gibb's free energy of any reaction as below:

$$\Delta G = nFE_o \quad \text{or} \qquad 1.4$$

$$\Delta G = 2FE_o \qquad 1.5$$

Where ΔG is the Gibb's free energy change, n is the number of electrons ($2e^-$ for 1 mole of H_2O), F is the Faraday constant (96485 C/mol) and E_o is the required potential. It is experimentally verified that ΔG for water splitting is +237.38 kJ/mol (water) or 2.46 eV. So by taking the absolute value of cell/equilibrium potential (1.23 V) and incorporating the entropy factor, the total amount of energy required for water splitting at 298 K can be written as:

$\Delta H_{ws} = \Delta H^{o}_{HH} = -\Delta H^{o}_{f} = \Delta G_{ws} + T\Delta S^{o}_{ws}$ 1.6

The last term represents the change in the entropy at STP which is 49 kj/mol and implies that this much energy will be gained from the surrounding (electrolyte) which can also be considered as input energy for water splitting process. Therefore, the highest amount of required potential can be written as:

$\Delta H^{o}_{HH} = V^{o}_{HH} = 2FE_{o} = 1.48$ V 1.7

The above equation 1.6 indicates that water electrolysis is an endothermic process at STP in the applied potential range of 1.23-1.48 V. Conceptually, electrolysis under the ideal condition (excluding all the ohmic resistance/loss processes) at the potential ≤ 1.48 V, the system will cool down or may operate isothermally if provided with continues supply of heat. **Equation 1.6** and **1.7** also show the possible drop of input/applied potential at elevated temperature.

The above discussion reveals that due to the positive Gibb's free energy change of water electrolysis, the reaction is non-spontaneous in nature. To make the reaction downhill, a potential difference of at least 1.23 V between the electrodes should be provided. However, by increasing/decreasing the temperature or changing the reaction conditions, the potential range can be broadened.

1.6.1. Electrodes Chemistry

The standard electrode potential required to derive the half-cell reactions taking place at the cathode and anode can be expressed by Nernst equation.

1.6.1.1. Reaction at Cathode

$2H^{+} + 2e^{-} \longrightarrow H_{2}$, $E^{o} = 0.0$ V vs RHE 1.8

$E = E^{o} + 0.059/2 * \log [H^{+}]^{2}$, by applying the logarithmic formula, we can write it as:

$E = E^o + 0.059*\log [H^+] = 0.0 + 0.059*pH$ 1.9

1.6.1.2. Reaction at Anode

$2H_2O \longrightarrow 2H^+ + O_2 + 4e^-$, E = 1.23 V vs RHE 1.10

$E = E^o + 0.059/4* \log [H^+]^4$

$E = E^o + 0.059*\log [H^+] = 1.23 + 0.059*pH$ 1.11

From the above equations, it is clear that potential difference of 1.23 V is required to execute the water splitting reaction. However, due to the ohmic resistance and other loss processes across the electrode-electrolyte interface, practically we need to provide potential higher than 1.23V, and this extra potential is called the overpotential (η). Therefore, the final cell potential can be written as:

$E_{applied} = 1.23 + \eta_{cathode} + \eta_{anode} + iR$ 1.12

It is also noteworthy to mention here that the applied cell potential is highly dependent upon the pH of the reaction medium (**Fig 1.3b**). Although, in overall water splitting process, the pH factor cancel each other, however, it is extremely important for measuring the potential with potentiostate for half-cell reaction. Therefore, we usually measure/normalize the potential against the '**Reversible Hydrogen Electrode'** to nullify the pH factor and thus can directly measure redox potential for the respective Faradaic reaction (**Equation 1.11**). **Fig 1.3** shows that the range of the applied potential systematically decreases/increases by varying pH of the reaction medium. More precisely, slope of the plot (potential vs pH) in the whole pH range relates the jump of 59 mV in the applied cell potential while increasing the pH by one degree.[19]

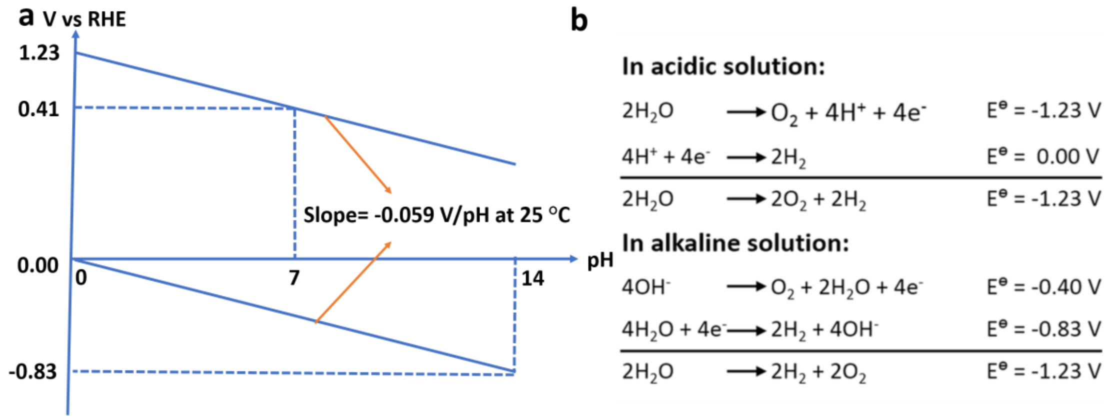

Figure 1.3 Schematic illustration of pH dependent cell potential for water splitting (a) pH vs potential graph with a slope of 0.059 V (b) water splitting reaction in acidic and basic medium and their corresponding cell potentials.

1.7. Figure of Merits and Water Splitting Catalysis

Electrochemical water splitting can be carried in a proper cell equipped with standard electrode set up (reference electrode, counter electrode and working electrode), conducting electrolyte and potential controller. In three electrodes system, the potential is controlled across the working electrode either for reduction or oxidation process, where the potential range depends upon the thermodynamics of a particular reaction. In overall water splitting process, two electrodes i.e., cathode and anode are used for the redox reaction. However, in half-cell reaction, only working electrode is decorated with desired catalytic materials and evaluated for their catalytic potential by performing various experiments. Various parameters including overpotential, Tafel slope, stability test, turnover frequency (TOF), Faradaic efficiency and electrochemical active surface area are discussed in details.

1.7.1. Overpotential (η)

Overpotential is one of the most imperative parameters to evaluate the efficiency and inherent competency of electrocatalyst for the challenging catalysis reaction. Electrochemically, each reaction has its equilibrium potential (EP), where overpotential is an extra potential required to spontaneously drive an electrochemical process from its EP. The EP for water splitting is 1.23 V vs RHE, which is the minimum required potential to split one mole of water at standard conditions.[20] Ideally, the applied potential should be equal to the EP to initiate an electrochemical reaction. However, in practice, the kinetic hurdles and various ohmic losses kill the ideal environment around the electrodes and, therefore, increase the demand of input potential that is called overpotential.[21] There are various possible origins of overpotential, for example activation overpotential, concentration overpotential, and resistance overpotential etc. The activation overpotential is the inherent property of catalyst which can be reduced by selecting active catalytic materials. While, concentration overpotential appears during the electrolysis process under given operating conditions. After the start of electrolysis process, the drop of concentration near the electrode leads to the overpotential probably due to the limiting diffusion and non-homogeneous distribution of ions. However, it can be controlled to some extent by stirring the reaction medium. Similarly, resistance at the interfaces of the system also contribute to the overpotential which is also called the junction resistance. It can be eliminated by measuring the iR compensated data. In addition, the bubbles formation on the surface of electrodes and their improper detachment may also contribute to the overpotential. **Equation 1.12** represents the final operating potential, which may vary for different materials/reaction. Therefore, low overpotential means that electrocatalyst and reaction conditions are suitable to initiate the electrolysis very close to the equilibrium potential. Moreover, the amount of current density obtained beyond the onset potential is also an important parameter to evaluate the consistent performance of electrode materials in a narrow potential range. Generally, an overpotential required to reach a current density of 10 $mAcm^{-2}$ is used in the literature for the comparison of electrocatalysts. However, this comparison is meaningful only, if all the catalysts are exposed in identical environment especially the pH of electrolyte and temperature around the electrodes.[19]

1.7.2. Tafel Slope

The voltage and current are the fundamental constraints in any electrochemical process. Nocera *et al.* have verified that varying the potential window basically corresponds to tune the driving force of electrode-electrolyte system.[22] In this regards, Tafel slope analysis is the most widely accepted parameter to investigate the kinetics and mechanistic details of electrochemical process. For multi-step reactions like OER/HER, the relation between current and applied potential is represented by following equation (**Equation 1.13**):

$i = i_o \exp^{(\alpha F\eta/RT)}$ 1.13

where α_a: equilibrium/transfer coefficient, η: overpotential, i_o: exchange current density, which shows the rate of reaction at an equilibrium potential. In logarithmic form, we can write this equation as:

$\ln i = \ln i_o + \alpha F\eta/RT$ 1.14

By taking natural log:

$2.303\log i = 2.303\log i_o + 2.303\alpha F\eta/RT$ 1.15

Dividing by 2.303

$\log i = \log i_o + 2.303\alpha F\eta/RT$ 1.16

The above equation can be rearranged as below:

$\eta = a + b \log i_o$ 1.17

This expression is known as Tafel equation, where 'a' is constant and 'b' is Tafel slope (2.303αF/RT). It can also be written as below:

$b = \delta\eta/ \delta\log(i) = 2.303\ RT/\alpha_a F$ 1.18

From the equation 1.18, Tafel slope is the rate of change of current with respect to overpotential during electrochemical reaction. From the steady-state polarization curve, if we take a current density (j) and plot log j against the overpotential. The linear fit of log j vs η gives a Tafel slope value which is the well balanced representative of an electrode process. It provides information about the reaction mechanism, rate-determining step and kinetics of the entire electrochemical reaction. Generally, smaller Tafel slope values means the kinetically fast electrode process (fast charge transfer) and vice versa. It is more useful to calculate it in the region of onset potential because Tafel slope may vary by selecting higher and lower potential region even for the same rate-determining step.[23] The details of relation between the Tafel slope and possible mechanism/rate-determining step for both HER and OER are discussed in section 1.9. However, it is noteworthy to mention here that solution resistance (Rs) and charge transfer resistance (Rct) may hamper the kinetics of OER process. More precisely, when the Rs value is greater than 6 Ω and catalyst exhibits a high current density (J_{max} greater than 100 $mAcm^{-2}$).[24] Therefore, for the true kinetics of catalytic reaction, electrochemical impedance spectroscopy (EIS) can be used. For this purpose, it is necessary to collect the data at least 100 mV of extra overpotential in addition to the overpotential observed from the cyclic voltammogram. In this way, the 1/Rct gives accurate equilibrium (exchange) current density at different high overpotential to present the kinetics of overall electrode process in the wide potential range and thus minimizes the experimental errors usually associated with the Tafel slope calculated from CV.[24]

1.7.3. Exchange Current Density (I_o)

Exchange current density is one of the decisive parameters to evaluate the reaction kinetics at equilibrium. The magnitude of exchange current density (sum of cathodic and anodic current) replicates the charge transfer ability between reactant molecules (electrolyte) and electrocatalyst. Therefore, high exchange current density signposts the kinetic favorability of the electrocatalytic reaction at specified potential, which can be attributed to the optimum interaction of reaction intermediates with the electrode surface. Despite a decent approach to reveal the rate of electrochemical reaction for a specified catalyst, it is very difficult to directly estimate it, since experimentally we can only get overall current density. Generally, by extending the linear fit of a Tafel plot (up to η = 0 V) the magnitude of exchange current density at equilibrium can be calculated. In addition, it can also be calculated from the charge transfer resistance of catalyst (**Equation 1.19**).[25]

$$I_o = RT/ n*F*\theta \qquad 1.19$$

Where R is universal gas constant, T is absolute temperature, n is the number of electrons transfer in electrochemical reaction (4 for OER and 2 for HER) and θ is charge transfer resistance in ohm.

1.7.4. Turnover Frequency (TOF)

Turnover frequency (TOF) is the “rate of product molecules evolved per unit time”. It can disclose the intrinsic power of the active sites of catalyst to recycle the desired process without damaging itself. High TOF for a catalyst reveals that it can periodically catalyze the chemical reaction for the selected product with high exchange rate.[26] It can be calculated from **equation 1.20** below:

$$\text{TOF} = (I * N_A) / (4 * F * n * A * \Gamma) \qquad 1.20$$

Where I (A) symbolizes the current density at a given overpotential; N_A is the Avogadro number, F is Faraday's constant (96485.3 C mol^{-1}), A is the geometric area of working electrode; n is the number of electrons involved in an electrochemical process and **Γ** shows the moles (mol) of metal atoms (surface concentration of atoms) deposited on the electrode. During catalysis, the electrochemical accessibility of all atoms is not possible, therefore it is very challenging to get the precise value of TOF. It is, however, the most widely accepted parameter to calculate the surface concentration of exposed metal atoms from the integral area of a reduction peak of redox couple.[24]

1.7.5. Faradaic Efficiency (FE)

Faradaic efficiency is an electrochemical parameter, which provides information about the selectivity of electrode materials for the quantification of a reaction product. During electrochemical reaction, the Faradaic current response is usually calculated from the redox reaction by measuring/detecting the evolved gases. In this way, the nature and purity of the desired product and origin of the current response can be analyzed. During water splitting reaction, both H_2 and O_2 gases are produced at cathode and anode respectively. For analysis, gas chromatography (GC) is one of the valuable tools that can be used to detect the evolved gases by directly injecting the sample in to the GC column. The evolved gases can also be quantified by GC, if compared with the internal standard calibration curve. For the O_2 measurement, O_2-sensitive electrode can also be used. In addition, water displacement method is one of simplest approaches for the quantification of molecular O_2 and H_2 while using the ideal gas equation (PV = nRT).[27] In this quantification method, it is assumed that all the electrons in the external circuit are generated purely from the water oxidation process which can subsequently reduce the protons (no charged contribution from capacitive current). FE of more than 95 % for both OER and HER validate the efficiency and selectivity of electrocatalyst for overall water splitting process.

$$\text{Faradaic efficiency} = V_{\text{experimental}} / V_{\text{Theoretical}} \qquad 1.21$$

Where theoretical values can be calculated from Faraday's law:

For OER: $\text{Volume}_{\text{(theoretical)}} = 1/4 * Q/F * V_m$ or $Q*V_m/4F$ 1.22

For HER: $\text{Volume}_{\text{(theoretical)}} = 1/2 * Q/F * V_m$ or $Q*V_m/2F$ 1.23

In equations 1.22 and 1.23, the number 1 means 1 mole of O_2/mole of H_2O, 4 means 4 moles of electrons/per mole of H_2O and 2 means 2 moles of electrons/mole of H_2O. If we don't multiply the above equation with V_m, then we can directly calculate the number of moles of evolved O_2 gas.

In the above equations,

Q = It (the amount of charged passed through electrode Unit =A.sec or Coulomb)

F = Faraday constant (96485 C mol^{-1})

V_m = Molar volume of gas (24.1 $Lmol^{-1}$, 293 K, 101 kPa)

Note: The experimentally produced volume of gas at different time intervals at fixed current is noted while running chronopotentiometry experiment. Similarly, the theoretical volume of gas (V_1, V_2, $V_3 \ldots V_n$) at different time intervals (t_1, t_2, $t_3 \ldots t_n$) at fixed current is calculated using equation 1.22 and 1.23 for OER and HER respectively. Finally, from the plot of volumes *vs* time, the Faradic Efficiency is calculated from slope and is equal to slope*100 (equation 1.21).

1.7.6. Chronopotentiometry and Chronoamperometry

Stability of electrocatalyst is among the most important parameters especially from the point of the commercialization of this technology. Therefore, it is worth mentioning that the lowest onset/over potential is meaningless, if the catalyst is not stable both at low and high current density. Water splitting is a multistep process with the formation of various involved intermediates. Industrially, it can be carried out in the harsh acidic/basic conditions and at high temperature. Therefore, the potential induced transformation and harsh operating condition deteriorate the long-term performance of electrocatalyst. Usually metal based catalysts oxidize to high oxidation state where the polarity index values of metal oxides are matched with water and consequently catalyst can leach out from the surface of working electrode towards electrolyte. Sometimes, the inactive phases are also generated on the surface of catalyst which can be observed from the stability test. Therefore, it is highly desirable to evaluate the persistent performance of electrode materials at least for 24 h in the conditions analogous to the commercial electrolyzers. Controlled current electrolysis (chronopotentiometry) and controlled potential electrolysis (chronoamperometry) are the two well-accepted experiments to evaluate the stability of catalysts under the operating conditions. In chronopotentiometry, the catalytic material is held at a constant current density per geometric surface area while the operating potential is measured as a function of time. Whereas in chronoamperometry, change and-/or consistency in the current is recorded with respect to the time at fixed applied potential. Apart from these, recycling of cyclic voltammetry (CV) and linear swap voltammetry can also be performed to assess the stability of electrocatalysts.[28]

1.7.7. Electrochemical Active Surface Area (ECSA)

Electrochemical surface area can be calculated from capacitive current response in the non-Faradaic region.

Double layer charging current (I_c) = $\nu\, C_{dl}$ 1.24

where 'ν' is the scan rate and C_{dl} is the double layer capacitance, which is equal to the slope of plot of 'ν' *vs* I_c at different scan rate.

ECSA = C_{dl}/C_s 1.25

where C_s is the specific capacitance of the sample measured in the presence of a given electrolyte and C_{dl} is the double layer capacitance in the non-Faradic region of the voltammogram. For transition metals, the reported value of C_s varies from 0.033 mF to 0.056 mF in alkaline conditions.[27]

1.8. Electrode Potential and Function of Electrocatalysts

In electrocatalysis, the required potential is applied across the electrodes immersed in an appropriate electrolyte. The function of potential source is to increase or decrease the electronic density around the electrodes particularly in a half-cell reaction to drive the oxidation/reduction reaction. These electrodes (current collector) are decorated with catalytic material, where the reaction is catalyzed at the interface of electrolyte-catalyst-electrode interface. Under the operating conditions, catalyst is electronically wired with electrode and ionically wired with electrolyte. It is well established that electrochemical reaction purely takes place at the surface of electrodes material with the adsorption and desorption of intermediates and therefore can be categorized as heterogeneous catalysis. The function of electrocatalyst is to accelerate the exchange/transfer of electrons/ions between the electrolyte and electrode while providing a surface for the stability of various involved intermediates during electrochemical reaction.[29] Therefore, the activation energy of various intermediates can be decreased by facilitating the reaction pathways taking place on the surface of electrodes.

In case of water splitting process, the onset potential determines the feasibility of a reaction at particular potential under the provided conditions. Like other catalytic processes, the flow of redox reaction in electrocatalysis also depends upon the comparative orbital energy levels at the interface of electrode-electrolyte and possibly electron will move from higher to lower energy orbitals. The beauty of electrochemistry is that, we can precisely control the potential difference between the electrodes and even potential/electronic density at the interface of electrode-electrolyte in a half-cell reaction.[29] Under the anodic conditions, the energy of HOMO and LUMO decreases because of removing electrons from the catalyst deposited on electrode. As a result, the movement of electrons become directional from electrolyte (source) towards the catalyst (sink). Consequently, oxidation of electrolyte (H_2O) takes place and electrons move towards the cathode (source) to complete the cycle by transferring electrons to protons (sink) in water splitting reaction. In this way, the redox processes become feasible at the surface of electrodes in the provision of required cell potential. However, for the smooth and fast process at low potential, nature and inherent ability of electrocatalyst can play a key role to facilitate the transport of charged species while following the Sabatier principle (SP).[21] The SP principle states that there should be an optimal bonding strength between the catalyst and the intermediates to enhance the smooth adsorption/desorption process for the catalytically assisted reaction. In case of strong interaction, the unfavorable desorption of intermediates minimize the possibility of available active sites for the new incoming intermediates. While week interaction is not suitable for the proper stabilization of intermediates and, therefore, hampers the ideal exchange of electrons and overlapping with the catalyst active sites. Therefore, the structural and electronic engineering of electrode materials is a promising pathway to tune the inherent catalytic properties of electrocatalysts for the optimum interaction and activation of various intermediates.[21]

1.9. Mechanism of Electrochemical Water Splitting

Mechanism of a reaction means the possible/proposed pathway followed for the entire reaction under the specific conditions. Being a multistep and complex reaction of electrochemical water splitting, the cell potential and mechanism followed by half-cell reaction, either OER or HER, depends highly upon pH of the reaction medium (**Fig. 1.3**). In principle, various ions (H^+ or OH^-) in a reaction medium could possibly change the energy level and nature of electrolyte, and can thereby modify the reaction pathways for the entire water splitting conversion chain reactions.

1.9.1. Mechanism of OER

Among the two half-cell reactions, OER is a multistep and multi-electron (4 step and $4e^-$) process, which generates O_2, electrons and protons. All the steps are thermodynamically uphill with positive Gibb's free energy. Various mechanisms have been proposed for OER in both acidic and basic medium. **Fig. 1.4a** represents the most accepted and well-studied pathway with the formation of various intermediates (M-OH*, M-O*, M-OOH*).[18] The blue line (acidic medium) and red line (basic medium) represent the step-wise formation/combination of various intermediates needed for the transfer of electron and proton. In addition, the blue and black lines reveal the direct (M-O combination) and indirect (M-OOH formation) approach to complete the cycle of water oxidation process. All these elementary steps indicate their dependency on pH of a reaction medium as evident from the diagram. In acidic medium, each step involves the transfer of electrons and protons with oxidation of two water molecules in the whole process and four proton-coupled electron transfer mechanism is followed by the release O_2 molecules. While in basic medium, the OH^- ion takes the lead with four electron transfer and ends up with the formation of O_2 and water molecules.[30] However, in either mechanistic approach, the rate determining step can be predicted from the Tafel slope value which though is still a challenge due to the complex nature of OER. It is believed that among the various steps, M-OOH formation (3rd step) is comparatively energy intense and the slowest step with high Gibb's free energy.[18] Therefore the smaller Tafel slope (≤ 60 mV/dec) is generally referred to later steps as a rate-determining step and vice versa. The mechanism of OER can also be explained in terms of the number of electrons/protons transferred during the whole reaction. If the Tafel slope value is ≈ 40 mV/dec, then it shows two electron and one proton coupled process. If the Tafel slope value is ≈ 60 mV/des, then it shows one electron and one proton process. If the Tafel slope is higher than 100 mV/dec, then it is termed as two protons and one electron process.

1.9.2. Mechanism of HER

HER is also a multistep process that takes place at the surface of electrode. Based on the periodic adsorption and desorption of H^+ coupled with electron transfer on the surface of catalyst, three different steps i) Volmer ii) Heyrovsky and iii) Tafel have been exclusively explored.[31] Despite various steps, the mechanism of HER relative to OER is relatively easier and well understood. The first step always involves the adsorption of H^+ on the active site of catalyst (M). It is noteworthy to mention here that the source of adsorbed proton depends upon the acidic and basic medium. In acidic medium, the source of protons is H_3O^+ ions (**Fig 1.4c**) while in basic medium, it is the water molecules (**Fig. 1.4d**). Subsequently, the release of H_2 molecules follow two possible pathways.[32] One possibility is the diffusion of protons (from solution) towards the previously adsorbed H atoms coupled with the electrons transfer from the electrode. The second step is known as reaction of 'atoms and ions' or Heyrovsky step and the mechanism is called the Volmer-Heyrovsky mechanism, followed by the desorption of molecular H_2. Second possibility is the adsorption of protons on the available active sites of catalyst in the vicinity of previously attached H-atoms. These two atomic hydrogens are likely combined (Tafel or combination reaction) to form H_2 molecule and the mechanism is called Volmer-Tafel mechanism. It is well established that possible reaction mechanism can be predicted from the value of Tafel slope ($b = nRT/nF$), which has been theoretically calculated from the Buttler-volmer equation for three limiting cases. 1) If the Volmer/discharge process is fast and desorption of molecular H_2 follows the combination reaction (Tafel step) as a rate determining step, then slope (2.3RT/2F) of 29 mV/dec is observed at 25 °C. 2). If the discharge process is fast and follows the Heyrovsky (ion + atom) pathway for the release of H_2, then Tafel slope (4.6RT/3F) of 38 mV/dec is observed. 3) If the discharge process (Volmer step) is the rate determining step, then regardless of either Tafel or Heyrovsky steps followed for the desorption of H_2, the slope (4.6RT/3F) of 120 mV/dec is observed.[31]

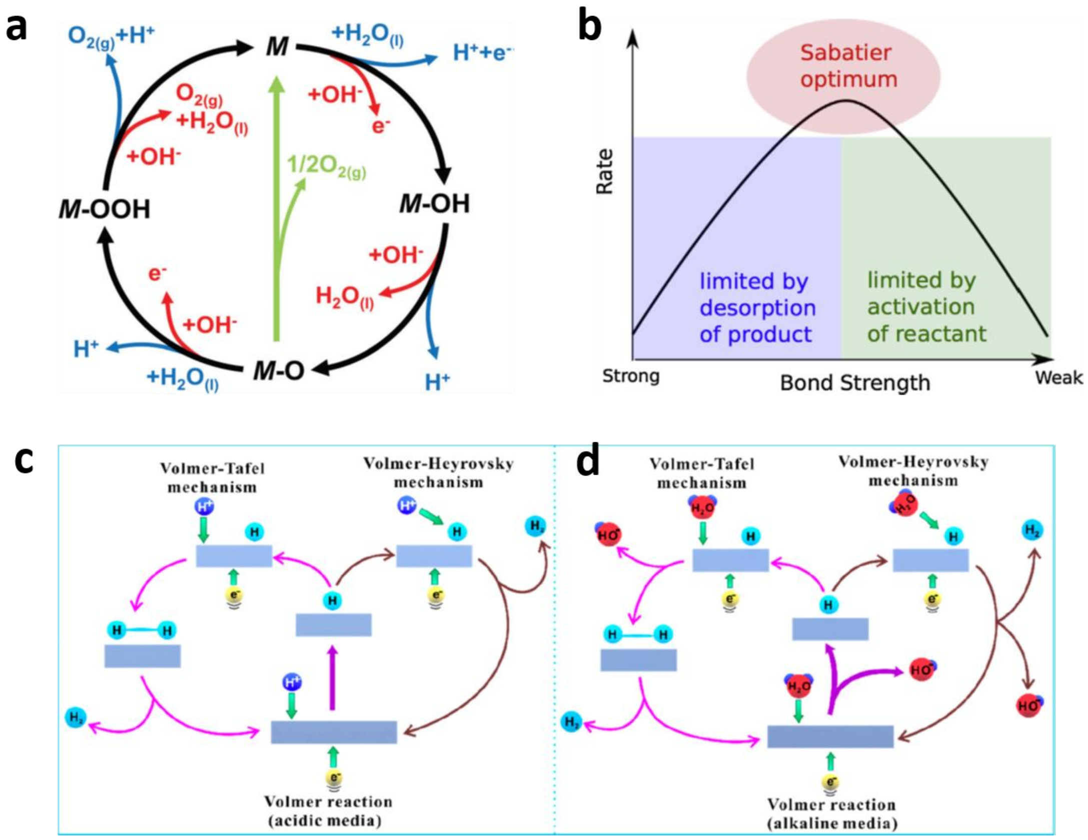

Figure 1.4 Mechanism of water splitting catalysis in acidic and basic medium (a) mechanism of OER in acidic medium (blue line) and basic medium (red line) (b) graph representing the Sabatier principle for the optimal interaction of intermediates with catalyst (c) mechanism of HER in acidic medium (d) mechanism of HER in basic medium.

1.10. Literature Review and Research Problem(s)

‘Water’ is one of the hydrogen enriched, naturally abundant and wide spread source on the planet. Like other electrolysis processes, water splitting can also be carried out *via* oxidation reaction (OER) and reduction reaction (HER) for the ultimate production of O_2 and H_2 at cathode and anode respectively. However, the feasibility and required energy for any chemical reaction depends upon their thermodynamic demand or Gibbs free energy change (ΔG), which is major parameter to decide the spontaneity of the reactions. Higher the ΔG, less favorable will be the reaction and vice versa. As discussed earlier, that higher ΔG (237 kJ/mol) means that at least 1.23 V potential should be provided for water splitting under ideal conditions.[18] However, during water electrolysis process, there is a complex mechanism at cathode and anode with multi-step processes and transfer of more than one electrons at the electrolyte-electrode interface hamper the feasibility of this reaction. In addition, various ohmic losses with the production of different intermediates (OH*, MOOH*, MO*) especially during water oxidation reaction further increase the activation barrier with an ultimate demand of high overpotential (300 to 600 mV) and makes the overall process even more challenging.[33] It can only be apprehended to develop highly stable electrocatalysts to efficiently catalyze the water splitting processes (OER & HER) at low overpotential. Many efforts have been made in last two decades to catalyze the water splitting process *via* both homogeneous and heterogeneous catalysis.[34] Among the homogeneous catalysts, Fe, Mn, Ir, Ru, and Co complexes have been widely explored with sufficient turnover frequencies (TOF's).[35,36] In addition to their high performance, the homogeneous catalysis takes place at molecular level and has also been extensively studied as a powerful tool to overcome the limitation of variety of catalysts for further advancement. However, the major drawback of the homogeneous catalyst is that they cannot be regenerated and separated from the reaction mixture and may lead to the production of side products and are, therefore, not much industrially favorable.

The alternative of homogeneous catalysis is the immobilization of catalyst at the surface of electrodes or complete fabrication of electrodes acting as catalysts. It has been investigated experimentally and computationally through extensive research work that Pt and Pd based catalysts are the state-of-the-art catalyst for HER.[37] These catalysts can catalyze HER at almost zero potential with the highest current density very close to the thermodynamic potential (0 V) due to the optimum adsorption of different intermediates with active center during catalysis. But these precious and rare earth metals cannot be used for large-scale catalytic applications. In addition, they are not stable in wide pH range due to the poisoning of active sites. To decrease the cost effect with improved stability, metal alloys formations, the formation of thin films on the earth abundant metals and their loading on various supports are among the effective approaches. Huajie Yin et al., have developed a strategy for the deposition of a thin layer of Pt nanowires over 2D Ni(OH) via electrochemical means.[38] The positive aspect of this work was the development of thin and uniform sheet of Pt nanowires and to gain comparative stability even in an alkaline medium unlike other HER catalysts. Richard et al. have synthesized Pt island on Ni NPs with high inherent strain in the structure.[39] The structural strain was endorsed due to the mismatch in the crystal structure of Pt and Ni. It was found that despite a small loading, such aligned growth of Pt with very thin islands (1.8 nm thick) with structural strain are credible for the higher mass and specific activity for HER. Similarly, Nanda et al. have recently reported that HER performance of Pt and Pd catalysts can be significantly improved by their loading them on a conducting N-doped graphene oxide.[40] The heteroatom in the whole structure not only stabilizes the metal NPs but also creates structural defects to further improve the number of active sites for catalysis. In a similar work, Liu et al. have reported ultrafine Ru quantum dots decorated on Ni_2P@N-doped carbon nanospheres.[41] It was observed that the growth of nanoscale materials embedded in N-doped carbon via thermal treatment can create a close contact between Ru, Ni and underlying support. Such an interfacial contact reinforce the transfer of charged species to consequently accelerate HER. However, the commercial electrolyzers have the potential to produce economic H_2 if solely integrated with the cost-effective and efficient electrode materials analogous to the noble metals. In this regards, Xuping Sun and co-workers have developed a series of different morphology of transition metal phosphides and selenides for HER catalysis.[42,43] Similarly, different metal chalgogenides, carbides, and metal free nanocomposite have also been developed for HER catalysis in the past few years.[44-47] Among the cost-effective electrocatalysts for HER, metal carbides are indeed very promising and emerging materials due to their unique d-band structure. They have high mechanical strength and stability in wide pH range especially MoC based material due to their Pt-like behavior. The first report of MoC was reported by Xile Hu et al. for HER in both acidic and basic medium.[48] Initially, there was no evidence about the origin of activity but later on it was found that it is basically the density of states (DOS), which can be increased near the Fermi level by tuning the size and electronic structure of metal carbides. In addition, their anchoring on various conducting supports can modify their d-band structure due to the electron transfer from metal to carbon, which are helpful to consequently control the optimum adsorption of H* intermediates that is needed for the dynamic release of molecular H_2.[32]

As mentioned earlier, in water splitting the main complication is the demand of high potential for the bottleneck anodic reaction (OER). During multi-step (4-step) OER process, different intermediates (OH*, OOH*, MO*) are thermodynamically uphill with high kinetic barrier and limit the overall water splitting process and conversion efficiency. To overcome this problem, RuO_2 and IrO_2 have been found among the best catalysts for water oxidation at minimum overpotential (220 mV). The catalysis process at the surface of RuO_2 is well studied and it has been found to depend upon the oxidation state of metal and that only the rutile type RuO_2 is highly active.[45] However, the use of RuO_2 in basic medium leads to the formation of water soluble RuO_4 *via* phase transformation process and deteriorate their stable and active phases needed for water oxidation.[45, 49] Recently, transition metal oxides (NiO, CoO, CuO) have been found to efficiently catalyze the water oxidation process.[50, 51] Similarly, metal chalcogenides, spinel family and various composite materials have been extensively explored, and promisingly some there are found highly active and even can outperform the benchmark electrocatalyst for OER.[30] But, to gain control over the formation of different unwanted oxides phases, small active sites and less stability in harsh conditions are still among the serious challenges in this regard. To address this problem, graphene and carbon nanotubes (CNTs) based nanocomposite materials have been explored to enhance their stability, conductivity and to control over the agglomeration of nanomaterials during catalysis. Recently, Fatemeh Razmjooei et al. have reported the heteroatoms (S, P, N, B) doped graphene supported Fe nanocomposites for electrocatalytic water oxidation.[52] The purpose of doping in this work was to generate electronegativity difference between carbon and heteroatoms to facilitate the water oxidation process. Govinhdhant et al. have developed very small Co quantum dots for alkaline water oxidation process.[53] But the agglomeration of small particles and alike composite materials drastically decrease their performance during long-term electrolysis. Among the transition metal based electrocatalysts, layer double hydroxide (LDH) have also been extensively explored for OER in basic medium. LDH are the 2D materials with brucite-like structure, where two metal layers with various oxidation states are interlinked by various cations and-/or anions.[54] Among the various combination of transition metals, Ni-Fe-LDH, Ni-Co-LDH, Co-Fe-LDH and Cu-Fe-LDH are highly active for OER due their exposed/accessible nature of active sites and inherent electronic/structural compatibility with water molecules.[55, 56] In addition, the presence of metals in various oxidation states impart high redox potential and easy formation of intermediates to overcome the kinetic barrier for multistep OER process. Due to the layered structure, LDH offer maximum accessibility of metal active sites, where the distance between two layers can be controlled by controlling the nature of cations and reaction condition.[56-58] In addition, after exfoliation of 2D structure, a series of LDH can also be used as support material to further increase the stability of overall hybrid material.[55,58] However, LDH are comparatively less conducting in nature. To address this issue, they have also been loaded on various conducting materials (GO, CNTs, g-C_3N_4) and even can be incorporated in to the porous structure (MOFs) to further ameliorate their catalytic performance for overall water splitting.[59] Currently, the nanostructuring of materials at atomic level is also an emerging area of research with the potential to resolve the low activity of heterogeneous catalysts. Various approaches have been introduced to stabilize single atom catalysts on conducting and porous supports.[60] Such type of electrode materials offer high surface area and maximum accessibility of atoms for catalysis. However, the agglomeration of single atoms during catalysis and continuous decrease in their catalytic performance are the associated problems. Despite a great effort in the last decades, there is still a dire need to develop cost-effective and stable nanomaterials with selective approach to uplift the electrolyzer part of the solar-assisted water splitting module.

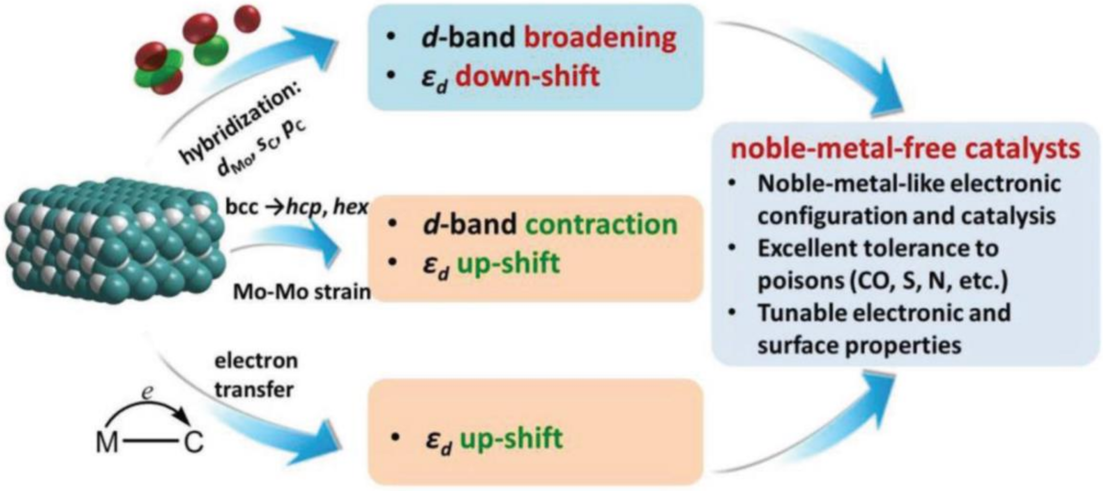

Figure 1.5 Schematic illustration of d band center (ε_d) of metal carbides and their effect on catalytic properties arise by electron transfer from the metals towards the carbon.

1.11. Nanomaterials/Nanoclusters and Scope of this Thesis

With the advancement in materials synthesis, one of the fascinating discovery is the exploration of the catalytic behavior of nanomaterials in nanoscale dimension.[61,62] More promisingly, moving from bulk to the nanoscale level and then to the subnanometric regime, new materials are emerged and are generally known as nanoclusters (NCs, size ≈ 2nm). These NCs assemblies behave like a molecule having excellent catalytic properties due to their high surface-to-volume ratio, high redox potential, exceptional electrical properties and thus have triggered enormous interest in catalysis and other fields of science as compared to their bulk analogues. Engineering their surface, core size and surface chemistry of the underlying support can further enhance their activity and diverse selectivity for catalysis but they are rarely reported. Electrochemical water splitting catalysis, the main focus of this research work, requires a decent control over the size and surface defects of nanoscale materials and their interface with the electrode materials. Therefore, to manipulate and explore the materials down to the nanoscale and sub-nanoscale (≤ 2nm) level for electrochemical water splitting with a major focus on OER catalysis is the major scope of this thesis. More precisely, we have focused the nanostructuring of transition metals (Ni, Cu, and Co) oxides/carbides and their decoration on various supports such as graphene oxide (GO), carbon nanotubes and porous polymeric structures, which are indeed worth-considering for the exploitation of their intrinsic electrocatalytic behavior.[63,64] Such a surface functionalized/engineered nanostructured meta/metal oxides and carbides are considered the potential candidates to efficiently catalyze the multistep OER and HER process in durable manner.

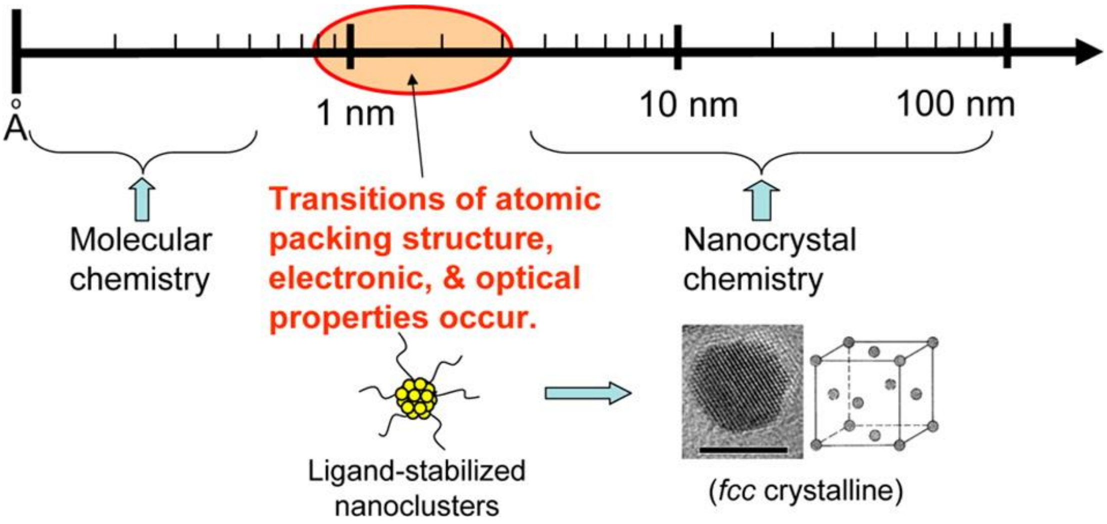

Figure 1.6 Schematic illustration of physicochemical properties of materials at the nanoscale length.

Chapter 2.

Experimental

2.1. Synopsis

All the experiments carried out during this research work are presented in this chapter. The first part will present the details of used chemicals, experiments and various approaches followed for the synthesis of desired material and controlled samples. The 2nd part of this chapter presents the introduction and basic principles of various physical techniques used for the structural and compositional analysis of the materials. The final part of this chapter highlights the electrochemical experiments, methods and various parameters acquired for oxygen evolution reaction (OER) and hydrogen evolution reaction (HER).

2.2. Experimental Section-1(Chapter 3&4)

2.2.1. Chemicals

Graphite powder (325 mesh, ≥80%, Alfa Aesar), potassium permanganate ($KMnO_4$, ≥98%, Sigma-Aldrich), potassium phosphate (H_3PO_4, ≥98%, Sigma-Aldrich), sulfuric acid (H_2SO_4, nickel nitrate hexahydrate ($Ni(NO_3)_2.6H_2O$, ≥98%, Sigma-Aldrich), cobalt nitrate hexahydrate ($CoNO_3.6H_2O$, ≥85%), Cu nitrate hexahydrate ($CuNO_3.6H_2O$, ≥85%), hydrobromic acid (HBr, 48%, Sigma-Aldrich), potassium hydroxide (KOH, ≥ 85%, Sigma-Aldrich), potassium phosphate (KH_2PO_4, ≥ 99%, Sigma-Aldrich), sodium borohydride ($NaBH_4$, ≥ 96 % Sigma-Aldrich), thiourea (CH_4N_2S, ≥99%, Sigma-Aldrich), diethyl ether [$(CH_3CH_2)_2$, ≥ 99%, Sigma-Aldrich, iridium(IV) oxide (IrO_2, ≥99.9%, Sigma-Aldrich) and polypropylene (average M_n ~5000, ≥ 99%, Sigma-Aldrich). All other solvents (methanol, ethanol, water) were used after double distillation.

2.2.2. Synthesis of Graphene Oxide (GO)

Graphene oxide (GO) was synthesized by using improved Hummers' method.[65] Briefly, 1 g of graphitic powder was dispersed concentrated H_2SO_4/H_3PO_4 (120 mL/13 mL; 9:1) in a 500 mL beaker. After 30 min of stirring, 6 mg of $KMnO_4$ was added and the temperature raised up to 50 °C for 18 h to ensure the complete oxidation of graphene. 150 mL of ice-cold water was then added to stop the oxidation reaction followed by the addition of 30 % H_2O_2 (3 mL). After stirring (1 h), the appearance of brown color indicated the formation of GO. The reaction mixture was centrifuged (4000 rpm) for 1h to obtain the solid product. The solid product was then washed thrice each with HCl, H_2O, and ethanol to remove the organic/inorganic impurities, which are formed during oxidation reaction. Finally, the product was washed many times with deionized water and dried at 60 °C for further use.

2.2.3. Chemical Functionalization of GO (G-SH)

The synthesized GO was functionalized using a modified method recently reported (**Scheme 2.1**). 30 mg of GO was washed twice with ether and ultrasonically dispersed in 30 ml of deionized water (DIW) for 2 h. HBr (1.5 mL) was then added dropwise and further sonicated for 30 min. The reaction mixture was then stirred for 45 min followed by the addition of 1.5 g of thiourea at room temperature (RT). The temperature was raised to 70 °C for 24 h under normal stirring. The reaction was then stopped and cooled down to RT under natural cooling. 15 mL of aqueous solution of KOH (3 M) was then added and the temperature decreased to 4 °C. The reaction was kept under vigorous stirring for 45 min. After stopping the reaction, the black suspension was collected *via* centrifugation at 8000 rpm. The solid product was washed thrice each with ethanol, ether, dimethylfarmamide (DMF), and finally, the solid product was ultrasonically dispersed in DIW (5 mL) and dried under vacuum at room temperature for 3 days to obtain the thiolated graphene oxide nanosheets (G-SH).

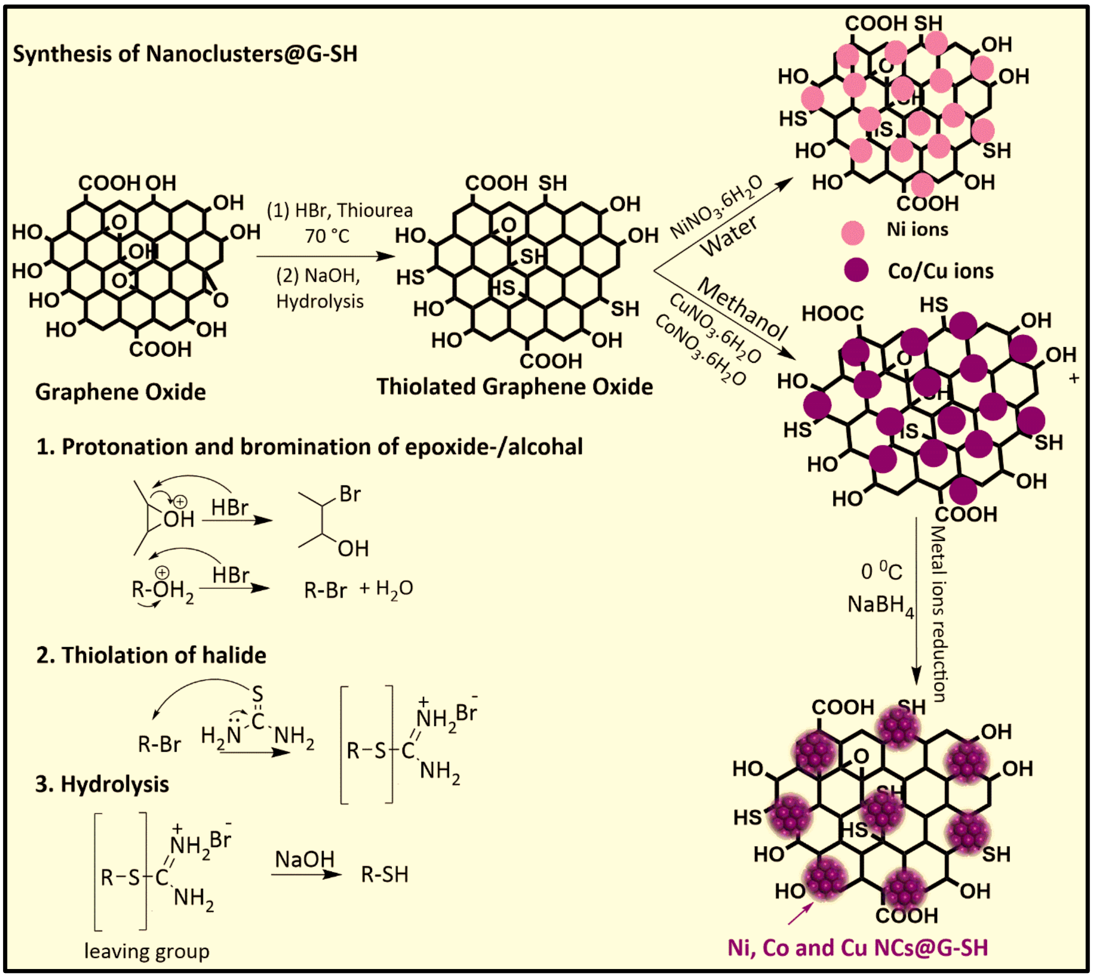

Scheme 2.1 Synthesis of thiolated graphene oxide (G-SH) nanosheets, loading with metal nanoclusters and the proposed reaction mechanism.

2.2.4. Synthesis of Ni/NiO@G-SH

Ni/NiO NCs were fabricated on thiolated graphene by using simple reduction method (**Scheme 2.1**) under ambient conditions. 20 mg of G-SH was ultrasonically dispersed in 20 mL of distilled water for 45 min in a 50 ml round bottom flask (RBF). The dispersed G-SH was further stirred for 30 min at room temperature. 10 mg of $Ni(NO_3)_2.6H_2O$ (2 mg of Ni metal) was then added and the RBF containing the reaction mixture was placed in an ice-bath under normal stirring. After 45 min, 3 mL of $NaBH_4$ (8 times to Ni atoms) was added dropwise under vigorous stirring and the reaction was allowed to complete for 24h at RT. Finally, the product was collected *via* centrifugation (8000 rpm), washed with water, methanol and dried at RT under vacuum.

2.2.5. Synthesis of Nanoclusters (Co/CoO@G-SH and Cu/CuO@G-SH)

In a typical procedure, 30 mg of G-SH was ultrasonically dispersed in methanol for 30 min in a 50 ml round-bottom flask (RBF). After about 30 min, 10 mg of cobalt salt was added into the brown G-SH suspension under constant stirring and continuous flow of N_2 at room temperature. The RBF containing reaction mixture was placed in an ice-bath and further stirred for 1 h to ensure the formation of G-SH complex. Afterward, 3 mL of $NaBH_4$ solution in ice cold water was added dropwise under vigorous stirring. The reaction was then allowed to complete for 24 h at room temperature. The product was collected *via* centrifugation (5000 rpm) and washed with DIW and methanol and then dried at RT under vacuum. Same procedure was followed for the synthesis of Cu/CuO@G-SH except the use of copper salt instead of cobalt salt. Moreover, during the reduction step, $NaBH_4$ was added at once to the ice cold reaction mixture for the formation of Cu/CuO@G-SH.

2.2.6. Synthesis of Metal Oxides (CuO/CoO) Nanoparticles on GO

For the synthesis of, NiO@GO, CoO@GO and CuO@GO, the same protocol was followed as above except the use of GO instead of G-SH and finally the samples were calcined at 300 °C for 2 h in an open atmosphere.[66]

2.3. Experimental Section-2 (Chapter 5)

2.3.1. Chemicals

Cobalt nitrate hexahydrate ($Co(NO_3)_2.6H_2O$, ≥98%), melamine ($C_3H_6N_6$ ≥99.9%) potassium hydroxide (KOH, ≥ 85%), 2-phenylethanthiol(PET ≥ 99%), Tetraoctylammonium bromide (TOABr, ≥99.9%) Iridium oxide(IV) oxide (IrO_2, ≥99.9%) and Pt/C (≥99.9%) were purchased from Sigma-Aldrich and used as received without further purification. All the solvents (methanol, ethanol, water, and acetone) were used after double distillation.

2.3.2. Synthesis of Co/Co(OH)$_2$@HCN

A mixture of 1 g of melamine (nitrogen source) was mixed with 153.45 mg (optimum, 3 wt% with respect to melamine) of cobalt nitrate hexa-hydrate

$[Co(NO_3)_2.6H_2O]$ and grinded with the help of mortar-pestle in low humidity environment, while keeping the temperature below 20 ºC. After continuous grinding, the color of the mixture turned blue, which indicated the formation of metal-melamine complex. After the addition of NaOH (0.1 M, 1 mL), the dried homogeneous mixture was transferred into the rectangular alumina crucible and placed in the center of the tube furnace. Without any post-treatment, the sample was initially degassed and then purged with Ar for 15 min. The internal temperature was then raised to 200 °C (for 1.5 h) with a ramping rate of 2 °C/min under the continuous supply of Ar to initiate the formation of various intermediates from melamine, while maintaining the pressure at 0.06 bar inside the tube furnace. After 1.5 h, the temperature was further raised to 550 ºC with the same ramping rate for 3 h. Finally, the solid black product was obtained, washed with 20 mL of water and methanol three times each. Same reaction with different weight percent (0.5 and, 5 and 10 wt%) of Co was carried out separately under the similar conditions. However, the reaction was found sensitive (beyond the range, 4wt% ±0.5), where irregular morphology was obtained by using lower or higher amount of Co under similar conditions. Similar trend was observed by using urea as a starting material instead of melamine.

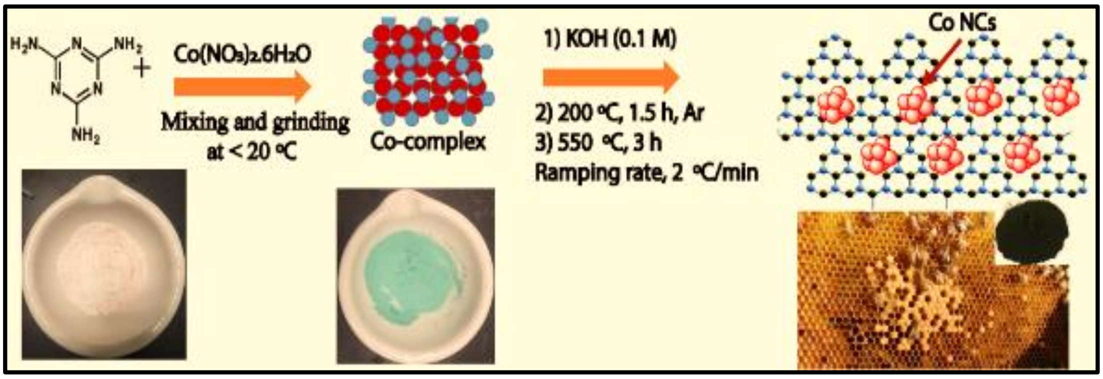

Scheme 2.2 Schematic illustration for the synthesis of $Co/Co(OH)_2$ NCs embedded in nitrogen enriched mesoporous carbon (NCs@HCN).

2.3.3. Synthesis of 2-Phenylethane Thiol Stabilized Co NCs (Co(PET)

The Co NCs were synthesized by modifying the previously reported method.[67] The $Co(NO_3)_2.H_2O$ (15 mg) was dissolved in dried THF (20 mL) followed by the addition of tetraoctylammonium bromide (TOABr, 80 mg), which resulted in a color change from pink to intense blue color. After 30 min, 2-phenylethane thiol (PET, 80 µL) was added and the reaction mixture was vigorously stirred for 6 h. Thereafter, freshly prepared solution of $NaBH_4$ (34 mg in 2 mL) in ice-cold water was added that resulted in the appearance of deep reddish color and the reaction was allowed for aging. After 12 h, the reaction was stopped, the THF soluble NCs were separated and then excess of methanol was added for precipitation followed by centrifugation. The PET stabilized NCs were repeatedly (4 to 5 times) washed with methanol and then re-dispersed in DCM for further use.

2.3.4. Synthesis of $Co(OH)_2$ NPs, Co_3O_4 and $Co(OH)_2$ NPs@g-C_3N_4

$Co(OH)_2$ was synthesized by dissolving $Co(NO_3).6H_2O$ (15 mg) in NaOH solution (0.1 M_{aq}, 5 mL) in a round bottom flask. After the formation of $Co(OH)_x$ complex, the sample was dried at 60 ºC in an open atmosphere. Finally, the grinded/dried sample was calcined at 350 °C for 2 h in open atmosphere to obtain $Co(OH)_x$ NPs. For the synthesis of Co_3O_4, the $Co(OH)_x$ was further calcined at high temperature (600 °C) for 3 h. The $Co(OH)_2$ NPs@g-C_3N_4 was synthesized following the same procedure. Initially, for the formation of g-C_3N_3, 0.5 g of melamine was placed in a muffle furnace for 4 h at 550 °C with a ramping rate of 5 °C/min as reported previously.[68] Then, $Co(OH)_x$ complex was added into the ultrasonically dispersed g-C_3N_4 (2 mg/ml, in water) and allowed to stir for 1 h. Finally, the reaction mixture was dried at 60 °C in oven, followed by thermal pyrolysis at 550 °C for 3 h.

2.4. Experimental Section-3 (Chapter 6)

2.4.1. Chemicals

Sulfuric acid (H_2SO_4, ≥85%, Sigma-Aldrich), nickel nitrate hexahydrate ($Ni(NO_3)_2.6H_2O$, ≥98%, Sigma-Aldrich), potassium hydroxide (KOH, ≥ 85%, Sigma-Aldrich), iridium(IV) oxide (IrO_2, ≥99.9%, Sigma-Aldrich) and Pt/C (≥99.9%, Sigma-Aldrich), multiwall carbon nanotubes (<5% metal oxide, Sigma-Aldrich), polyvinylpyrrolidone (Mwt, 40,000 g/mol) sodium borohydride ($NaBH_4$, ≥96%, Sigma-Aldrich). All the solvents (methanol, ethanol, water, and acetone) were used after double distillation.

2.4.2. Synthesis of Nickel Carbide NPs@N-Doped Carbon Nanotubes (Ni/Ni_3C@NCNT)

A mixture of 1 g of melamine (source of carbon and nitrogen) mixed with certain amount (60 mg, 150 mg, and 260 mg) of ($Ni(NO_3)_2.6H_2O$ was grinded with the help of mortar-pestle in low humidity environment. After the formation of homogeneous mixture, the solid mixture was transferred into a rectangular alumina crucible covered with a lid. The crucible was placed in the central part of the tube furnace that was initially degassed and then purged with Ar for 15 min without any post-treatment and. The internal temperature was then raised to 600 °C (for 5 h) with a ramping rate of 2 °C/min under the continuous supply of Ar, while maintaining the 0.06 bar pressure inside the tube furnace by controlling with the external valve. After 5 h, the solid black product was obtained, washed with water and methanol three times each. Same reaction with different weight percent (0.5, 2, and 4 wt%) of Ni was carried out separately under the similar conditions for the controlled growth of NCNT of different diameter. The samples were assigned as 0.5-Ni/Ni_3C@NCNT, 2-Ni/Ni_3C@NCNT and 4-Ni/Ni_3C@NCNT. In addition, to verify the optimal conditions and growth mechanism, various reactions were run by varying the temperature, time, ramping rate and critically the stoichiometry of the precursors. No CNT were observed in the absence of Ni salt.

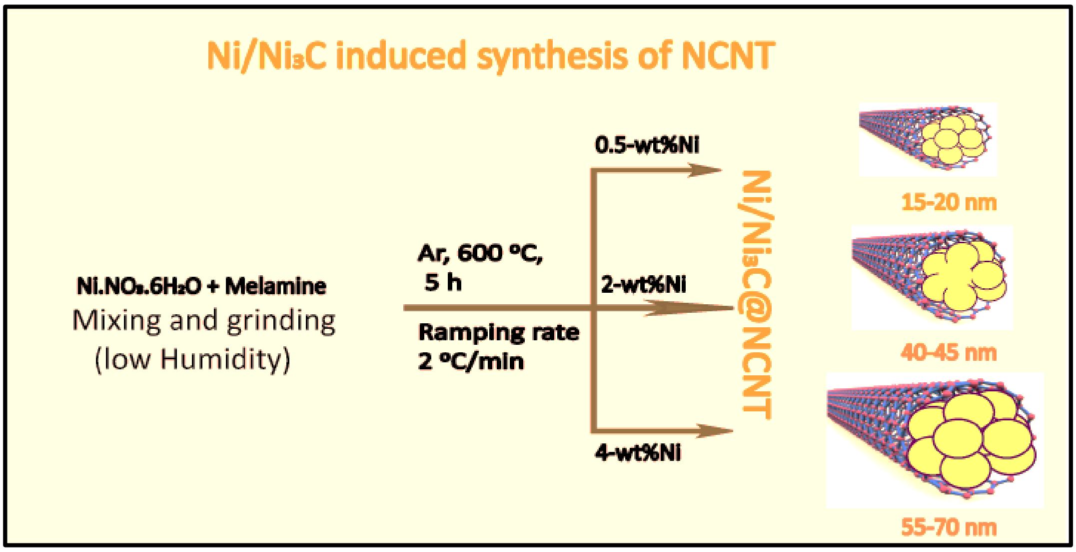

Scheme 2.3 Schematic illustration for the synthesis of Ni/Ni_3C@NCNT via solid state method with controlled morphology/size by controlling the precursor and reaction conditions.

2.4.3. Synthesis of Ni NPs and NiO@NCNT

For the synthesis of Ni NPs, mixed 20 mg of $NiCl_2.6H_2O$ and polyvinylpyrrolidone (85 mg) in 40 mL of water. After stirring for 1 h, an ice cold aqueous solution of $NaBH_4$ (2 mL, 0.5 mM) was added into the reaction mixture resulting in an immediate appearance of brown colour which indicated the reduction of metal ions. Further, the reaction was allowed for aging under stirring reaction. After 6 h, the reaction was stopped and the final product was collected with centrifugation and washed several time with water. For the synthesis of NiO@CNT, the commercial CNT (10 mg) were ultrasonically dispersed in water (15 mL) for 30 min followed by the addition of $Ni(NO_3).6H_2O$ (0.5 mM, 2mL) and then stirred for further 30 min for the uniform distribution of metal ions. The reaction mixture was dried at 70 °C under vacuum and then placed in a muffle furnace at 500 °C (5 °C/min ramping rate) for 2 h in an open atmosphere. The black solid product was finally washed with methanol for further use.

2.5. Physical Techniques Used for Materials’ Characterization

The surface morphology and texture of the synthesized samples were analyzed with Field Emission Scanning Electron Microscope (FEI NOVA SEM-450 at 10 kV using through-lens detector) and Scanning Transmission Electron Microscopy (STEM) equipped with FEI NOVA-SEM-450. Elemental composition was carried out with INCAX-Act Energy Dispersive X-ray Spectroscopy (EDS) equipped with JASCO V77 spectrophotometer. The ICP-OES analysis was conducted to determine the amount of metal content before and after catalysis. Absorption pattern of nanoclusters was acquired with UV-Visible spectrophotometer (Shimadzu 1601), whereas Raman spectrometer (FER-SCI-1024BRX, model TEC-420) equipped with laser ($\lambda = 785$ nm) was used to investigate the graphitic structure of N-doped carbon and the possible vibration modes of oxides/hydroxides before and after catalysis. For porosity and surface area analysis, BET surface area analyser (Quantachrome Nova 2200e) was used. Powder X-ray diffractometer (D2 phaser, Bruker) data was collected to analyze the crystal structural and phase purity of the materials. X-ray Photoelectron Spectroscopy (XPS) using PHI 500 Versa Probe II spectrometer (UIVAC-PHI) and High Resolution Transmission Electron Microscope (HRTEM, JEM2100F, JEOL, 200

KV) were used to investigate the chemical environment/oxidation state and internal composition of the materials respectively.

2.6. Basic Principles Behind the Physical Techniques Used

2.6.1. Fourier Transform Infrared Spectroscopy (FT-IR)

The term spectroscopy means to study the interaction of light/electromagnetic radiation (EMR) with matter and their behavior. In single atom, the electrons are filled in the highly quantized atomic orbitals which can only be excited/replaced by providing appropriate and sufficient energy. However, after the formation of bond, the atomic orbitals of bonded atoms become overlapped and integrated into molecular orbitals of different energy known as electronic levels. The energy of those bonded electrons is highly dependent upon the nature and extent of overlapping of atomic orbitals. These electronic energy levels are further divided into vibrational and rotational levels. After the interaction of matter with electromagnetic radiations of energy lower than the electronic states, the excitation of molecule between the vibrational levels takes place while absorbing infrared radiations (400-4000 nm) produced by interferometer (**Fig. 2.1**). The vibrational excitation basically takes place in the bonded electrons, where the bond act like a spring between the two rigid atoms. After absorption, the intensity of the transmitted radiations is simultaneously detected in the wide range. It is worth mentioning here that oscillation of bonds is basically dependent upon the extent of polarity of charges between the bonded atoms i.e., dipole movement, whereas the position of the peaks depends upon the reduced mass of the atoms and strength of the bond. Higher the reduced mass lower will the wavelength and vice versa. In this way, each functional group has their own polarity and strength of the bond. Therefore, FT-IR spectroscopy is highly regarded for the detection of various functional groups not only in molecular framework but also the surface functionality of nanomaterials. It is a non-destructive technique and can measure all type of the samples (Gas, liquid, solid), however, need a separate configuration of sample inlet/detector for desired use. In our case, we have used attenuated FT-IR instrument, where the powder samples were directly placed on the quartz crystal and scanned in the range of 500 to 4000 nm. The final data was plotted between % transmittance and wavelength.

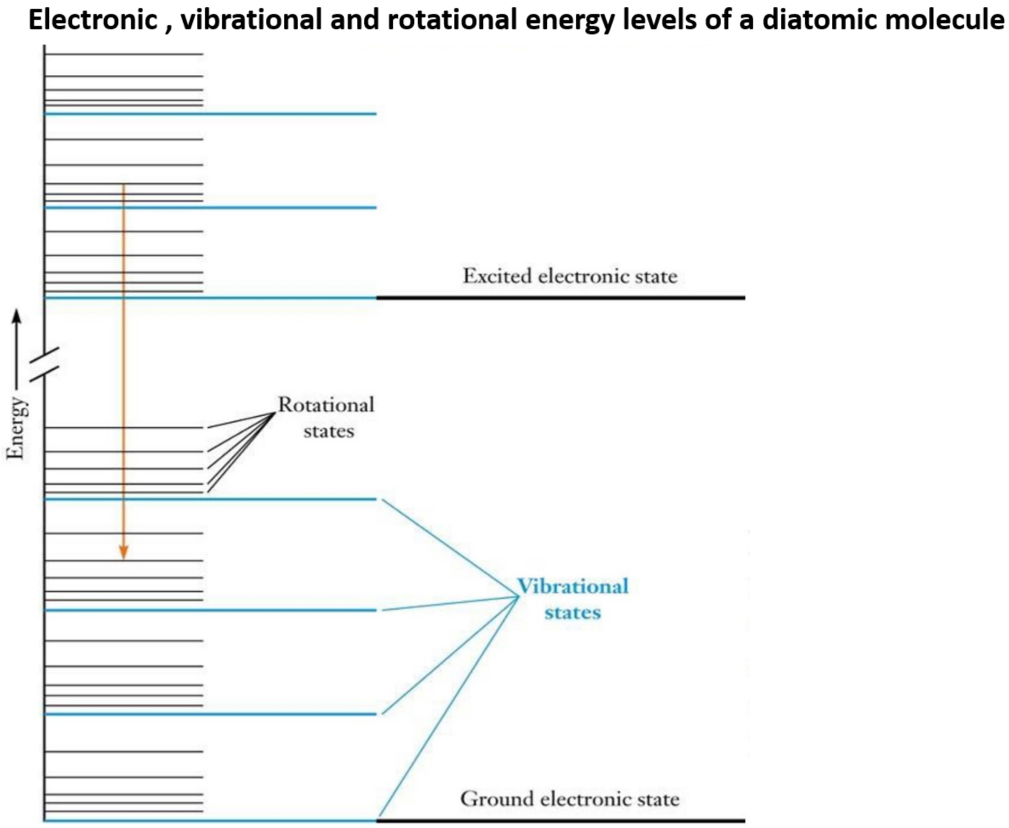

Figure 2.1 Representation of various energy levels/sub-levels in diatomic molecules. The electronic levels have further sub-energy vibrational and translational levels. The IR absorption takes place by the excitation between two vibrational levels.

2.6.2. Raman Spectroscopy

The information we get from the sample depends upon the range of EMR to hit the sample. Suppose we are using a range of UV-visible spectrum to target a sample, it is obvious to cause electronic excitation which gives us information about the bonding in molecule. However, by using the monochromatic beam of radiations, possibly the energy will not correspond to any electronic excitation. In this way, the electron is forced to approach the lower and unstable energy level (virtual state) and will immediately come back to the lower energy state (**Fig. 2.2**).[69] In Raman spectroscopy, the highly intense monochromatic laser beam is used to hit the sample which interact both elastically and inelastically. The response of elastic interaction is called Rayleigh scattering and takes place predominantly, which means that electron comes back to the same energy level which is considered as main component of spectrum. While some of the electrons (1 in 30 million) lose energy during interaction and end up with those excited vibrational levels (EVL) which are closer to the ground electronic states, therefore, release photon of low energy than the incident radiations. This response is called stokes component of the spectrum. Similarly, a few electrons initially from EVL come back to ground electronic states with release of higher energy photon than the incident one and the response is called 'anti-stokes' of the spectrum. These stokes and anti-stokes are called Raman effect and represent the inelastic interaction. However, the intensity of stokes is higher than that of anti-stokes due to the maximum probability of electrons in the ground vibrational level (GVL) and thus feasible for the excitation/de-excitation with high probability (**Fig. 2.2**). Therefore, normally we take the 'Stokes' response and plot it between the intensity of scattered photon *vs* the difference in frequency of the incident and emitted photons.[70]

Currently, there are about 25 types of Raman spectroscopy and thus becoming an important characterisation technique in material science especially for 2D material.[69] It provides information about the materials' structural defects, crystal distortion, amorphous nature, and perturbation effect after chemical functionalization or doping.[71, 72] However, during Raman analysis, the main problem is to eliminate/minimize the unwanted Rayleigh lines. In addition, the parasitic radiation/fluorescence phenomenon further masks the Stokes response. To overcome these problems, we need to use the enchantment approaches during analysis i.e., background removal, monochromatic beam, suitable range of beam, and tunable applied potential. In addition, techniques like resonance scattering enhanced techniques, surface enhanced Raman scattering, tip enhanced Raman scattering, and transmission Raman scattering etc are the advanced forms of Raman spectroscopy to enhance the intensity of the desired scattered photons.[70] It is noteworthy to mention here that all the movements in the material (gas, liquid and solid) are not Raman active. In principle, the inelastic interaction of light leaves the matter in a modified form (rotational and vibrational level). For instance, in case of crystal lattice, the Raman effect creates quantum vibrational levels known as phonons (quasi-particles). In molecules/lattices, generally the charges are distributed over the entire structure in the applied magnetic field, however, intends to be in equilibrium state. This behavior is an intrinsic property of molecules/crystals and may create a dipole in the structure, which may be anisotropic in nature. This anisotropic property of molecules (rotational-/vibrational motions) and crystal lattices (vibrational motion) is called the polarisability and dielectric susceptibility respectively, which is the origin of Raman activity. Thus, only those motions are Raman active which create a polarisability (for molecule rot-vib motions and dielectric susceptibility for crystal lattice vibration motion) from the oscillatory movement of the interatomic displacement. This makes it complementary to the FT-IR spectroscopy where only the dipole moment is required.[70] During analysis, we have used the solid/powder samples placed on the sample holder. After collecting the data, the background/fluorescence data was removed and plotted wavenumber *vs* the intensity of scattered radiations.[72]

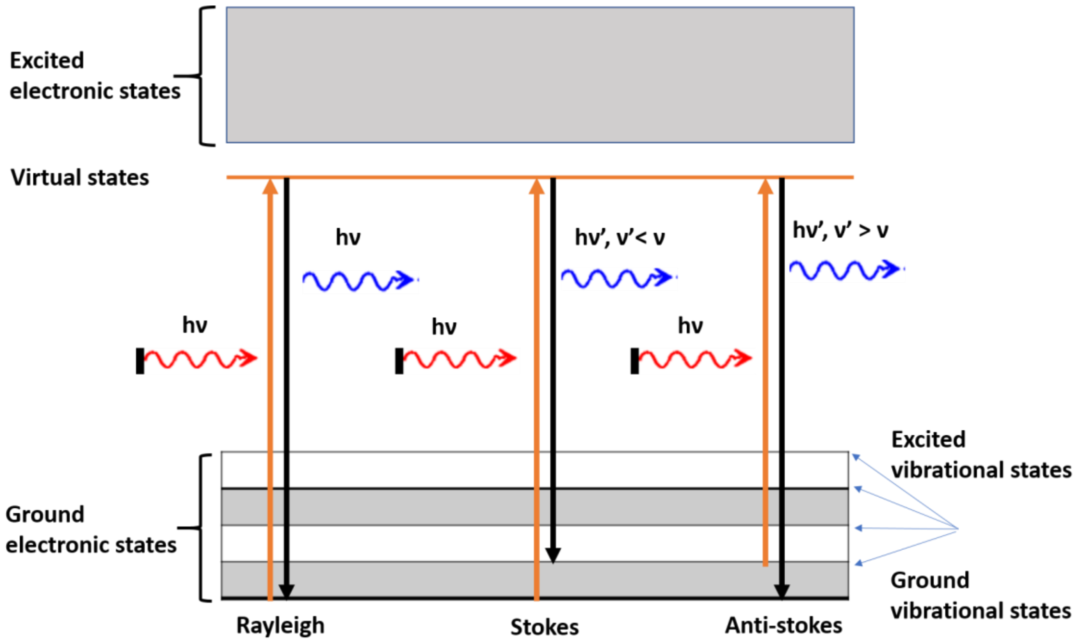

Figure 2.2 Representation of various energy levels between two electronic levels. The different arrows represent the Raman effect and scattering phenomenon after the interaction of monochromatic beam of laser with sample.

2.6.3. Powder X-ray Diffraction (P-XRD)

In material science, XRD is one of the valuable techniques to determine the crystal structure, phase purity, crystallite size and identification of various known and unknown compounds. In this technique, the X-rays of metals (Cu kα rays in our case, λ = 1.54 nm) are used to hit the crystalline sample. The electronic component of the incident rays interact with the electronic density of the ions in the crystal lattice and become diffracted into many specific directions (**Fig. 2.3**). The crystalline structure usually consists of layered lattices one upon another with repeated 'unit cells' in 3D manner. Therefore, the simultaneous diffraction from the group of planes may possibly be from 1st, 2nd, and 3rd layers. The diffracted radiations coming out of the crystal structure having i) same phase ii) wavelength difference of integral multiple of lambda can possibly overlap constructively, however, they need to follow the condition given in **equation 2.1** (**Fig. 2.3**).[73]

$AB + BC = n\lambda$ 2.1

n is the whole number, λ is the wavelength. Since, AB = BC = Sinθ

Now, we can write

$2d\text{Sin}\theta = n\lambda$ (Bragg's equation) 2.2

The **equation 2.2** means that each diffraction will follow the Bragg's law, which is limited to few θ values. It means that all the other diffractions will be out of phase and will cancel each other which is known as destructive interference. Secondly, the d spacing (distance between two layers) will be of the same order of magnitude as wavelength of the incident beam. However, it can be addressed by selecting the source of radiations.

During analysis of the sample, the θ values and intensities of peaks are the characteristics properties of each crystal lattice and thus give a unique diffraction pattern of various compounds. Before analysis, the polycrystalline sample is grinded into a fine powder to ensure the random and homogeneous distribution/orientation of tiny crystals. In this way, the incident radiation interacts with various facets/planes and thus can generate the possible diffraction pattern from all directions with proper d spacing while following the Bragg's law.[73] However, it is necessary to use the monochromatic beam of radiations (generally Cu or Mo kα lines), otherwise the Bragg's law cannot be followed in case of undefined lambda (λ). In this regard, the monochromator is used to filter the X-rays coming from the X-ray tube before reaching the sample. Moreover, the distance between three spots i.e., X-rays source, sample and detector is same with two different possible configurations. In one case, during scanning of sample, the sample and detector are rotated with θ and 2θ values respectively. In this way, the detector could collect the diffracted radiation with an angle double of the incident radiation (2θ). In other case, the sample holder remains static while both X-rays source and detector are rotated. However, in both cases the data is plotted between 2θ *vs* intensities of the peaks, where each peak represents the possible diffraction (constructive interference) from the planes with specific orientation.

However, the intensity of the peaks represents the number of planes and atomic scattering points in the crystal lattice, whereas the peak width gives information about the crystallite size. Smaller the particle/crystallite size, broader will be the peak and vice versa.[74] In the spectrogram, each sample has its own diffraction pattern which acts like a fingerprint. In addition, it also gives information about the crystallinity of the sample, phase purity, percent composition, d spacing, and crystal structure by searching and comparing with the extensively available database. However, it is very difficult to completely analyze the unknown sample only by using XRD. In this research work, all of our samples were in powder form and analyzed by preparing a thick layer on the amorphous glass slide. All the samples were scanned in the 2θ range of 20°-80° at the scan rate of 0.05.

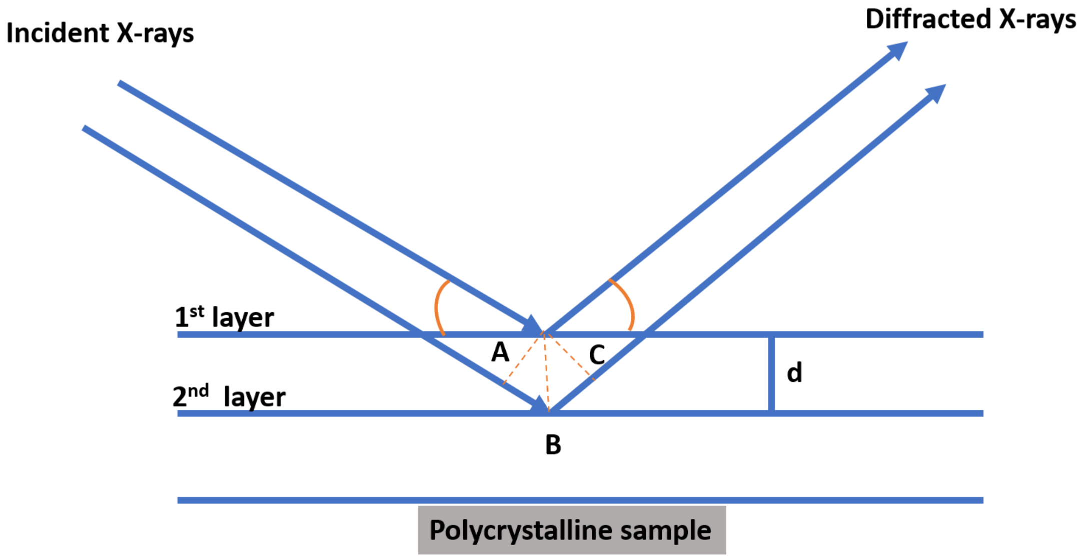

Figure 2.3 Diagram represents the X-rays diffraction pattern from the two consecutive layers (a, b) of the crystalline sample, where theta is the angle between the incident rays and plane of the sample. d is the distance between two layers also known as d spacing.

2.6.4. Electron Microscopy (EM)

Electron microscope is an advanced version of optical microscope, where the electron beam is used as source of light/radiations for high resolution imaging. It is well understood that minimum separation between two object that can be images depends upon the wavelength of source of light as given by formula $d = \lambda/2n\mathrm{Sin}2\theta)$, where λ is the wavelength and n is the refractive index of the transmission medium. Our eyes cannot see when the wavelength of incident radiations on the object is lower than 400 nm. Similarly, the optical microscope has limited resolution up to 200 nm. It means lower the wavelength of light to see an object, higher will be the resolution and *vis* versa. Based on this concept, unlike the optical microscope, the electrons behave like a wave with high energy which is the most suitable source of energy in EM. However, the wavelength of electrons depend upon the speed and applied potential which can be fortunately controlled. Thus, based on the resolution, design and the mode of interaction of electron beam with sample, EM can be categorized as scanning electron microscope (SEM), transmission electron microscope (TEM) and high-resolution transition electron microscope (HRTEM), which are discussed in the next part in bit more detail.

2.6.5. Scanning Electron Microscopy (SEM/STEM)

Scanning electron microscopy is a versatile technique to study the surface topology, texture, shape, and size of nanoscale materials. During analysis, a vertically aligned/adjusted electron gun (LaB_6 field emission gun in our case, 30 kV) produces a primary electron beam (PEM) to hit the sample in a high vacuum chamber. The energy, and focusing of the beam can be controlled by changing the applied potential and electromagnetic lenses respectively and the position of beam with respect to sample can be controlled by following the navigation within certain limit. After the interaction of PEM with sample, the electrons become elastically/inelastically scattered and produce a variety of signals in different directions. Among the various signals, the electrons scattered from the object surface (secondary electrons, SE) and some electrons emerging from the deeper location up to a few nanometers (back scattered electrons, BSE) are primarily considered in SEM analysis (**Fig. 2.4**). The SE electrons have comparatively high kinetic energy which are escaped from the surface with high intensity and gives information about the surface texture. While, the BSE electrons are generated when the trajectory of the incident electrons is changed due to their interaction with atomic nuclei of the material, and their kinetic energy thus depends upon the atomic mass of the material and provides information about the underlying part. These scattered electrons are directed towards appropriate detector i.e., generally through-lens detector (TLD). In contrast, in STEM analysis, a separate and specially designed detector is used which is placed at the backside of the sample. The collected electrons are then processed to generate a STEM image. The quality of the STEM image is highly dependent upon the several parameters i.e., applied potential, focusing, spot size and the nature of the sample. The samples of different nature can be used for analysis, which may be moisture free powder, completely dried liquid samples on appropriate grids, or even very thin films that are transparent to electrons at low voltage. The conductive samples are ideal for SEM analysis because the number of electrons reaching to the detector are high. In this regard, during analysis, various conducting substrates or sample holders i.e., carbon, alumina stubs, copper foil etc. are used. If the sample is magnetic or not conducting/less conducting in nature, then thin film of heavy metals (Pd, Pt, Au) up to few nanometer is coated on the surface of sample to minimize build-up of electrons on the sample (charging effect) and meanwhile enhance the conductivity and contrast of sample. In our case, all the samples were powder in nature and well-dried before analysis. Before analysis, the powder samples (1 to 2 mg) were placed on the alumina stubs/Cu foil, pressed and then carefully removed the loosely bound sample on surface with air blower. However, for STEM analysis, the highly diluted samples were dispersed/sonicated and then a carbon coated copper grid was dipped in the dispersion medium for 30 sec. After the deposition of sample on the grid, it was dried in vacuum and used for further analysis.

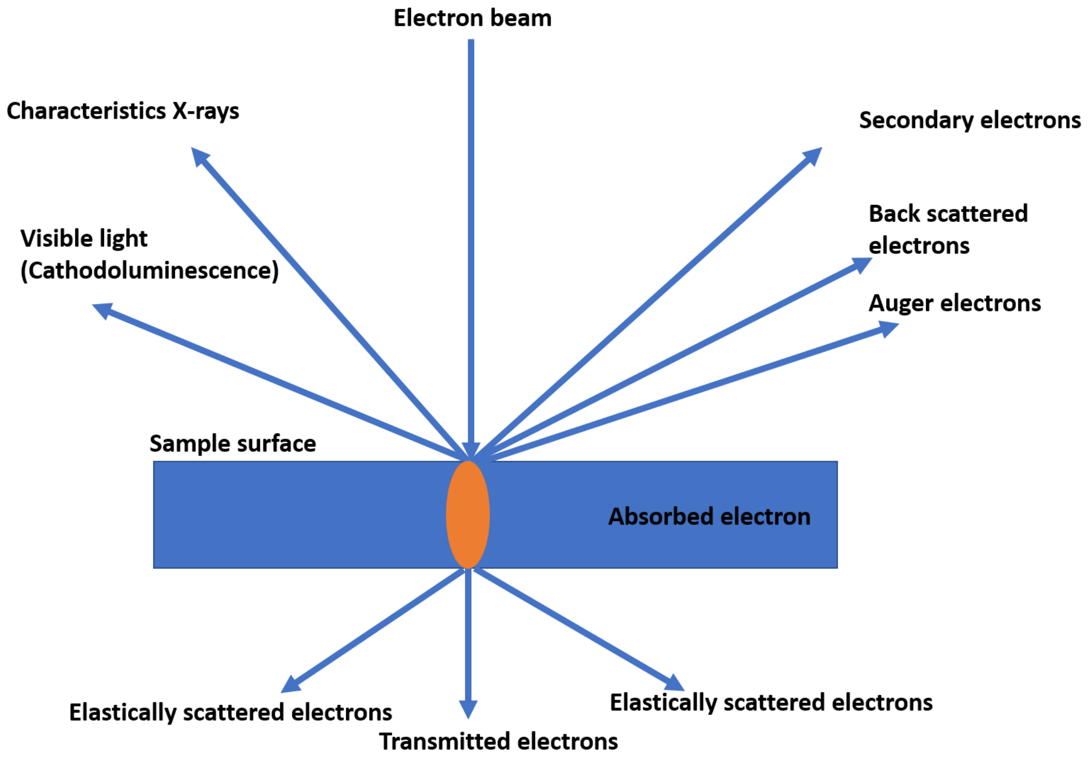

Figure 2.4 Diagram represents the interaction of electron beam with sample and all possible processes taking place during SEM analysis.

2.6.6. Energy Dispersive X-ray Spectroscopy (EDX)

EDX analysis can be used for the elemental composition of material. It is not a separate technique but extra X-ray detector is equipped with SEM instrument to collect the X-rays radiations originated from the internal part of the sample. During EDX analysis, comparatively high energy is needed to allow the electron beam inside the sample. After the interaction of electron beam with sample, consequently the electrons are ejected from the lower shell (K and L) of the atoms and generate vacancies. To fill those vacancies, the electrons from the higher orbital jump to the lower orbital with release of X-rays radiations (**Fig. 2.3**). The energy of these radiations directed towards the photomultiplier tubes (PMTs) is highly dependent upon the atomic mass of the material. The PTMs is a highly sensitive detector which has photo emissive material with the ability to further enhance the intensity of ejected rays. In this way, the different nuclei with the help of their corresponding X-rays are detected, thereby not only could detect the nature of a component but also quantify the % composition of each element in the whole sample. Based on this principle, elemental mapping can also be carried out to examine the distribution of each components in the whole sample. During elemental mapping, X-rays coming from different nuclei present in the sample produce different contrast owing to their different atomic masses and percent composition. Generally, higher the atomic mass, higher will be the energy of X-ray radiation which usually gives intense and separate contrast from the neighboring element and therefore are of great interest to unveil the homogeneity and position of various component in the bulk sample. Interestingly, both powder sample and thin film can be used with same sample preparation procedure as needed for SEM analysis. However, during EDX analysis, a separate detector and comparatively high applied potential (≈20-30 kV) is used to energize the electron beam for the X-rays generation.

2.6.7. Transmission Electron Microscopy (TEM/HRTEM)

It is an advanced version of electron microscope with resolution up to ≈ 0.2 nm (even down to 0.1 nm in HRTEM) that can be used to image both the external and internal features, composition and crystalline nature of the material with high magnification. The structure of TEM is more or less similar to SEM and consists of an electron gun, electromagnetic lenses, sample stage/holder, and detectors. However, in TEM the high potential (100-400 kV) is provided to generate the electron beam in a high vacuum chamber. The highly energetic electrons are directed towards the sample by controlling the potential across the electromagnetic lenses which are assembled around the beam path. Unlike the SEM analysis, the high energy electrons in TEM are transmitted through the sample to create a projection image displaying the information about the internal structure of the sample. More promisingly, the advanced version of TEM with high resolution (0.1 nm) also known as high resolution transmission electron microscope (HRTEM) is capable to focus/visualize the single crystallite and lattice points/fringes for the determination of the exact structure and size. At high resolution, the electrons are diffracted from the lattice planes according to the Braggs law to produce a proper diffraction pattern which gives information about the d-spacing and nature of the crystal structure/unit. During TEM analysis, it is necessary to prepare the sample in the form of very thin film to ensure the transmission of electrons. In this regard, usually a copper grid (0.25 cm^2) coated with a very thin film of carbon (5-20 nm) is used to support the sample. We have also used the same support for TEM/HRTEM analysis. First, the highly diluted samples were dispersed and sonicated in appropriate solvent, preferably organic solvents such as methanol, ethanol and DCM because they can easily be evaporated. Then, 10 to 15 µL of dilute sample was drop-casted on carbon coated Cu grid in a dust free environment followed by drying in a vacuum desiccator. The grids loaded with sample are placed in a sample-holder and analyzed in the range of applied potential (≈100-400 kV) while creating a proper vacuum inside the TEM chamber.

2.6.8. X-rays Photoelectron Spectroscopy (XPS)

In order to probe the chemical environment, electronic states and composition of the material, XPS is one the most versatile and highly valuable surface characterisation technique (up to 10 nm). It is based on the photoelectric effect, where the X-rays are used to hit the sample to eject the photoelectrons following the **equation 2.3** (**Fig. 2.4**a).

$$E_{\text{kinetic energy}} = h\nu - E_{\text{binding energy}} \qquad 2.3$$

Based on the kinetic energy of photoelectrons, their binding energy can be measured. During the interaction of radiations (X-rays) with the sample, possibly the electrons are ejected both from the surface and core level orbital of the material.[75] The energy needed for the outer orbital falls in the range of UV-range, therefore dealing with surface electrons called ‘Ultraviolet photoelectron spectroscopy (UPS)’ which gives us information about the bonding in molecules. However, in XPS analysis we are dealing with the core level electrons, therefore, it needs to provide soft X-rays (200-2000 kV) to irradiate the sample. During excitation, the electrons from the inner core are ejected and create vacancies. To fill those vacancies, transition of electrons (from higher to lower orbital) takes place with the release of energy in the form of auger electrons or fluorescence (**Fig. 2.5**b).[75] However, the probability of either of these processes depends upon the position of electron in the sub-shell from where the electron drops and atomic number of the element. Generally, the probability of the auger electron dominates in lighter elements.[76] In this regard, to follow the equation 2.2, the monochromatic beam of X-rays (usually Al k_α hν =1.49 keV and Mg k_α hν =1.25 keV) is used. When these monochromatic radiations hit the sample, consequently all the electrons (from outer and inner shell) are ejected from the surface atoms with different kinetic energies depend upon the position of electrons in the atom. The electrons closer to the nucleus (in L and M shell) are tightly bound and needs higher energy and are, therefore, ejected with less kinetic energy and *vis* versa. These photoelectrons and auger electrons with different kinetic energies are accelerated in a circular trajectory (path) to reach the detector slit, which measures their kinetic energy. It is worth to mention here that in XPS analysis, electrons only in the specific orbitals of elements in different rows of the periodic table i.e., 1s (for 1st and 2nd period, C & N row), 2p (2nd and 3rd period, Ti & Ni row), 3d (5th period, Pd row), 4f (6th period, Au row) are ideal and conventionally accepted for XPS analysis, which can be used to probe the electronic state/environment of each element. The electrons ejected from these orbitals are systematically collected based on difference in their kinetic energies by tuning the applied potential across the circular path. The detector detects/measures the kinetic energy of photoelectrons/auger electrons originating from a particular orbital. However, the kinetic energy of photoelectrons is dependent upon X-rays source unlike the auger electrons. Therefore, it is highly recommended to mention the source and plot the data in the form of binding energy to ensure the perfect fitting of both peaks arising from each electron. During analysis, thin film on the conducting FTO/ITO is used while creating ultra-high vacuum environment to minimize the interaction of radiations/electrons with unwanted species. Initially, it scans the sample in whole range (0 to 2000 eV) with appearance of peaks against each component in the corresponding position to get a scan or survey spectrum. For in depth analysis and to create a core level spectrum, the sample is then scanned in a specific range for the desired element(s). After analysis, the data is plotted/deconvoluted against the standard (C 1s in our case), assign the peak position and splitting pattern. In each chapter, we have presented both the scan and deconvoluted spectra of our desired samples and labeled properly.

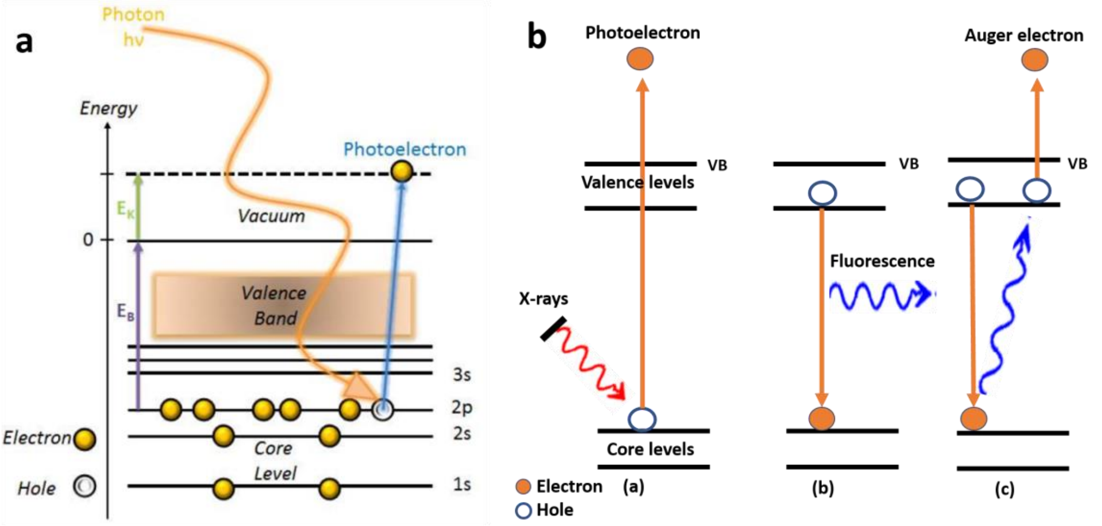

Figure 2.5 Diagram represents the photoelectric effect and electrons generation during XPS analysis (a) production of photoelectron and way of interaction of X-rays with core level electrons (b) the production of photoelectrons, auger electrons and fluorescence phenomenon simultaneously takes place during the excitation and refilling of vacancies. However, the photoelectrons ejected from the specific core levels are collected by the detector

2.6.9. Electrochemical Measurements

For the electrochemical study, Gamry potentiostat 600 was used throughout the experiments. The electrochemical experiments were acquired in acidic (0.5 M H_2SO_4), neutral (phosphate buffer, PBS) and basic medium (1 M KOH). For all those experiments carried out in the basic medium, the possible Fe impurities in KOH were removed following the standard method.[77] Before each experiment, the glass cell was washed with 5% HCl solution and dried in an oven to remove any impurities. In a three-electrode setup, fluorinated tin oxide (FTO, $\geq 12\Omega$, working electrode), Pt wire (counter electrode), and Ag/AgCl & Hg/HgO (reference electrodes) were employed in a standard electrochemical cell. Before analysis, 5 mg of sample was dispersed and sonicated in methanol (1 mL). 300 uL of the sample was then mixed with nafion (10 uL, 3 wt %) and sonicated for 1 h for the homogeneous ink formation. Prior to the deposition of sample, FTO was initially sonicated (10 min) and then washed with water, isopropyl alcohol (IPA) and acetone respectively. For all the electrochemical experiments, equal amount (20 uL, 0.5 mg/cm^2) of catalyst was deposited on FTO by simple drop-casting followed by natural drying. Potential recorded in all the experiments are presented *vs* reversible hydrogen electrode (RHE) converted by using standard Nernst equation (**equation 2.4**). The voltammograms were collected at 5 mV/s with 10% iR compensation (auto corrected in Potentiostate 600 Gamry). Tafel slope was calculated from the plot of overpotential (η) *vs* log j using steady state polarization curves. For stability tests i.e., chronoamperometry (CCE) and chronopotentiometry (CPE) were performed at 10 and 50 mA/cm^2. Double layer capacitance (C_{dl}) was calculated from the non-Faradaic region (1.07-1.17 V vs RHE) at different scan rate while taking average value of current in the voltammogram for accuracy. Other electrochemical parameters and catalytic activities i.e., electrochemically active surface area (ECSA), mass activity, exchange current density and turnover frequencies (TOFs) were calculated by using standard equations (Chapter 1).[78, 79] Electrochemically active sites were calculated from the integrated area of the reduction peak of redox couple in the steady state polarization curve. Electrochemical impedance spectroscopy (EIS) was acquired in the frequency range of 0.1 Hz to 1 MHz at amplitude of 5 mV, whereas the data is sometimes multiplied with -1 to get a symmetric Nyquist plot. During EIS experiments, the overpotential was only changed incrementally (10 mV) during the collection of EIS data for the calculation of Tafel slope.

$$(E_{RHE} = E_{exp} + 0.0591 * pH + E_{Ag/AgCl}/_{HgHgO} \qquad 2.4$$

Where, the electrode potential of Ag/AgCl = 0.197 V and Hg/HgO = 0.0982).

2.7. Oxygen Measurements and Faradic Efficiency

The qualitative analysis, quantification of water splitting and conversion efficiency was measured by calculating the Faradaic Efficiency (FE). The purity of molecular oxygen was monitored by collecting it in an air-tight syringe from the head space of the electrochemical cell operating under the continuous anodic potential at 10 mA/cm^2. The gas collected at regular intervals of time was then analyzed using gas chromatography (GC, Agilent 6890A) equipped with thermal conductivity detector (TCD). Two parallel columns i.e., fused silica column (30, 0.25 mm) and packed

MoleSiev 5 Å column, were simultaneously used for the complete separation of gases based on their relative retention time in comparison with the standard calibration curve, while using He (99.999 %) as the carrier gas.[80] In addition, water displacement method was also used for the quantification of molecular O_2. In this set-up, During continuous potential electrolysis (CPE) at 10 mA/cm^2 for 1 h, the generated O_2 molecules were accumulated in the vicinity of anodic part of electrochemical cell and then allowed to move in a 'Z' shaped capillary tube (diameter 10 mm) to a vertically aligned and water filled inverted burette (graduated with minimum scale of 10 µL) in a water bath or may be collected in specially designed round bottom flask (**Fig. 2.6**). Initially, the cell was purged with N_2 for 10 min followed by chronopotentiometry (CPE) experiments for 60 min, while noting the initial volume. During CPE, the decrease in the volume of water was monitored, which is directly related to an increase in the volume of gas in the head space of the burette. Theoretical value was calculated from the current produced while assuming that all the electrons are generated by the OER reaction. FE was calculated by using standard **equation 2.5** (details are given in chapter 1).[81]

$$(FE= mole_{exp} \text{ of } O_2/ mole_{theoretical} \text{ of } O_2*100) \qquad 2.5$$

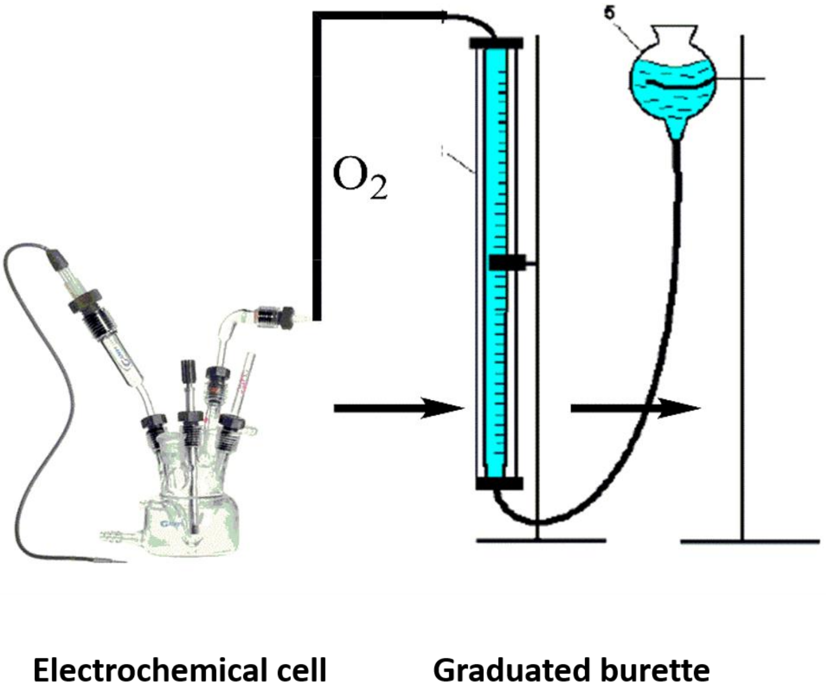

Figure 2.6 Schematic illustration of the assembly, used for the quantification of molecular oxygen and Faradaic efficiency via water displacement method. The blue color represents the water filling connected with electrochemical cell which can be replaced by the pressure exerted by O_2 produced inside the cell.

Chapter 3.

Ultrasmall Ni/NiO Nanoclusters on Thiol-Functionalized Graphene Oxide Nanosheets for Durable Oxygen Evolution Reaction

3.1. Synopsis

The demand of high anodic potential for oxygen evolution reaction (OER) owing to its sluggish kinetics limit the overall efficiency and practical applications of electrochemical water splitting process. Though, transition metal oxides are envisioned as the potential contenders in this quest due to their high redox potential, nevertheless their low conductivity and instability are among the formidable challenges that need to be addressed. In this chapter, we have demonstrated the chemical functionalization of GO with thiol functionality and controlled loading of Ni/NiO NCs (ca.~ 2 nm). A detailed discussion of selective functionalization, their role in the exfoliation of GO and effective stabilization of NCs is presented in this chapter. In the 2nd part of this chapter, the electrochemical performance of these nanohybrids and their comparative study with analogues bulk samples is presented. This study mainly highlight the unique role of supported NCs in term of various electrochemical parameters (CV, LSV, Tafel slope, Stability, EIS, TOF, and ECSA). In addition, we have also tried to explore the kinetics of electrode material for OER with both CV and EIS (very rarely reported), reaction mechanism and possible synergistic effect at the interfaces. We have further verified the role of our hybrid material by performing/comparing the pre-post electrochemical experiments including the effect of Fe impurities in electrolyte.

3.2. Introduction

The rapid depletion of unwarranted and exhaustible fossil fuels is a serious threat to the environment endowing a substantial amount of CO_2 (surpassing 400 ppm) at an alarming rate and thus leading to global warming. To counter these formidable energy and environmental challenges, the demand for sustainable energy production is on the rise globally.[82] In this regard, water being an abundant and widely distributed source of energy and its ability for the production of green electrons, protons (H^+), and oxygen (O_2) is an attractive candidate to exploit safe, clean and sustainable H_2 based economy.[83, 84] Electrochemical water splitting is among the holy grails of the chemistry to meet the future energy demand. However, the overall efficiency of water splitting is still limited due to the demand of high anodic potential for the half-cell oxygen evolution reaction (OER). During the recent past, serious efforts have been made to enable this process kinetically feasible at a potential reasonably close to its thermodynamic limit (1.23 V). RuO_2 and IrO_2 are still the benchmark catalysts, which can potentially catalyze the multistep OER process in wide pH range, and even conventional electrolysis relies on these precious catalysts.[85] However, their scarcity and high cost limit their large-scale applications. The design of cost-effective earth abundant and more efficient catalyst is, therefore, highly desired to trim down the high anodic bias for OER in the water splitting process.[84,86]

In addition to the high anodic potential and the high cost of noble metals-based catalysts, it has recently been established, both experimentally and theoretically, that the high Gibbs free energies of different intermediates (M-OH, M-O, MOOH) are indeed the major kinetic and thermodynamic barriers in OER process. Moreover, the high nucleophilic character of 'M-O' bond drastically inhibits the attack of the incoming nucleophile (OH^-) and thus impedes the chain reaction for the ultimate production of O_2 molecules.[18] Geologically abundant metal oxides, sulfides, selenides, phosphides, and double layer hydroxide (LDH) have been widely studied in this regard.[30, 87, 88] Among these, metal oxides particularly Ni oxides/hydroxide are still the leading candidate to catalyze the OER process at minimum overpotential due to their optimal redox potential and active sites.[89, 90] Moreover, their alloy and nanohybrid forms can further encourage their inherent redox properties.[91] However, their poor conductivity, less number of active sites and poor durability of catalyst are still the common impediments which seriously hamper the overall water splitting process. An attractive solution to address many such formidable challenges is the nanostructuring/nanoscaling of metal oxides to ensure their high electrocatalytic activity, selectivity, durability and maximum exposure of active sites.[92, 93] For instance, the use of metal nanoclusters (NCs, ≤ 2 nm)) with drastically reduced dimensions, relative to their bulk analogues, is an emerging area of interest having a number of unique and exciting size dependent properties. Moving from bulk to NPs and then to the subnanometric regime, unique catalytic and electronic properties have emerged due to the quantum confinement and high surface-to-volume ratio.[94, 95] Moreover, the less number of core atoms with open electrochemical accessibility further enhances their dynamic redox potential for challenging reactions like OER.[96] In this regard. Frei *et al.,* have recently demonstrated that the Co_3O_4 NCs supported on mesoporous silica (SBA-15) are highly active for water oxidation under mild conditions with high turnover frequency.[63] Similarly, Fominykh *et al.,* reported ultrasmall and well-dispersed colloidal NiO nanocrystals as an efficient electrocatalyst for water oxidation with high electrochemically active surface area.[97] Recently, Gong *et al.,* reported a decent Ni/NiO@Cr_2O_3 triphase electrocatalyst, where Cr_2O_3 decreases the oxidation of nanoscale Ni core retaining the abundant Ni/NiO interphases for long-term water splitting process.[98] Previously, Hussain's group has reported ultrasmall (1-2 nm) and monodisperse Ni_6 and Ni_4 nanoclusters to rationally induce the redox flexibility for OER by controlling the number of core Ni atoms with maximum exposed active sites.[99] However, the uniform dispersion of such ultrasmall and chemically stable nanoclusters/nanoparticles on highly conducting surfaces, like carbon nanotubes or graphene, is among the daunting challenges to ensure the practical use of alike nanoscale materials in nanocatalysis. Therefore, serious efforts are being made to exploit the inherent potential of metal and graphene based nanohybrids as highly effective materials with ultimately tuned electronic and catalytic properties desired for OER.[46] Recently, Razmjooei *et al.*, reported the effect of different heteroatoms (N, S and P) doped graphene oxide (rGO) hybrid materials for OER.[52] They found that the doping of heteroatoms, particularly 'S' atom, is very useful to improve the interaction of active catalytic centers with the adsorbed intermediates and thus facilitate the OER process. Moreover, the conductivity and physicochemical properties of the GO can also be significantly enhanced by chemical exfoliation and selective functionalization using wet chemistry.[100]

Taking into account the recent trends in the designing of potential electrocatalysts and nanoscale materials for OER, herein we report the effective decoration of thiolated graphene oxide nanosheets with ultrasmall and uniform Ni/NiO NCs to study the synergistic role of such stable electrocatalysts toward the sustainable OER process. The regioselective functionalization of graphene oxides *via* wet chemistry is one of the prudent approaches for the controlled and selective incorporation of thiol functionality (-SH). Besides, chemically linked Ni/NiO NCs with the thiolated and well exfoliated 2D graphene oxide nanosheets were expected to result in superior catalytic activity for OER because of better conductivity, stability, high surface to volume ratio and reasonably enhanced electronic density around the NCs to eventually facilitate the heterogeneous electron transfer (HET) at the graphene-S-Ni interphase. To the best of our knowledge, the ultrasmall and uniform distribution of Ni/NiO NCs particularly on the thiolated graphene oxide nanosheets is the first ever report for OER, and we believe that these findings will open up new research directions toward the better design of highly stable and effective functionalized graphene-based nanohybrids to make water splitting a practically viable process for the sustainable production of hydrogen.

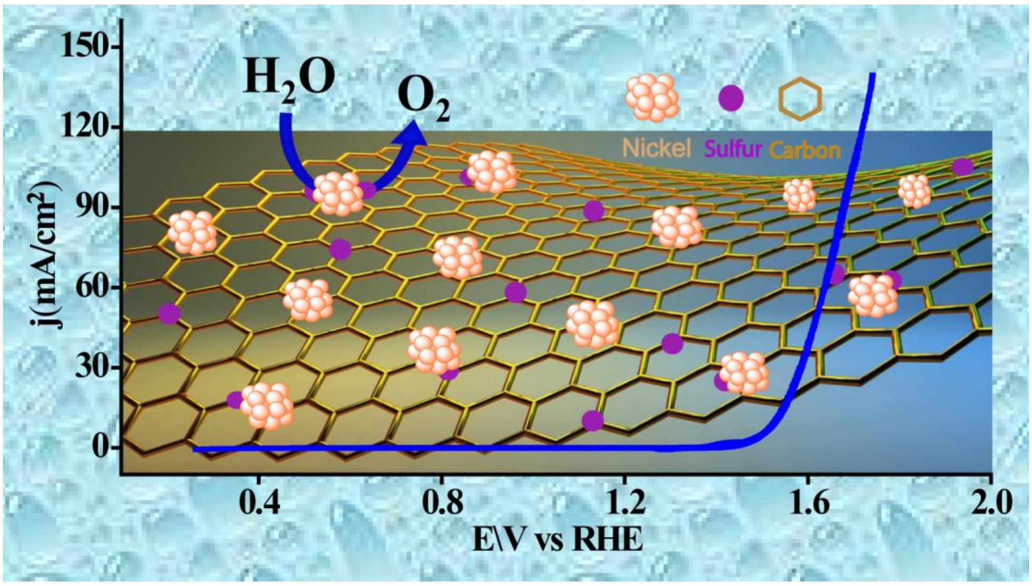

TOC 3.1 Table of content representing the thiolated GO loaded with Ni/NiO nanoclusters for water oxidation. The green voltammogram represents the OER performance.

3.3. Results and Discussion

3.3.1. Functionalization of Graphene Oxide and Nanoclusters Synthesis

Graphene oxide (GO) is an oxygen enriched material entirely consisting of aldehyde, ketone, carboxylic acid, epoxide and alcohol functional groups. Among these functional groups, epoxide and alcoholic groups can be selectively modified with reactive thiol group.[101] Epoxide ring with electrophilic carbon (next to O) is very reactive functional group due to its high ring and angle strain. However, the reactivity of electrophilic carbon and ring opening reaction of epoxide present in GO is very selective and preferably takes place with HBr among the whole series of halogen acids.[102] After bromination, the substitution of bromide is usually very easy, even in the presence of a weak nucleophile, because of its appropriate electronegativity and leaving group ability. Similarly, the hydroxyl groups (-OH) bound with sp^3 carbon in GO may also undergo nucleophilic substitution reaction (S_N2) in the presence of acid catalysts. As evident from the synthetic **Scheme 2.1,** after the dispersion of GO, HBr was added and the reaction mixture sonicated to enhance the probability of bromide ions to attack on the epoxide ring, which is thermodynamically more feasible than the bromination of alcohols at room temperature. However, at high temperature, the bromination and the attack of the nucleophile (thiourea) can take place simultaneously. Before the addition of KOH, the reaction mixture was placed in an ice bath to facilitate the exothermic acid-base neutralization reaction to yield sufficient thiol-modified GO for subsequent deposition of ultrasmall metal/metal oxide NCs.

During the loading of the metal/metal oxide NCs, the reaction was deliberately carried out in aqueous medium to facilitate the formation of an outer thin layer of metal oxide. Before the addition of reducing agent, the temperature of reaction mixture was maintained at 0 °C to ensure the formation of uniform and smaller NCs. Under these reaction conditions, there is a chance of adsorption of unhybridized thiourea and sulfur containing by-products on the surface of chemically functionalized GO, which may impede the formation of metal NCs and become difficult to control their size, morphology and catalytic activity. Therefore, before the formation of Ni/NiO NCs, modified thiolated-GO was repeatedly washed with dimethylfarmamide (DMF) to ensure the removal of the unwanted adsorbed species on modified GO as confirmed by XPS. The overall structural framework, incorporation of heteroatoms and the electronic network due to π-π bonds in the nanostructure of GO is known to have unique contribution in the development of GO based nanocomposites in numerous application.[103] Moreover, the selective functionalization of GO with ($-NH_2$, -SH, -OR) can further enhance its physicochemical properties i.e., electrical conductivity, surface area, exfoliation, extended π-π networking and more specifically their covalent interaction with metals.[104-106] Thiol functionality stands tall for its strong interaction with metals due to their high polarizability and strong electron donating ability that can significantly alter the surface chemistry of the nanomaterials.[107] To this end, we employed thiolated and well-exfoliated flower-like graphene nanosheets as conducting organic support to generate/immobilize ultrasmall Ni/NiO NCs to address the instability issues of transition metal/metal oxide for sluggish OER process (as discussed in the last section 3.3.3).

3.3.2. Compositional and Structural Characterization

It is noteworthy, that the characteristics peak of ‘SH’ is not visible in FT-IR spectrum, which may be due to the insufficient number of the thiol functional group below the limit of detection or inherently low IR absorption ability of thiol. However, it can be seen from the comparative FT-IR spectra (**Fig. 3.1**a) that after functionalization and loading of metal/metal oxide NCs, the partial reduction of graphene takes place and a decrease in the peak intensity of carbonyl and alcohol functionality is observed.

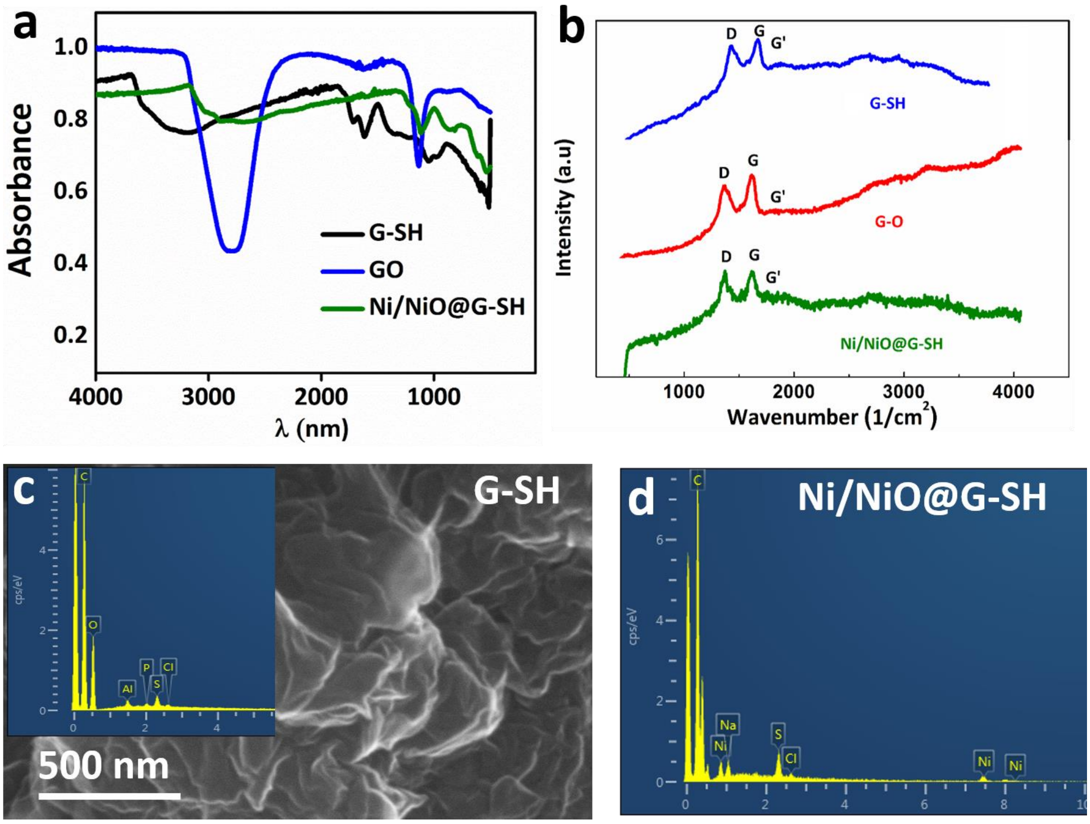

Figure 3.1 FT-IR, Raman spectroscopic and SEM/EDX analysis (a) FT-IR spectra of GO, G-SH and Ni/NiO@G-SH. Raman spectra of G-SH, GO and Ni/NiO@G-SH. (c) SEM image and EDX (Inset of c) analysis of G-SH. (d) EDX spectrum of Ni/NiO@G-SH.

Because of the chemical functionalization and partial reduction of GO, the exfoliation and defect sites are generated which can be probed from the appearance of the D and G bands in the Raman spectrum. Typically, the two prominent peaks, i.e., G band and D band in the range of 1570- 1600 cm^{-1} (sp^2$_{C\text{-}C,}$ E_{2g} symmetric mode) and 1350-1370 cm^{-1} (defects and sp^3$_{C\text{-}C}$, A_{1g} symmetric mode) respectively are the characteristics peaks. The 'D' band of GO is very sensitive to the effect of perturbation, doping and functional groups. Therefore, the exfoliation and extent of defective sites can be quantified from the intensity ratio (I_D/I_G) of these two bands.[108] The I_D/I_G ratio of 0.73, 0.80, and 1.02 was observed for GO, G-SH, and Ni@NiOG-SH respectively as shown in the **Fig. 3.1**b. The increasing order in the intensity ratio indicates the sensitivity of the D band with functionalization and disorder in the structure.[109] Moreover, the appearance of 2D band at~2700 cm^{-1} (two phonons double resonance phenomenon) at slightly higher intensity for G-SH and Ni/NiO@G-SH indicates the few layers of graphene oxide nanosheets.[110]

The synthesized Ni/NiO@G-SH nanohybrid was also characterized with SEM/EDX to study the surface texture and elemental composition. The presence of C, O, and S in G-SH, while C, O, S, and Ni in the EDX spectrum of Ni/NiO@G-SH indicates the expected chemical composition of the nanohybrid. The SEM images of GO before and after the functionalization are given in **Fig. 3.2**. The highly dense and layered structure of the GO can be seen, which is due to the interlayer stacking phenomenon. After functionalization, the expected well-exfoliated structure of G-SH nanosheets is evident from the SEM image, which shows a decent control over restacking of GO layers. The TEM images of G-SH further indicate the thin layers of nanosheets with an average thickness of~2 to 3 nm. However, due to the ultrasmall size, it is very difficult to visualize the particles of Ni in SEM and TEM analysis at low resolution. Therefore, Ni/NiO@G-SH nanohybrid was carefully examined under high resolution transmission electron microscope (HRTEM) as shown in **Fig. 3.2**. At low magnification, the particles are not very much clear due to their ultra-small size and inherently low contrast of Ni metal. The thin layers of the functionalized GO can be seen extended in two-dimensional (2D) manner and look like the flower's petals (**Fig. 3.2**a). At higher magnification, the ultra-small particles with an average size of *ca.*~2 nm (calculated *via* image j) can be clearly seen uniformly distributed over the thiolated graphene oxide nanosheets with 'd' spacing of 2 Å **(Fig. 3.2**b**)**. The intercrossed fringes can be seen in the randomly taken image, which obviously indicate the crystalline nature of Ni/NiO NCs and look like a part of graphene network. Typically, the equivalent interplanar spacing of 2 Å can be indexed to (111) of 100% relative intensity plane found in the Ni and NiO cubic structure.[111] The corresponding fast Fourier transform (FFT) pattern is shown in the inset of **Fig. 3.2**d. Moreover, the selected area electron diffraction (SAED) image suggests the proper crystalline structure with intense diffraction probably from the (111) plane of Ni/NiO nanocrystals (**inset, Fig. 3.2**c).

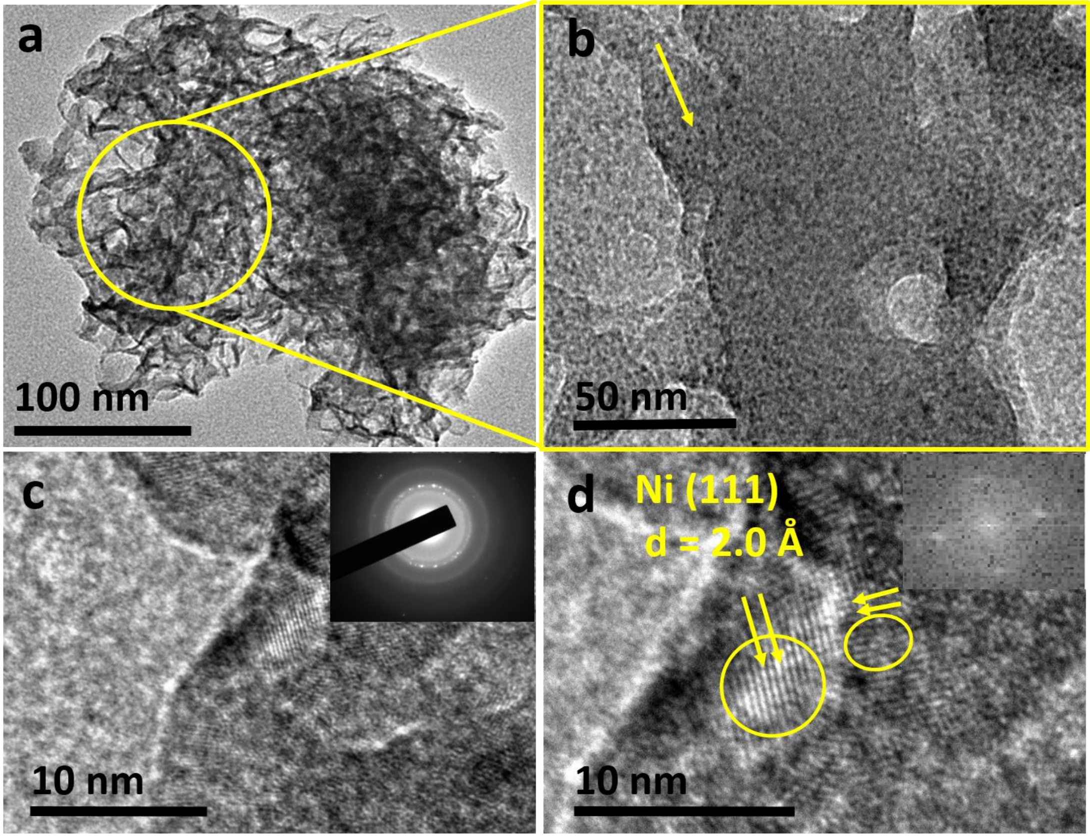

Figure 3.2 Transmission electron microscope (TEM) images of Ni/NiOG-SH nanohybrid at (a) Low magnification (b) High magnification (c) HRTEM image of Ni/NiO@G-SH nanohybrid, Inset shows the SAED pattern (d) Magnified HRTEM image of the fringes appearing in 'c' from the diffraction of Ni (111) and the corresponding Fast Fourier Transform (FFT) pattern.

The exact composition, chemical nature, functionalization and the possible oxidation states of the metal in Ni/NiOG-SH was examined with X-ray photon spectroscopy (XPS) in comparison with G-SH. The C1s (E= 284.5 eV) was used as the internal standard. The XPS survey spectrum of G-SH shows the presence of C, O, and S at the corresponding positions (**Fig. 3.3**a). The XPS C 1s deconvoluted core spectrum shows peaks at 284.63, 285.17, 285.54 and 169.19 eV corresponding to the C=C, C-C, C-O/C-S and C=O respectively (**Fig. 3.3**b). But due to the close binding energy values, the C 1s core spectrum cannot be precisely used to differentiate between the C-O, C-S, and the desired C-S-H bond. However, for high accuracy, the S2p core spectrum of 'S' (**Fig. 3.3**e) can be used that shows a peak at 163.71 eV with a splitting factor of 1.18 eV, which can be clearly assigned to R-C-SH bond.[101] The XPS survey spectrum after the metal loading also shows the signatures of C, O, S and Ni atoms (**Fig. 3.3**a). The C 1s and Ni 2p deconvoluted core spectra of 'C' and 'Ni' are shown in **Fig. 3.3**c, d. In the 2p core spectrum of the Ni, the intense peaks at 852.83 eV ($2p_{3/2}$) and 871.24 eV ($2p_{1/2}$) with 2:1 ratio represent the metallic nickel (Ni^0) while peaks at 855.11 eV ($2p_{3/2}$) and 873.15 eV ($2p_{1/2}$) correspond to Ni^{2+} with splitting factor of 18 ± 2 eV. We have also recorded the XPS spectrum after etching the surface oxides and found that both spectra are exactly similar which validate the presence of nickel in two different oxidation states ($Ni^{0/2+}$) as an intrinsic constituent of these nanohybrids. The additional and unwanted peak at 169.51 eV in the core spectrum of G-SH and Ni/NiO@G-SH can be assigned to S-O/O-S-O, which may be produced due to the formal oxidation of sulfur during analysis. In notable addition, after the loading NCs, the peak at 163.71 eV corresponds to S 2p shifts to 164.13 eV, which shows the possible transfer of electrons from thiol to metal. The somewhat lower binding energies of Ni(0) and Ni(II) than the expected values further validate the above observation.[111]

The characterization techniques demonstrate the successful functionalization of GO and subsequent decoration of thiolated graphene with Ni/NiO NCs. The TEM characterization is consistent with Raman data showing a few layers of GO nanosheets which can enhance the conductivity and potentially mediate the cross synergistic effect between chemically introduced impurities and abundantly availability empty π* orbitals.[112] Moreover, the well-exfoliated thin layers of GO nanosheets show that chemical functionalization increases their stability and in-turn their availability for the uniform distribution of crystalline metal NCs. Such morphology and uniform NCs with drastic decrease in their dimensions greatly enhance the surface and interfacial structure for the optimum catalysis process. From the XPS data, the reshuffling of the electronic density can be critically probed. Usually, the electronic density is shifted from the metal to the vacant π* orbital abundantly available on the GO. In contrast, an interesting trend was observed after metal deposition that can be seen in the 2p core spectrum of thiol

(**Fig. 3.3**e, f). The S 2p peak at 163.71 eV shifted to 164.13 eV after metal loading with the same splitting factor (1.18 eV), which shows the possible transfer of electronic density from thiol to metal to establish the covalent interaction with eventual enhancement of electronic density in the vicinity of NCs. These results support the synergistic effect between the thiolated-GO nanosheets and metal NCs that is worth exploring in various such catalytic reactions.[113, 114]

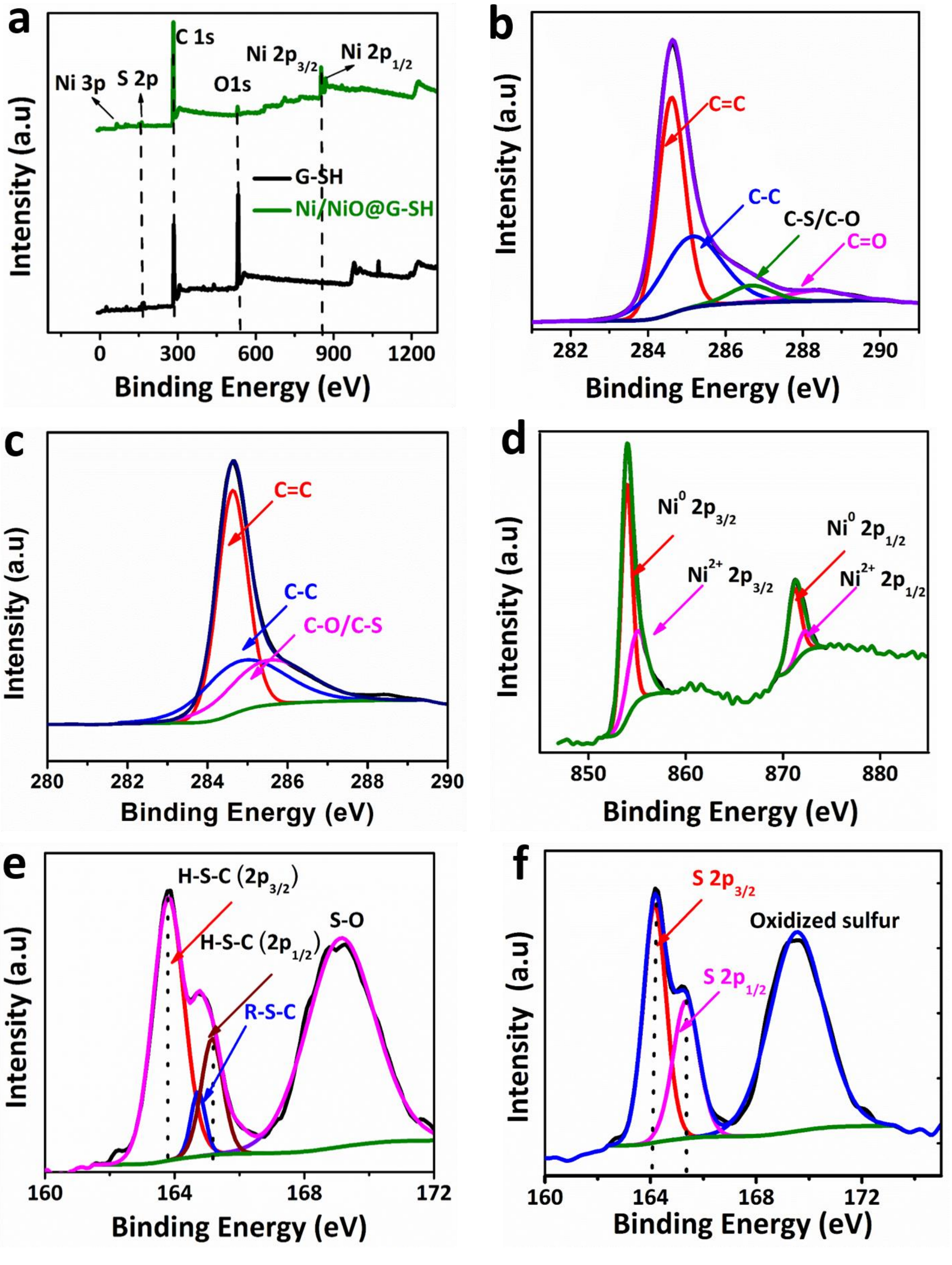

Figure 3.3 XPS analysis of G-SH and Ni/NiO@G-SH (a) XPS survey scan of thiol functionalized graphene oxide (G-SH) & Ni/NiO@G-SH nanohybrid (b) C 1s core

spectrum of G-SH (c) C 1s core spectrum of Ni/NiO@G-SH nanohybrid (d) Ni 2p core level spectrum on Ni/NiO@G-SH. sulfur 2p core level XPS spectra of (e) G-SH and (f) Ni/NiO@G-SH.

3.3.3. Electrochemical Evaluation

Electrocatalytic activity of all the synthesized materials (Ni/NiO@G-SH, NiO@GO, G-SH, and IrO_2) were initially evaluated for OER by taking cyclic voltammograms (CV, **Fig. 3.4**a). The appearance of redox peak of $Ni^{2+/3+}$ in the CV shows the electrochemical accessibility of Ni as an active catalytic site.[115] Interestingly, water oxidation was initiated at an onset potential of 1.46 V with minimum overpotential (230 mV) and highest current density of 140 mA/cm^2 was achieved at 1.7 V by Ni/NiO@G-SH nanohybrid showing superior activity among the Ni and graphene based nanocomposites reported so far and even better than the state-of-the-art catalyst (IrO_2) for water oxidation (**Table 3.1**. A 10 mA/cm^2 current density was achieved at η = 270 mV with an increase in the overpotential after the starting point of water oxidation, which shows the potential role of catalyst to harness solar light in the photovoltaic cell with 10 % photon conversion efficiency (PCE). Moreover, the large inflation in current density per small change of potential indicates the fast heterogeneous electron transfer (HET) process, which is very impressive for the supported heterogeneous electrocatalysts.

The sluggish OER process at low overpotential can only be driven by the support of intrinsic catalytic behavior to easily facilitate the 4 electrons transfer process between the catalyst and the adsorbed species.[116] However, the fast heterogeneous electrons transfer as well as easy adsorption and desorption of different intermediates (OH, OOH and O*) from the surface of the catalyst depends upon the energy level of ‘d’ orbital of the metal and the physicochemical properties of support.[117] Among the transition metals, the energy of the ‘d’ orbital of Ni (particularly NiO) is comparable to the ‘2p’ orbital of the oxygen, which can effectively overlap with optimum adsorption of hydroxyl specie (OOH) and ultimately facilitate the dynamic release of O_2 molecules.[118] Moreover, this intrinsic behavior can further be improved by providing a synergistic environment where Ni can not only settle in a stable electronic environment but can maintain the optimal redox couple ($Ni^{2+/3+}$) for OER in a cyclic manner. The surface functionalization of graphene with thiol as a strong electron donor and Ni-based nanohybrid was, therefore, proven as the judicious selection to fulfill the aforementioned requirements of the competent catalyst for OER.

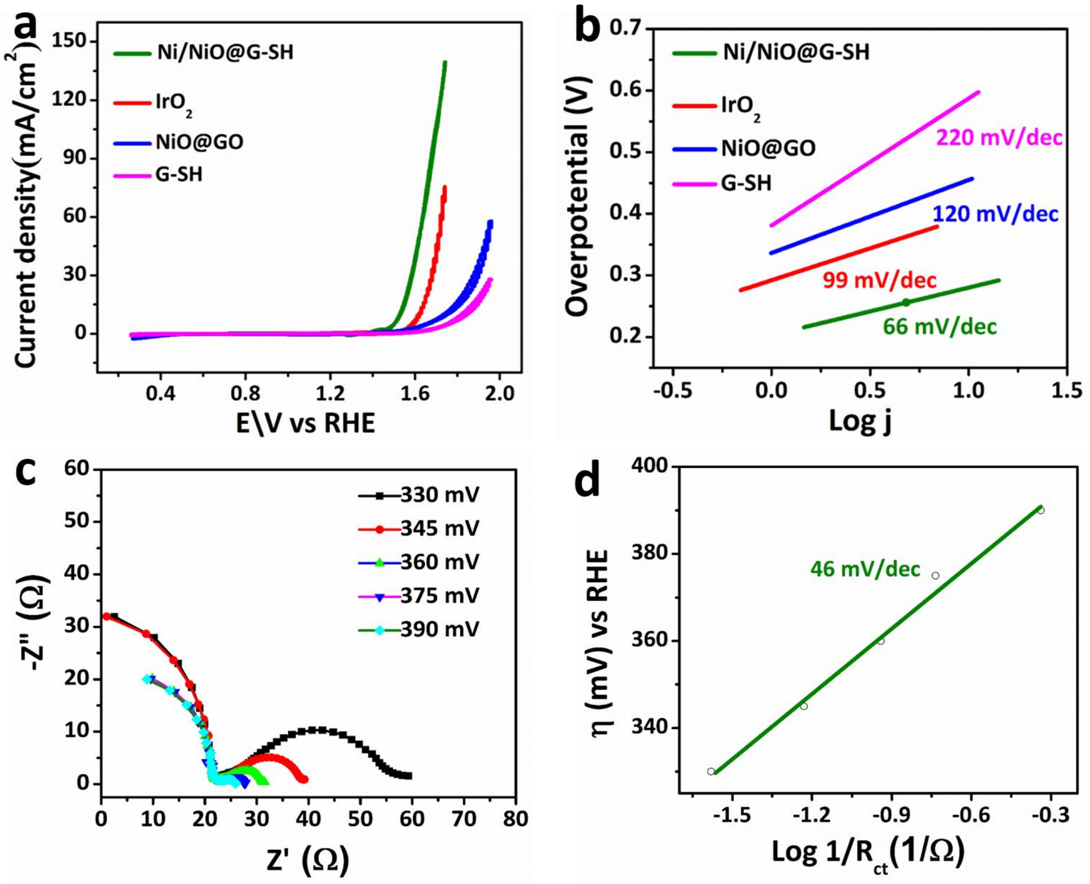

Figure 3.4 Electrocatalytic parameters for OER in 0.1 M KOH for (a) cyclic voltammograms (CV) of Ni/NiO@G-SH, G-SH, Ni@GO and IrO_2 in 0.1M KOH with scan rate of 5 mV/s (10% *i*R corrected). (b) Corresponding Tafel plots. Electrochemical impedance spectroscopy of Ni/NiO@G-SH (c) Nyquist at various overpotential with an increase of 15 mV (d) Corresponding Tafel plot of applied potential *vs* inverse Rct on logarithmic scale.

It can be seen from the cyclic voltammogram (**Fig. 3.4**a), that after the oxidation peak of Ni, the realization of such a high current density in a narrow regime of potential very close to the redox peak of Ni is a clear evidence of fast kinetics of OER. Such behavior of voltammogram especially for water oxidation supports the fast transfer of electrons probably at the graphene-S-Ni interface. Tafel slope is the representative of well-balanced conversion chain of the water splitting process. For Ni-based electrocatalysts, the Tafel slope generally falls in the range of 40 to 200 mV/dec, depending upon the kinetics and mechanism of the reactions taking place at the surface of catalysts.[107] Tafel slopes of 66, 99, 120, and 220 mV/dec were observed for Ni/NiO@G-SH, IrO_2, NiO@GO and G-SH respectively (**Fig. 3.4**b). The smaller Tafel slope (66 mV/dec) for the Ni/NiO@G-SH electrode materials even with high solution resistance (Rs, 21 Ω) recognizes the fast kinetics and intrinsic catalytic response that may be due to the large number of active interphases at the surface of exfoliated GO nanosheets which assist the electron transfer between the electrode/electrolyte interfaces.

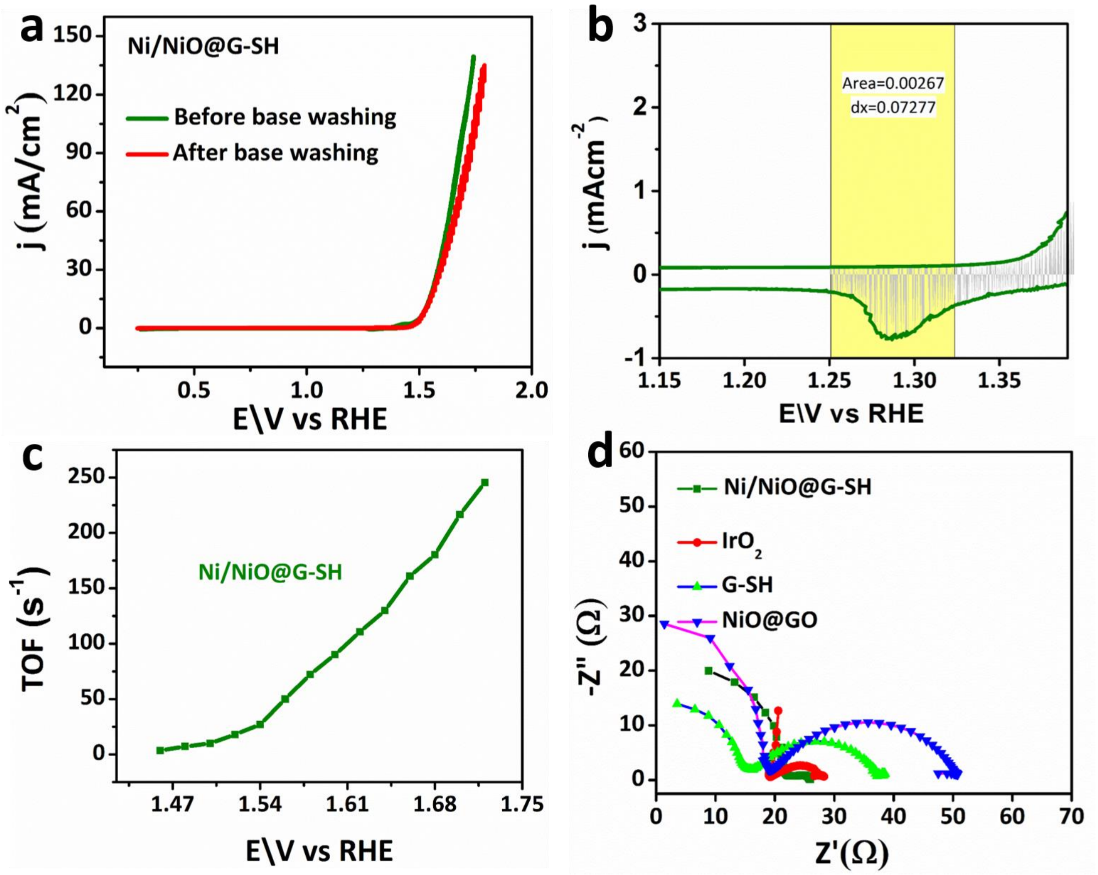

Figure 3.5 Electrocatalytic parameters for OER in 0.1 M KOH (a) Polarization curve of Ni/NiO@G-SH before and after base purification in 0.1M KOH solution with scan rate of 5 mV/s (b) area under the curve of the reduction peak of $Ni^{2+/3+}$ redox couple in the potential range (1.23-1.325 V vs RHE) used for calculation of active sites/TOF(c) Turnover frequencies (TOFs) of Ni/NiO@G-SH at various potential. Electrochemical impedance spectroscopy (d) Nyquist plots of Ni/NiO@G-SH, IrO_2, NiO@GO, and G-SH in the frequency range of 0.1 Hz to 1 MHz at 1.6 V vs RHE in 0.1M KOH.

The above kinetic study was acquired close to the onset potential at slow scan rate (5 mV/s), where the small current density (j) and overpotential suggest the feasible region for this study. But critically, the solution resistance (Rs) and charge transfer resistance (Rct) may hamper the kinetics of OER process.[24] However, this problem can be resolved by taking 100 % *i*R correction data under certain conditions, but it may not be possible when the Rs value is greater than 6 Ω or greater than the charge transfer resistance (Rct) for active catalyst.[119] To exactly reflect the inherent kinetics from the precise exchange current density by excluding the influence of Rs, we also calculated the Tafel slope from the electrochemical impedance spectroscopy (EIS). For this purpose, it is necessary to collect the data at a potential no lesser than 120 mV of extra overpotential in addition to the overpotential observed from the cyclic voltammogram. In this way the 1/Rct gives exact values of the exchange current density at different high overpotential to present the kinetics of overall electrode process in the wide potential range and thus minimizes the experimental errors usually associated with the Tafel slope calculated from CV.[24, 120] The Nyquist plots and the corresponding Tafel slope from the plot of applied potential *vs* inverse Rct on logarithmic scale are shown in the **Fig. 3.4**c. The Tafel slope of 46 mV/dec calculated from EIS indicates the third step (M-OOH formation) as a rate-determining step, which means that Ni/NiO@G-SH electrode materials potentially facilitate the energy-intensive step in OER process**.** Moreover, the smaller value recognizes the suitability of the provided system during catalysis as well as the resistance-free nature of catalyst, which is much needed to address the sluggish kinetics of OER. This concept can also be seen in the hysteresis-free polarization curve of Ni/NiO@G-SH (**Fig. 3.4**a).

The electrocatalytic performance of Ni based catalysts is very sensitive to the possible ‘Fe’ impurities present in the KOH. To investigate the effect of ‘Fe’ impurities, we purified the base following the reported method,[77] and no considerable effect was observed on the onset potential after purification. However, decrease in the current density (9 mA/cm^2) and increase in the overpotential (8 mV) at 10 mA/cm^2 was observed as shown in the **Fig 3.5a.** It shows that onset potential is the inherent property of Ni/NiO@G-SH hybrid material, whereas the current density can be fluctuated due the presence of minor iron impurities for this particular catalyst. Moreover, the effect of iron impurities is more prominent during the thin film formation electrochemically deposited from the high concentration of base (0.1 M KOH).[121] To better understand the catalytic performance, we assumed that Ni is electrochemically accessible and calculated their turnover frequencies (TOF) (**Fig. 3.5**c). The highest TOF (i.e., 245 s^{-1}) at 1.72 V shows the fast reaction taking place at the Ni/NiO@G-SH electrode materials and is much better than the previously reported colloidal and small NiO nanocrystals that may be attributed to the vital role of functionalized graphene nanosheets.[97] However, the TOF was found very sensitive to the potential range selected for the integration of area under the curve of the metal reduction peak. During the integration process, by selecting a wide potential range (1.183-1.341) or only the intense area of the reduction peak in small potential window (1.215-1.309), a change in the area under the curve was observed that eventually shows different surface concentration of the metal with high uncertainty. To resolve this issue, an optimum potential range (1.250 - 1.328 V) was selected for the related calculations (**Fig. 3.5**b).

The electrochemical impedance spectroscopy (EIS) was also carried out to investigate the catalytic behavior in term of their charge transfer at the electrolyte-electrode interface. The comparative Nyquist plots for three-electrodes system is shown in **Fig. 3.5**d. The basic parameters i.e., charge transfer resistance (Rct) and series resistance (Rs) are given in **Table 3.1**. In the Nyquist plots, the diameter of the semicircle describes the kinetics of the respective electrochemical process. The smaller the diameter of the semicircle, faster will be the kinetics. It is quantitatively evident from the smaller value of Rct for Ni/NiO@G-SH, which validates the role of catalyst to decrease the resistance of the system and ultimately make OER process feasible at sharp anodic bias with an exponential increase in the current density.[119] Moreover, the smaller Rct value also suggests the catalyst role in OER process rather than any residual process (**Fig 3.5**d**)**. During OER electrolysis, the harsh conditions (basic medium) generally deteriorates the performance of catalysts due to the leaching of sample, loss of activity, aggregation, and/or its transformation into various inactive phases. For this purpose, control current electrolysis (CCE) and control potential electrolysis (CPE) experiments were carried out to evaluate the long-term stability of catalyst (**Fig. 3.6**a). Expectedly, during CPE, 10 mA/cm^2 current density was maintained for more than 3 days (85 h) for Ni/NiO@G-SH at an overpotential of 270 mV. After the long-term electrolysis, the negligible increase (50 mV) in the potential was observed that may be due to the adsorbed species or the bubbles formation on the working electrode during electrolysis. To the best of our knowledge, among the transition metal/metal oxide and the graphene-based electrocatalysts, it is one of the most durable OER electrocatalysts. Moreover, the comparative stability test for Ni/NiO@G-SH and Ni@GO electrode materials was also run at 1.55 V to validate the persistent response at high current density i.e., 20 mA/cm^2 (**Fig. 3.6**b). The continuous increase in the current density shows the gradual activation and electrochemical accessibility of active sites at high anodic potential.[122] The activity and stability of catalyst can also be acknowledged from the stable polarization curves before and after the long-term electrolysis (**Fig. 3.6**c). Moreover, the negligible increase in Rct (4-7 Ω), even after the long term oxidation process, demonstrates the presence of resistance free and active Ni/NiO interphases to persistently catalyze the OER process resisting the long-lasting effect of the adsorbed species (**Fig. 3.6**d).[98]

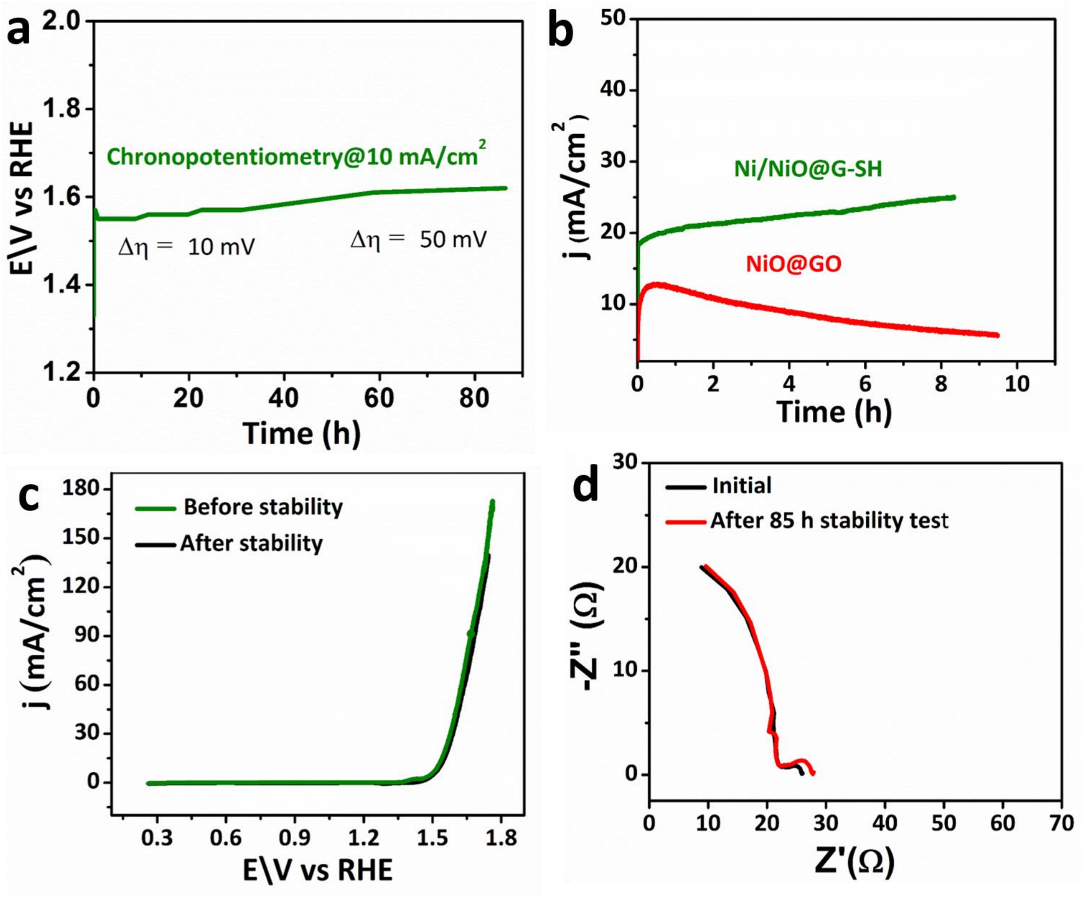

Figure 3.6 Electrocatalytic parameters for OER in 0.1 M KOH (a) controlled potential electrolysis (CPE) of Ni/NiO@G-SH at 10 mA/cm^2 in 0.1 M KOH with incremental change in the overpotential (b) chronoamperometry of Ni/NiO@G-SH and NiO@GO at 1.6 V in 0.1M KOH without *i*R correction (c) Polarization curve of Ni/NiO@G-SH before and after long term stability test (e) EIS before and after 85 h stability.

We have further calculated different electrochemical parameters, that is, electrochemically active surface (ECSA) from double layer capacitance (Cdl) in the non-Faradic region (**Fig. 3.7**a-d), mass activity, and exchange current density (**Fig.**

3.7f), which are summarized in **Table 3.1**. From the cyclic voltammograms collected for Cdl, we can see comparatively a large increase in the current density by increasing the scan rate in the non-Faradic region (**Fig. 3.7**a-d**).** However, due to the smaller potential window and using FTO as working electrode, a fluctuation in the current density in the non-Faradaic region due to the high capacitive behavior and sometime may create uncertainty in the results. The highest current response confirms that Ni/NiO@G-SH nanohybrid provides maximum exposed active sites and high mass activity with deposition of 0.5 mg/cm^2 of the sample. This can be primarily attributed to the combinatorial effect of chemically exfoliated G-SH nanosheets and ultrasmall Ni/NiO NCs with high surface to volume ratio, where the electrons can easily diffuse to the surface active sites of small NCs and thus can mediate the electronic state of the Ni$^{2+/3+}$ persistently.

It is noteworthy that the robustness of the catalyst can be enhanced when there is an optimum adsorption of the substrate (intermediates) on the surface of the catalyst and this optimum adsorption, in turn, depends upon the oscillation of the electronic density, compatibility of orbital energy levels of metals with adsorbed species and controlled engineering of the surface available for catalysis.[123] Thus, it is important to understand the possible mechanism of catalysis to facilitate the sluggish OER process. The less number of core atoms in metal NCs and their eventual catalytic accessibility on the support further enhance their redox potential at the nanoscale length.[124] From the superior electrocatalytic performance, it is obvious that Ni/NiO NCs supported on conducting surface (G-SH) have the ability to mechanistically drive the challenging OER process. In our case, the development of Ni/NiO@G-SH nanohybrid materials was designed by taking into account several factors including (i) chemical functionalization of GO to avoid its restacking as evident from its TEM characterization (ii) the formation of ultrasmall Ni/NiO NCs on the conductive and chemically modified surface of graphene nanosheets to minimize their catalysis-induced aggregation (iii) the creation of slightly reducing environment around the Ni to mediate the recycling potential of redox couple as evident from the XPS and stability test (iv) enhancement in the cross-synergistic effect between the graphene nanosheets and metal NCs due to the strong donor ability of 'S' as evident from the XPS and (v) the presence of empty 'd' orbitals of sulfur, which can accept the electronic density *via* back-donation from the metal by bringing closer the energy of 'd' orbital of Ni and '2p' orbital of oxygen in H_2O for optimum overlapping that can facilitate the dynamics of different intermediates to make the OER process more efficient at low overpotential.[125] We anticipate that such feasible two-way synergistic effect and reshuffling of electronic density in such nanohybrid materials may be responsible to provide the abridged energy barrier to prevent the poisoning of catalyst and eventually impart the extra-stability even at high anodic potential.

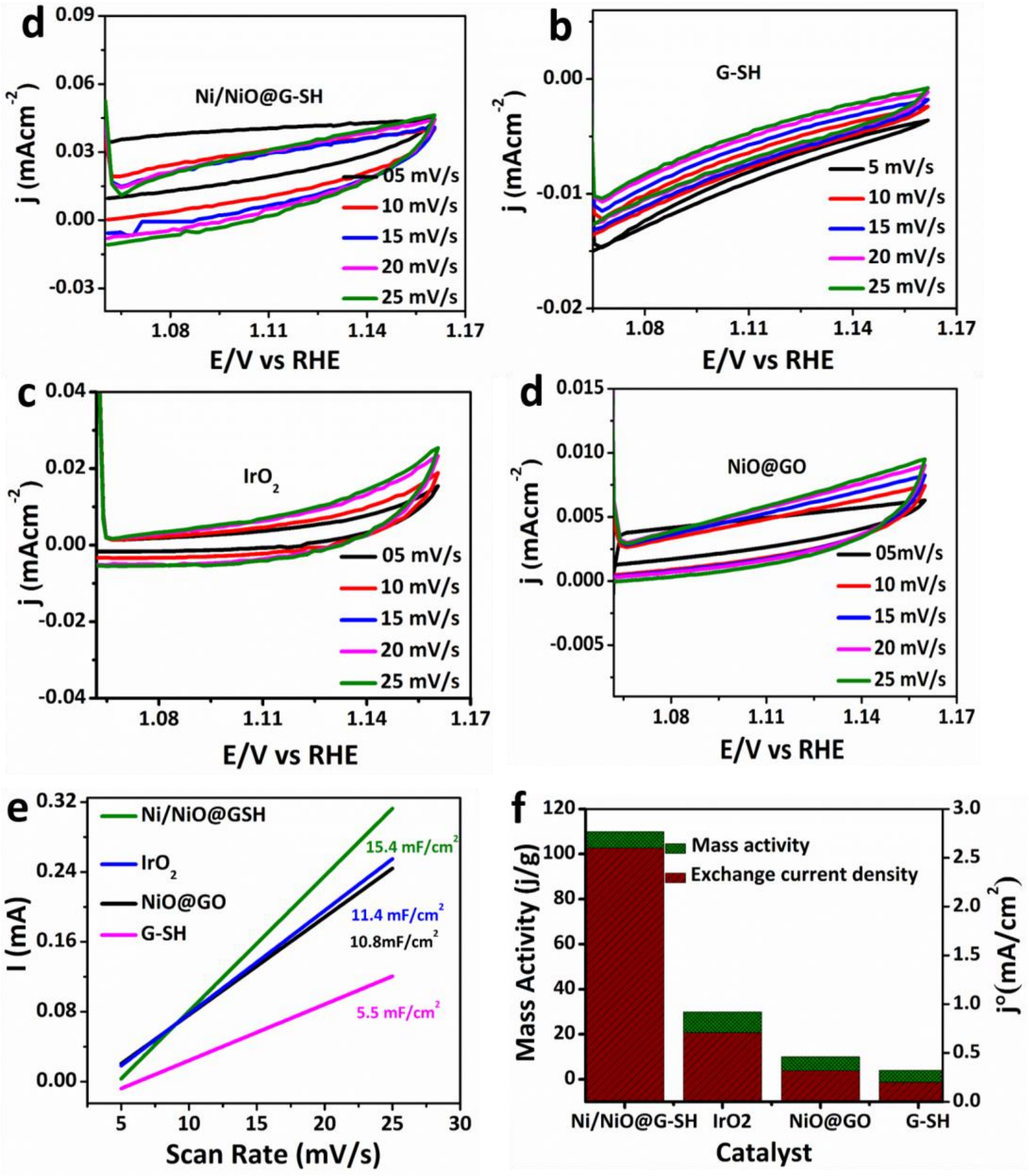

Figure 3.7 Electrocatalytic parameters for OER in 0.1 M KOH (a) Polarization curves of (a) Ni/NiO@G-SH (b) NiO@GO (c) IrO_2 (d) G-SH at different scan rate (5 to 25 mV/s) in the potential window of 1.07 to 1.17 V vs RHE (e) plots of average capacitive current (J) as a function of scan rate, where slope = double layer capacitance (C_{dl}) (f) comparison graph of mass activity (0.5 mg/cm^2 each catalyst) and exchange current density. Detailed calculations methods are given in the Chapter 1.

Table 3.1 Electrocatalytic parameters of Ni/NiO@G-SH calculated from steady-state CVs and OER electrolysis

Electrocatalysts	**η@10 mA/cm^2**	**Tafel slope (mV/dec)**	**Stability (h)**	**Mass activity (A/g)**	**j_0 (mA/cm^2)**	**C_{dl} (mF/cm^2)**	**Rs (Ω)**	**Rct (Ω)**
Ni/NiO@G-SH	270	46	85	110	2.6	3.13	22	2.5
IrO_2	392	99	-	30	0.71	2.01	18	9
NiO@GO	520	120	8	10	0.32	0.65	19	20
G-SH	600	220	-	4	0.20	0.10	15	32

η; Overpotential, A/g; Ampere/gram, F; Faraday, Rs; Solution resistance, Rct; charge transfer resistance, C_{dl}: Double layer capacitance, j_0: Exchange current density

3.4. Conclusion

Transition metal/metal oxide based nanohybrids, comprised of earth abundant elements, are very promising electrocatalysts for OER due to their high redox potential. However, their low conductivity, instability and slow kinetics for the sluggish OER is still a bottleneck for overall water splitting process. Electrochemically active assemblies comprised of functionalized nanostructured system are emerging candidates in this regard that need to be exploited. In this regard, we have reported the design and synthesis of ultrasmall and highly stable Ni/NiO NCs chemically linked to the thiol functionalized and highly conducting exfoliated graphene nanosheets as highly efficient and durable electrocatalysts to address OER challenges. The nanohybrid material was thoroughly characterized using FT-IR, Raman spectroscopy, SEM, EDX, HR-TEM and XPS, which shows the successful functionalization and effective decoration of thiolated graphene with Ni/NiO NCs. During electrocatalysis, a sharp onset potential of **1.46 V** and a current density of 180 mA/cm^2 at 2 V was observed for such hybrid electrocatalyst in 0.1 M KOH solution. A steady state current density of 10 mA/cm^2 was achieved for more than 3 days, which stands out among the graphene based electrocatalysts to warrant its use for the cost-effective production of hydrogen in water splitting process. Owing to their low onset potential and high stability, we believe that such a stable behavior of nanoscale material under the harsh basic conditions permits its recycling potential for OER. We anticipate that highly conducting graphene nanosheets and periodic recoiling of electronic density at the Ni-S-graphene nanointerfaces facilitates the redox fluctuation of electrochemically active $Ni^{2+/3+}$

species in a cyclic manner to impart extra stability. Moreover, the chemical functionalization of graphene nanosheets is a viable way to significantly improve its anchoring ability, conductivity, and the heterogeneous electron transfer ability at the electrode and electrolyte interface needed to speed-up sluggish electrochemical reactions like OER. From these results, we foresee the potential behavior of new alike materials by engineering the surface chemistry of graphene to enhance its ability to support metal/metal oxide NPs/NCs for superior electrocatalytic applications. Loading of bimetallic nanoparticles/nanoclusters on graphene can further enhance the bifunctional catalytic behavior for overall water splitting and other redox reactions.

Chapter 4.

Controlled Assembly of Cu/Co-Oxide Beaded Nanoclusters on Thiolated Graphene Oxide Nanosheets for High Performance Oxygen Evolution Reaction

4.1. Synopsis

The deployment of water splitting module is highly desired for the sustainable production of H_2 as future energy carrier. However, the sluggish kinetics and demand of high anodic potential are the bottlenecks for half-cell oxygen evolution reaction (OER) that severely hamper the overall conversion efficiency. Based on the remarkable performance of Ni NCs in chapter 1, here we will further elaborate the incorporation of thiol functionality on the surface of graphene oxide (GO) to achieve chemically exfoliated nanosheets to enhance its conductivity and trapping ability for metal oxides in nanoscale dimensions (≈ 2nm). We will show the effect of functionalization and reaction conditions on the size and shape transition metal oxides (Cu@CuO_x and Co@CoO, size ≈2nm). The materials were characterized using various advanced techniques (TEM/HRTEM, XPS, XRD and Raman spectroscopy) to explore the nature, composition and chemical linkage of NCs-G-SH. In the 2nd part of this chapter, we will describe the detail and comparative analysis of electrochemical performance with major focus on how the NCs and our hybrid materials play a unique role for water oxidation catalysis in terms of overpotential, Tafel slope, EIS, ECSA and long term stability test. Carbon based material are generally oxidized providing anodic bias and may contribute to the Faradaic current or deteriorate the catalytic performance. In this regard, we have quantitatively analyzed the water oxidation conversion efficiency in terms of Faradaic Efficiency while using Cu and Co NCs as electrode materials. For in depth analysis, the pre/post spectroscopic characterization was also carried out to explore structural/compositional stability and ultimate active phases of NCs for OER.

4.2. Introduction

The depletion of exhaustible fossils fuels at an alarming rate and their adverse effect on the environment and associated problems are prompting the need for the development of viable alternative energy resources.[126] In this regard, the exploration of sustainable energy resources (sun, water, wind and biomass) and its storage in the form of electricity or chemical bonds has become a developing trend globally.[127] Electrochemical water splitting for the production of clean 'H_2' as a potential energy carrier is one of the most promising approaches in the transition towards carbon-neutral energy systems.[15] However, this reaction is still limited due to its sluggish kinetics and the demand of high input potential mainly by oxidative half–cell oxygen evolution reaction (OER) during water splitting process and thus hamper the overall conversion efficiency and practical applications of this module. Although IrO_2 and RuO_2 are the benchmark catalysts for OER exhibiting good catalytic activities but their scarcity and high cost limit their practical applications.[120] Therefore, development of cost-effective and more efficient catalytic systems is an appealing solution in this quest to make the water splitting process more efficient, economical and practically a viable process for H_2 production. Transition metal-based OER electrocatalysts are very promising and reasonable choice in this regard, not only due to their natural abundance and low-cost but also because of their inherent high electrocatalytic potential for OER.[128]

During multistep $4e^-$ OER process, the positive Gibbs free energies for the adsorption/formation processes of various involved intermediates (OH^-, O^-, and OOH^-) on the surface of electrode make the whole process thermodynamically uphill. Thus, for the spontaneous OER, it is necessary to provide a potential of at least 1.23 V, corresponding to the Gibbs free energy of water splitting process (237.2 KJ/mol).[129] Moreover, the endothermic nature of this process and a few kinetic barriers (wire resistance and solution resistance etc.) adversely affect the electrochemical environment around the electrode, thereby requiring higher input potential and thus hampering the overall water splitting conversion efficiency.[130] Over the past few decades, great efforts have been made for the development of cost-effective and more efficient electrode materials (i.e., metal oxides, layer double hydroxides, chalcogenides including sulfides, selenides and phosphides, spinal family, metal carbides and metal alloys etc.) for OER especially for the alkaline electrolyzers.[91, 131-133] Moreover, their hybrid materials with various conducting substrate i.e., carbon nanotubes (CNT), graphene oxide (GO), and heteroatoms doped carbon have also been extensively explored to further enhance their catalytic potential.[134, 135] Among all these materials, metal oxides based electrocatalysts are still the leading catalysts due to their high redox potential for OER and inherently tunable orbital energy levels and active sites.[128] However, their low conductivity, instability, less number of active sites and in general the durable accessibility/exposure of active sites during catalysis are indeed the major impediments that need to be addressed with an objective to significantly enhance the electrocatalytic performance of metal oxides for long-lasting OER. Nanostructuring of the materials (both structural and electronic engineering) is one of the promising pathways to enhanced catalytic properties while addressing the above-mentioned challenges.[94] For instance, metal nanoclusters (NCs, size ≈2nm) are the new emerging materials in water splitting catalysis due to a drastic decrease in dimensions, intriguing size dependent catalytic/electronic properties that have sparked an immense interest in catalysis science.[94, 136] With nanoscale dimensions, NCs have high surface to volume-ratio, discrete electronic levels, maximum accessibility of surface/active sites and intrinsically low diffusion barrier for electrons from the core towards the surface.[124] Hence, metal NCs engender a bunch of non-recombinant electrons for the fruitful catalysis unlike the bulk materials. In this regards, Frei *et al.* have reported for the first time the SBA-15 templated mesoporous Co_3O_4 NCs for OER with high turnover frequency (TOF).[63] Later on, Fominykh *et al.* reported the use of ultrasmall colloidal NiO_x nanocrystals for OER and found that uniform distribution of NCs exhibited high electrochemical active surface area as compared to their bulk analogues and alike materials.[97] Similarly, atomically monodispersed Ni_6 NCs supported on carbon black were reported by Kauffman *et. al.* for OER catalysis.[96] It has been observed that small NCs are highly sensitive towards the intermediates and can provide alternative pathways for catalysis especially when loaded on a conductive support. We have also previously explored the thiol stabilized Ni_6 and Ni_4 NCs for OER and found that by decreasing the number of metal atoms in the core of nanoclusters significantly enhance the OER at low overpotential.[99] More recently, we explored the $Co(OH)_2$ NCs hosted on N-doped mesoporous carbon and NiO_x NCs on functionalized graphene oxide (GO) for OER, and found that NCs are indeed highly regarded for OER, where the number/exposure of active sites, and stability can be significantly improved by assembling them on a suitable conductive support.[25, 134, 137]

Among the various conducting supports, GO has emerged as the subject of intense research as an essential component of electrode materials owing to its excellent mechanical strength and unparalleled thermal and superior electronic properties.[138]

Moreover, due to the surface functionality and extended π orbitals of GO network that can overlap with d orbitals of metals to endorse the nucleation and growth of NPs/NCs and encourage the fruitful reshuffling of electronic density across the catalyst-support interface. Herein, we report the design and synthesis of Cu@CuO NCs and Co@CoO beaded nanoclusters grown on thiolated graphene oxide (G-SH) nanosheets to efficiently catalyze the OER in alkaline medium. It is noteworthy, that regioselective thiolation and exfoliation of GO is one of the judicious approaches to stabilize metal oxides in nanometric (≈2 nm) regime, which can enhance the catalytic potential of metal nanostructures in terms of surface active centers, conductivity and enhanced synergistic effect to facilitate the heterogeneous electron transfer (HET) rate at the GO-S-Cu/Co interphases for the extended period of OER at low anodic bias.

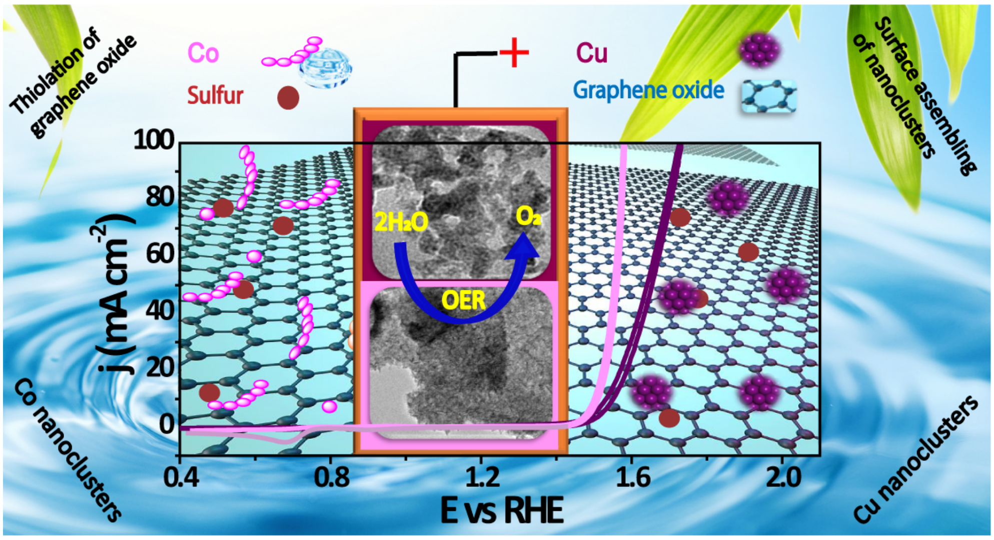

TOC 4.1 Table of content representing the thiolated graphene oxide nanosheets loaded with Cu-Co-oxides beaded nanoclusters for OER. The inset rectangle represents the TEM images loaded on FTO with corresponding cyclic voltammograms.

4.3. Results and Discussion

4.3.1. Functionalization of GO and Synthesis Cu/Co Oxide Nanoclusters

Graphene oxide inherently consists of oxygenated functional groups such as carbonyl, carboxyl, hydroxyl, epoxy and alkoxy groups, on both the graphene basal plane and edges.[139] These oxygenated groups change the hybridization of the attached carbon atoms from planar sp^2 to a tetrahedral sp^3 structure, which in turn increases the d-spacing and overall network of the GO and associated physicochemical properties and, therefore, have unique contribution in material science.[103, 138] Although the van der Walls interactions among the GO layers make it hydrophilic and facilitate the exfoliation and hydration in aqueous media, nevertheless, the immediate restacking of various layers hampers the conducting/catalytic properties of GO and is thus detrimental to its use as a support material in heterogeneous catalysis.[139] To address this formidable challenge, chemical exfoliation achieved by the functionalization of GO is one of the appealing and effective strategies.[101] Among the various functional groups in GO, epoxide and -OH can be selectively modified by nucleophilic substitution reaction. Promisingly, epoxide ring with electrophilic carbons (next to O) is very reactive functional group due to its high ring and angle strain. While focusing this high reactivity of epoxide ring and the strong interaction of thiol (-SH) for metals, -SH functional group was introduced *via* a rarely explored selective epoxidation and substitution reaction on the surface of GO (**Scheme 2.1**). Initially, GO was treated with hydrobromic acid (HBr) at room temperature, which resulted in the protonation of epoxide oxygen, enhancing the electrophilicity of the adjacent carbons, and selective nucleophilic addition and substitution reactions on epoxide ring and -OH groups, respectively. At higher temperature, dehydration and partial dehydrobromination took place, which provided highly brominated chemically reduced graphene oxide. Following that, the thiourea containing nucleophilic sulfur center was reacted with bromine moieties to form isothiouronium salts, which were subsequently hydrolyzed by base (NaOH) to form G-SH. It is noteworthy, that before the addition of base, the reaction mixture was placed in an ice-bath at 0℃ to facilitate the exothermic acid-base neutralization reaction to eventually increase the incorporation of more thiol groups. The motivation behind the incorporation of thiol functionality was to chemically exfoliate the GO with decent control over the restacking phenomenon and, meanwhile, to significantly enhance the conductivity, extended pi-pi (π-π) conjugation and more importantly the trapping ability for the development of metal-G-SH hybrid material, which is highly regarded for electrocatalysis. To this end, Cu/CuO NCs and Co/CoO BNCs were successfully loaded on the surface of chemically exfoliated/functionalized G-SH with decent control over their size and uniform distribution (hereafter called NCs@G-SH and BNCs@G-SH respectively). During the loading of NCs/BNCs, reaction was carried in methanol under the argon blanket at 0 °C to assist the reduction step of metal ions with stoichiometric amount of $NaBH_4$ for controlled nucleation under the provided conditions thereby generating the M-MO-G-SH ('M' stands for metal) nanointerfaces across the whole hybrid material.[140]

4.3.2. Structural and Compositional Characterization

After the functionalization, the change in the structural network was probed from the D band ($Sp^2_{c\text{-}c}$ E2g symmetric mode) and G band (defects and $sp^3_{C\text{-}C}$, A1g symmetric mode) around 1365-1620 cm^{-1} in a typical Raman spectrum (**Fig. 4.1**a). In fact, D band is highly sensitive to perturbation and structural defects, which are usually generated after chemical functionalization and doping and thereby relative intensity (I_D/I_G) can be used to examine the extent of defective sites and change in GO framework.[108] The I_D/I_G ratio of 0.77 and 0.81 was observed for GO and G-SH respectively. Notably, significant increase in I_D/I_G i.e., 1.81 and 1.82 after loading of Co and Cu respectively, ascribed the defects enriched framework of GO, which can significantly alter the structural strain and thus can increase the active sites for catalysis. Moreover, the appearance of new peaks around 2400 cm^{-1} indicate the few layers of G-SH nanosheets.[110]

The as-synthesized hybrid materials were initially characterized with FT-IR spectroscopy, where a decrease in the intensity of OH vibration indicates the possible functionalization (discussed in chapter 3, **Fig. 3.1**a). The presence of '–SH' group however cannot be ascertained with the FT-IR spectrum due to the inherently low sensitivity of –SH or its presence below the detection limit of FT-IR spectroscopy. However, the detection of C, O, S, Co and C, O, S and Cu in the EDX spectra after loading of Co and Cu respectively validate the expected composition and successful loading of metals (**Fig. 4.1**e**,** k). In addition, the formation of G-SH and its interaction with metal was elucidated by XPS analysis, which will be discussed in the later part.

The morphology, size and shape of all the synthesized hybrid materials was examined by scanning electron microscopy (SEM) and high resolution transmission electron microscopy (HR-TEM). **Fig. 4.1**b shows the well-exfoliated SEM image of G-SH, which indicates that inter-layer stacking can be controlled by chemical functionalization and even can be further improved after the loading of metal. The SEM images of Cu/CuO@G-SH and Co/CoO@G-SH are shown in the **Fig. 4.1**d**,** j displaying that G-SH nanosheets become dark after metal loading. Although, the elemental mapping indicates the uniform distribution of both Cu (**Fig. 4.1**f-i) and Co (**Fig. 4.1**l-O), but the size and shape of nanoclusters is not much visible that is due to their ultrasmall size, and inherently low and indistinguishable contrast under the low energy

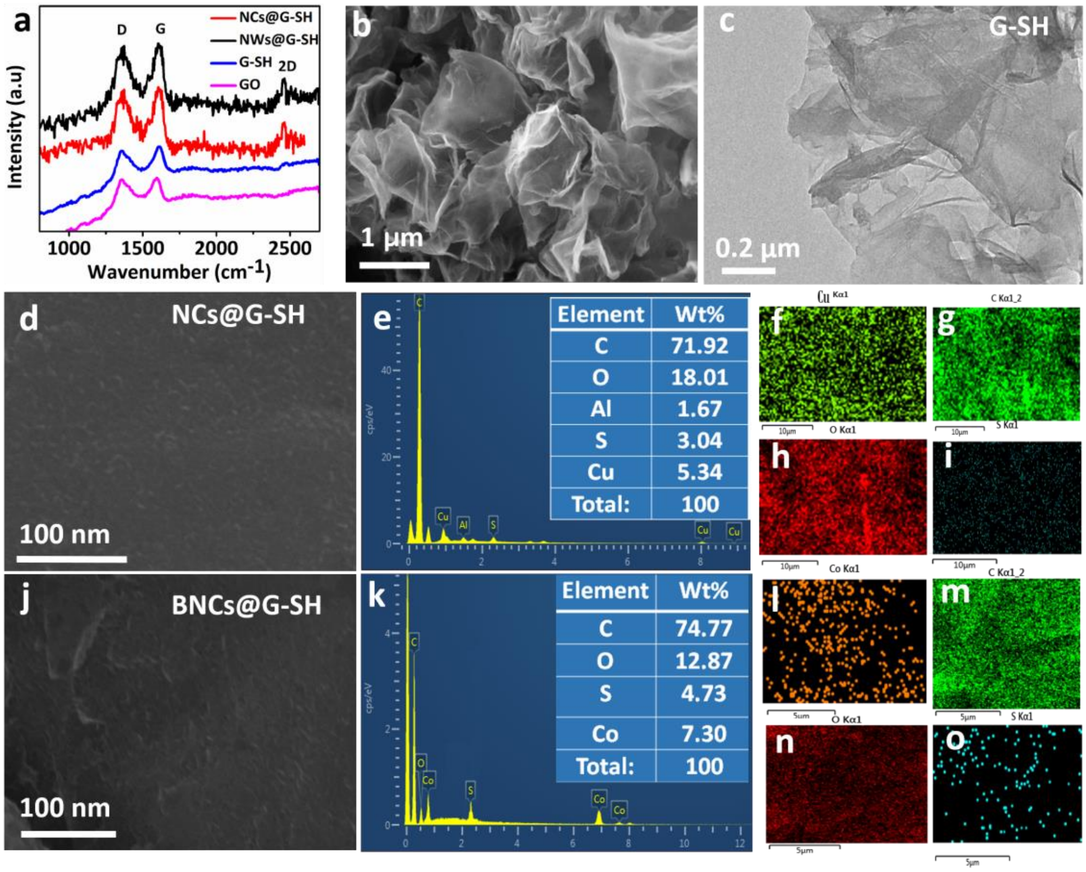

Element	Wt%
C	71.92
O	18.01
Al	1.67
S	3.04
Cu	5.34
Total:	100

Element	Wt%
C	74.77
O	12.87
S	4.73
Co	7.30
Total:	100

Figure 4.1 TEM/SEM/EDX analysis of GO, G-SH, Cu NCs@G-SH, and Co BNCs@G-SH (a) Raman spectra (b, c) SEM and TEM images of G-SH respectively (d, e) SEM image and EDX analysis of NCs@G-SH and (f-i) corresponding elemental mapping (j, k) SEM image and EDX analysis of BNCs@G-SH and (l-O) corresponding elemental mapping.

focusing beam of SEM. In this regard, we performed the TEM analysis, which reveals that G-SH is highly exfoliated and looks like ultrathin nanosheets (≈ 2nm) (**Fig. 4.1**c). It endorses the significance of chemical functionalization to exfoliate the dense structure of GO and affirms the defects enriched network as observed in Raman spectroscopy. The TEM images also show that the contrast of nanosheets is improved after metal loading, and the fairly uniformly distributed black dense spots in the magnified image represent the ultrasmall Cu NCs (**Fig. 4.2**a, b). In addition, the intense dense spots in some places possibly represent the clusters aggregated upon the underlying clusters during the sample preparation/assembling process. Interestingly, Co

NCs (< 2nm) were more or less orderly arranged and assembled on the surface of G-SH, however, followed different pattern of arrangement (**Fig. 4.2**d, e). In the magnified images, the ultrasmall dots of NCs are more visible gives an impression like beads and thus we call them beaded NCs. Such a uniform distribution and interconnection in nanoscale dimensions is useful to increase the metal-metal and metal-support interaction and thus can change the intrinsic catalytic behavior of overall hybrid materials. Although, the growth mechanism of NCs is not the domain of this article, however the above observations give insight that incorporation of thiol functionality not only enhance the exfoliation but also tailor the growth, shape, size and directional arrangement/assembling of the metal NCs. In order to probe the crystallinity and true crystal structure of the material on nanoscale, HRTEM analysis was performed where the visible lattice fringes found in both Cu and Co revealed the crystalline nature of the metal/metal oxides. In the magnified HRTEM image of Cu **(Fig. 4.2**c**)**, the d spacing of 0.20Å and 0.24Å can be indexed to the miller indices of (111) and (220) in the cubic structure of metallic Cu and CuO respectively. Similarly, the d spacing of 0.21Å and 0.20Å for Co correspond to the miller indices of (200) and (100) of cubic CoO and metallic Co respectively (**Fig. 4.2**f). The HRTEM analysis indicate that both Co and Cu are present in both metallic (core) and oxide phase (surface).

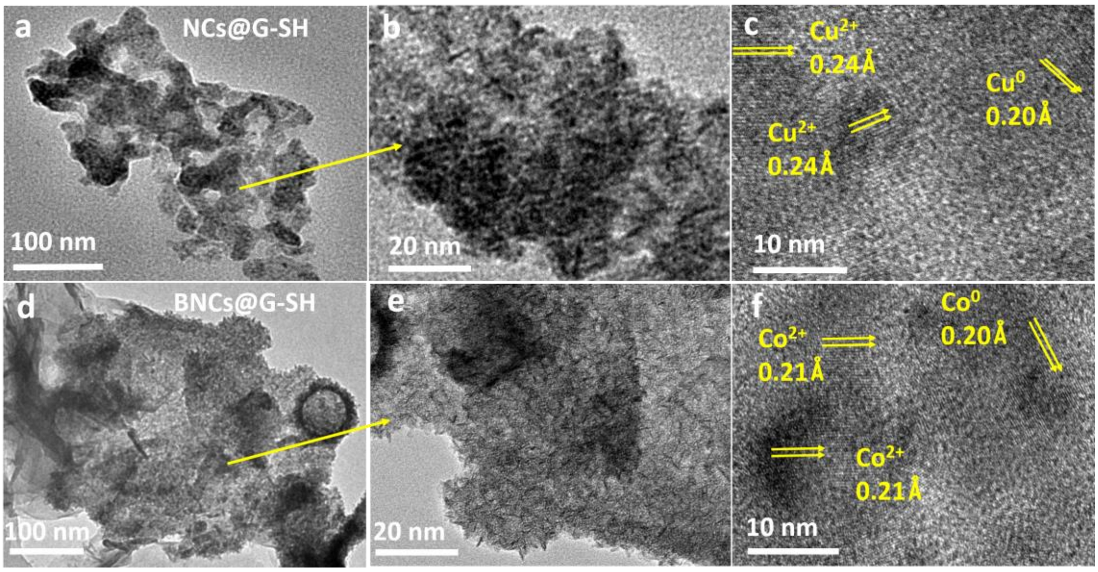

Figure 4.2 Transmission electron microscopy of Cu NCs@G-SH and Co BNCs@G-SH (a, b) TEM images of NCs@G-SH at low and high magnification respectively (c) HRTEM analysis of NCs@G-SH (d, f) TEM images of BNCs@G-SH at low and high magnification (g) HRTEM image of BNCs@G-SH.

To further elucidate the composition and crystallinity of GO and G-SH, they were characterized by X-ray diffraction (XRD) and their XRD patterns are shown in (**Fig. 4.3**a). The peak around 2θ ≈ 25° represents the characteristic peak of GO, which is present in all the samples. However, the slight broadness in the peak after functionalization and loading of metal indicates the reduced nature of GO, and meanwhile masks some peaks of the metal/metal oxides in this region. During XRD analysis, metal NCs peaks got noise-buried and less intense-/broad peaks were observed probably due to their ultrasmall size and less crystallinity that resulted in less X-rays diffraction. However, after deep scan analysis, the XRD spectrum of Cu/CuO@G-SH exhibited peaks at 2θ value of 43.5° and 50.3° corresponding to the diffraction of x-rays arising from the (111) and (220) reflection planes of metallic Cu (inset of **Fig. 4.3**a, JCPDS No. 04-0836).[141] The peaks at 2θ = 36.6°, 42.5, and 61.8° belong to the diffraction pattern arising from the (111), (200) and (220) crystal planes of cubic CuO (JCPDS No. 01-078-0428). Similarly, the XRD pattern of BNCs@G-SH exhibited diffraction peaks at 2θ = 36.6°, 42.6° and 62.7° due to (111), (200) and (220) diffraction pattern of *fcc* CoO phase (JCPDS No. 43-1004), but no peak was observed for metallic cobalt.[142] However, the lattice fringes in the HRTEM analysis validate the diffraction from the more exposed planes with 100% relative intensity of metallic and oxide phase of both Cu and Co.

To probe the electronic states and exact composition of catalysts, the samples were characterized by X-ray photoelectron spectroscopy (XPS). From the XPS survey spectrum, it is clear that G-SH purely consists of C, O, and S at their corresponding positions (**Fig. 4.3**b). Similarly, the appearance of peaks for Co and Cu in their respective survey scan reveal the successful loading of metals. However, for the true chemical environment, the core level spectrum of each atom (C, S, Cu and Co) was individually studied. The core spectrum of C1s can be deconvoluted into several peaks. The peaks at 284.7, 285.5, 286.4 and 288.2 eV can be attributed to C=C, C-C, C-O/C-S, C=O respectively (**Fig. 4.3**c).[143] The sharper and well-defined peak arising from C=C bond signifies an improved conjugated/aromatic system of graphitic network enhanced *via* selective epoxidation. Due to the close binding energy, the chemical environment of C-S and C-O bonds cannot be precisely distinguished from the C1s core spectrum, therefore a high resolution S2p spectrum was obtained.

The in-depth spectrum of S2p shows three peaks at 163.5 (S2p$_{3/2}$), 164.7(S2p$_{1/2}$), and 168.5 eV(S-O) (**Fig. 4.3**d).[101] The intense peak arising from H-S-C bond at 163.5 eV clearly indicates a successful grafting of predominantly thiol groups onto the graphene surface. While, the peak at 168.5 eV can be attributed to unwanted oxidation by-products (S-O) produced during analysis. However, after metal loading, the decrease in the intensity of S-O and an increase in the intensity of S-H peaks implies that S-H peaks are buried and thus not susceptible for oxidation (**Fig. 4.3**i). In addition, the presence of OH in the O 1s spectrum rules out the substitution of all the alcohol groups (**Fig. 4.3**e, f). In the Co/CoO@G-SH nanohybrid, the core level spectrum of Co shows peaks at 777.17 eV and 795.7 eV corresponding to 2p$_{3/2}$ and 2p$_{1/2}$ of Co^0, while peaks at binding energy of 781.4 eV and 798.2 eV can be attributed to Co^{2+} 2p$_{3/2}$ and 2p$_{1/2}$ respectively with characteristics splitting factor of ~16 eV arising from the spin-orbit coupling. In addition, the shake-up satellite peak at 786.7 eV (shoulder peak merged with 2p$_{3/2}$) further confirms the presence of Co^{2+} as reported previously (**Fig. 4.3**g).[137] Similarly, the core spectrum of Cu 2p of Cu/CuO@G-SH shows peaks at binding energy of 934.5 eV and 954.6 eV corresponding to Cu^{2+} 2p$_{3/2}$ and Cu^{2+} 2p$_{1/2}$ respectively (**Fig. 4.3**h). The energy difference between 2p$_{3/2}$ and 2p$_{1/2}$ levels is about ≈20 eV arising from the spin-orbit coupling of CuO$_x$ nanostructure.[144] In addition, the overlapped satellite peaks between 940 eV and 945 eV are also the characteristic peaks of Cu^{2+} with a d^9 system in the ground state (absent in Cu$_2$O) and are in good agreement with the reported data for Cu 2p levels in CuO$_x$ phase.[50] The deconvoluted copper 2p spectrum also shows peaks at 932.5 and 952.5 eV corresponding to 2p$_{3/2}$ and 2p$_{1/2}$ of metallic copper (Cu^0). It is noteworthy to mention that after loading of metals, no apparent change in the XPS spectrum is observed except in the binding energy of H-S-CH shifted slightly towards the higher side (from 163.5 to 164.9 eV), which may be due to the transfer of electronic density from thiol towards the metal to possibly generate a covalent linkage.

All these characterization techniques confirm the successful exfoliation of GO sheets, incorporation of –SH, and the loading of Cu NCs and Co BNCs with decent control over their size (~ 2nm). It is, therefore, evident that thiol functionalization of GO not only control the restacking phenomenon of G-SH nanosheets but also assist in the nucleation and growth of ultrasmall metal/metal NCs. Moreover, the XRD, XPS and HRTEM analysis indicate that both metals are present in metallic and oxide phases

(Co^0@$Co^{II}O_x$ and Cu^0@$Cu^{II}O_x$) and are uniformly distributed throughout the structure. These ultrasmall metals aggregate in various redox states, their possible covalent linkages with thiol and abundant π and π* orbitals of conjugated framework significantly enhance the synergistic effect of catalysts and the conducting support and are direly needed during catalysis.[112]

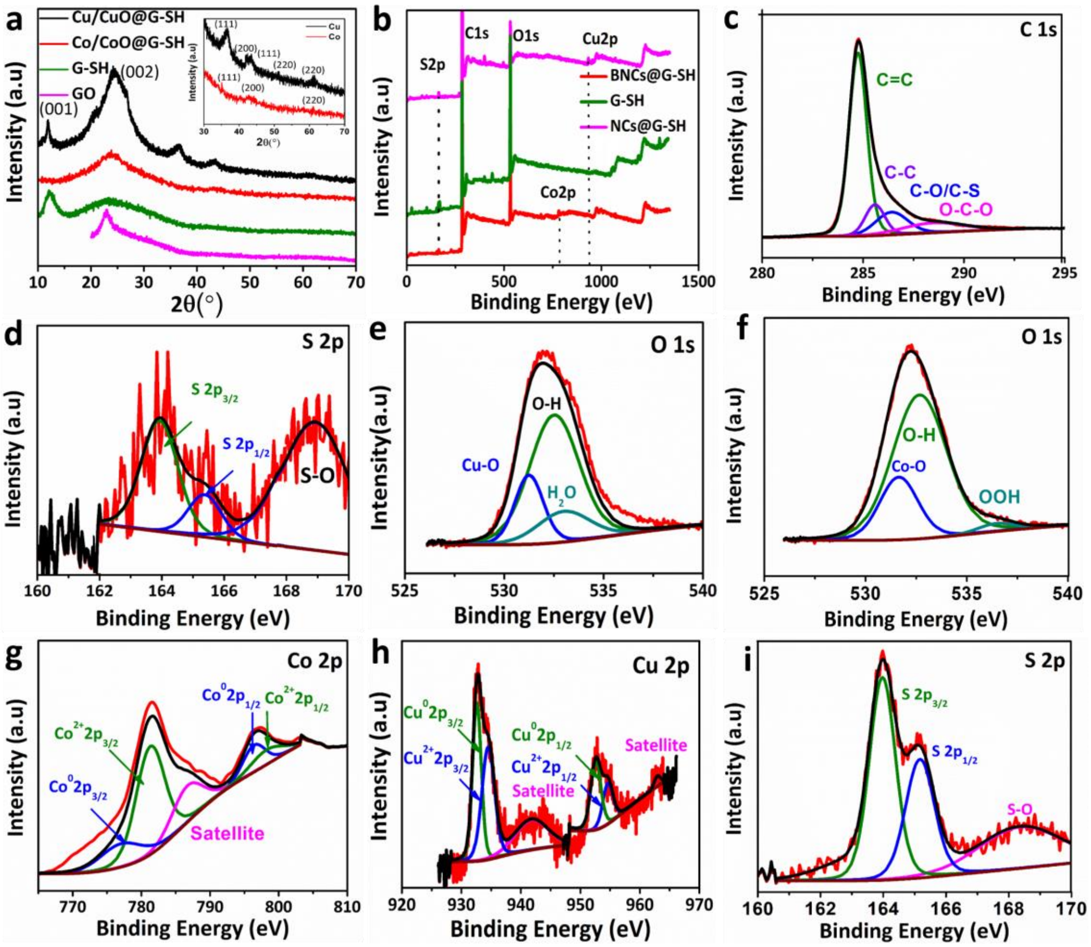

Figure 4.3 X-rays diffraction and XPS analysis of G-SH, Cu NCs@G-SH and Co BNCs@G-SH (a) XRD pattern of GO, G-SH, Cu NCs@G-SH, and Co BNCs@G-SH, where the inset graph represents the magnified part of spectrum of G-SH (c) C 1s core level spectrum of G-SH (d) S 2p core level spectrum of G-SH (e-f) O 1s core level spectrum of NCs@G-SH and BNCs@G-SH respectively (f) Cu 2p core level spectrum (g) Co 2p core level spectrum (h) S 2p core level spectrum of G-SH after metal loading.

4.3.3. Electrochemical Oxygen Evaluation Reaction

The electrocatalytic performance of the as-synthesized catalysts, analogous samples and benchmark electrocatalyst towards OER was evaluated in alkaline medium (1 M KOH). The standard electrochemical measurements were performed while using electrochemical workstation (Gamry 600) equipped with three electrodes electrochemical cell. **Fig. 4.4** represents the *iR*-corrected polarization curves collected at the scan rate of 5 mV/s. By comparing the relative catalytic activity, especially the overpotential and corresponding current density, the poor performance of analogous samples (NiO@GO and CuO@GO) is clear from the higher onset potential. In contrast, the overpotential needed for water oxidation is significantly decreased by using NCs@G-SH and BNCs@G-SH and their performance is comparable to benchmark RuO_2 electrocatalyst. An overpotential of 290 mV, 310 mV and 300 mV is needed for BN*C*s@G-SH, NCs@G-SH and IrO_2 respectively to afford a current density of 10 mA/cm^2 under the similar conditions - an important figures-of-merit of catalysts for the solar fuel devices with 10% conversion efficiency.[9, 145] The activities near the onset potential of NCs@G-SH and BN*C*s@G-SH are comparable to IrO_2, however, surprisingly outperform the benchmark catalyst in attaining a higher current density while extending the potential window anodically (**Fig. 4.4**a**)**. Such energetic behavior of electrode materials, especially BNCs@G-SH, manifests their superior performance as compared to their bulk-/analogous samples. For further verification, we have investigated the kinetics of the reaction from the Tafel slope (plot of log j *vs* η). As shown in **Fig. 4.4**b, the slopes of BNCs@G-SH (54 mV/dec) and NCs@G-SH (66 mV/dec) are very similar, which implies that both these electrocatalysts possibly have the same rate determining step and reaction mechanism. Moreover, the smaller Tafel slopes of both NCs than IrO_2 (99 mV/dec), analogous samples (**Table 4.2** designate the favorable kinetics of the OER conversion chain reaction on the surface of ultrasmall metal/metal oxide anchored on the chemically modified G-SH.[139] Moreover, in order to better understand the factors responsible for the fast kinetics, the electrochemical impedance spectroscopy (EIS) was also performed with major focus on the charge transfer (R_{ct}) resistance (**Fig. 4.4**c). The R_{ct} (diameter of semicircle in Nyquist plots) value is a well-balanced quantitative representation of the inherent charge transfer ability of catalyst across the electrode-electrolyte interface. **Fig. 4.4**c displays the Nyquist plots, where the smallest R_{ct} values of BNCs@G-SH (15 Ω) and NCs@G-SH (20 Ω) corroborates the minimum resistance and strong electronic coupling across the whole hybrid materials for HET and thus can kinetically assist OER in a narrow potential window.

However, during catalysis, the potential induced transformation of electrode material into various inactive phases, leaching of sample, and aggregation phenomenon especially in case of NCs hamper the catalytic performance. In this regard, long-term durability test i.e., control potential electrolysis (CPE), was conducted (**Fig. 4.4**d). During CPE, 1.55 V and 1.58 V was needed (without *i*R correction) for BNCs@G-SH and NCs@G-SH respectively to hold a current density of 10 mA/cm^2 for 50 h. Such a persistent performance over a long time implies the availability of regenerated active sites for the periodically assisted OER, and meanwhile rules out the leaching of sample or potential induced transformation to inactive phases.[146] Moreover, the sustained current response is also evident from the CVs before and after stability test with no loss in current density or increase in the overpotential, unlike the bulk samples **(Fig. 4.5**a, b**)**. Hence, the synthesized nanohybrid materials portray the enhanced intrinsic potential due to nanostructuring and uniform surface assembling on nanoscale length.[134] Thus, optimal interaction of catalyst with various intermediates during OER would be the key reason for the fast mobility of charged species (ions and electrons), while possibly avoiding the long-lasting retention of the surface adsorbed species.[139]

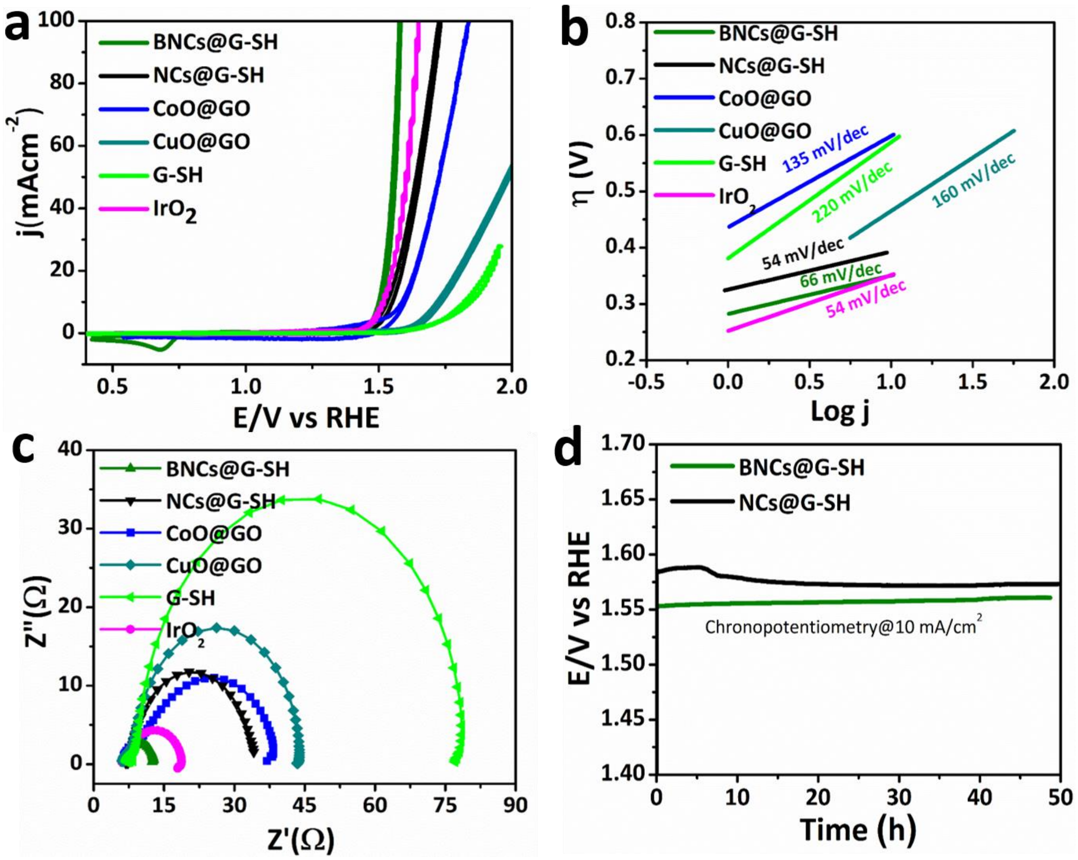

Figure 4.4 Electrocatalytic evaluation for OER in alkaline medium (1 M KOH) (a) Polarization curves of Co BNCs@G-SH and Cu NCs@G-SH in comparison with analogous samples and benchmark catalyst (IrO_2) (b) corresponding Tafel plots (c) Nyquist Plots collected in the frequency range of 0.1 Hz to 1 MHz at DC potential of 0.5 V (d) chronoamperometry test at the potential of 1.6 V for 50 h.

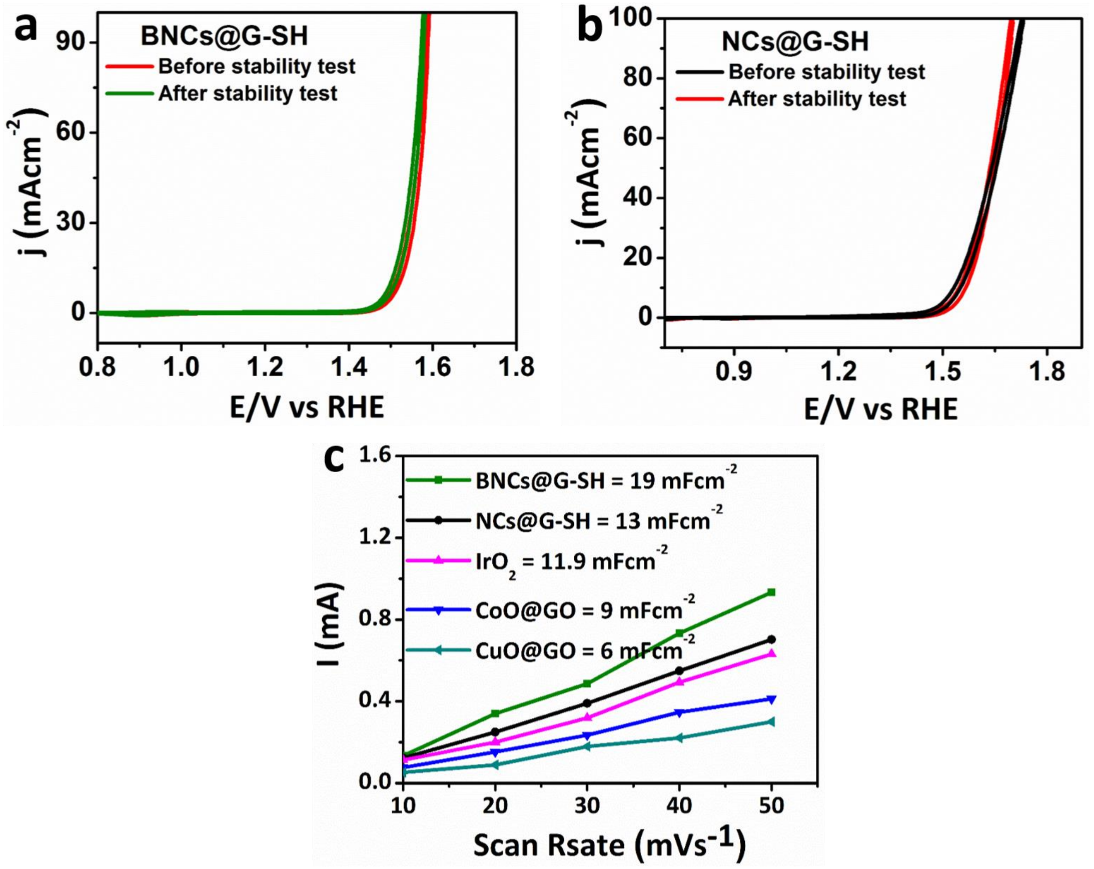

Figure 4.5 Polarization curves before and after stability test for 50 h (a) Co BNCs@G-SH (b) Cu NCs@G-SH (c) plots of average capacitive current (J) as a function of scan rate, where slope = double layer capacitance (C_{dl}).

To further investigate the electrocatalytic performance of these materials, double layer capacitance (Cdl) was calculated, which is equal to electrochemical active surface area (ECSA). As shown in the **Fig. 4.5**c, the Cdl values determined for BNCs@G-SH (19 mF/cm^2) and NCs@G-SH (13 mF/cm^2) are higher than IrO_2 (11.9 mFcm^{-2}), and also better than NPs@GO (9 and 6 mFcm^{-2} for Cu and Co respectively). To figure out the inherent efficiency of electrochemically accessible active sites, the turn over frequency (TOF) at 1.7 V**,** exchange current density and mass activity were also determined and are given in **Fig. 4.6**. The highest TOF@1.7 V of BNCs@G-SH (80 s^{-1}) and NCs@G-SH (60 s^{-1}) obviously display the role of available active sites per unit mass and their efficiency per unit time for OER. These results demonstrate that nanostructuring of the catalytic material especially on conducting surface could provide a plethora of accessible active sites and hetero-interphases, and thus can increase the chance of possible collision-/interaction with intermediates needed for the enhanced surface catalysis.[147, 148] In addition, the comparatively higher activity of BNCs@G-SH can be attributed to the unique arrangement of BNCs on the surface of nanosheets and comparatively smaller size, which further increased the exposed surface and more promisingly horizontal contact for the harmonized synergy of nanoscale catalysts and the conducting support.[134]

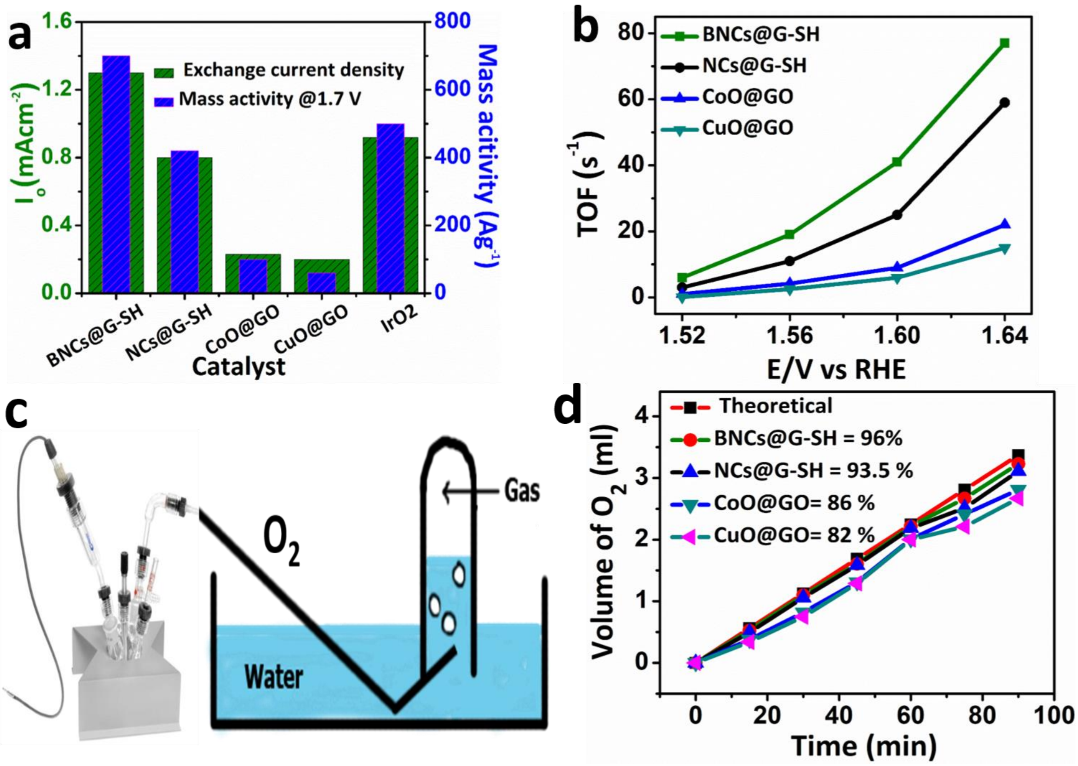

Figure 4.6 Electrocatalytic parameters of Cu NCs@G-SH, Co BNCs@G-SH in (a) exchange current density and mass activity (b) plots of TOF at various potentials (c) assembly of water displacement method for O_2 measurement (d) plot of time vs volume of generated O_2 during OER under anodic potential at 10 mA/cm^2.

We assume that metal/metal oxides are the actual active catalytic sites for OER, and the G-SH assists in the nucleation and immobilization of metal/metal oxide NCs and charge transfer ability. However, due to the presence of various oxygenated functionalities on the surface of G-SH, the oxidation of carbon and production of unwanted gases (H_2O_2, CO) cannot be ruled out. It can, however, be better confirmed from the Faradaic Efficiency (FE) for the ultimate production of O_2 molecules. In this regard, we applied the water displacement method according to our previous report (see experimental part, chapter 2).[137] FE of BNCs@G-SH(≈ 96 %) and NCs@G-SH (≈ 93.5 %) implies the selectivity of electrode material for OER, and meanwhile rules out the possibility of any side reaction (**Fig. 4.6**c, d). In order to better understand the true electronic nature of such ultrasmall nanostructures after catalysis, we analyzed the electrolyte before and after OER using ICP-OES to quantify Cu or Co, if any (**Table 4.1**). The absence of Cu or Co in the electrolyte validates the strong electronic contact of catalyst-support, thereby eliminating the dissolution of catalysts in the electrolyte that is generally expected in case of higher oxidation states of metals. Moreover, the XPS analysis shows a slight shift of binding energy for Cu^{2+} towards the higher side and the appearance of a new peak for Co at 282.5 eV (Co^{3+}), which can be attributed to the hydroxide and oxyhydroxide layer formation as reported previously (**Fig. 4.7**).[149] Meanwhile, the disappearance of peaks for the metallic Co and Cu also indicates the surface oxidation or partial adsorption of oxygen containing groups under long-term OER reaction, which is consistent with the behavior of transition metal oxides. Hence, we believe that $Co^{II/III}$-OOH and $Cu^{II}(OH)_x$ redox couple may be the actual active phases to govern OER. Similarly, the redox peak in CVs and stability test also assists the periodicity of OER process and the reconstruction of active sites and thus can prevent the catalysts from leaching-/dissolution or irreversible conversion to inactive electronic states.[150]

Table 4.1 Composition (wt%) of Cu/CuO@G-SH and Co/CoO@G-SH analyzed with EDX and ICP-OES before and after catalysis

		Wt%							
Catalysts	**Analysis**	**Cu**	**Co**	**C**	**S**	**O**	**K**	**Al**	**Total**
Cu/CuO@G-SH	EDX	5.34	-	71.92	3.04	18.01	-	1.67	100
Co/CoO@G-SH	EDX	-	7.30	74.77	4.73	12.87	-	-	100
Cu/CuO@G-SH	ICP-OES	5.89	-	-	-	-	0.28	-	-
Co/CoO@G-SH	ICP-OES (After catalysis)	-	6.89	-	-	-	0.31	-	-
Electrolyte	ICP-OES (After catalysis)	-	-	-	-	-	10.01		

ICP-OES: Inductively coupled plasma optical emission spectroscopy, EDX: energy dispersive X-rays spectroscopy, NCs: Nanoclusters, The Al comes from the sample holder used during EDX analysis, where K comes from the basic electrolyte

From the remarkable OER performance of these electrocatalysts, it is realized that catalytic potential of transition metal oxides can be significantly improved by nanostructuring, and their strong electronic interaction with conducting supports is also equally important. Hence, the consequent robustness reasonably warrants an optimum catalyst-intermediates interaction for the kinetically fast periodicity of OER, herein endorsed by electronic, geometric, surface assembling and underlying support. Thus, the plausible reason behind the ameliorated performance of these electrocatalysts might be due to i) the chemical modification of GO to control its restacking to a great extent as evident from the SEM/TEM images ii) incorporation of thiol functionality to facilitate the formation and covalent interaction of ultrasmall metal/metal oxide NCs with G-SH through S-metal bond and get defects enriched carbon network as observed in XPS and Raman spectrum iii) control over the size of metal oxide nanoclusters below 2 nm (see HRTEM images) to maximize the surface to volume-ratio and accessibility of active sites as evident from high ECSA and TOF iv) *in-situ* decoration of NCs/BNCs on chemically modified and conducting surface not only endow a strong electronic contact but also the cross-synergistic interaction to consequently modulate the electronic structure and specific redox potential of NCs as evident from XPS, smaller R_{ct} and stability test. Thus, the surface assembling of metal/metal oxides in the subnanometric regime on a conductive support with uniform distribution is useful to sensitize the transport of the charged species at the catalysts-electrolyte interface thereby can significantly energize the OER.[96]

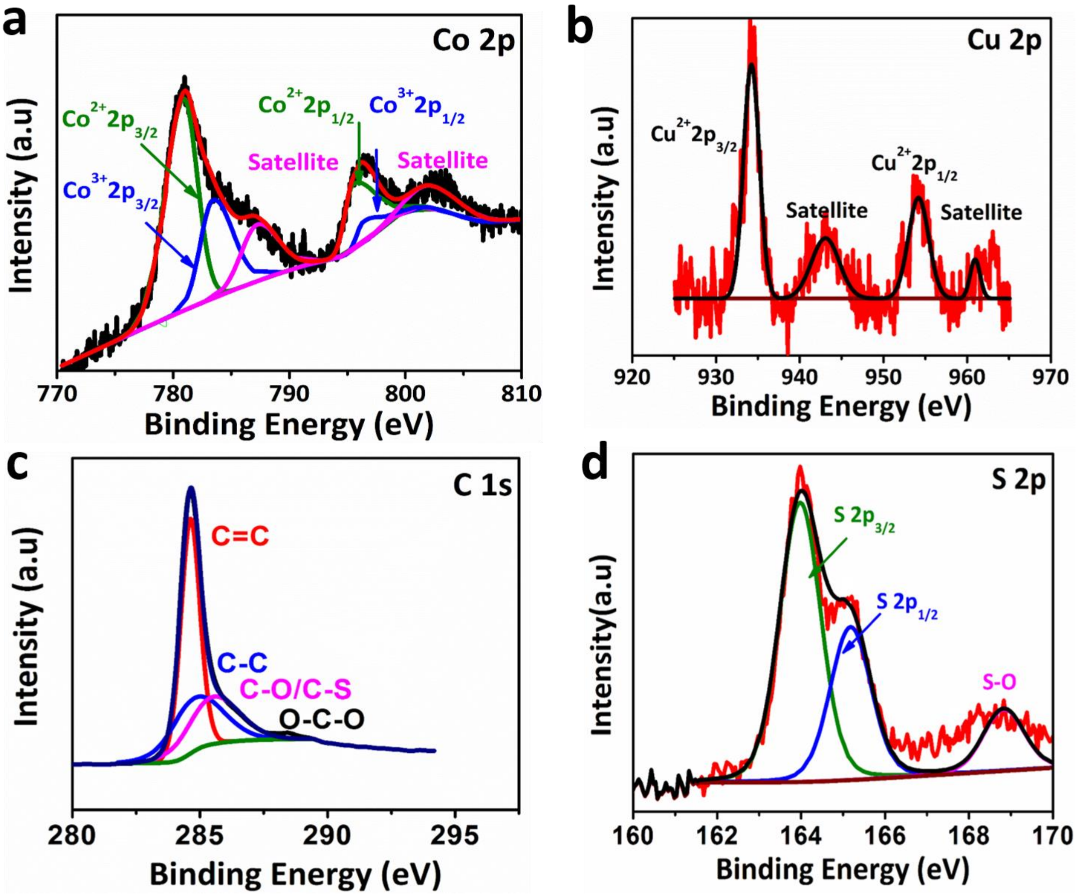

Figure 4.7 XPS spectra after catalysis of (a) Co 2p core level spectrum (b) Cu 2p core level spectrum (c) C 1s core level spectrum (d) S 2p core level spectrum of G-SH after catalysis.

Table 4.2 Electrocatalytic parameters of Cu/CuO@G-SH and Co/CoO@G-SH nanohybrid calculated from steady state CVs and OER electrolysis

Catalysts	η@10mAcm^{-2} (mV)	Tafel Slope (mVdec^{-1})	$R_{ct}(\Omega)$	TOF@1.64 V (s^{-1})	ECSA (cm^{-2})	Mass Activity (Ag^{-1})
BNCs@G-SH	260	54	5	77	475	700
NCs@G-SH	290	79	12	60	325	445
IrO_2	270	66	7	-	299	498
CoO@GO	360	135	26	21	225	92
CuO@GO	490	160	29	14	150	65

η: overpotential. j_0: exchange current density, C_{DL}: double layer capacitance, ECSA: electrochemically active surface area, Rs: solution resistance, Rct: charge transfer resistance, BNCs: beaded nanoclusters, NCs: nanoclusters, G-SH: thiolated graphene oxide, GO: graphene oxide

4.4. Conclusion

We report the thiol functionalized graphene oxide (G-SH), *via* selective epoxidation reaction, as highly conducting support for the formation and covalent attachment of cost-effective meta/metal oxides nanoclusters. While modifying the underlying support, ultrasmall Cu/CuO NCs and Co/CoO BNCs were produced without their obvious aggregation, thanks to the immobilization effect of highly exfoliated G-SH scaffold. The ultrasmall NCs were found highly efficient electrocatalyst for OER, where BNCs@G-SH and NCs@G-SH afford a current density of 10 mA/cm^2 at 290 mV and 310 mV overpotential respectively with the Faradic efficiency higher than 95%. Moreover, the smaller Tafel slope of 54 mV/dec and 66 mV/dec for BNCs@G-SH and NCs@G-SH respectively imply the fast kinetics of OER with most likely same reaction mechanism. In addition, the smaller charge transfer resistance (R_{ct}) and persistent OER performance indicate the resistance free nature of hybrid nanomaterials and thus can expedite the smooth transport of the charged species across the electrode-electrolyte interphase. Meanwhile, the superior performance of BNCs@G-SH also shows that both surface structure and dimensionality are vital on nanoscale length, where the unique arrangement of BNCs with respect to nanosheets signposts highly exposed active sites, hetero-interphases and strong-/larger electronic contact. In contrast, the same metal oxide (Cu and Co) nanoparticles loaded on stacked GO with large size legs behind our nanohybrids while considering the overpotential, kinetics and stability. Thus, it is worth concluding that nanoscale assembling of transition metal/metal oxide affirm high redox potential and chemically modified/exfoliated G-SH with high electron transport ability could synergistically merge their respective potential for the stimulating OER. This study also offers worth exploring promises towards the design and development of new potential electrode materials by strong chemical and electronic coupling at the nanoscale length with the objective to completely-/partially replace the costly integrated catalytic module for water splitting.

Chapter 5.

Ultrasmall Co/Co(OH)$_2$ Nanoclusters Embedded in N-Enriched Mesoporous Carbon Network for Durable Water Oxidation Catalysis

5.1. Synopsis

Metal nanoclusters (NCs, size ≤ 2 nm) are the emerging materials in catalysis due to their unique catalytic-/electronic properties i.e., high surface to volume ratio, high redox potential, plethora of surface active sites and dynamic behavior on suitable support during catalysis. This part of dissertation focuses on the possible chemistry behind the solid-state strategy for the synthesis of Co/Co(OH)$_2$ embedded N-doped porous carbon (synthesis, Chapter 2). The role of precursors and reaction conditions for the simultaneous growth of Co NCs and mesoporous network is optimised and confirmed scanning/transmission electron microscopic analysis. By performing the electrochemical characterization, the promising role of NCs in comparison with ligand stabilized NCs and analogues samples for OER is investigated. In this chapter, we have tried to explain how the NCs and porous support can facilitate the bi-continues movement of the charged species at the electrode-electrolyte interface due to the nanoscale interfacial collaboration. Generally, supported NCs offer maximum exposure of stable active sites, that is verified in terms of various electrocatalytic parameters (CV, stability test, mass activity, TOF, etc.). The selectivity and conversion efficiency of electrode materials is further verified by measuring the Faradaic Efficiency by using gas chromatography and complimentary water displacement method. The structural and electronic flexibility of supported NCs is studied with electron microscopy and XPS analysis. In this particular case study, XPS and Raman spectroscopy were used to describe the combinatorial effect of electronic states and polarisability in the fast cleavage of water molecule.

5.2. Introduction

Electrochemical or solar driven water splitting is an evolving technology because of its potential to offer almost an unlimited molecular H$_2$, an evergreen energy carrier with zero carbon footprint.[15] It can decrease the deleterious consequences caused by exhaustible fossil fuels on the environment around the globe.[151] However, on a large scale, the realization of this potential technology is still limited by the demand of high input potential and slow kinetics of the oxygen evolution reaction (OER), which mainly relies on the use of precious and earth scarce metals (Ir and Ru etc.) as catalysts.[15, 152] Being a longstanding challenge it is, therefore, highly desired to develop cost-effective and competent electrode materials for efficient and long-lasting OER process reasonably close to the thermodynamic potential (1.23 V) or even replace the benchmark precious metals based electrocatalysts. Over the past few decades, a great effort has been made to develop earth-abundant metals (Mn, Fe, Co and Ni) based electrocatalysts including oxides, chalcogenides, layered double hydroxides (LDH), and numerous hybrid materials.[131, 132, 153, 154] Though transition metal oxides, hydroxides/(oxy)hydroxides are of paramount importance due to their low cost and logically inherent catalytic potential for OER particularly in alkaline electrolyzers.[90] Nevertheless, their less stability, poor efficiency, less conductivity, low exposure of surface active sites and high charge transfer resistance are the common impediments that badly limit their electrochemical performance.[30] In this quest, optimization of electrode materials in terms of structural and electronic engineering is on rise to circumvent the associated problems, with an objective to maximize the number of electrochemically accessible active sites, robustness and execution of kinetically fast OER at low overpotential in a sustainable manner.[155] Meanwhile, nanostructuring (structural and electronic engineering) of the materials particularly oxides/hydroxides in the subnanometric regime (size ≈2 nm) and their immobilization on a suitable support is indeed an appealing option, and recently has attracted significant interest in catalysis science.[124, 156] In such nanoscale materials, exciting electronic and intriguing catalytic properties are emerged due to a drastic decrease in their dimensions and quantum confinement.[94] In this size regime, due to the less number of atoms in the core, NCs offer maximum accessible active sites to behave like molecular catalysts and thus high efficiency for challenging reactions like OER - a bottleneck process in the deployment of water splitting modules.[136, 157] In our previous report, the atomically monodisperse Ni_6 and Ni_4 NCs were studied for OER with an overpotential of 1.50 V and 1.52 V respectively, where the smaller Ni_4 NCs (size < 2nm) offered better electrochemical accessibility of active sites and high redox behavior, which are indeed very encouraging to facilitate the easy and non-recombinant diffusion of electrons towards the surface for catalysis.[99] More recently, we reported supported Ni/NiO NCs on thiolated graphene oxide nanosheets (GO-SH) to mediate OER at 1.46 V due the periodic reshuffling of electronic density across the Ni-NiO@GO-SH nanointerfaces. Au_{25} NCs loaded on CoSe (2D material) have also been reported to facilitate the easy adsorption/desorption of intermediates (O^-, OH^-, OOH^-) to subsequently mediate the dynamic release of O_2 molecule during OER. Similarly, Kauffman et al., have also reported the use of atomically monodisperse Ni NCs supported on the carbon black for OER. Based on both theoretical and experimental approach, it was suggested that small aggregates of the metal are inherently more flexible to provide an alternative pathway for catalysis as compared to their bulk analagous.[96] Despite the fact that nanostructuring of the supported transition metal based electrocatalysts, particularly in the subnanometric regime in comparison to nanosheets/nanorods and nanoparticles (NPs), is an appealing pathway to effectively tune the hidden catalytic potential, however, it is rarely documented for OER and thus becoming a growing hotspot in nanocatalysis.[25, 158] It is, therefore, imperative to explore the controlled and facile assembling of the transition metal oxides/hydroxides in the subnanometric regime and more promisingly their optimum loading on highly conductive/flexible supports e.g., carbon, GO, g-C_3N_4, CNTs, MOFs etc. that may further embellish the economic interest and knowledge in the field of water splitting and beyond.[159, 160]

Motivated by this necessity, we report a novel, one step and a facile solid-state strategy for the development of ultrasmall Co/$Co(OH)_2$NCs residing in honeycomb like 3D carbon network (HCN) as highly efficient and stable water oxidation catalyst using cost effective precursors ($Co(NO_3).6H_2O$ and melamine) **(Fig. 2.3)**.[161] The ultrasmall NCs and their assembly on supramolecular N-enriched graphitic structure was achieved by the controlled polymerization of melamine while blocking some of the terminal amine groups by creating cobalt-melamine complex under the optimal conditions without using any template and-/or directing agents. Consequently, the unique texture of the hybrid material with multimodal porosity and open channels not only support the infiltration of electrolytes and-/or charges but may also enhance the synergistic effect with NCs in nanoscale dimensions.[162]

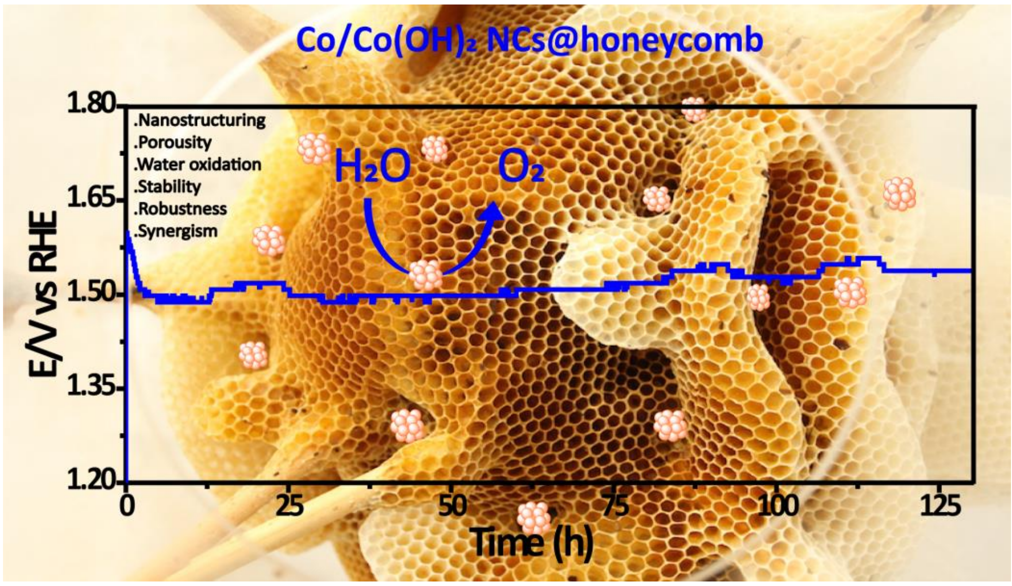

TOC 5.1 Table of content representing the Co/Co(OH)$_2$ nanoclusters embedded in honeycomb like N-doped mesoporous carbon for OER. The green line shows the long-term stability for OER.

5.3. Results and Discussion

5.3.1. Synthesis and Characterization of Co/Co(OH)$_2$@HCN

The schematic illustration for the synthesis of HCN loaded with Co@Co(OH)$_2$ is presented in the **Scheme 2.2**. Melamine, a cyclic organic molecule with terminal amine groups, can be used as a precursor of C and N and simultaneously to stabilize metal NCs.[163] During thermal treatment, it passes through different intermediates i.e., melam, melem and melone to produce a highly stacked g-C_3N_4 structure due to the HN-C-N bond formation with the release of NH_3 and molecular H_2.[161] The produced H_2 and NH_3 can be used as reducing agent and for nitrogen doping respectively. Interestingly, by controlling the step-wise polymerization or using soft/hard template including various ions, the nanoarchitecture of the graphitic network in various forms can be desirably controlled and catalyzed under optimal conditions.[164] In view of this concept, following the solid state strategy, the Co-melamine complex was produced while grinding/mixing of the precursors in low humidity environment by lowering the temperature below 20 °C with the immediate appearance of blue color complex.

It is noteworthy that, during continuous and gradual thermal treatment, the polymerization of melamine takes place.[161] However, we hypothesize that the chemical linkage of the metal with melamine *via* terminal amine groups and uniformly distributed intercalated OH^{-1} ions may not allow the growth of the stacked graphitic carbon network due the absence of melamine-melamine linkage. It is, therefore, very critical to decrease the π-π stacking and promote polymerization that could possibly dictate the supramolecular rearrangement of the organic precursor in 3D porous framework without any templating agent.[161] Meanwhile, the stepwise thermal treatment produces the H_2/NH_3 rich reductive environment, which may facilitate the nucleation and growth of NCs followed by their assembly on nitrogen enriched honeycomb like carbon network (HCN), hereafter called NCs@HCN. The scanning electron microscope (SEM) and scanning transmission electron microscope (STEM) analysis show the formation of honeycomb-like porous carbon framework in a 3D manner **(Fig. 5.1**b, c**)**. This is most probably due to the prior formation of Co-complex at molecular level, which can block some of the terminal amine groups and thus hinder the development of highly stacked graphitic structure. No porous structure was obtained when melamine was replaced with urea, which further validate our hypothesis.

To further visualize the morphology of NCs@HCN in a more appropriate way, gold sputtering was performed to significantly improve the surface contrast under SEM analysis, which clearly indicates the existence of multilevel (meso-/macro) pores homogenously distributed over the entire structure (**Fig. 5.1**c). Moreover, it also shows the presence of the macropores (1-2 µm) that are formed due to the internal connection of the sheets. Similarly, the TEM images also show the highly extended layered and open structure morphology with micrometer size cavities, which are probably generated during the aggregation of melamine that can significantly facilitate the diffusion of electrolytes and smooth transport of the charged species during catalysis **(Fig. 5.2**a, b**)**.[149] It is noteworthy that an optimum stoichiometry of the precursors and controlled ramping rate is required to ensure the diffusion controlled growth of ultrasmall NCs, otherwise irregular morphology is formed**.** The surface area and pore size distribution of NCs@NHC was estimated from N_2 adsorption-desorption isotherms in comparison with g-C_3N_4 **(Fig. 5.1**e, f**)**. High surface area (78.34 m^2/g) and typical type-IV isotherm with H1-type hysteresis loop indicate that NCs@HCN is macro-/mesoporous in nature with pore size distribution centering around 7 nm with pore volume of 0.006 cm^2/g. A slight increase in the pore volume (from 0.006 to 0.017 cc/g) after etching of Co with acid (0.5 M HCl) suggests the embedded nature of NCs in the pores of carbon skeleton, which can enhance the effective synergistic interaction during catalysis.[165] The ultrasmall Co NCs, however, are not much visible by SEM/STEM analysis due to their inherent low contrast, embedded and small nature. The NCs with a size of approximately 2 nm uniformly distributed in the HCN are clearly visible in the form of dispersed dots under TEM analysis (**Fig. 5.2**d). HRTEM analysis is presented in **Fig. 5.2**c, which indicates the crystalline nature of NCs as evident from the crystal fringes

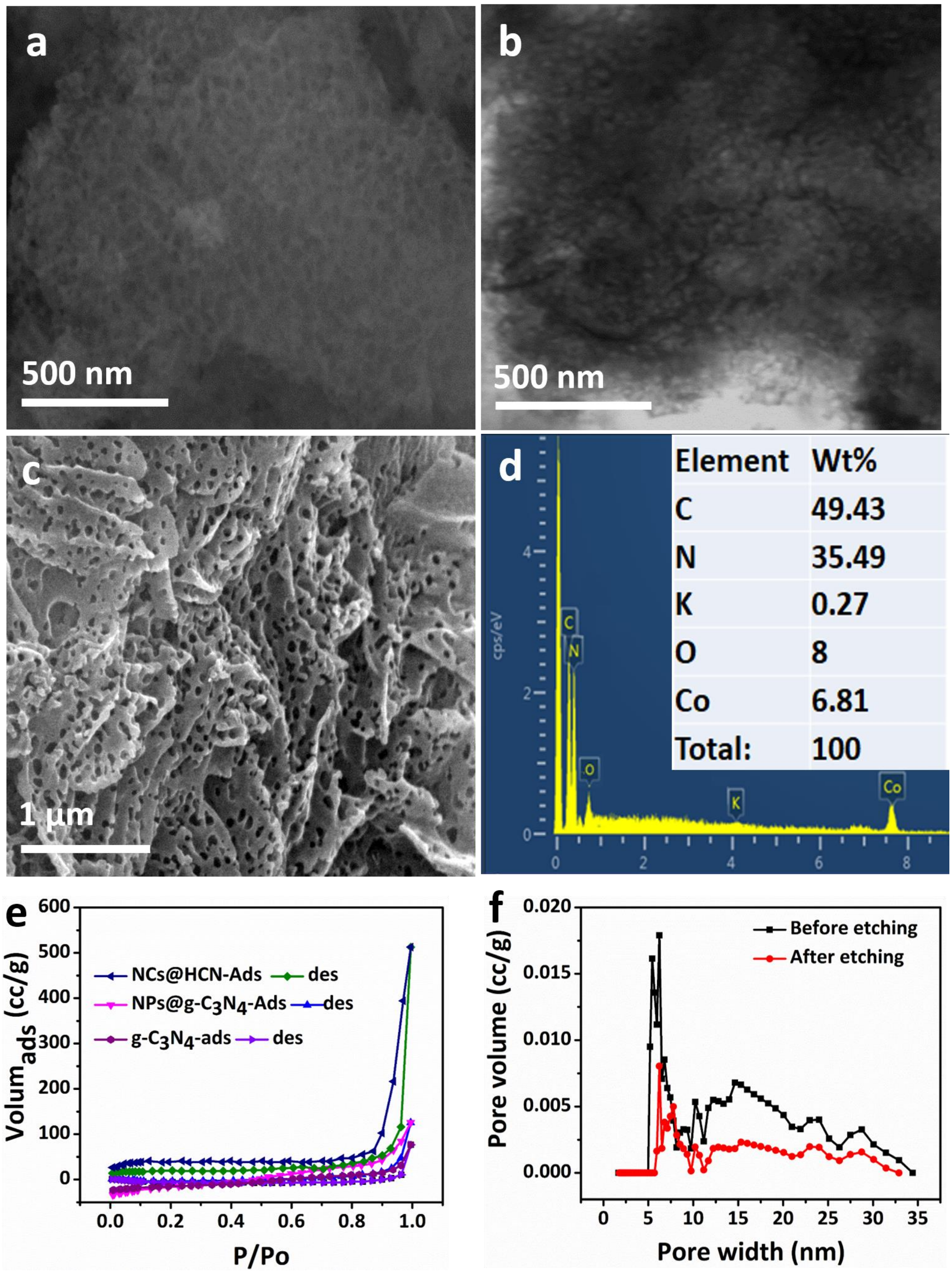

Element	Wt%
C	49.43
N	35.49
K	0.27
O	8
Co	6.81
Total:	100

Figure 5.1 Scanning/Transmission electron microscopic (SEM/STEM) analysis of Co/Co$(OH)_2$@HCN (b) SEM image (c) STEM image looks like honeycomb (d) SEM image after gold sputtering and (e) EDX analysis. BET surface area of NCs@HCN (78.34 cc/g) in comparison with Co NPs and g-C_3N_4 (a) corresponding Isotherm and (b) pore size distribution of NCs@HCN before and after metal etching centering 7 nm.

randomly taken with d spacing (layer spacing) of 0.24 Å and 0.20 Å, which correspond to 101 and 100 reflection planes of the hexagonal layered structure of Co$(OH)_2$ and

FCC structure of metallic cobalt respectively. The in-situ growth of NCs@HCN is also evident from XRD pattern, where the reflection from the (001), (100), (011), (110), (003), (111)**,** (200) and (201) crystal planes exactly match with the brucite layered structure of $Co(OH)_2$ (JCPDS No.074-1057) **(Fig. 5.2**e**)**.[166] In addition, the peaks arising from the reflection plane (100), (200), and (220) indicate the presence of crystalline FCC structure of metallic Co (JCPDS No.15-0806). The smaller intensity of the peaks, probably due to the possible presence of amorphous carbon, further suppress the reflection from the crystalline planes. The nature of the graphitic structure was further confirmed with Raman spectroscopy, where the appearance of the broad peak could be assigned to the overlapping of several peaks of N-C=N (1400 cm-1), N(-C-N) 1600 cm^{-1} and Sp^2 C (1380 cm^{-1}) vibration.[167] To further investigate the chemical environment, oxidation and electronic states, X-ray photoelectron spectroscopy (XPS) was acquired as shown in the **Fig 5.3**. The deconvoluted Co 2p core level spectrum indicates the co-existence of Co^0/Co^{2+}. The peaks at 777.4 eV and 796.3 eV correspond to $2p_{3/2}$ and $2p_{1/2}$ of the metallic Co^0, while peaks at 781.3 eV and 798.7 eV can be attributed to $2p_{3/2}$ and $2p_{1/2}$ of the Co^{2+} respectively with satellite peaks around 786.3 eV (**Fig. 5.3**a).[163] In addition, the peaks at ~782.5 eV validate the presence of Co-N, which indicates the Co and carbon network interaction via heteroatom and could be highly beneficial to enhance the catalytic potential.[163] The core level spectrum of O 1s was deconvoluted into 03 major peaks, which can be assigned to Co-O (528.7 eV), Co-OH (530.6 eV) and surface adsorbed water molecules (532.5 eV) (**Fig. 5.3**b). Similarly, a set of peaks in the core level spectrum of C 1s reveals the presence of sp^2 hybridized carbon C=C (284.2 eV), C=N-C (285.7 eV), and C-O/C=O (288.2 eV) (**Fig. 5.3**c). The N 1s core level spectrum was also deconvoluted into a set of 04 peaks corresponding to C-N=C (398.3 eV triazine network), N-(C)3(399.6 eV, tertiary-N), pyrrolic type nitrogen (C-N-H, 400.9 eV) and a shake-up satellite peak (402.3 eV) as presented in the Fig 3d.[168] The higher intensity of tertiary-N indicates the presence of considerable units of heptazine present in the whole structure. Furthermore, the XPS survey spectrum (**Fig. 5.7**a) shows that the whole composite is composed of only C, N, O and Co (≈6 wt%, from XPS), where the metal loading of approximately 6.38 wt% was further confirmed by ICP-OES analysis (**Table 5.1**).

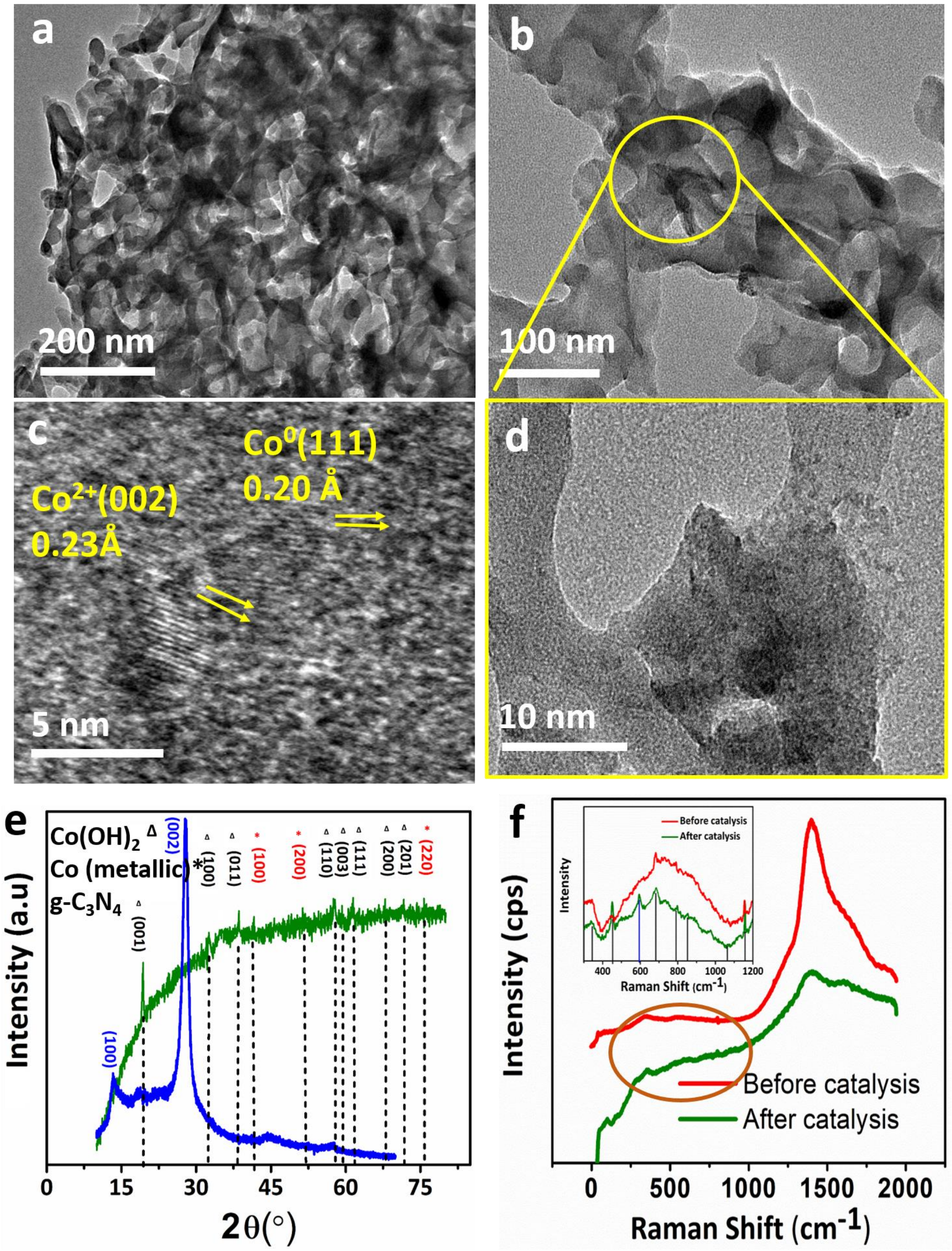

Figure 5.2 Transmission electron microscopic (TEM) analysis of Co/Co$(OH)_2$@HCN (a) TEM image of bulk sample (b) is the magnified TEM image (c and d) are the HRTEM images with crystalline fringes, where the small spots represents the NCs in 'd' (e) XRD pattern of Co/Co$(OH)_2$@HCN in comparison with g-C_3N_4 where the 'Δ' and '*' represent the miller indices of Co$(OH)_2$ and metallic cobalt respectively. Raman spectra before and after catalysis. The broad peak may be due to the overlapping of various peaks of N-C=N (1400 cm-1), N(-C-N) 1600 cm^{-1} and Sp^2 C (1380 cm-1) vibration. The inset graph represents the magnified part of the metal-oxides and (oxy)hydroxides characteristic region.

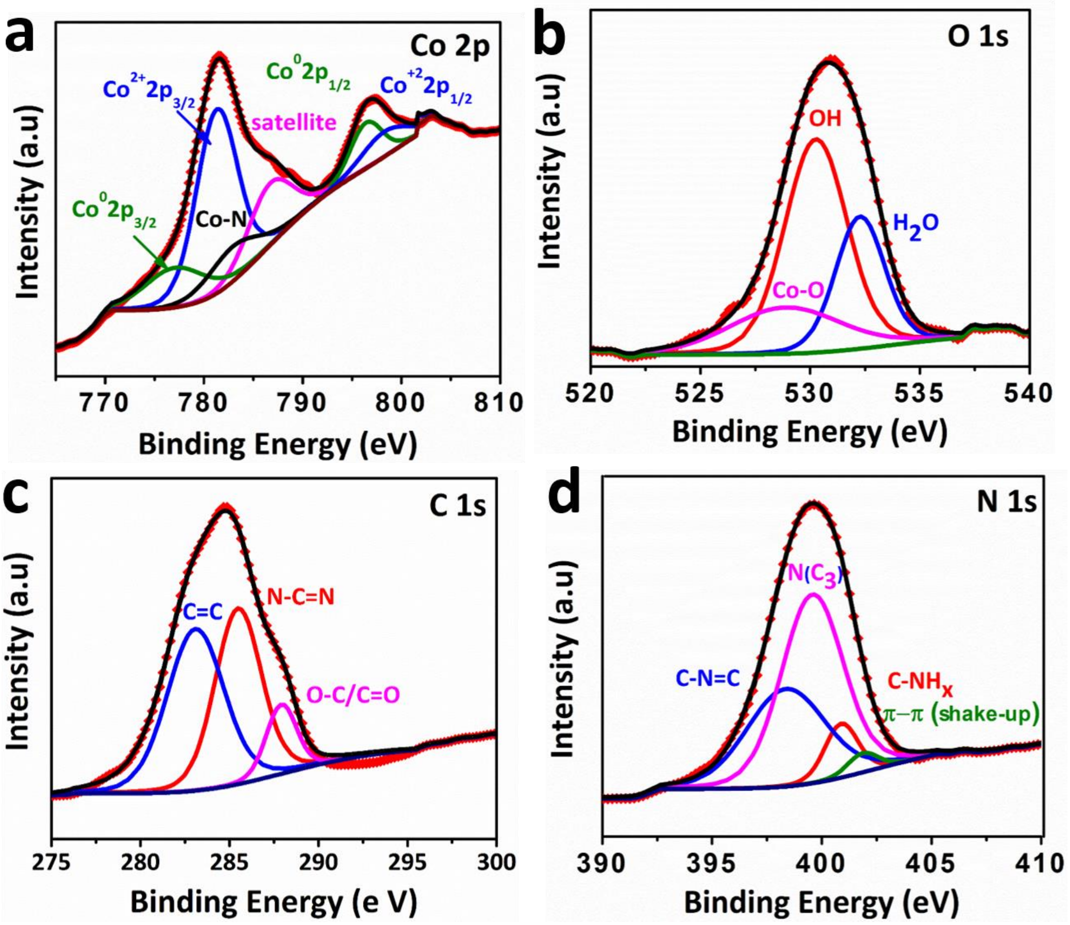

Figure 5.3 XPS analysis. Core level spectrum of (a) Co 2p (b) O 1s (c) C 1s (d) and N 1s.

5.3.2. Electrochemical Water Oxidation Catalysis

The OER performance of NCs@HCN was evaluated with a standard three electrodes set-up in 1 M KOH in comparison with benchmark electrocatalysts (IrO_2) and analogue samples with a major focus on the $Co(OH)_2$ NPs@g-C_3N_4 as shown in **Fig. 5.4** and **Table 5.2**. As evident from the steady state polarization curve of NCs@HCN, after the oxidation of Co, the OER process starts at very low onset potential of 1.44 V followed by a sharp increase in the current density in a very narrow potential window showing their superior performance **(Fig. 5.4**a**)**. An overpotential of 230 mV and 260 mV is required for NCs@NHC to achieve a current density of 10 mA/cm^2 and 50 mA/cm^2 respectively and thus clearly outperforms the benchmark (IrO_2) electrocatalyst, which requires an overpotential of 320 mV and 390 mV respectively to achieve the same current density**.** Similarly, Tafel slope of 44 mV/dec, 69 mV/dec and 78 mV/dec was observed for Co NCs@HCN, RuO$_2$, and NPs@g-C$_3$N$_4$ respectively. The smaller Tafel slope (44 mV/dec) of Co NCs @NHC validates the fast kinetics of electrode process to propel the electrons towards the external circuit. This behavior is highly consistent with the exponential increase in the current density just after the onset potential and maximum current density of 1000 mA/cm^2@1.61 V with an increment (100 mA/cm^2@0.1 mV overpotential) **(**inset of **Fig. 5.4**c**)**.[169] The electrode kinetics was further investigated with electrochemical impedance spectroscopy (EIS). Interestingly, the extremely small R_{ct} (1.4 Ω) of NCs@HCN<RuO$_2$ (4.9 Ω) < NPs@g-C$_3$N$_4$ (9.2 Ω) justify the favorable and inherently resistance-free nature of electrode materials **(Fig. 5.4**d**)**. Consequently, it can efficiently propel the electrons-/ions across the electrode-/electrolyte interface and thus can not only enhance the electrode kinetics but also can reasonably decrease a part of overpotential arising from the internal resistance of catalyst and catalyst/electrode interface.[146, 149]

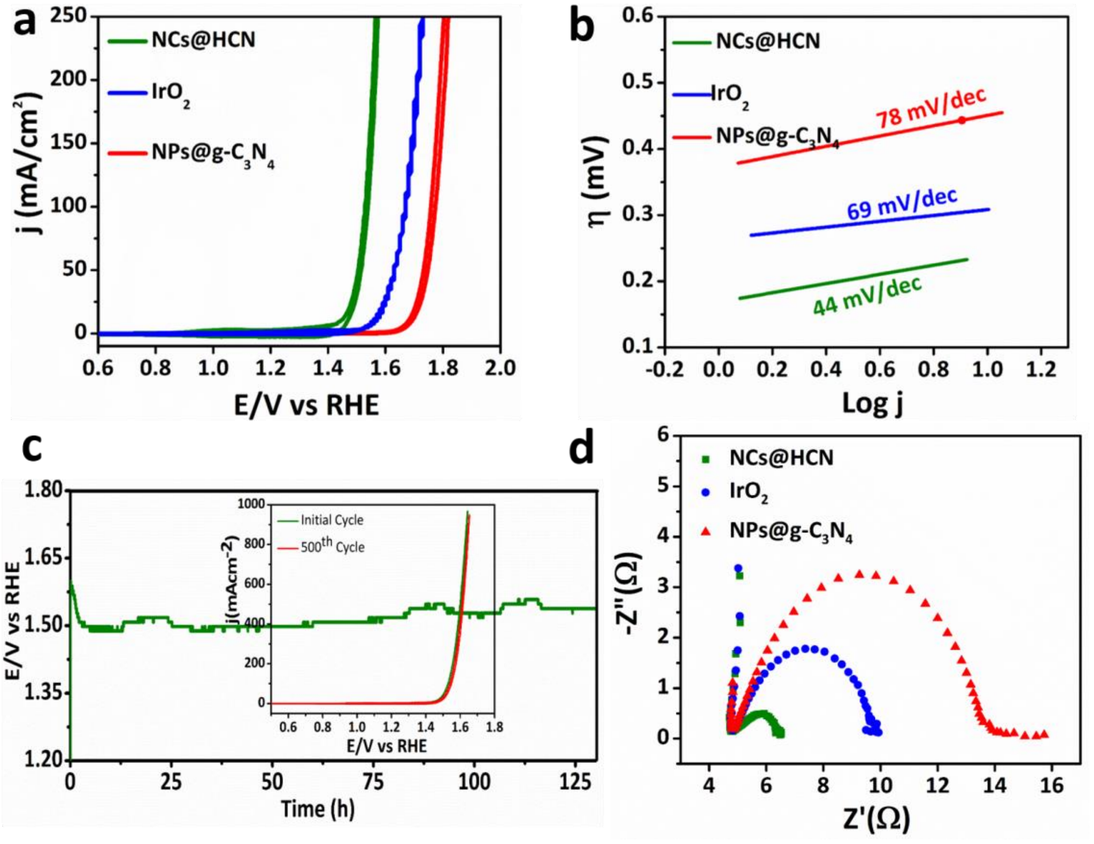

Figure 5.4 Electrocatalytic activities in 1 M KOH (a) cyclic voltammograms (CVs) of Co/Co(OH)$_2$@HCN, IrO$_2$ and Co(OH)$_2$ NPs@g-C$_3$N$_4$ (b) corresponding Tafel slopes (c) controlled potential electrolysis for 130 h@50 mA/cm^2, where the inset graph represents the CVs before and after catalysis.

Stability is one of the important parameters to evaluate the recycling potential and corrosion resistive nature of electrocatalysts especially in view of their commercial applications.[170] In this regard, prolonged experiment of OER was conducted to evaluate their ability to sustain a current density of 50 mA/cm^2 **(Fig. 5.4**c**)**. Promisingly, an increase in the overpotential by only 4 mV after 130 h validates the sustained OER process. The possible fluctuation in the stability graph (**Fig 4**c) is due to the excessive bubbles formation on the surface of electrode. To our surprise, no decay in the voltammogram before and after 500 cycles **(**inset of **Fig. 5.4**c**),** even under harsh conditions, was observed that further supports the reliability of hydroxide NCs hosted in carbon network extended in 3D manner.[149] For further justification, we also compared the activity and stability of NCs@HCN with bare Co NCs. However, the unsupported NCs were found highly unstable that may be due their aggregation under the OER conditions, thus strengthening the significance of supported NCs not only to endorse the synergistic effect but also their recycling potential.

It is generally believed, that anodic oxidation of carbon based material can hardly be avoided and thus it is important to probe the origin of generated current and subsequent Faradic efficiency.[171] In this regard, molecular O_2 (at 10 mA/cm^2) was measured with gas chromatography (details are given in experimental, chapter 2) at different time intervals and was qualitatively analyzed against internal standard calibration curve. Moreover, for the quantitative analysis, the molecular O_2 was measured with water displacement method (see experimental, chapter 2), where the displaced volume of water with molecular oxygen was measured under the continuous water electrolysis for 90 min (**5.5**a). Expectedly, high purity of molecular O_2 with a Faradic efficiency higher than 95 % minimizes the possibility of any side products, which is reasonably possible at the surface of competent and selective electrode materials to favor the prior water oxidation catalysis at low anodic bias before any reaction could take place.[81] To further probe the catalytic potential, electrochemically active surface area (ECSA) was estimated from the double layer capacitance (C_{dl}) (**Fig. 5.5**b), while assuming that all the surface atoms in NCs are accessible.[172] Similarly, the exchange current density and mass activity was also calculated (**Fig. 5.5**c). Remarkably higher ECSA area (300 cm^{-2}), exchange current density and mass activity of NCs than that of NPs and IrO_2 can be attributed to the ultrasmall nature and layered structure of hydroxide NCs with highly exposed/accessible active sites. Moreover, their stabilization on the porous carbon network with abundant doped nitrogen consequently generates hybrid heterostructure with plentiful nanointerfaces and surface active sites. Such nanoscale interfacial collaboration can facilitate the easy adsorption/desorption of reaction intermediates (O$^-$, OH$^-$, OOH$^-$) to possibly buffer the four electrons process needed for OER catalysis.[173] More promisingly, the high TOF (350 s^{-1}@1.56, **Fig. 5.5**d) and slight increase in Cdl (from12 mF to 13.8 mF/cm^2) after catalysis (**Fig. 5.6**a, b) highlight the regeneratable behavior of active sites (hydroxide/oxyhydroxide) and thus can maintain the OER conversion chain reaction in durable manner.[149] This behavior is even more evident from the long term chronopotentiometry@50 mA/cm^2 experiment, which indicates the continuous activation and potential of embedded/surface active sites (**Fig. 5.4**d).

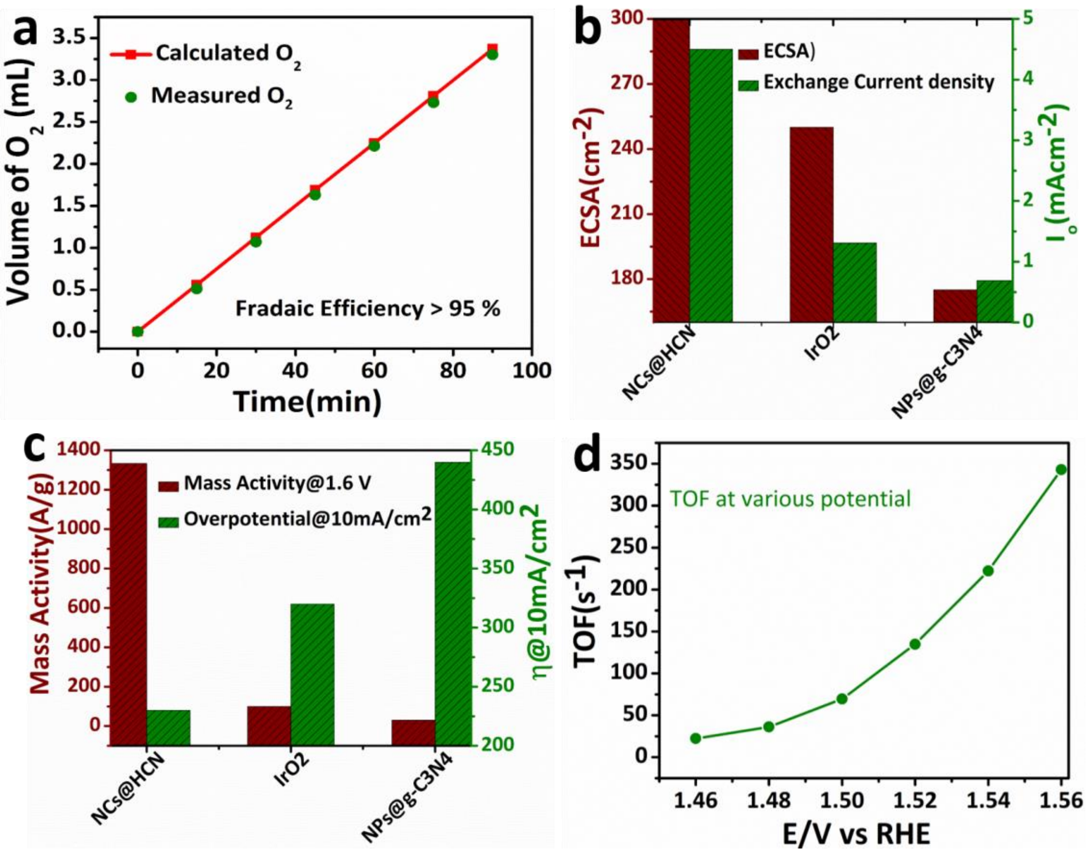

Figure 5.5 Electrocatalytic parameters (a) plot of Time vs generated Volume of O_2 measured both experimentally and theoretically for NCs@HCN to calculate the Faradic Efficiency (>95%) (b) electrochemical active surface area and exchange current density (c) comparison of mass activity and overpotential@10 mA/cm^2 in comparison with benchmark and analogue sample (d) Graph of Turnover frequency (TOF) vs required potential with maximum TOF = 350 s^{-1}@1.56 V.

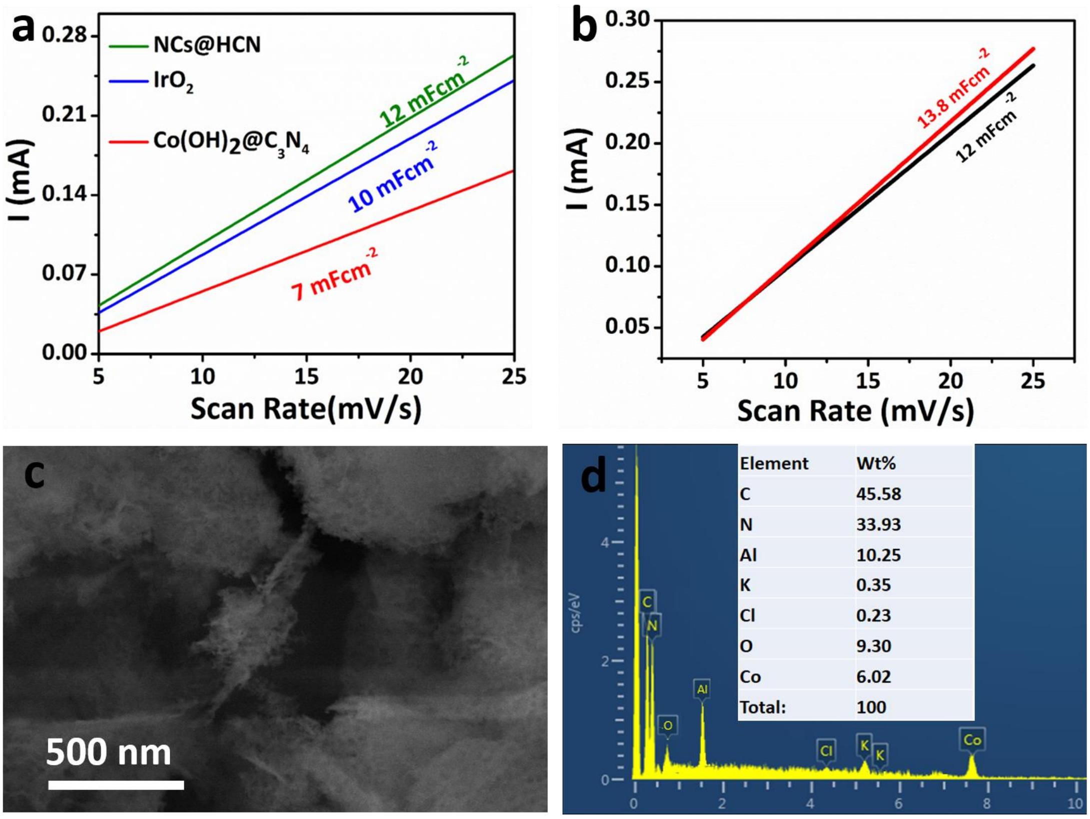

Element	Wt%
C	45.58
N	33.93
Al	10.25
K	0.35
Cl	0.23
O	9.30
Co	6.02
Total:	100

Figure 5.6 Electrocatalytic parameters and evaluation before and after catalysis. Plot of scan rate vs current in the non-faradaic region of CVs at different scan rate (5-25 mV/s), where the slope = double layer capacitance (a) before catalysis (b) after catalysis (d, e) SEM/EDX analysis of Co/Co(OH)$_2$@HCN after catalysis with percent composition of the elements, where the Al comes from the sample holder, while K and Cl may be adsorbed from the electrolyte during catalysis.

Table 5.1 % Composition of Co NCs@HCN analyzed with EDX and ICP-OES before and after catalysis

	Wt%							
Elements	**Co**	**C**	**N**	**O**	**K**	**Cl**	**Al**	**Total**
EDX (bulk sample) Before catalysis	6.81	49.43	35.49	8	0.27	-	-	100
EDX (thin film) After catalysis	6.02	45.58	33.93	9.30	0.35	0.23	10.25	100
ICP-OES (Before catalysis)	6.38	-	-	-	0.31	-	-	-
ICP-OES (After catalysis)	5.89	-	-	-	0.28	-	-	-

ICP-OES: Inductively coupled plasma optical emission spectroscopy, NCs: Nanoclusters,
The Al comes from the sample holder. The increase in the K and appearance of Cl may be their adsorption from the electrolyte on the surface of catalyst. The increase in the ‘O’ represent the hydroxide(oxy)hydroxide layer formation. The slight decrease in the wt% of Co may be due to the leaching of sample.

The supported NCs based electrocatalyst was further characterized to probe the ameliorated catalytic performance, mechanical strength and true electronic states of these electrode materials. In this regard, the elemental analysis (SEM/EDX) after stability test validates that the sample is only composed of C, N, O, and Co (≈6 wt%) showing its mechanical strength and corrosion resistive nature (**Fig 5.6**c, d). The minute weight loss (< 0.1 %), analyzed with ICP-OES (≈ 5.89%, **Table 5.1)** may be due to the leaching of sample or partial phase transformation during catalysis. However, after catalysis, the XPS analysis indicates the true electronic states, where along with the Co^{2+} the appearance of new peak at slightly higher side (**782.2 eV)** can be attributed to $2p_{3/2}$ of Co^{3+}**(Fig. 5.7**b**)**. In addition, the absence of peak for Co^0, and relative decrease in the intensity of Co^{2+} strongly support the potential induced conversion of NCs to (oxy)hydroxide ($Co^{III}O_x$-OH) that may further ameliorate the oxophilicity of the material by imparting electronic flexibility in accordance to the previous report.[149, 174] These results further support our calculation about the slight increase in the number of active sites and thus surface area after catalysis. The formation of thin layer of (oxy)hydroxide was also observed with the appearance of a characteristic new peak around 595 cm^{-1} in the Raman spectrum (**Fig. 5.2**f), which represents the collective vibration of Bg mode of oxygen in the metal-(oxy)hydroxide due to the change in their polarizability.[175] The sensitivity of such collective vibration coupled with the electronic charge/state may endorse the structural/electronic flexibility, which could facilitate the polarization of water molecules and electron transfer during catalysis.[50] We believe, that such a competent and sustained behavior is most likely due to the inherently generated optimum redox potential induced by interconvertible redox couple ($Co^{0/2+/3+}$). Moreover, large number of active sites on the surface of ultrasmall supported NCs and their stable/regeneratable behavior is highly regarded to propel the fast transport of electrons ($4e^-$) between the catalyst and adsorbed species for the dynamic release of O_2 molecule with high selectivity.[176]

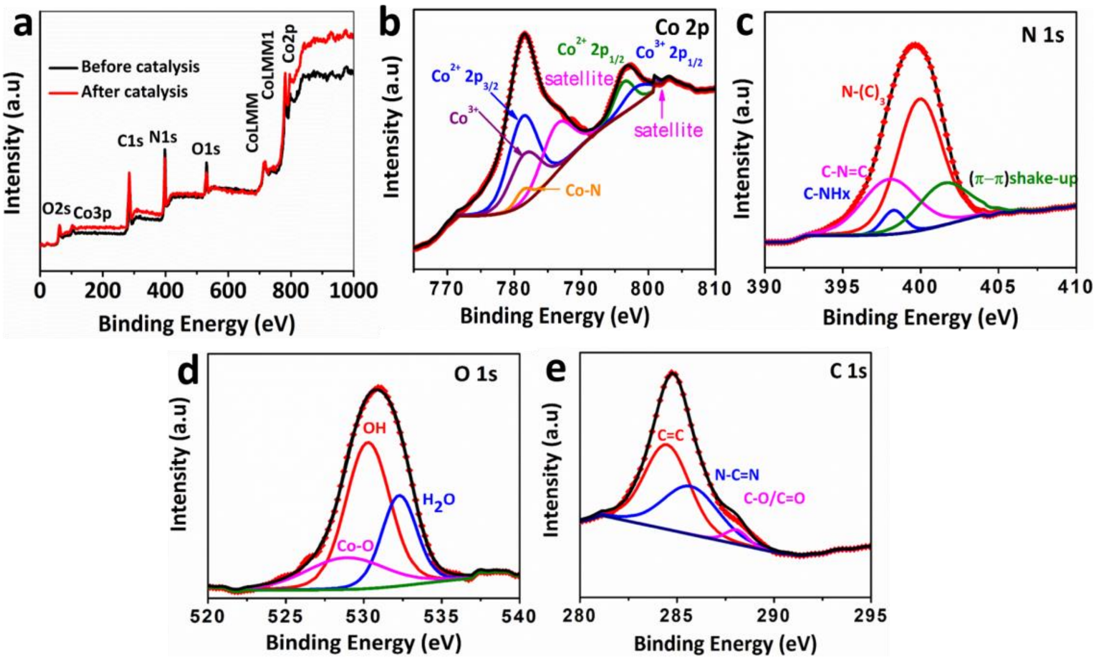

Figure 5.7 XPS analysis after catalysis (a) survey scan of Co/Co(OH)$_2$@HCN before and after catalysis. Core level spectrum of (a) Co 2p (b) N 1s (c) O 1s (d) C 1s.

Table 5.2 Electrocatalytic parameters of Co NCs@HCN calculated from steady state CVs and OER electrolysis

Electrocatalysts	η@10 mA/cm²	Tafel slope (mV/dec)	j_0 (mA/cm²)	Mass activity (A/g)	C_{dl} (mF/cm²)	ECSA	Rs (Ω)	Rct (Ω)
NCs@HCN	220	44	4.5	1336	12	300	4.76	1.4
Co NPs@g-C_3N_4	440	78	0.69	33	7	175	4.69	9.2
IrO_2	320	69	1.31	103	10	250	4.73	4.9

η: overpotential, j_0:exchang current density, C_{dl}: double layer capacitance, ECSA: electrochemically active surface area, Rs: solution resistance, Rct: charge transfer resistance, NCs: nanoclusters

5.4. Conclusion

In summary, we report relatively simple yet effective solid state approach for the in-situ growth of ultrasmall Co/Co(OH)$_2$ NCs assembled in honeycomb like N-carbon network (HCN). The experimental results indicate that initially developed chemical linkage, specifically in Co-melamine in a low humidity environment and temperature, is helpful to conveniently prepare the precursor without any pre/-post treatment/annealing. This chemical linkage *via* terminal amine groups may hinder the generic growth of stacked graphitic carbon network and thus are critical to render the supramolecular rearrangement of the precursors in 3D manner with simultaneous assembling of Co NCs. The highly dispersed ultrasmall NCs in various oxidation states embedded in HCN with numerous nanointerfaces across the Co/Co(OH)$_2$@HCN hybrid heterostructure with extended and open channels could be highly useful for the continuous electrons-/ions pathways and thus can greatly enhance the catalytic potential. Remarkably, the low onset potential (1.44 V), smaller Tafel slope (44 mV/dec), high stability (> 130 h) and Faradic efficiency higher than 95 % obviously affirm the robust performance of these electrocatalysts owing to their high redox potential and maximum accessible/regeneratable active sites. Moreover, the unique texture of the material with multimodal porosity and open channels not only support the infiltration of electrolytes/charges but may also enhance the concerted synergistic interaction in the nanoscale dimension, which can be further engineered by controlling the coupling of inorganic and organic precursors to develop novel and tunable nanoscale materials in future.

Chapter 6.

Controlled Engineering of Nickel Carbide Induced N-Enriched Carbon Nanotubes for Hydrogen and Oxygen Evolution Reactions in Wide pH Range

6.1. Synopsis

The research work presented in the earlier chapters focused on the development of supported metal/metal oxides NCs only for OER. However, the design of cost-effective and competent electrochemical water splitting module that is functional in a wide pH range is also a formidable challenge for viable H_2 production. Herein, we present the proposed mechanism behind the solid-state approach for the synthesis of Ni/Ni_3C nanoparticles (NPs) induced engineering of nitrogen-enriched carbon-nanotubes (NCNT) by the pyrolysis of melamine with $Ni(NO_3).6H_2O$ at various stoichiometric ratios (0.5-wt%, 2-wt% and 4-wt% of Ni). We have explored the effect of size of Ni/Ni_3C NPs and reaction conditions to control the subsequent size of NCNT. The catalytic potential and structural integrity of *in-situ* self-assembled hybrid materials of different sizes (≈ 15 to 65 nm) are explored both for OER and HER in a broad pH range (0-14). The detailed electrochemical evaluation shows the effect of nanostructuring of the Ni/Ni_3C NPs and subsequently the diameter of the NCNT on their catalytic potential in comparison with analogous samples. We have also highlighted how favorable electronic modulation of Ni/Ni_3C, structural strain of NCNT, and possible concerted synergistic effect of the hybrid/doped nanocarbons with metal carbides holds a great potential for electrode reactions. In addition to the pH effect on catalysis, this study also describes the pre-/post spectroscopic characterization to unveil the possible changes in the structure and morphology of the hybrid materials. While studying the individual role of Ni/Ni_3C and NCNT, we also tried to dig out the possible reasons behind the catalytic potential of these electrocatalysts. We believe that such modular strategies tailoring the structural-performance relationship may provide the guidance towards the designing of commercially viable electrocatalysts in this regard.

6.2. Introduction

H_2 is one of the promising candidates as a 'fuel of future' with zero carbon footprint and highest mass energy density (120-142 MJ Kg^{-1}).[177, 178] In this regard, water electrolysis with production of molecular hydrogen and oxygen is one of the promising pathways for the sustainable 'H_2' based economy in near future.[11, 155] However, this hype is still elusive due to the (ii) absence of H_2 on our earth (ii) the two half-cell reactions i.e., hydrogen evolution reaction (HER) and oxygen evolution reaction (OER) are highly energy intense processes plaguing the overall water splitting process with low conversion efficiency (iii) lack of high performance and cost-effective electrode materials to robustly catalyse the half-cell reactions in the same electrolyte and operate at wide pH range.[179, 180]

Furthermore, during the water splitting process, both the cathodic (HER) and anodic (OER) reactions are thermodynamically less favourable and kinetically slow. Ideally, electrolysis can be carried out providing at least the thermodynamic potential of 1.23 V at ambient conditions. But the loss of energy due to their endothermic nature and many other factors i.e., series resistance (Rs) and different heterojunction resistance slow down the electrolysis reaction and further increase the demand of high input potential generally called the overpotential.[181] Hence, it is essential to make this process electrochemically more feasible at low overpotential. The Pt based electrocatalysts are considered the champion of HER, while IrO_x/RuO_x based electrocatalysts are the well-known benchmark electrocatalysts for OER.[182] However, their widespread use is economically not favourable being rare-earth metals and thus their high cost. In this regard, a great effort has been devoted in the last two decades towards the rational design and development of economical but effective electrode setup (Pt/Ir-free) that is projected as a vital integrated part of the solar-electrochemical water splitting technology.[15, 183, 184] Earth abundant metals (Fe, Co, Ni, Cu etc.) based electrocatalysts and their hybrid materials (oxides, layer double hydroxide, chalcogenide, pinictide and carbide etc.) have been widely investigated in this regard.[54, 88, 151, 185, 186] Interestingly, some of the catalysts have been found very efficient and even comparable to the state-of-the-art electrocatalysts for HER and OER.[187-189] Despite all these developments, the demand of high overpotential at neutral-pH, less electrical conductivity/stability in the harsh electrode-electrolyte interface and mismatch in the bifunctional behaviour in the same electrolyte (acidic or basic) are still the formidable challenges that need to be addressed.[190, 191] Hence, the coupling of tunable nanostructures to rationally modulate the electronic structure with high surface charge density, and exposure of superficial active sites with high conductivity are highly desirable for the electrode assemblies that can offer a smooth and efficient transport of the charged species (ions and electrons) for the competent electrochemical water splitting module.[84, 155, 192, 193]

In the recent past, transition metal carbides in particular and their hybrid materials in general have been investigated and are being envisioned as potential electrode materials for overall water splitting.[194, 195] The emergence of unique electronic structure more or less similar to Pt, high conductivity, exceptional mechanical strength and stability in a wide pH range is the elegance of metal carbides for OER. Thus, they have experienced a rapid rise in their search as potential rare-earth metals based electrocatalysts in this regard.[196, 197] In addition, their chemical linkage with 1D material i.e., CNT as support offers several architectural advantages such as (ii) 1D architecture effectively prevent the metal carbide NPs from the agglomeration (ii) it may enlarge the solid-electrolyte interface and maximize the available surface area for electrochemical process (ii) and 1D nano-architecture also facilitate the electron transport along 1D and radial direction and thus are envisioned to boost the vibrant and self-supported catalytic potential for overall water splitting process possibly in a wide pH window.[194] Tewodros Asefa et al., have developed for the first time cobalt embedded NCNT and it was observed that doping of heteroatoms significantly change the electronic structure and catalyse the HER in a wide pH range.[179] Similarly, Yongye Lian et al., have recently developed the Ni-Fe embedded nanocarbons for overall water splitting attaining the current density of 10 mA/cm^2 at 1.58 V in two-electrodes system.[84] They found that the nanoscaling of the carbon, doping of heteroatom and their coupling with metal may provide the bifunctional catalytic behavior. Similarly, Xile Hu et al., have reported MoC NPs as highly active electrocatalysts for HER in both acidic and basic mediums.[198] Jing Jiang et al., have further demonstrated the bifunctional catalytic behavior of MoC and metallic cobalt embedded in the NCNT.[199] Meanwhile, Ting Ouyang et al., also reported the use of Co/β-Mo_2C@N-CNT heterostructure in this regard and demonstrated both theoretically and experimentally that interfaces between the Co, Mo_2C and N-CNT could enrich the active sites and can greatly promote the electron transfer during OER and HER in alkaline medium.[200] More recently, Qihua

Yang et al., have developed NCNT by pyrolysing the melamine/formaldehyde resin and found that in addition to the doping of heteroatoms, controlled morphology and diameter of the carbon nanotubes have pivotal role in improving the electrocatalytic potential of CNT. Thus, metal carbide and their hybrid materials with NCNT has great potential and arguably becoming the thriving candidates yet facing the challenges to further modernize their electrocatalytic potential in wide pH range.[197, 201, 202]

To envisage all the above efforts in addressing the problems associated with catalytic module, herein we report a one-step synthesis of nickel/nickel carbide (Ni/Ni_3C) anchored with nitrogen enriched carbon nanotubes (NCNT) of three different diameters and their bifunctional catalytic role in OER/HER, promisingly at all the tested pH values (0-14). The Ni/Ni_3C@NCNT were synthesized by the stoichiometrically controlled pyrolysis of inexpensive precursors (Ni and melamine), where the self-assembled Ni/Ni_3C NPs not only can assist in-situ engineering of NCNT but also play a key role in electrocatalysis in both acidic and basic conditions. To the best of our knowledge, the controlled integration of inorganic-organic counter-part into a single structure (Ni/Ni_3C@NCNT) particularly at the expense of Ni/Ni_3C and its decisive role in the water splitting at a wide pH range (0-14) will be the ever first report. We anticipate that this hybrid material simultaneously carries the nanostructuring, precise electronic modulation and the doped heteroatom (nitrogen), which are appreciable to mutually engineer the tuned structure. Thus, can integrate the structural architectural in term of their dynamic catalytic potential for OER/HER- a rising interest towards the real electrolyzer, however, rarely documented.[203]

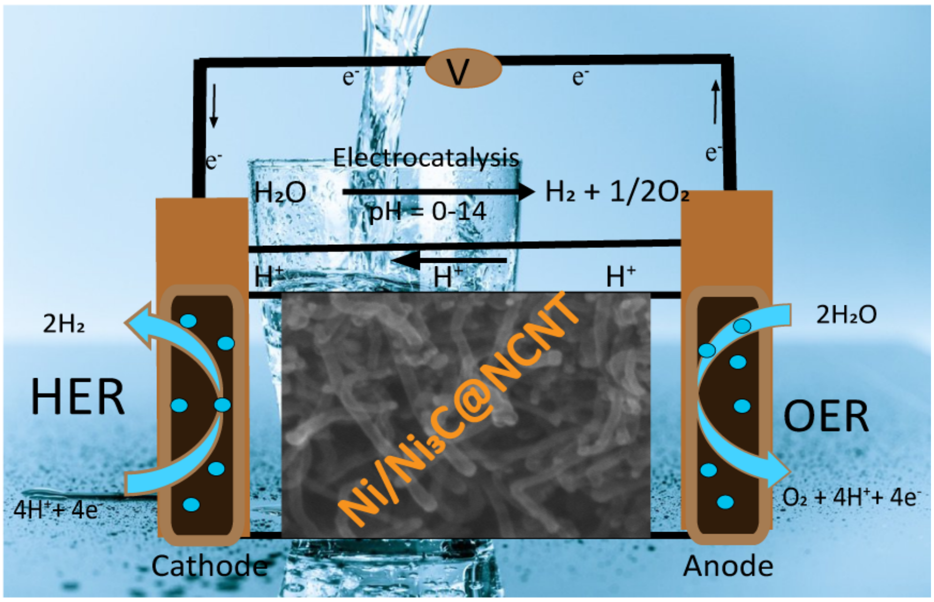

TOC 6.1 Table of content representing the electrochemical cell assembled with Ni/Ni_3C@NCNT as electrode material for OER and HER in wide pH range. Inset (between two electrodes) is the SEM image of Ni/Ni_3C@NCNT.

6.3. Results and Discussion

6.3.1. Material Characterization

The optimized synthetic pathway for the Ni/Ni_3C NPs induced engineering of NCNT with controlled diameters *via* solid-state method is shown in the **Scheme 2.3**. Transition metals NPs in their solid state are known to act as catalyst, where the self-assembling and outgrowth of the carbonaceous materials around the solid material depends upon the temperature, organic precursor, support material, crystal facets and particularly the size of metal NPs.[202, 204-206] In this regard, stoichiometrically controlled pyrolysis of Ni and melamine (source of C and N) was carried out under optimized conditions (see experimental part). The amount of Ni was repeatedly tested and optimized to control the aggregation/sintering of NPs usually taking place at high temperature. During thermal pyrolysis of reaction mixture in the inert environment, the in-situ generated reductive environment produced by organic precursor (melamine) can reduce the metal ions to Ni NPs acting as catalytic material for the diffusion of nitrogen enriched gaseous carbon to develop Ni-CN bond.[84, 207, 208] Thus by controlling the size of Ni NPs, the controlled growth of NCNT anchored with Ni/Ni_3C was successfully achieved, as discussed in the proposed mechanism (section 6.3.2). The morphology, shape, size and composition of the Ni/Ni_3C@CNT of different diameters were studied with scanning electron microscopy (SEM), scanning transmission electron microscopy (STEM) and energy dispersive spectroscopic (EDS) analysis. From the SEM/STEM analysis, the prefect tube type morphology is evident with the Ni/Ni_3C NPs at the tips of the tubes with white contrast (**Fig. 6.1**a-c). By increasing the melamine/metal ratio, the increase in the diameter of the tubes (average 18 nm, 38 nm and 65 nm) is clearly observed in the **Fig. 6.1**a-c, which is important due to their structure-performance relationship in catalysis. At high resolution, both the SEM images also show that the nanotubes are several micrometres long and crisscrossed with perfect appearance of Ni/Ni_3C NPs at the end point of each nanotube. Moreover, the SEM/STEM images also show that the diameters of the CNT are sensitive to the size of the NPs. By increasing the wt% of Ni, an increase in the size of Ni/Ni_3C NPs was observed and subsequently the outgrowth of NCNT with different diameters, which can possibly validate the anchoring of the Ni/Ni_3C, hybridization of Ni-C and the origin of the nanotubes via tip growth mechanism (discussed in the later part). The elemental mapping further confirms the superposition of the Ni metal present at the end point of the CNTs, while the elongated intense spot represents the corresponding tube skeleton (**Fig. 6.2**h-i). From the TEM analysis, the successive increase in the size of Ni/Ni_3C by increasing the wt% of Ni is observed that reasonably supports the possible hybridization of Ni with C in all samples as observed in SEM analysis. Moreover, the increase in the diameter of the NCNT shows the growth of NCNT induced by Ni/Ni_3C NPs due to the possible covalent linkage (**Fig. 6.1**d-f) (proposed mechanism).[84] From the **Fig. 6.1**g, it can be clearly seen that NCNT are hollow/tubular in nature with Ni/Ni_3C at the tips of NCNT, whereas no metal NPs are present inside the tubes. Moreover, it was observed from the TEM images that in case of small size of Ni/Ni_3C NPs, preferably the bamboo-shaped NCNT were formed, which are indeed very helpful in electrocatalysis due to the presence of numerous defects (**Fig. 6.1**d).[199] The structural defects and carbonaceous nature is also evident from the appearance of D and G bands in the Raman spectroscopy (Figure S8). The HRTEM analysis further unveil the crystalline structure of Ni/Ni_3C NPs surrounded by carbon shell as evident from the perfect characteristic fringes of Ni and C (**Fig. 6.1**j). The lattice spacing of 2Å corresponds to (111) plane of Ni present both in the crystal structure of metallic Ni and Ni_3C (JCPDS card No. 00-006-0697), while lattice spacing of 0.23 Å corresponds to (002) plane of the hexagonal structure of graphitic-C shell (**Fig. 6.1**j) and are in well agreement with the results obtained from the XRD analysis of bulk sample. As shown in the **Fig. 6.2**a, there is a slight increase in the intensity of peaks while increasing the concentration of metal. However, the crystallinity and diffraction pattern of all the samples is same with respect to the position of 2θ values. The reflection peaks marked with circles (o) at 2θ value of 39.8°, 42.3°, 44.8°, 48.4°, 58.4° correspond to (110), (006), (113), (200), and (116) miller indices, which exactly match with the diffraction pattern of crystalline rhombohedral phase of the Ni_3C (JCPDS card No. 00-006-0697). While the diffraction pattern marked with square (□) indicates the presence of the face centered cubic (FCC) structure of the metallic Ni with lattice parameter (a = 0.35238 nm, JCPDS card No. 00-004-0850) (**Fig. 5.2**a). These results clearly indicate the presence of well crystalline Ni/Ni_3C in the whole hybrid material.[209] In addition, the peak at ~26.5° due to the reflection from (002) crystal plan resembles to graphitic-carbon lattice slightly changes to lower 2θ values that may be due to the concomitant presence of the nitrogen impurities. The TEM/SEM results clearly indicate that metallic Ni is present in the core well-wrapped by Ni_3C and carbon shell, thus generating the Ni-Ni_3C-NCNT heterointerfaces present throughout the structure, which may be the most striking aspect of this material for their pivotal role in catalysis.

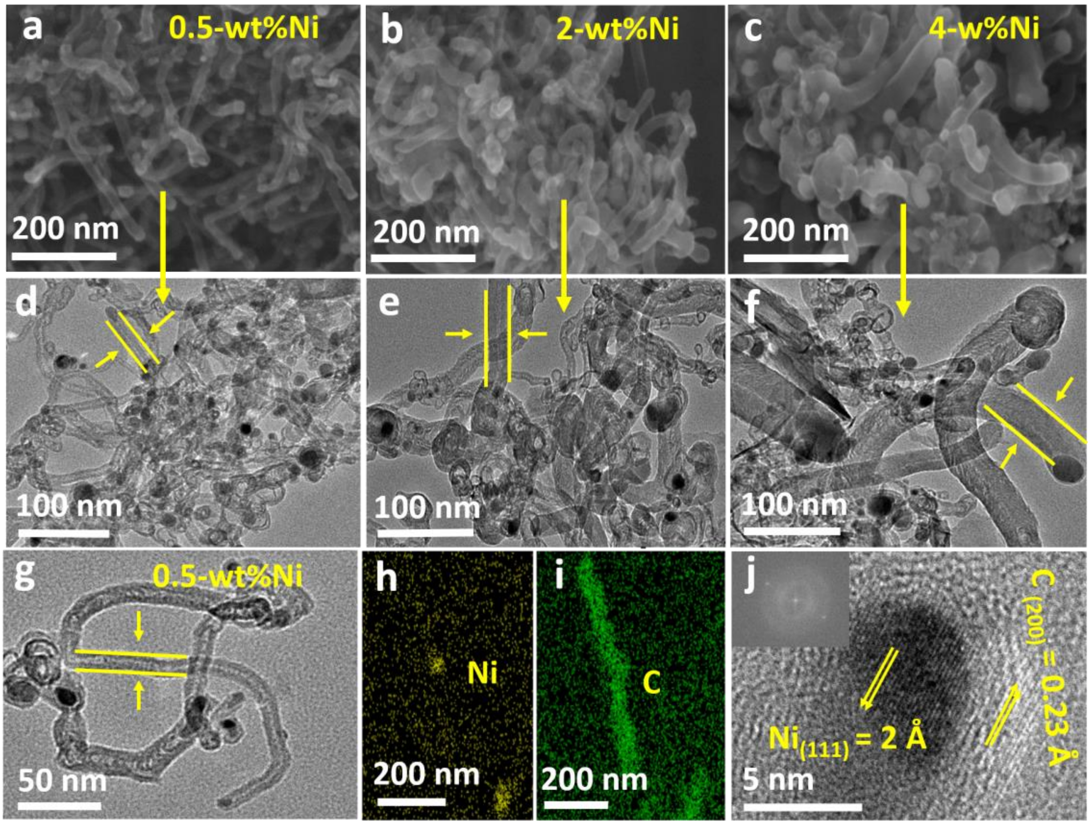

Figure 6.1 Scanning/transmission electron microscopic analysis of Ni/Ni_3C@NCNT. SEM image of a) 0.5-Ni/Ni_3C@NCNTs (b) 2-Ni/Ni_3C@NCNT (c) 4-Ni/Ni_3C@NCNT (d-f) TEM images of 0.5-Ni/Ni_3C@NCNT, 2-Ni/Ni_3C@NCNT, 4-Ni/Ni_3C@NCNT respectively, where the arrows indicate the diameter of NCNT (g) TEM image of 0.5-Ni/Ni_3C@NCNT showing the hollow nature of the nanotubes. (h, i) elemental mapping, where the intense spots represent the superposition of Ni and C (j) HRTEM image of 0.5-Ni/Ni_3C@NCNT, where the inset is the FFT pattern.

To further explore the chemical structure, electronic states and chemical environment, X-ray photoelectron spectroscopy (XPS) was carried out in this regard. The XPS survey spectrum shows the presence of C, N and Ni with relative intensity in the whole hybrid material (**Fig. 6.2**b). In the 2p core level spectrum of the metal, Ni is present in two different environments in the Ni/Ni_3C illustrating the same structural composition as observed in the XRD pattern (**Fig. 6.2**c). The peaks at 853.17 eV and 870.41 eV can be attributed to $2p_{3/2}$ and $2p_{1/2}$ of Ni^0, while the peaks at 855.18 eV and 872.17 eV correspond to Ni^{2+} $2p_{3/2}$ and $2p_{1/2}$ in Ni_3C respectively with a splitting factor of 17 eV.[210] The main peak for Ni^{2+} is slightly shifted towards the higher side, which may indicate the possible transfer of electronic density from the Ni to C.[211, 212] Moreover,

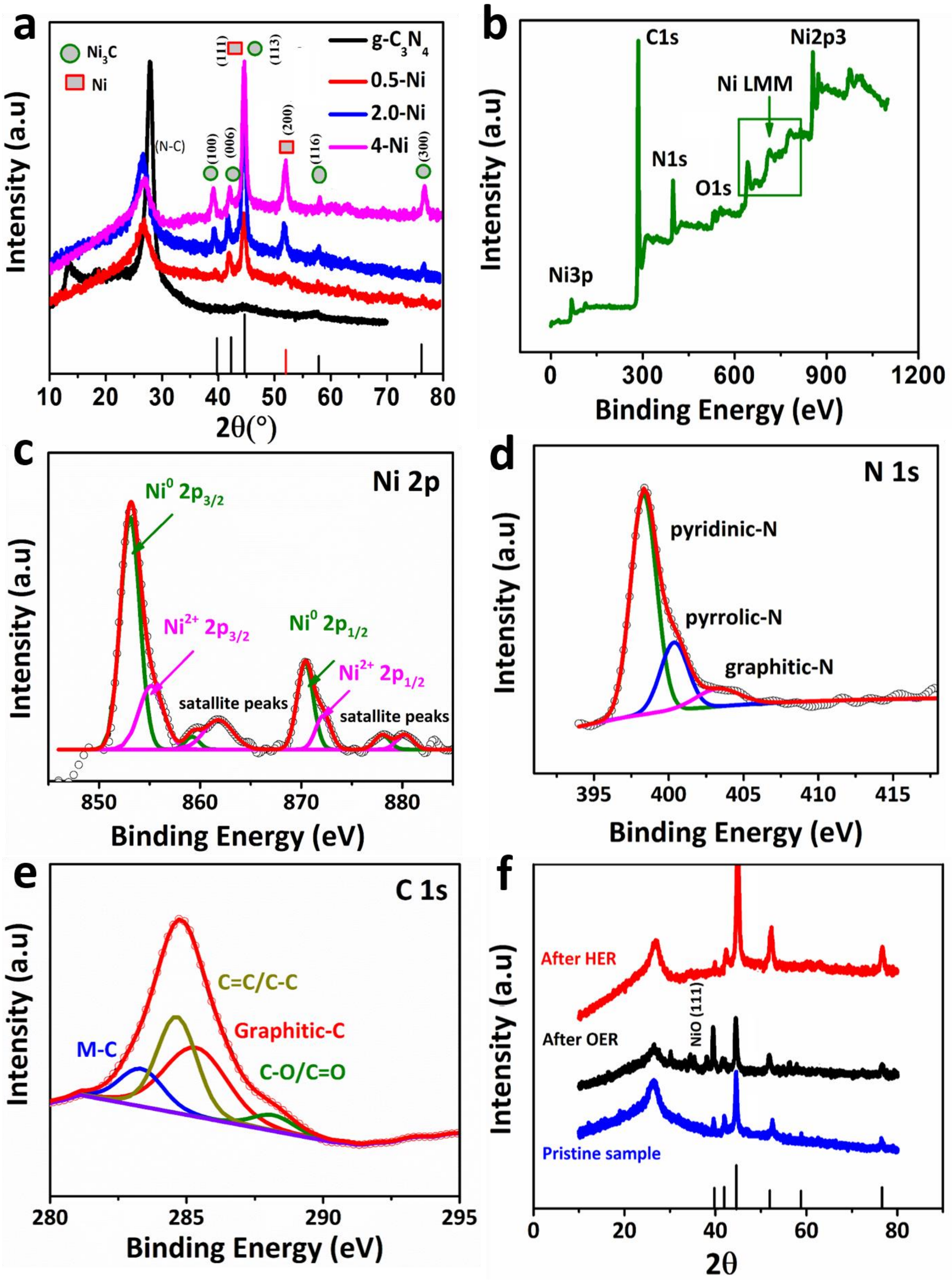

Figure 6.2 XRD and XPS analysis of Ni/Ni$_3$C@NCNT (a) XRD pattern of Ni/Ni$_3$C@NCNT hybrid material with different stoichiometry of Ni in comparison with g-C$_3$N$_4$ (b) XPS survey scan of 0.5-Ni/Ni$_3$C@NCNT (c) core level XPS spectrum of Ni 2p (d) XPs core level spectrum of N 1s (e) core level XPS spectrum of C 1s (f) XRD pattern of 0.5-Ni/Ni$_3$C@NCNT before and after stability test.

the peaks at 859.12 eV and 862.18 eV can be assigned to the satellite peaks usually appearing in the presence of Ni^0 and Ni^{2+} with splitting factor of 6 and 7eV respectively.

Usually, the satellite peaks appear with difference of 6 eV, however, an increase of 1 eV for Ni^{2+} typically indicates the insertion of carbon into the structure of Ni, which can modify the screening of core hole for the 4sp electrons that are less localized.[213] The small peak of oxygen in the survey scan may be due to the slight surface oxidation of metal carbide after their exposure to the air. The high resolution core level spectrum of C 1s with four major peaks in the range of 281 to 290 eV is given in the **Fig. 6.2**e. The peaks at 283.1 eV, 284.6 eV, 285.16 eV, and 288.12 eV can be assigned to Ni-C, C=C/C-C, C-N, and C-O/C=O bond respectively.[214] Similarly, three peaks at 398.58 eV, 401.81 eV and 403.08 eV in the core level spectrum of N 1s correspond to pyridinic, pyrrolic and quaternary/graphitic nitrogen (**Fig. 6.2**d).[200] It means that doped nitrogen is present in three different forms, but pyridinic-N and pyrrolic-N are present in higher quantity as evident from the comparative intensity of peaks and meanwhile strongly support the sufficient doping of nitrogen in the backbone of the carbon network. From the above results and discussion, it can be deduced that the whole structure is composed of Ni/Ni_3C NPs chemically linked with nitrogen doped carbon nanotube of different diameters. Such heterostructure containing metal in different oxidation state, and various nitrogen impurities have garnered much attention that can not only reinforce the bond of NCNT with metal by donating free loan pair of electron but also can engender the active sites and nanointerfaces in the vicinity of Ni/Ni_3C, which are direly needed for electrocatalysis.[214, 215]

6.3.2. Proposed Growth Mechanism

The Ni/Ni_3C@NCNT of different diameters (15-80 nm) were synthesized by pyrolyzing melamine as a prudent selection of C and N source with certain amount of Ni salt. During synthesis, we have optimized various parameters i.e., temperature, pressure, gas flow and even the position of crucible inside the tube furnace. Finally, the size of Ni/Ni_3C and subsequently the diameters of nanotubes was controlled by controlling the stoichiometric amount of the precursors while providing the optimum reaction conditions (see experimental part). During the overall synthesis, the sensitivity and growth of the NCNT to the reaction conditions was carefully analysed. Typically, the growth of CNT follow either base growth model or tip growth model depending upon the interaction with support material and gradual carbonization.[216] The support material loaded with minimum requirement of metal NPs in solid state can act as catalyst with the ability to diffuse the vapors coming from the organic precursor, where the faceted surface of metallic nuclei can template the cap formation to facilitate the controlled diffusion and assembling of gaseous carbon.[201, 216] In light of this concept, the temperature (> 550 °C), inert environment, high vacuum and controlled flow of gas (Ar/N_2) was ideally provided.[84] It is, therefore, reasonable to assume that the thermal treatment of the metal ions under the Ar/N_2 blanket surrounded by reducing species coming from the organic precursor could reduce the metal, whereas the in-situ generated Ni NPs can catalytically induce the outgrowth of NCNT, however, depends upon the size of the Ni/Ni_3C NPs possibly *via* tip growth mechanism.[94, 217] The presence of Ni/Ni_3C at the tips of the NCNT can be seen from their superposition carefully analysed with SEM, HRTEM, and elemental mapping (**Fig. 6.2**). However, after the repeated experiments, we believe that thermally induced reaction between the controlled mixing of melamine and metal salt (Ni) are critical to warrant the formation of Ni NPs of various sizes acting as catalyst followed by controlled feeding of nitrogen enriched gaseous carbon to facilitate size/morphology and controlled engineering of NCNT.[208, 216] The above hypothesis was experimentally further strengthened by varying the stoichiometry, temperature and reaction time while monitoring the end product with SEM analysis. We repeatedly observed that at low temperature (< 500 °C), only the Ni/Ni_3C NPs embedded inside the nitrogen enriched carbon matrix are formed, which display the partial growth and interstitial dissolution in the less energetic environment.[218] Similarly, at high temperature (> 600 °C) and even by increasing the reaction time, the metal NPs become agglomerated and growth of non-homogeneous carbonaceous shell around the NPs was observed. It is also worth-noticing here that by increasing the melamine/metal ratio, an increase in the size of the metal carbide NPs was observed, that may be due to uncontrolled growth (sintering & Ostwald ripening) of NPs at high temperature.[219] Therefore, varying the concentration of precursors lead to development of Ni/Ni_3C NPs of various sizes and corresponding carbon feeding through eventually dictate the diameter and length of NCNTs, which was also found sensitive to the temperature and reaction time. In this scenario, while monitoring the time and temperature effect, the controlled growth of the NCNT in the nanometric regime of different size/morphology (average, 15-75 nm) was finally achieved by controlling the metal/melamine ratio at 600 °C providing Ar blanket for 5 h (**Fig. 6.1**a-f). These observations strengthen our hypothesis about the initial formation of Ni/Ni_3C NPs and then tempted engineering of the NCNT by stoichiometrically controlled pyrolysis of the Ni/melamine, otherwise irregular morphology is formed under the similar conditions.

6.3.3. Electrocatalytic Evaluation for Water Splitting

6.3.3.1. Oxygen Evolution Reaction

Electrocatalytic performance for OER was initially evaluated in 1 M KOH in three-electrodes system using Pt wire, Ag/AgCl, and FTO as counter electrode, reference electrode, and working electrode respectively. Initially, a series of cyclic voltammograms (CVs) were collected for 0.5-Ni_3C@NCNT, 2-Ni/Ni_3C@NCNT, 4-Ni/Ni_3C@NCNT and IrO_2 with overpotential of 280 mV, 410 mV, 490 mV and 380 mV respectively to attain the current density of 10 mA/cm^2 (**Fig. 6.3**a). All the polarization curves with redox peak of $Ni^{2+/3+}$ show the electrochemical accessibility of the Ni for electrocatalytic water oxidation, whereas the lowest overpotential (230 mV) for 0.5-Ni/Ni_3C@NCNT indicates their superior performance by comparing with benchmark electrocatalyst. Similarly, Tafel slope of 58 mV/dec, 120 mV/dec, 150 mV/dec, and 99 mV/dec, was calculated for 0.5-Ni/Ni_3C@NCNT, 2-Ni/Ni_3C@CNT, 4-Ni/Ni_3C@NCNT, and IrO_2 respectively, where the lowest Tafel slope for 0.5-Ni/Ni_3C@NCNT display the kinetically fast OER process (**Fig. 6.3**c). Moreover, the kinetic study was also assessed from the charge transfer resistance (R_{ct}) with electrochemical impedance spectroscopy (EIS) (**Fig. 6.3**e). From the semicircles of the comparative Nyquist plots at low frequency (high Z), the R_{ct} values increases in the order i.e. $Ni_{0.5\%}$<$Ni_{2\%}$ < $Ni_{4\%}$. This behavior validates the comparatively fast transfer of electrons between the electrolyte-electrode interfaces, which is much convenient with smaller diameter of the NCNT and small particles size of the Ni/Ni_3C NPs. These results are also in consistent with CV pattern, where a rapid rise in the current density was observed at the same potential for 0.5-wt%Ni that even reached ≈120 mA/cm^2 with an increase in the potential window.[169] These findings have a close resemblance with Tafel slopes of all the catalysts that not only justify the kinetic trend of the respective electrode materials but also exhibit the structure/size-performance relationship of the conducting NCNT and their synergistic interplay with nanoscale heterointerfaces present in the Ni/Ni_3C. Therefore, they can reasonably facilitate the fast transport of the charge species (ions and electrons) during the electrochemically driven OER process.[169]

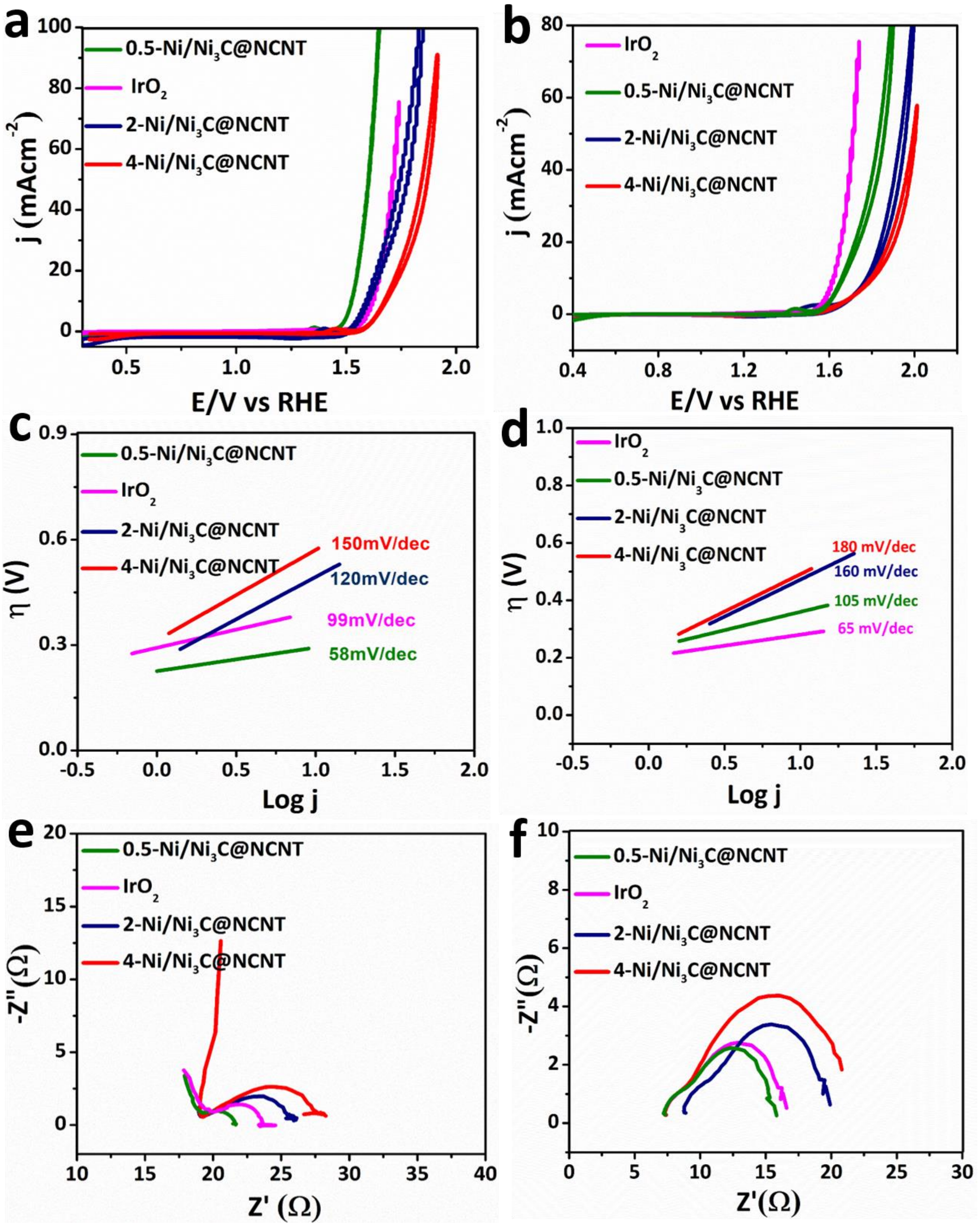

Figure 6.3 Electrocatalytic activity of Ni/Ni_3C@NCNT for OER in 1 M KOH and 0.5 m H_2SO_4 (a) polarization curves for OER in 1 M KOH (b) polarization curves for OER in acidic medium (0.5 M H_2SO_4) (c, d) corresponding Tafel plots for OER (e, f) Nyquist plots for OER in basic and acidic medium respectively.

Further, the OER activity was also assessed in the acidic medium (0.5 M H_2SO_4) that, however, is very rarely documented. As expected, the same catalytic trend for OER at pH = 0 was observed as in the alkaline solution, which shows the potential role of precise nanostructuring and their redox flexibility in different electrolytes (**Fig.**

6.3b). More precisely, in addition to the sufficient amount of Ni/Ni_3C, the presence of pyridinic-N not only can increase the electrical conductivity but may also the surface wettability to assist the adsorption of different intermediates (OH, OOH) during OER.[220, 221] The detailed comparative catalytic activity of different electrode materials is given in the table (**Table 6.1**). It is pretty much visible that OER activity assessed in the alkaline medium is fairly better than that acquired in the latter case, which shows that such hybrid materials may adopt different conversion mechanism and rate-determining step for OER, which is also evident from different Tafel slopes dependent on the pH of the charge transport medium (**Fig. 6.3**d).[30] However, from the smaller Tafel slope (58 mV/dec for 0.5-Ni/Ni_3C@NCNT), low onset potential (1.46 V), and high current density >100 mA/cm^2, it can be deduced that hydroxyl ions can conveniently hold the OER process in basic medium, where the high concentration of OH^- can substantially abstract the H^+ from water molecules to kinetically assist the chain reactions at low overpotential.[30] Although, we have no spectroscopic evidence, but the execution of fast electrode reaction thermodynamically at low overpotential suggested that integrated active redox couple of $Ni^{2+/3+}$ in this hybrid material may optimally interact with different intermediates (M-O^-, M-OH, M-OOH^-) in the multistep OER process probably due to the reshuffling of electronic density across the heterointerfaces between Ni, Ni_3C, N-CNT.[169, 200] It has been investigated, that in metal carbide the electronic density shifts from metal to carbon due to the electronegativity difference, where the doped nanocarbon of small diameter having intrinsic structural strain and high surface density, which strongly favor the concerted synergistic effect with metal carbide active sites.[211, 222] In this way, the metal in variable oxidation state (Ni^0/$Ni^{2+/3+}$), their chemical linkage and electron transfer with nanocarbon can possibly wave the orbital energy level in favor of optimum adsorption/desorption process and thus remain fruitful to assist the energy intense step (MOOH formation, RDS) during anodic reaction as evident from the smaller Tafel slope.[84] To further evaluate the stability of OER performance, controlled potential electrolysis (CPE) was assessed in both alkaline (**Fig. 6.4**a) and acidic medium (**Fig. 6.4**b). An overpotential of 280 mV, 410 mV and 490 mV is needed for 0.5-Ni, 2-Ni, and 4-Ni at pH = 14, while 400 mV, 540 mV, and 560 mV overpotential was observed at pH = 0 to achieve the current density of 10 mA/cm^2 during sustained OER process. It is notable, that OER in acidic medium need high overpotential while low overpotential is needed in basic medium particularly for 0.5-Ni/Ni_3C@NCNT ($\Delta\eta$ = 10 mV/10 h) displaying their strong resistance against the corrosion and phase transformation of catalyst usually taking place during the long sluggish OER process. Moreover, the polarization curves before and after the stability test exhibit no notable decrease in the current density with negligible increase in the overpotential even after multistep stability test (24 h) showing its recycling potential (**Fig. 6.4**e)

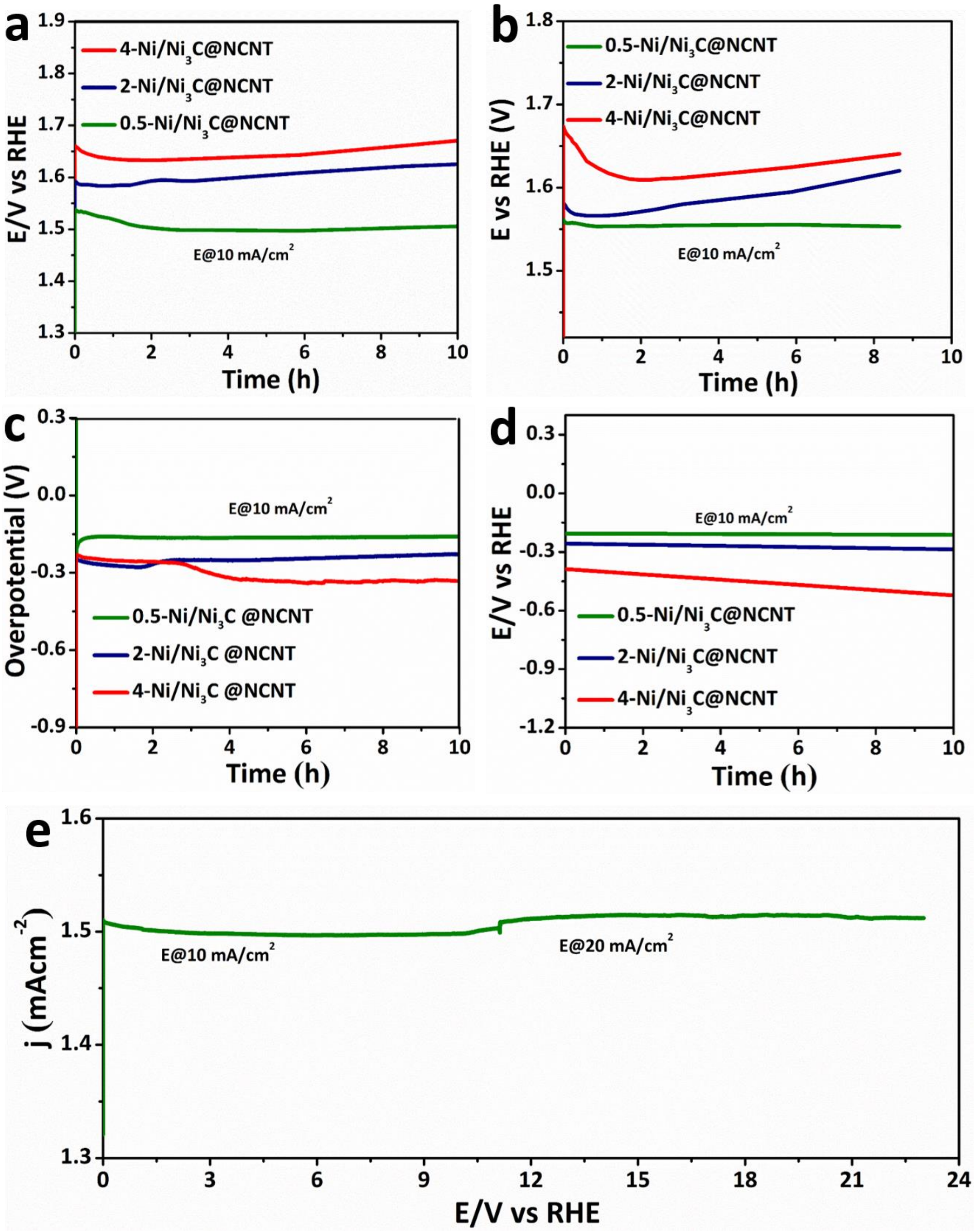

Figure 6.4 Stability test of Ni/Ni$_3$C@NCNT at 10 and 20 mA/cm^2 in basic and acidic medium for (a) OER in 1 M KOH (b) OER in 0.5 M H$_2$SO$_4$ (c) HER in 0.5 M H$_2$SO$_4$ (d) HER in 1 M KOH (e) multistep stability test for OER at 10 and 20 mA/cm^2.

6.3.3.2. Hydrogen Evolution Reaction

The efficiency of electrocatalyst was also assessed for HER in both acidic (pH = 0) and basic (pH = 14) medium by applying a negative bias (**Fig. 6.5**). All the parameters are given in the **Table 6.1** for comparison with the state-of-the-art catalyst (Pt/C). For all the catalysts the overpotential was found in between 210-280 mV in acidic and 290-425 mV in alkaline medium. Unlike the OER, smallest overpotential in acidic (η = 210 mV) and alkaline medium (η = 290 mV) was observed for 0.5-wt% Ni to achieve the current density of 10 mA/cm^2.[223] Generally, HER process in alkaline solution is associated with high overpotential because of the simultaneous dissociation of water molecules and the desorption of H atoms. In addition, high solution resistance due to the lake of proton (H^+) can further reduce their activity. However, nanostructuring, hybridization of metal with conducting carbon network with numerous structural defects due to the doped impurities (N) can significantly change the electronic structure and surface loyalty of the electrode material to address the associated problems.[195, 224] The expected catalytic potential is evident from the observed catalytic trend for HER in both acidic and alkaline mediums (**Fig. 6.5).** More specifically, an increase in the overpotential (from 210 to 280 mV, 0.5 M H_2SO_4) and Tafel slopes clearly demonstrate that HER activity of Ni/Ni_3C@NCNT is highly dependent upon the size of the Ni/Ni_3C NPs and diameters of the NCNTs (**Fig. 6.5**c). Further, a sequential decrease in the R_{ct} (from 7 to 3 Ω, 0.5 M H_2SO_4) (**Fig. 6.5**e) of the as-synthesized materials obviously validates the comparative charge transfer and conduction ability, which can be realized from their reasonable HER performance (**Table 6.1**) and high stability under both harsh acidic and alkaline conditions (**Fig. 6.4**c and d). It is anticipated that the presence of metallic Ni and electron rich nanointerfaces across the Ni-Ni_3C interface are highly regarded to facilitate H^+ adsorption and overall charge transfer ability across the electrode-electrolyte interface.[115] From the literature, it is well established that HER performance can be improved by optimizing the electronic structure of the electrode material in such a way to stabilise the H^+ with optimum chemisorption energy on the surface of catalyst.[155, 225] In this regard, the electronic structure of the metal `carbides are emerging in this quest due to the possible contraction of d-band of metal after the hybridization with nanocarbon. Consequently, it can increase the density of states (DOS) near the Fermi level, which are indeed promising for the 'H^+' adsorption as reported previously.[196, 225]

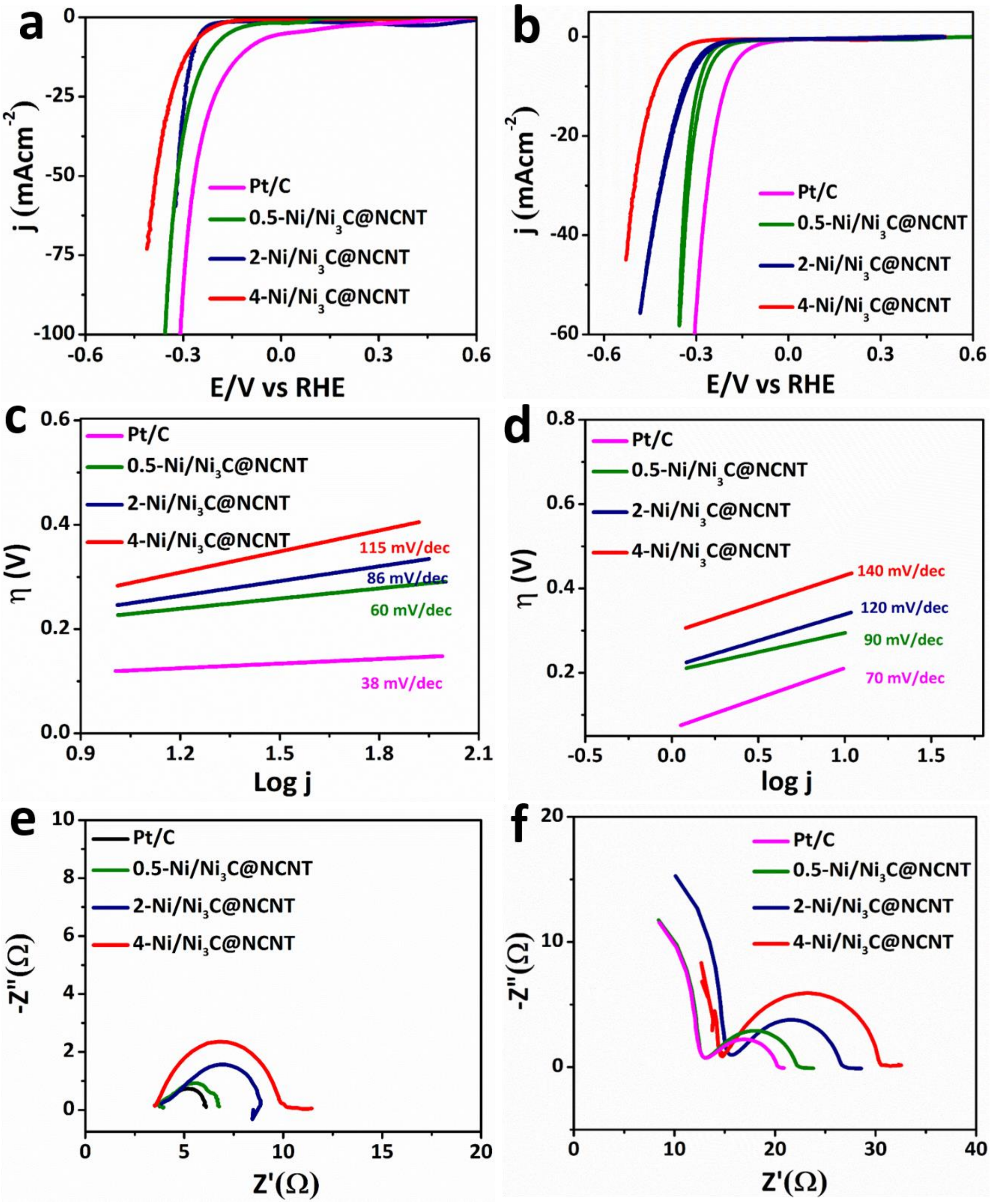

Figure 6.5 Electrocatalytic activity of Ni/Ni_3C@NCNT for HER in 1 M KOH and 0.5 M H_2SO_4 (a) polarization curves for HER in acidic medium (0.5 M H_2SO_4) (b) polarization curves for OER in 1 M KOH (c, d) corresponding Tafel plots for HER (e, f) Nyquist plots for HER in basic and acidic medium respectively.

Therefore, owing to the superior performance of the hybrid material in particular 0.5-Ni/Ni_3C@NCNT, it can be expected that modified electrodes could optimally adsorb the 'H^+' intermediates as a result of ameliorated electronic structure. Further, to kinetically understand this concept in depth, Tafel slope is the representative of an electrochemical reaction to scrutinize the kinetic favourability and rate determining step (RDS) at equilibrium. The smallest Tafel slope (60 mV/dec) of 0.5-wt%Ni calculated from the steady state polarization curve in acidic medium justifying that adsorption of the H^+ is the RDS *via* Volmer-Heyrovsky mechanism, which may fluctuate by changing the nature of the electrode material.[226]

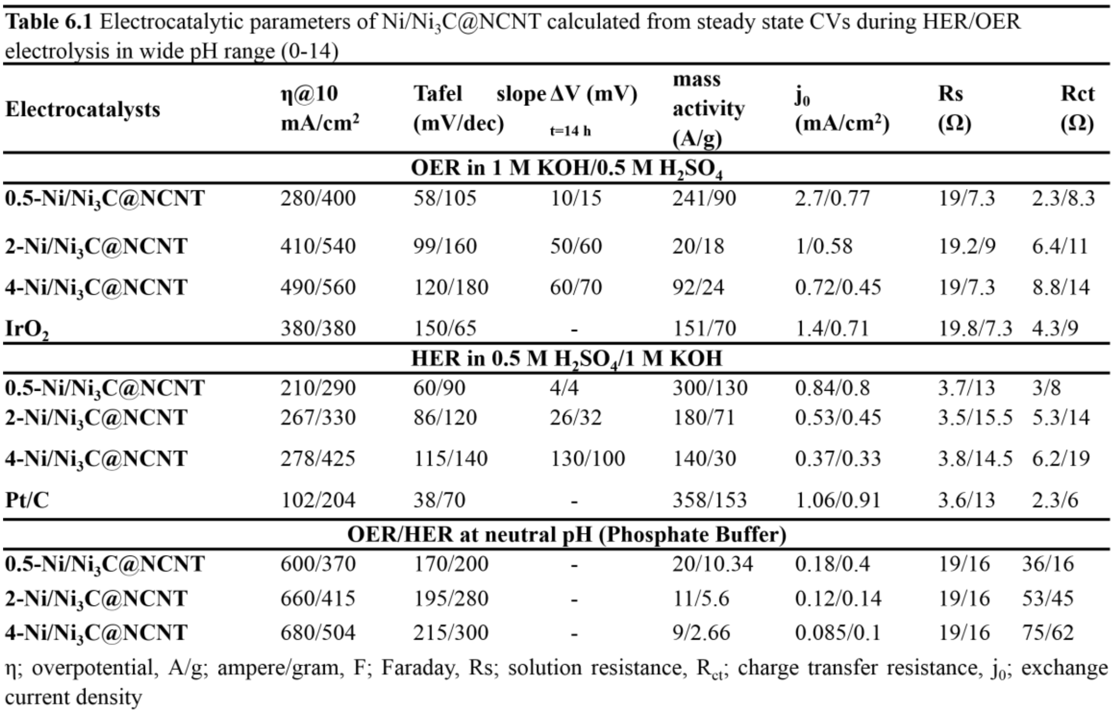

Table 6.1 Electrocatalytic parameters of Ni/Ni_3C@NCNT calculated from steady state CVs during HER/OER electrolysis in wide pH range (0-14)

Electrocatalysts	**η@10 mA/cm²**	**Tafel slope (mV/dec)**	**ΔV (mV) $_{t=14\ h}$**	**mass activity (A/g)**	**j_0 (mA/cm²)**	**Rs (Ω)**	**Rct (Ω)**
			OER in 1 M KOH/0.5 M H_2SO_4				
0.5-Ni/Ni_3C@NCNT	280/400	58/105	10/15	241/90	2.7/0.77	19/7.3	2.3/8.3
2-Ni/Ni_3C@NCNT	410/540	99/160	50/60	20/18	1/0.58	19.2/9	6.4/11
4-Ni/Ni_3C@NCNT	490/560	120/180	60/70	92/24	0.72/0.45	19/7.3	8.8/14
IrO_2	380/380	150/65	-	151/70	1.4/0.71	19.8/7.3	4.3/9
			HER in 0.5 M H_2SO_4/1 M KOH				
0.5-Ni/Ni_3C@NCNT	210/290	60/90	4/4	300/130	0.84/0.8	3.7/13	3/8
2-Ni/Ni_3C@NCNT	267/330	86/120	26/32	180/71	0.53/0.45	3.5/15.5	5.3/14
4-Ni/Ni_3C@NCNT	278/425	115/140	130/100	140/30	0.37/0.33	3.8/14.5	6.2/19
Pt/C	102/204	38/70	-	358/153	1.06/0.91	3.6/13	2.3/6
			OER/HER at neutral pH (Phosphate Buffer)				
0.5-Ni/Ni_3C@NCNT	600/370	170/200	-	20/10.34	0.18/0.4	19/16	36/16
2-Ni/Ni_3C@NCNT	660/415	195/280	-	11/5.6	0.12/0.14	19/16	53/45
4-Ni/Ni_3C@NCNT	680/504	215/300	-	9/2.66	0.085/0.1	19/16	75/62

η; overpotential, A/g; ampere/gram, F; Faraday, Rs; solution resistance, R_{ct}; charge transfer resistance, j_0; exchange current density

6.3.3.3. Electrochemical Evaluation in Phosphate Buffer

The electrochemical performance was also tested at neutral pH (phosphate buffer) both for HER and OER that is more desirable being an environmentally benign and less corrosive environment for catalysis. An overpotential of 370-450 mV and 280-360 mV was observed for OER and HER respectively, however, with small current density that may be due to the unfavorable transport of OH^-/H^+ ion in the charge transport medium (**Fig. 6.6**). These results in comparison with those obtained at pH = 0 & 14 substantiate the effective role of OH^- and H^+ ions in the kinetics of anodic and cathodic reactions.[227] Although, the current results at pH =7 are not comparable to those at extreme pH, but it can be predicted that transition metal carbide can be reasonably engineered with desired nanocarbon to come up with exciting electrochemical performance essential for neutral-pH electrolyzer and even can be opted for the sea-water electrolysis

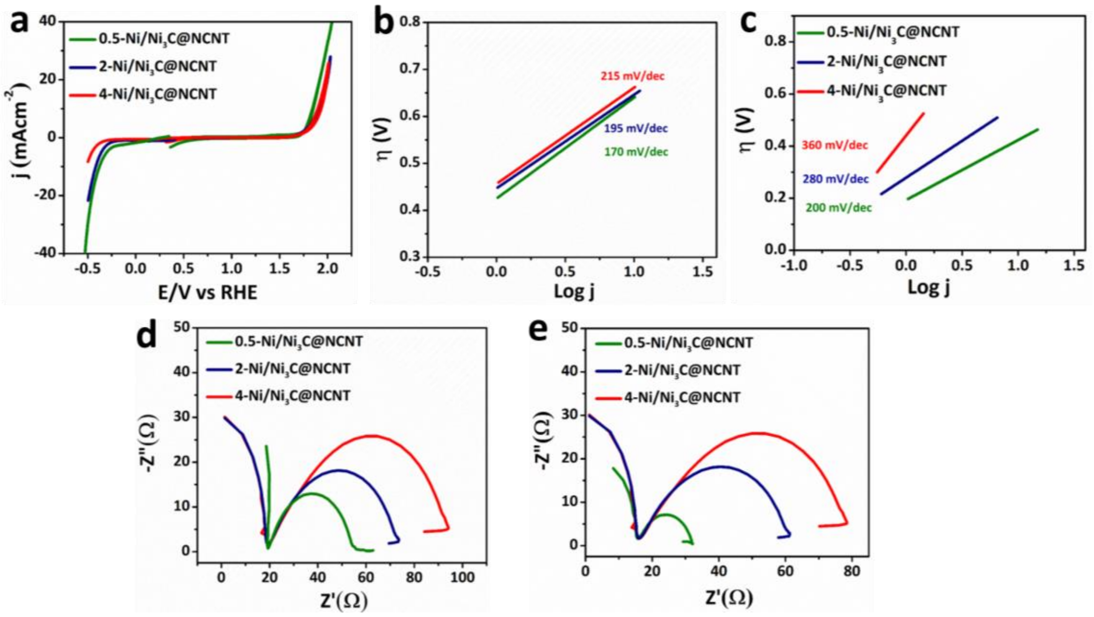

Figure 6.6 Electrocatalytic activity of Ni/Ni_3C@NCNT in phosphate buffer (pH ≈ 7) (a) polarization curves for OER and HER (b) Tafel plots for OER (c) Tafel plots for HER (d, e) Nyquist plots for OER and HER respectively.

6.3.3.4. Kinetic Study with EIS

As discussed, all the designed materials in comparison with state-of-the-art catalysts have been individually evaluated under the extreme pH and neutral electrolyte for OER/HER. However, by comparing all, the superior catalytic performance was observed for HER and OER at pH = 0 and 14 respectively, while moderate activity at neutral-pH. Therefore, we tried to probe the true kinetics of redox reactions (OER & HER) in term of Tafel slope in a more advanced way (from EIS) of the highly active (0.5-wt% Ni) material. Although Tafel slope calculated from the CV is a representative of well-balanced electrochemical reaction (as discussed above), nevertheless, the solution resistance (> 6 Ω) and ohmic losses deteriorate the true kinetics across the electrode and electrolyte interface and thus can create the uncertainty in the exchange current density. In that case, Tafel slope may not perfectly depict the true kinetics of the electrode process.[24] To minimize the experimental errors, we have calculated the Tafel slope from the EIS by excluding the effect of R_s both for OER (**Fig. 6.7**a, b) and HER (**Fig. 6.7**c, d) while providing extreme pH. It was a striking observation that the Tafel slope of 42 mV/dec and 40 mV/dec was calculated from EIS for OER and HER respectively, which are very close to those obtained from the CV (58 mV/dec & 60 mV/dec respectively). These results not only suggest the catalyst hold electrode processes with the above suggested mechanisms for OER (M-OOH$^-$ formation, RDS) and HER (Volmer-Heyrovsky, RDS), but also validate the true kinetics.[200]

6.3.3.5. Faradaic Efficiency (FE)

For the selectivity of electrocatalyst especially the carbon based electrode materials for OER, it is important to verify the origin of the current which can be probed from the purity of the evolved gases. For this purpose, initially, the qualitative analysis of molecular O_2 was repeatedly performed at regular time intervals with gas chromatography under anodic conditions. The produced molecular O_2 was then quantified against internal standard calibration curve.[80] Interestingly, the detection of molecular oxygen purely indicates the water oxidation process and subsequently the current response with FE higher than 95 % (**Fig 6.8**a). For further verification, the quantitative analysis was also performed with water displaced method (as discussed in the experimental section) using ideal gas equation, where we assumed that all the electrons in the external circuit are generated from the water oxidation process which can subsequently reduce the protons.[81] FE higher than 96 % in the latter case has a close resemblance with the prior one in comparison with the theoretical value indicating the extent of accuracy of two different approaches for quantitative analysis. In addition, it can also be deduced that prior water oxidation process mediated by the efficient catalyst system could minimize the possible side reactions usually taking place under anodic bias.

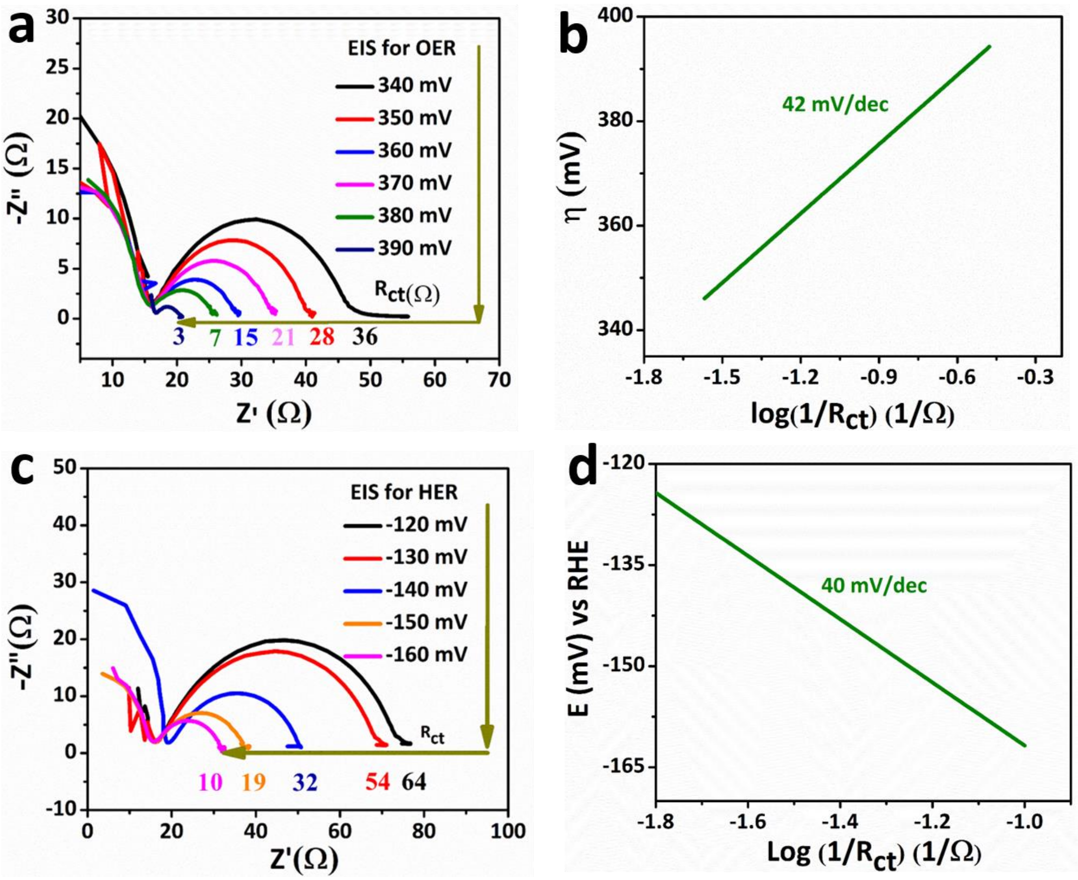

Figure 6.7 Electrochemical impedance spectroscopy (EIS) in the frequency range of 0.1 Hz to 1 MHz (a) Nyquist plots at various AC potential for 0.5-Ni/Ni_3C@NCNT for HER in 0.5 M H_2SO_4 and (b) corresponding Tafel plot (c) Nyquist plots at various AC potential for 0.5-Ni/Ni_3C@NCNT for OER in 1 M KOH and (b) corresponding Tafel plot. The arrows indicate the relationship of overpotential with $R_{ct.}$

6.3.3.6. Electrochemically Active Surface area, TOF and Cdl Study

To further evaluate, the turnover frequency (TOF) (**Fig. 6.8**b), exchange current density (j_o) (**Fig. 6.8**c, d), double layer capacitance (Cdl) (**Fig. 6.8**e) and subsequently

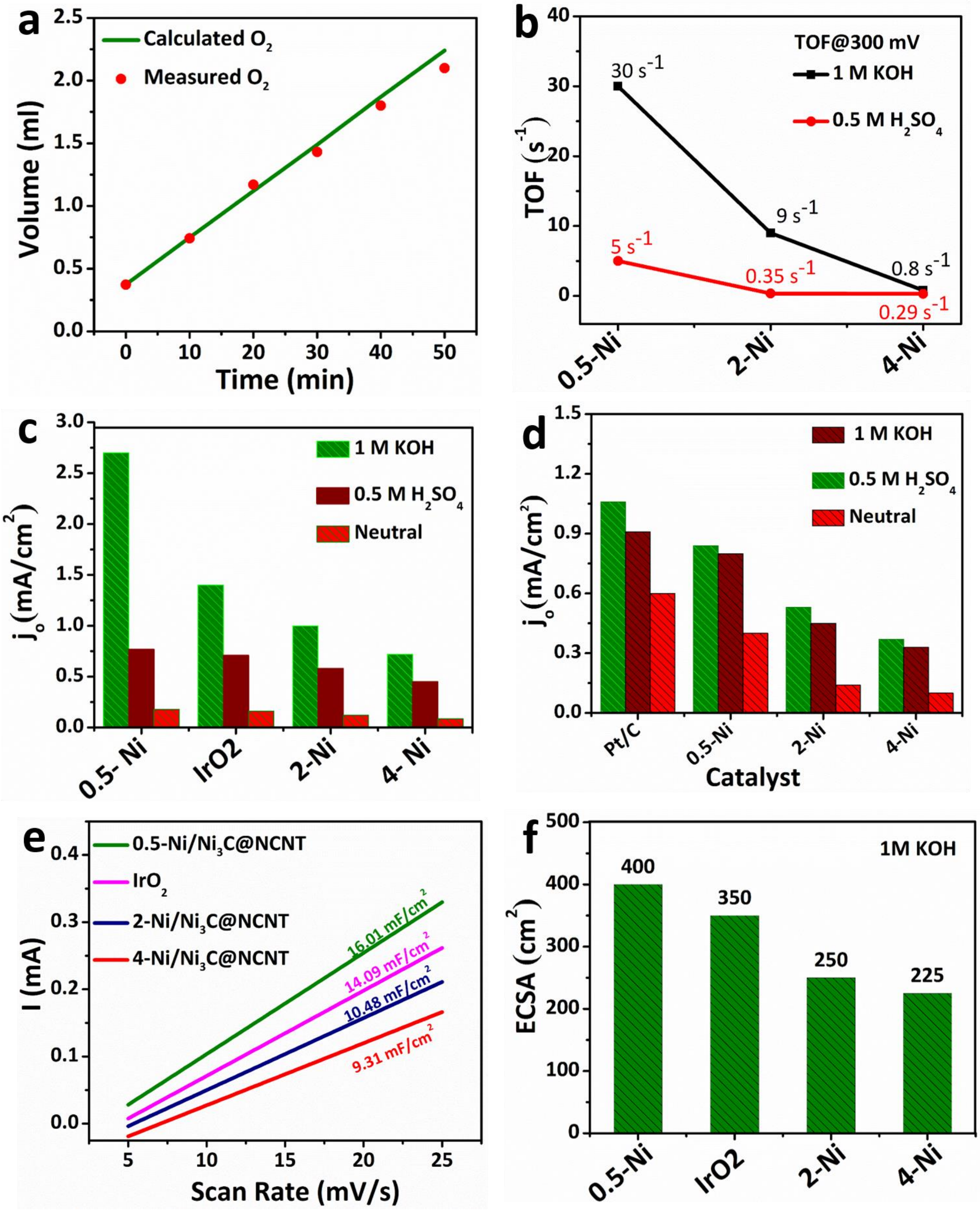

Figure 6.8 Electrocatalytic parameters (a) plot of Time vs measured volume of the evolved gas collected and compared with theoretical efficiency for the Faradic efficiency (b) Turn over frequency (TOF) of Ni/Ni_3C@NCNT. Exchange current density (j_o) graph of Ni/Ni_3C@NCNT calculated from EIS for (c) OER in 1 M KOH (d) and HER in 0.5 M H_2SO_4. (e) graph of capacitive current (mA) vs scan rate, where the slope is equal to double layer capacitance (Cdl) (f) electrochemically active surface area (ECSA) of Ni/Ni_3C@NCNT in 1 M KOH calculated from the Cdl. ECSA = Cdl/Cs, where Cs (from 0.033-0.056 mF in alkaline conditions) is the specific capacitance.

electrochemical active surface (ECSA) (**Fig. 6.8**f) was also calculated by using different standard equations summarized in the **Table 6.1**(detailed calculation methods are given in chapter 1). As clear from the polarization curves, the non-Faradic region for Cdl shows the incremental increase in the current density by increasing the scan rate (05-25 mV/s). The smaller current density at low scan rate increases the chance of non-Faradic reaction, where the successive increase in the current density by increasing scan rate indicates that modified electrodes have complete capacitive behavior (**Fig. 6.8**e). More the capacitive behavior, higher will be the ECSA.[146] AN increase in the Cdl value with decreasing the size Ni/Ni_3C of the NCNT validates that nanoscaling of the material could warrants abundant active sites, their sufficient electrochemical accessibility and high TOF. However, there is a minor difference in the ECSA of different electrocatalysts which entails that ECSA may not be the only deciding parameter to govern the electrocatalytic performance of electrocatalyst.

6.3.3.7. Structural and Compositional Study after Catalysis

During electrocatalysis, phase transformation, change in the composition and structure of catalyst during catalysis are the serious problems associated with electrochemical water splitting under the harsh acidic/basic conditions. From the XRD pattern collected after stability test, no notable change in the crystal structure was found especially after HER (**Fig. 6.2**f). Similarly, EDX analysis after stability test indicates the same composition and morphology of the Ni/Ni_3C@NCNT, which clearly demonstrates the mechanical strength and corrosion resistive nature of overall composite materials (**Fig. 6.10**). However, small peak at (002) in the XRD pattern (**Fig. 6.2**f) and small quantity of oxygen was observed in the EDX analysis, which may be due to the NiO_x thin layer formation during water oxidation catalysis.[228] For more in depth analysis, XPS analysis was carried out after stability test. The core spectrum of Ni indicates the shifting towards the higher side (from 856 eV to 858.3 eV). In addition, the increase in the intensity of oxygen peaks in survey spectrum was also observed. These results suggest the possible formation of NiO/NiOOH formation on the surface of catalyst (**Fig. 6.12**a). [137] However, no Fe impurities were found in the XRD or EDX analysis after the stability test which justify the purity of KOH and eliminate the role of Fe in the OER/HER process.[77]

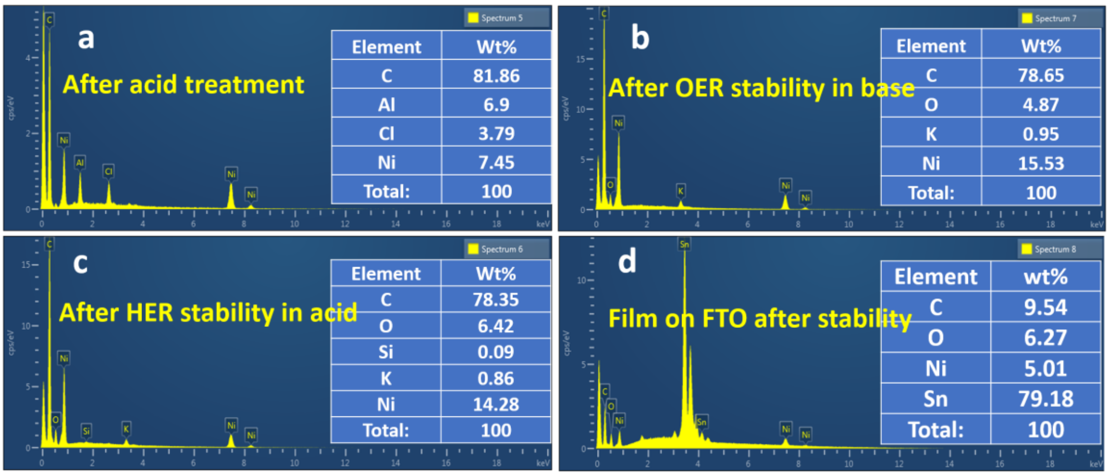

Element	Wt%
C	81.86
Al	6.9
Cl	3.79
Ni	7.45
Total:	100

Element	Wt%
C	78.65
O	4.87
K	0.95
Ni	15.53
Total:	100

Element	Wt%
C	78.35
O	6.42
Si	0.09
K	0.86
Ni	14.28
Total:	100

Element	wt%
C	9.54
O	6.27
Ni	5.01
Sn	79.18
Total:	100

Figure 6.9 Energy dispersive spectroscopic (EDS) analysis of 0.5-Ni/Ni_3C@NCNT (a) after acid treatment, where Cl comes after treatment with HCl (b) after OER stability test in base, where potassium (K) ions adsorbed from the electrolyte (c) after HER stability test in acid, Si and K may come from the H_2SO_4 (f) EDS analysis of thin film on FTO collected after stability test, where tin (Sn) comes from FTO. All the insets represent the corresponding percent composition.

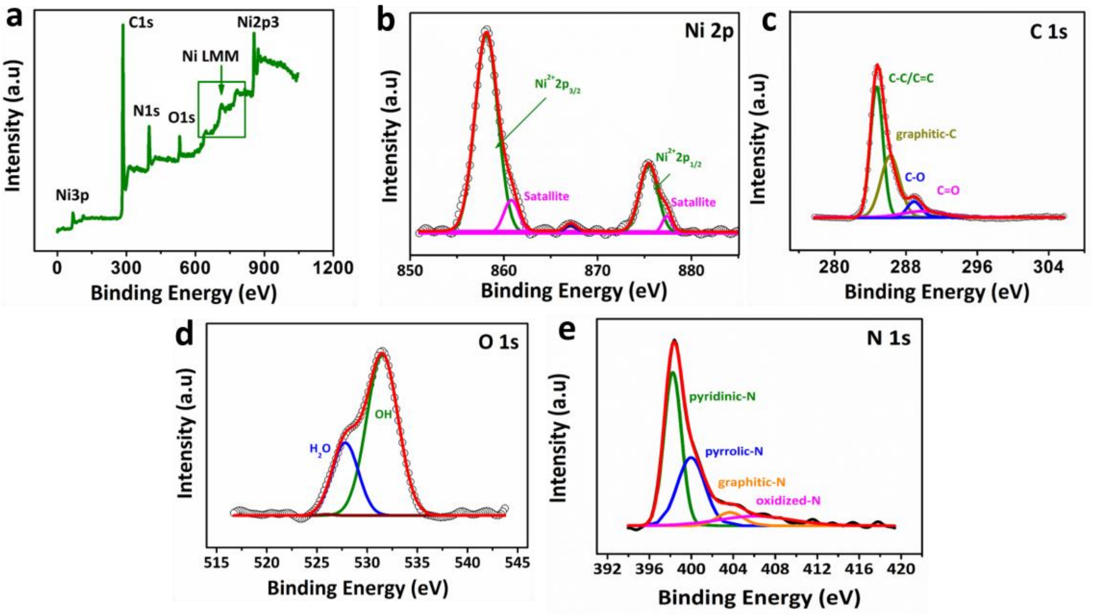

Figure 6.10 XPS analysis of 0.5 Ni/Ni_3C@NCNTs after catalysis (a) Survey scan (b) core level spectrum of Ni 2p (b) core level spectrum of C 1s (c) core level spectrum of O 1s (e) core level spectrum of N 1s.

6.3.3.8. Leaching Effect of Ni/Ni_3C NPs on Electrochemical Performance

To know which part of the hybrid materials dominantly controlled the catalytic activity, the best catalyst was dispersed in 1 M HCl and stirred for 24 h at 60 °C to remove or to leach out the metal NPs present at the tips of NCNT, centrifuged and dried the sample. Electrochemical characterization of the best catalyst at pH = 0 & 14 indicates that NCNT also take part in both OER and HER. Although, it is difficult to completely remove the metal content due to their strong chemical linkage, but the significant drop in the activity after the acid treatment is much clear from an increase in the overpotential and decrease in the current density after leaching (**Fig. 6.13**). Moreover, increase in the Tafel slope (from 58 to 92 mV/dec for OER and from 60 to 110 mV/dec for HER) and increase in the R_{ct} (2.3 to 9.5 Ω for OER and 3.7 to 8 Ω for HER) clearly indicates the partial killing of metal carbide and their drastic effect on the kinetics and charge transfer ability possibly loses due to the destruction of nanoscale heterointerfaces between Ni-Ni_3C-C. Based on these results, it can be attributed that Ni/Ni_3C is the key part of the entire hybrid material to subsidize a great potential for efficient OER/HER processes.[224] However, the chemical linkage with NCNT obviously extend substantial electrochemical performance in a wide pH window due to their concerted synergistic effect and concomitant presence of various nitrogen impurities.[214]

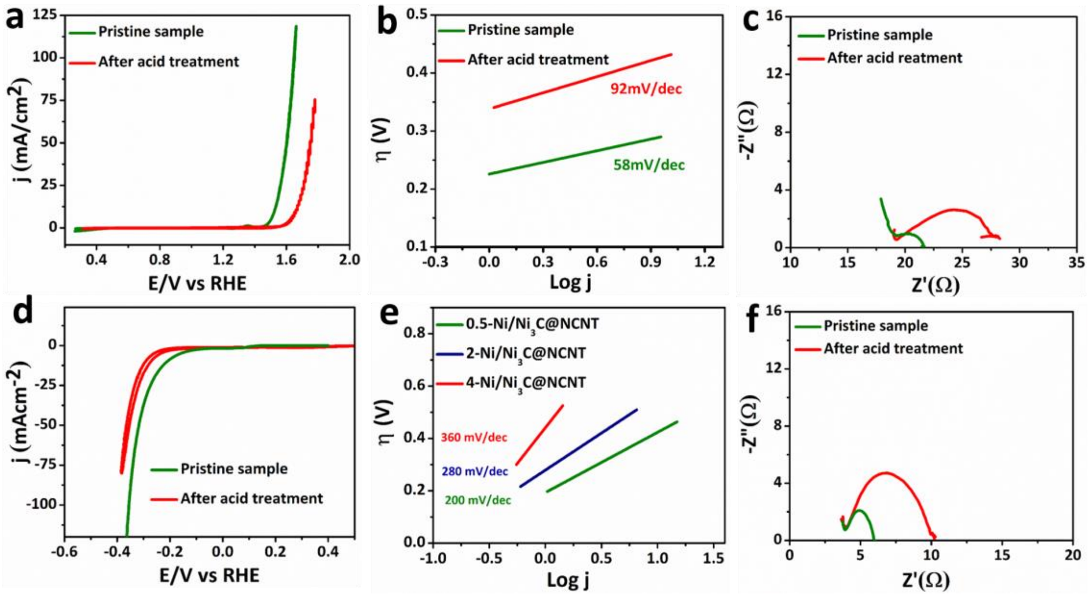

Figure 6.11 Electrocatalytic activity of 0.5-Ni/Ni_3C@NCNT before and after acid treatment (a) polarization curves for OER in 1 M KOH (b) Tafel plots for OER (c) Nyquist plots for OER (d) polarization curves for HER in 0.5 M H_2SO_4 (e) Tafel plots for HER (f) Nyquist plots for HER.

6.3.3.9. Origin of the Electrochemical Performance

In general, the results demonstrate that both OER and HER performance is dependent on the nanoscaling of Ni/Ni_3C, diameter of NCNT, their strong chemical linkage, high conductivity of nanocarbon and concomitant presence of the nitrogen impurities. However, it is really encouraging to propose the possible driving force behind the HER/OER processes accelerated by such engineered hybrid materials. It is generally believed, that decreasing the size of the material and diameter of the NCNTs increase the structural strain, surface-to-volume ratio and conductivity, which can inherently enhance the easy diffusion of electrons towards the available surface for catalysis.[99] Moreover, the *in-situ* doping of heteroatoms into the framework of NCNTs anchored with active Ni/Ni_3C leads to the electronic modulation and constitutes heterointerfaces, hydrophilicity, and thus can potentially enhance their inherent redox potential for electro-driven OER/HER reactions.[229] As evident from the XPS results, both pyrrolic-N, pyridinic-N, graphitic and quaternary-N are present in the backbone of CNTs. Such impurities not only coordinate with metal but also helpful to stabilize the metal carbide during catalysis. In addition, it can create the electron deficient and efficient carbon sites in the whole framework.[200] In case of the pyridinic-N and pyrrolic-N, the ‘C’ adjacent to nitrogen become electrophilic and nucleophilic in nature respectively. Such a bifunctional character and possible transfer of electronic density across the heterointerfaces is indeed helpful, where the stress-free adsorption/desorption process of involved intermediates can be accelerated as evident from the kinetic study.[230] Moreover, the hybridization of metal in different oxidation states with nanocarbons and particularly doped carbon possibly modulate the electronic structure and increase the host-guest electronic interaction between Ni-Ni_3C and C.[84] Thus, it is anticipated that integration of Ni/Ni_3C NPs and NCNT with controlled morphology and diameter in nanoscale dimension are credible for their persistent and bifunctional catalytic performance in the extended pH window.

6.4. Conclusion

In summary, one-step solid state synthesis of Ni/Ni_3C NPs anchored with nitrogen-doped carbon nanotube (NCNT) of three different diameters (average, 18 nm, 42 nm and 65 nm) is demonstrated as bifunctional catalysts for OER and HER, in a wide pH range (0-14). The synthesized hybrid materials from the inexpensive precursors i.e., melamine & $Ni(NiO_3).6H_2O$ were carefully examined with SEM/STEM and HRTEM and noted that during pyrolysis, the size of Ni/Ni_3C heterostructure can be in-situ controlled by controlling the stoichiometry of Ni/melamine providing optimum conditions, which in turn dictates the engineering of the NCNT of different size *via* tip growth mechanism. Further, the results demonstrate the presence of Ni/Ni_3C NPs at the tips of the several micrometers long and hollow nanotubes with sufficient doping of nitrogen in various forms i.e., pyridinic-N(53.40%), pyrrolic-N(28.01%) and graphitic-N(18.59%). During electrocatalysis, up to 4-wt % of Ni, all the catalysts show appreciable bifunctional catalytic trend with superior performance of 0.5-Ni/Ni_3C@NCNT hybrid material and fall in the range of those few electrocatalysts, which have been reported so far at all pH both for OER and HER (Table S3). Interestingly all the electrochemical parameters i.e., overpotential, Tafel slope, R_{ct}, exchange current density, and mass activity were controlled by controlling the size of Ni/Ni_3C NPs, doped nanocarbon and their internal chemical linkage, which demonstrate the decisive role of nanoscaling and structural architectural in electrocatalysis. However, the OER activity in basic medium and HER activity in acidic medium were found superior than those acquired by reversing the pH. From the current results, it can be deduced that nanostructuring, nitrogen doping and hybridization of the organic-inorganic component largely affect the electronic modulation of the hybrid materials. Thus, the presence of different heterointerfaces i.e., Ni-Ni_3C, Ni_3-C, Ni_3C-C and C-pyridinic-N, C-pyrolic-N would obviously allow the strong reshuffling of electronic density due to the existence of electron deficient and enriched centers which may optimally and dynamically compensate for different intermediates needed for the smooth HER/OER. We foresee great potential of such cost-effective hybrid materials (metal carbide, and NCNT) to better understand the structure-properties relationship with modern techniques with the support of computational study. Additionally, development of multi-metal carbide with controlled size/shape, surface engineering and electronic engineering can further enhance their redox potential and intriguing electronic properties and may replace the existing nanoscale high cost (Pt/Ru/Ir-based) materials.

Chapter 7.

Summary and Outlook

This dissertation focuses on the design and development of novel and scalable protocols for the synthesis of cost-effective nanoscale materials particularly transition metal/metal (Co, Ni and Cu) oxides and carbides for water splitting catalysis at low overpotential. The electrochemical water splitting is a valuable approach to assist the solar-driven water splitting technology for sustainable H_2 production. The viable production/storage of molecular H_2 is the potential contender not only to replace the existing fossil fuels by boosting fuel cell technology but also can be used for many industrial applications.

In this regard, we have organized this dissertation in the following manner. The Chapter 1 deals with opportunities/resources of the energy conversion/storage, background of the field, and potential of H_2 as a future energy carrier. It also highlights the electrode chemistry, types of water splitting process, possible mechanism for water splitting in both acidic and basic medium, problems faced by the electrode materials, possible solution to the associated problems, various electrocatalytic parameters and the scope of this dissertation. The 2nd chapter deals with selective experimental work/protocols which have been developed for the synthesis of various supported metal/metal oxides nanoclusters (NCs) and metal carbides, physicochemical and electrochemical characterization and fundamental principles behind the techniques (FT-IR, Raman, SEM/EDX, XRD, TEM/HRTEM, and XPS) used for structural elucidation.

During this research work, we have initially developed the thiol functionalized graphene oxide (G-SH) nanosheets *via* epoxidation reaction to improve their conductivity as support materials, trapping ability for the immobilization of ultrasmall metal/metal oxides (Ni, Cu and Co) NCs and their comparative electrochemical evaluation for water oxidation catalysis (Chapter 3 & 4). We have investigated and experimentally found that chemical functionalization using wet chemistry is one of the promising approaches to control the restacking of GO and meanwhile its surface modification with thiol that can play a key role in controlling the size, shape and uniform distribution of metal/metal oxides NCs in the subnanometric regime. These ultrasmall NCs (size ≈ 2nm) offer high electrochemical active surface area, maximum accessibility of active sites and high redox potential for OER while endorsing the fast heterogeneous electron transfer owing to the concerted synergistic effect. All the supported NCs have been found much more active than their bulk analogues, and Ni/NiO@G-SH nanohybrid outperforms all the NCs with low onset potential (1.46 V), smaller Tafel slope (46 mV/dec) and high stability (84 h). No visible decrease in the stability even in harsh conditions indicates the stable and active layer formation on the surface of catalyst. The spectroscopic investigations revealed that redox couple $M^{2+/3+}$ (for Ni and Co) and M^{2+} in the form of (oxy)hydroxides and hydroxide layer formation respectively are credible to govern the OER performance in periodic manner.

Taking in to account the remarkable performance of ultrasmall NCs, we have extended this work and developed a facile solid-state strategy for the in-situ growth of $Co/Co(OH)_2$ NCs embedded in N-doped mesoporous carbon network (HCN) for OER (Chapter 5). In this one step approach, the melamine (carbon and nitrogen source) and Co complex was thermally treated at fixed temperature (550 ºC) under Ar blanket. We have investigated that during thermal treatment, the H_2 released from the melamine can possibly reduce the metal ions and meanwhile develop a porous carbon network loaded with Co NCs. HRTEM analysis indicates the uniformly distributed Co NCs (size ≈ 2 nm) embedded in the porous network of N-doped carbon. From the extremely low onset potential (1.34 V), high current density (1000 mA/cm^2@1.6 V) and outstanding stable performance (5 days), it can be concluded that electrocatalytic performance of NCs is highly sensitive to the nature of support and can be potentially tuned for the challenging reaction. We have spectroscopically (XPS and Raman spectroscopy) investigated that during OER, reversible CoOOH layer formation takes place coupled with a change in their polarisability, which indicates that both the structure and electronic flexibility during catalysis could destabilize the water molecule and thus execute the oxidation process at low overpotential.

All the above NCs were evaluated only for OER in alkaline medium. However, it is of equal importance to develop those bifunctional catalytic materials which are equally functional in extreme pH conditions. In this quest, we extended the above solid-state strategy for the synthesis of Ni/Ni_3C NPs tempted growth of N-doped carbon nanotubes (NCNT) of different sizes (by varying the ratio of Ni precursor from 0.5 to 4 wt%) as bifunctional electrocatalyst for water splitting in a wide pH window. We have experimentally verified that stoichiometric combination of $Ni(NO_3)$, melamine and their thermal pyrolysis at 550 °C in the inert environment are necessary for the controlled growth of $NiNi_3C$ NPs. Meanwhile, the NPs dependent growth of NCNT indicates the tip growth mechanism on the surface of Ni/Ni_3C NPs, which was verified with SEM/TEM analysis. The spectroscopic investigation and HRTEM analysis unveil the presence of Ni NPs at the tips of NCNT and their chemical linkage with N-doped graphitic carbon. The electrocatalytic performance of different synthesized samples was evaluated by comparing with benchmark electrocatalyst (IrO_2) and analogous samples i.e., NiO, CNT, and Ni NPs in the wide pH range both for OER and HER. Promisingly, all the synthesized hybrid materials were found active for OER/HER, where 0.5-Ni/Ni_3C@NCNT (average size ≈ 15-20 nm) showed remarkable activity for OER ($\eta_{10\text{-base/acid/neutral}}$ = 280/400/600 mV, Tafel slope$_{\text{base}}$= 42 mV/dec) and HER ($\eta_{10\text{-acid/base/neutral}}$ = 210/290/370 mV, Tafel slope$_{\text{acid}}$ = 40 mV/dec). The size dependent catalytic potential is probably due to the internal structural strain, structural defects induced by the presence of doped nitrogen (pyridine-N, pyrrolic-N and graphitic-N) and electronic modulation of d-band center that usually takes place in metal carbides. We believe, that metal carbides have a great potential for overall water splitting due to their appreciable mechanical strength, high conductivity, high stability in harsh condition and tunable electronic properties. It is also worth mentioning, that carbon based materials have high probability to oxidize under anodic condition. However, from the high Faradaic efficiency it has been justified that selectivity of electrode materials can be tuned by nanostructuring and controlled engineering (structural/electronic) at the nanoscale length.

This thesis entitled '*Development of Nanocatalysts for Water Splitting-A Sustainable Source of Energy'* completely summarizes the published work and meanwhile generates various worth practicing ideas for the development of new nanoscale materials in this regard. The surface functionalization of GO (Chapter 3) is the motivation for the incorporation of -SH, $-NH_2$ and even substituted aromatic compounds *via* selective epoxidation reaction. Such modified and conductive functional 2D materials are appreciable as stable materials that could possibly generate a chemical linkage with array of noble/non-noble metals NCs and their alloys as novel electrode materials. It has been exclusively studied that bimetallic transition metal oxides are converted into (oxy)hydroxides during water oxidation catalysis and are considered as benchmark electrocatalysts for water splitting. Therefore, pre-synthesis of Ni-Fe and Ni-Co (oxy)hydroxides is a new trend via anodization or electrodeposition. However transition metals are inherently less conductivity in nature. In this regards, thin films of thiol functionalized GO would be a promising support and good current collector to further modernize their performance, stability and even their integration in an electrolyzer.

It is well established that metal sulfides especially MoS_2 and WS_2 are highly active materials for HER. However, their exfoliation and stabilization up to a few layers of nanosheets is a formidable challenge. Although, thiol containing organic linkers are generally used which have a strong affinity with metals and thus can control over their restacking, however, unfortunately it usually deteriorates their performance due to the blockage of active sites. In this quest, layer-by-layer assembling of highly dispersed thiol functionalized GO and MoS_2/WS_2 as model catalyst is worth exploring. This unique approach may not only address the associated problems with metal chalcogenides but also due to synergistic effect between 2D nanosheets, which would extend their catalytic potential in water splitting and related energy conversion processes.

This thesis also explores the effective and simple solid-state strategy for the in-situ growth of both metal/metal oxides NCs, metal carbides and carbon nanotubes. Such type of simple and scalable approaches can be exercised for the variety of metals, but it will require a careful optimization of reaction conditions. It is noteworthy to mention here that $Co/Co(OH)_2$ NCs in the mesoporous carbon network were found highly active and durable among all the NCs reported so far. Therefore, we foresee a great potential of NCs and their loading on various conducting but porous support not only for the immobilization of NCs but also to ensure their exposure during electrochemical process for the dynamic release of a variety of intermediates during multistep processes. In this quest, metal organic frameworks (MOFs), covalent organic frame works (COFs) and covalent triazene frameworks (CTFs) are among the ideal candidates for the controlled assembling of nanoscale materials. The porosity and structural network can be easily controlled by controlling the nature and bulkiness of linkers/precursors to consequently control the size and interaction of NCs with support framework. Such type of support materials can even be used for the stabilization of single atom catalyst due to the presence of heteroatoms in the whole skeleton.[60] We have developed a highly conducting and graphitized carbon based nanoflowers (NF) extended in 3D manner by simply polymerizing vinyl alcohol. However, a variety of monomers and their derivatives can be used to improve the porosity and surface structure for the effective stabilization of metal/metal oxides *via* thermal impregnation methods (**Fig. 7.1**).

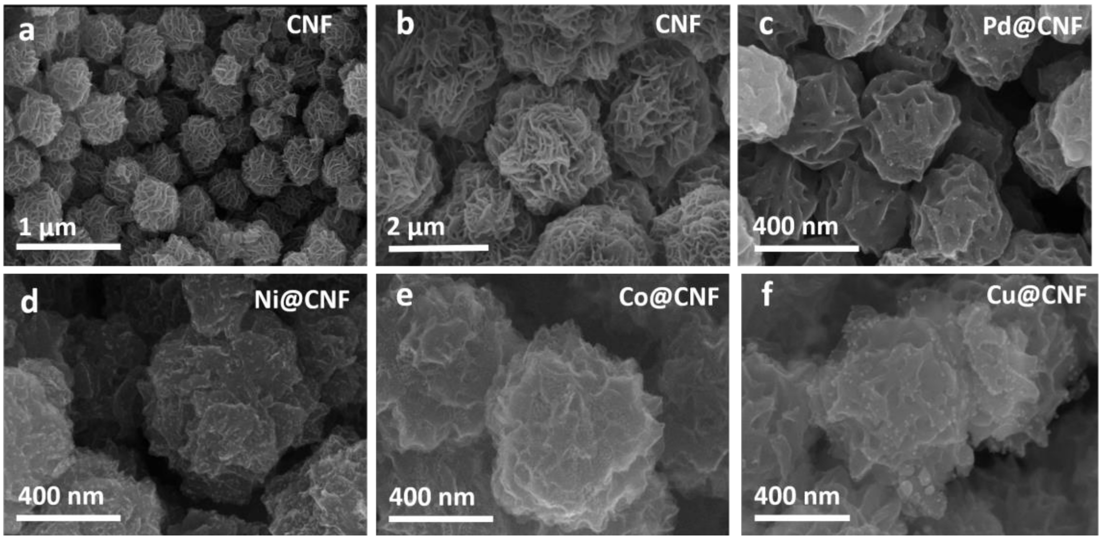

Figure 7.1 SEM images of carbon nanoflowers (CNF) supported with transition metals (a, b) CNF at low and high magnification (c-f) CNF supported Pd, Ni, Co and Cu metals/metal oxides NPs respectively.

Solution based chemistry is another approach for the stabilization of molecular metal NCs, which are atomically monodisperse in nature with precise number of atoms in the core of the cluster (e.g., Ni_6 and Ni_4) capped with organic linker.[99] These molecular metal NCs are the emerging materials in catalysis and behave like a molecule with unique electronic/catalytic properties, high ECSA, variable number of core atoms and recently found very active both for HER and OER.[96, 136, 231] We have developed uniformly distributed Ni, Cu and cobalt NCs capped with thiol based linkers as model catalysts for water oxidation (**Fig. 7.2**). The field of molecular metal NCs is brimming with possibilities especially monometallic and multimetallic transition metal NCs (from Mn to Cu) are open for the young researchers. The catalytic properties of such materials are highly sensitive to the number of atoms in the core of clusters and underlying support. Their catalytic properties and selectivity can be further enhanced by doping metal impurities and loading on various conducting support.[99] Their surface chemistry can also be easily controlled to tune their oxophilic/aerophilic nature by using/replacing suitable linkers which are needed for the easy removal of molecular H_2/O_2. Due to the quantum confinement and molecular-like properties especially those of noble metal NCs (Au_{25}, Au_{36}, Au_{38}, Ag_{44}, etc.) results in their strong absorption coefficients.[232] [233] Their immobilization on a variety of semiconductor can be exploited for harvesting light and energy conversion in photo-electrochemical water splitting and CO_2 reduction. Such atomically monodisperse molecular metal NCs with clear crystalline structure are among the ideal candidates for theoretical modeling, mechanistic investigation and structure-performance relationship. We believe, that these emerging materials will ultimately abridge the homogeneous and heterogeneous catalysis at the interface of molecular and nanoscale length.

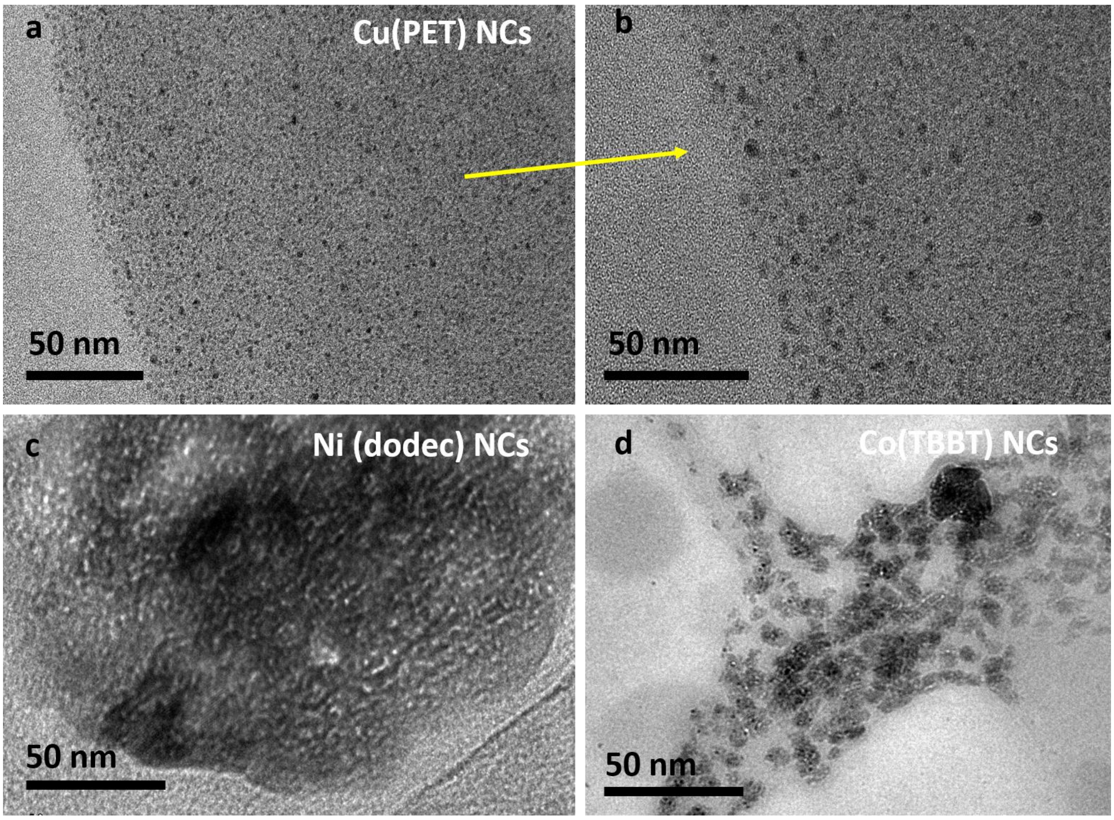

Figure 7.2 TEM images of thiol stabilized metal NCs (a) Cu NCs (d) Ni NCs (d) Co NCs, where PET: 2-phenyleethan thiol, Dodec: dodecan thiol, TBBT: para-tertiary butyl benzene thiol.

References

1. McCardell, S., Energy Around the Globe. In *Energy Effectiveness*, Springer: 2018; pp 15-24.

2. Fuqiang, W.; Ziming, C.; Jianyu, T.; Yuan, Y.; Yong, S.; Linhua, L., Progress in concentrated solar power technology with parabolic trough collector system: A comprehensive review. *Renewable and Sustainable Energy Reviews* **2017,** *79,* 1314-1328.

3. Korkas, C. D.; Baldi, S.; Michailidis, I.; Kosmatopoulos, E. B., Occupancy-based demand response and thermal comfort optimization in microgrids with renewable energy sources and energy storage. *Applied Energy* **2016,** *163*, 93-104.

4. Muhich, C. L.; Ehrhart, B. D.; Al-Shankiti, I.; Ward, B. J.; Musgrave, C. B.; Weimer, A. W., A review and perspective of efficient hydrogen generation via solar thermal water splitting. *Wiley Interdisciplinary Reviews: Energy and Environment* **2016,** *5* (3), 261-287.

5. Jiang, C.; Moniz, S. J.; Wang, A.; Zhang, T.; Tang, J., Photoelectrochemical devices for solar water splitting–materials and challenges. *Chemical Society Reviews* **2017,** *46* (15), 4645-4660.

6. Carlson, K. M.; Gerber, J. S.; Mueller, N. D.; Herrero, M.; MacDonald, G. K.; Brauman, K. A.; Havlik, P.; O'Connell, C. S.; Johnson, J. A.; Saatchi, S., Greenhouse gas emissions intensity of global croplands. *Nature Climate Change* **2017,** *7* (1), 63-68.

7. Mohammed, S. J.; Mansoori, G. A., A Unique View on Carbon Dioxide Emissions around the World. *Global Journal of Earth Science and Engineering* **2017,** *4,* 8-17.

8. McKone, J. R.; Lewis, N. S.; Gray, H. B., Will solar-driven water-splitting devices see the light of day? *Chemistry of Materials* **2014,** *26* (1), 407-414.

9. Hisatomi, T.; Domen, K., Reaction systems for solar hydrogen production via water splitting with particulate semiconductor photocatalysts. *Nature Catalysis* **2019,** *2* (5), 387-399.

10. Nocera, D. G., The artificial leaf. *Accounts of chemical research* **2012,** *45* (5), 767-776.

11. Roger, I.; Shipman, M. A.; Symes, M. D., Earth-abundant catalysts for electrochemical and photoelectrochemical water splitting. *Nature Reviews Chemistry* **2017,** *1*, 0003.

12. Joya, K. S.; Joya, Y. F.; Ocakoglu, K.; van de Krol, R., Water-splitting catalysis and solar fuel devices: Artificial leaves on the move. *Angewandte Chemie International Edition* **2013,** *52* (40), 10426-10437.

13. Ardo, S.; Rivas, D. F.; Modestino, M. A.; Greiving, V. S.; Abdi, F. F.; Llado, E. A.; Artero, V.; Ayers, K.; Battaglia, C.; Becker, J.-P., Pathways to electrochemical solar-hydrogen technologies. *Energy & environmental science* **2018,** *11* (10), 2768-2783.

14. Holladay, J. D.; Hu, J.; King, D. L.; Wang, Y., An overview of hydrogen production technologies. *Catalysis today* **2009,** *139* (4), 244-260.

15. Ardo, S.; Rivas, D. F.; Modestino, M. A.; Greiving, V. S.; Abdi, F.; Alarcon-Llado, E.; Artero, V.; Ayers, K. E.; Battaglia, C.; Becker, J.-P., Pathways to Electrochemical Solar-Hydrogen Technologies. *Energy & environmental science* **2018**.

16. Zheng, X.; Hou, Y.; Bao, C.; Yin, J.; Yuan, F.; Huang, Z.; Song, K.; Liu, J.; Troughton, J.; Gasparini, N.; Zhou, C.; Lin, Y.; Xue, D.-J.; Chen, B.; Johnston, A. K.; Wei, N.; Hedhili, M. N.; Wei, M.; Alsalloum, A. Y.; Maity, P.; Turedi, B.; Yang, C.; Baran, D.; Anthopoulos, T. D.; Han, Y.; Lu, Z.-H.; Mohammed, O. F.; Gao, F.; Sargent, E. H.; Bakr, O. M., Managing grains and interfaces via ligand anchoring enables 22.3%-efficiency inverted perovskite solar cells. *Nature Energy* **2020**.

17. You, B.; Sun, Y., Innovative strategies for electrocatalytic water splitting. *Accounts of chemical research* **2018,** *51* (7), 1571-1580.

18. Dau, H.; Limberg, C.; Reier, T.; Risch, M.; Roggan, S.; Strasser, P., The mechanism of water oxidation: from electrolysis via homogeneous to biological catalysis. *ChemCatChem* **2010,** *2* (7), 724-761.

19. Joya, K. S.; Joya, Y. F.; De Groot, H. J., Ni-Based Electrocatalyst for Water Oxidation Developed In-Situ in a HCO3−/CO2 System at Near-Neutral pH. *Advanced Energy Materials* **2014,** *4* (9), 1301929.

20. Song, F.; Busch, M. M.; Lassalle-Kaiser, B.; Hsu, C.-S.; Petkucheva, E.; Bensimon, M. l.; Chen, H. M.; Corminboeuf, C.; Hu, X., An unconventional iron nickel catalyst for the oxygen evolution reaction. *ACS central science* **2019,** *5* (3), 558-568.

21. Medford, A. J.; Vojvodic, A.; Hummelshøj, J. S.; Voss, J.; Abild-Pedersen, F.; Studt, F.; Bligaard, T.; Nilsson, A.; Nørskov, J. K., From the Sabatier principle to a predictive theory of transition-metal heterogeneous catalysis. *Journal of Catalysis* **2015,** *328*, 36-42.

22. Brodsky, C. N.; Hadt, R. G.; Hayes, D.; Reinhart, B. J.; Li, N.; Chen, L. X.; Nocera, D. G., In situ characterization of cofacial Co (IV) centers in Co4O4 cubane: Modeling the high-valent active site in oxygen-evolving catalysts. *Proceedings of the National Academy of Sciences* **2017,** *114* (15), 3855-3860.

23. Burstein, G., A hundred years of Tafel's Equation: 1905-2005. *Corrosion Science* **2005,** *47* (12), 2858-2870.

24. Anantharaj, S.; Ede, S.; Karthick, K.; Sankar, S. S.; Sangeetha, K.; Karthik, P.; Kundu, S., Precision and correctness in the evaluation of electrocatalytic water splitting: revisiting activity parameters with a critical assessment. *Energy & Environmental Science* **2018,** *11* (4), 744-771.

25. Munir, A.; Haq, T. u.; Qurashi, A.; Rehman, H. u.; Ul-Hamid, A.; Hussain, I., Ultrasmall Ni/NiO nanoclusters on thiol-functionalized and-exfoliated graphene oxide nanosheets for durable oxygen evolution reaction. *ACS Applied Energy Materials* **2018,** *2* (1), 363-371.

26. ul Haq, T.; Mansour, S. A.; Munir, A.; Haik, Y., Gold-Supported Gadolinium Doped CoB Amorphous Sheet: A New Benchmark Electrocatalyst for Water Oxidation with High Turnover Frequency. *Advanced Functional Materials* **2020**, 1910309.

27. Munir, A.; Haq, T. U.; Hussain, I.; Ullah, I.; Hussain, S. Z.; Iqbal, J.; Qurashi, A.; Rehman, A.; Hussain, I., Controlled Assembly of Cu/Co-oxide Beaded Nanoclusters on Thiolated Graphene Oxide Nanosheets for High Performance Oxygen Evolution Reaction. *Chemistry–A European Journal* **2020**.

28. Munir, A.; Haq, T. u.; Hussain, I.; Qurashi, A.; Ullah, U.; Iqbal, M. J.; Hussain, I., Ultrasmall Co@Co(OH)2 Nanoclusters Embedded in N-Enriched Mesoporous Carbon Network as Efficient Electrocatalysts for Durable Water Oxidation. *ChemSusChem* **2019,** *12*, 5117-5125.

29. Burke, M. S.; Enman, L. J.; Batchellor, A. S.; Zou, S.; Boettcher, S. W., Oxygen evolution reaction electrocatalysis on transition metal oxides and (oxy) hydroxides: activity trends and design principles. *Chemistry of Materials* **2015,** *27* (22), 7549-7558.

30. Suen, N.-T.; Hung, S.-F.; Quan, Q.; Zhang, N.; Xu, Y.-J.; Chen, H. M., Electrocatalysis for the oxygen evolution reaction: recent development and future perspectives. *Chemical Society Reviews* **2017,** *46* (2), 337-365.

31. Zhu, J.; Hu, L.; Zhao, P.; Lee, L. Y. S.; Wong, K.-Y., Recent Advances in Electrocatalytic Hydrogen Evolution Using Nanoparticles. *Chemical reviews* **2019**.

32. Morales-Guio, C. G.; Stern, L.-A.; Hu, X., Nanostructured hydrotreating catalysts for electrochemical hydrogen evolution. *Chemical Society Reviews* **2014,** *43* (18), 6555-6569.

33. Liang, K.; Guo, L.; Marcus, K.; Zhang, S.; Yang, Z.; Perea, D. E.; Zhou, L.; Du, Y.; Yang, Y., Overall Water Splitting with Room-Temperature Synthesized NiFe Oxyfluoride Nanoporous Films. *ACS Catalysis* **2017,** *7* (12), 8406-8412.

34. Tee, S. Y.; Win, K. Y.; Teo, W. S.; Koh, L. D.; Liu, S.; Teng, C. P.; Han, M. Y., Recent Progress in Energy-Driven Water Splitting. *Advanced Science* **2017**.

35. Concepcion, J. J.; Tsai, M.-K.; Muckerman, J. T.; Meyer, T. J., Mechanism of water oxidation by single-site ruthenium complex catalysts. *Journal of the American Chemical Society* **2010,** *132* (5), 1545-1557.

36. Cornils, B.; Herrmann, W. A.; Beller, M.; Paciello, R., *Applied Homogeneous Catalysis with Organometallic Compounds: A Comprehensive Handbook in Four Volumes*. John Wiley & Sons: 2018; Vol. 4.

37. Liu, D.; Li, L.; You, T., Superior catalytic performances of platinum nanoparticles loaded nitrogen-doped graphene toward methanol oxidation and

hydrogen evolution reaction. *Journal of colloid and interface science* **2017,** *487*, 330-335.

38. Yin, H.; Zhao, S.; Zhao, K.; Muqsit, A.; Tang, H.; Chang, L.; Zhao, H.; Gao, Y.; Tang, Z., Ultrathin platinum nanowires grown on single-layered nickel hydroxide with high hydrogen evolution activity. *Nature Communications* **2015,** *6*, 6430.

39. Alinezhad, A.; Gloag, L.; Benedetti, T. M.; Cheong, S.; Webster, R. F.; Roelsgaard, M.; Iversen, B. B.; Schuhmann, W.; Gooding, J. J.; Tilley, R. D., Direct growth of highly strained Pt islands on branched Ni nanoparticles for improved hydrogen evolution reaction activity. *Journal of the American Chemical Society* **2019,** *141* (41), 16202-16207.

40. Barman, B. K.; Sarkar, B.; Nanda, K. K., Pd-coated Ru nanocrystals supported on N-doped graphene as HER and ORR electrocatalysts. *Chemical Communications* **2019,** *55* (92), 13928-13931.

41. Chi, J.-Q.; Zhang, X.-Y.; Ma, X.; Dong, B.; Zhang, J.-Q.; Guo, B.-Y.; Yang, M.; Wang, L.; Chai, Y.-M.; Liu, C., Interface Charge Engineering of Ultrafine Ru/Ni2P Nanoparticles Encapsulated in N, P-Codoped Hollow Carbon Nanospheres for Efficient Hydrogen Evolution. *ACS Sustainable Chemistry & Engineering* **2019,** *7* (21), 17714-17722.

42. Tang, C.; Cheng, N.; Pu, Z.; Xing, W.; Sun, X., NiSe nanowire film supported on nickel foam: an efficient and stable 3D bifunctional electrode for full water splitting. *Angewandte Chemie* **2015,** *127* (32), 9483-9487.

43. Tian, J.; Cheng, N.; Liu, Q.; Xing, W.; Sun, X., Cobalt phosphide nanowires: efficient nanostructures for fluorescence sensing of biomolecules and photocatalytic evolution of dihydrogen from water under visible light. *Angewandte Chemie International Edition* **2015,** *54* (18), 5493-5497.

44. Chen, W.-F.; Muckerman, J. T.; Fujita, E., Recent developments in transition metal carbides and nitrides as hydrogen evolution electrocatalysts. *Chemical communications* **2013,** *49* (79), 8896-8909.

45. Wu, H. B.; Xia, B. Y.; Yu, L.; Yu, X.-Y.; Lou, X. W. D., Porous molybdenum carbide nano-octahedrons synthesized via confined carburization in metal-organic frameworks for efficient hydrogen production. *Nature communications* **2015,** *6*, 6512.

46. Li, J.; Zhao, Z.; Ma, Y.; Qu, Y., Graphene and Their Hybrid Electrocatalysts for Water Splitting. *ChemCatChem* **2017,** *9* (9), 1554-1568.

47. Han, A.; Chen, H.; Sun, Z.; Xu, J.; Du, P., High catalytic activity for water oxidation based on nanostructured nickel phosphide precursors. *Chemical Communications* **2015,** *51* (58), 11626-11629.

48. Vrubel, H.; Hu, X., Molybdenum boride and carbide catalyze hydrogen evolution in both acidic and basic solutions. *Angewandte Chemie International Edition* **2012,** *51* (51), 12703-12706.

49. Danilovic, N.; Subbaraman, R.; Chang, K.-C.; Chang, S. H.; Kang, Y. J.; Snyder, J.; Paulikas, A. P.; Strmcnik, D.; Kim, Y.-T.; Myers, D., Activity–stability trends for the oxygen evolution reaction on monometallic oxides in acidic environments. *The journal of physical chemistry letters* **2014,** *5* (14), 2474-2478.

50. Joya, K. S.; de Groot, H. J., Controlled surface-assembly of nanoscale leaf-type Cu-oxide electrocatalyst for high activity water oxidation. *ACS Catalysis* **2016,** *6* (3), 1768-1771.

51. Han, L.; Yu, X. Y.; Lou, X. W. D., Formation of Prussian-Blue-Analog Nanocages via a Direct Etching Method and their Conversion into Ni–Co-Mixed Oxide for Enhanced Oxygen Evolution. *Advanced Materials* **2016,** *28* (23), 4601-4605.

52. Razmjooei, F.; Singh, K. P.; Yang, D.-S.; Cui, W.; Jang, Y. H.; Yu, J.-S., Fe-Treated Heteroatom (S/N/B/P)-Doped Graphene Electrocatalysts for Water Oxidation. *Acs Catalysis* **2017,** *7* (4), 2381-2391.

53. Govindhan, M.; Mao, B.; Chen, A., Novel cobalt quantum dot/graphene nanocomposites as highly efficient electrocatalysts for water splitting. *Nanoscale* **2016,** *8* (3), 1485-1492.

54. Xu, M.; Wei, M., Layered Double Hydroxide-Based Catalysts: Recent Advances in Preparation, Structure, and Applications. *Advanced Functional Materials* **2018,** *28* (47), 1802943.

55. Yang, M.; Lu, W.; Jin, R.; Liu, X.-C.; Song, S.; Xing, Y., Superior Oxygen Evolution Reaction Performance of Co3O4/NiCo2O4/Ni Foam Composite with Hierarchical Structure. *ACS Sustainable Chemistry & Engineering* **2019,** *7* (14), 12214-12221.

56. Kuai, C.; Zhang, Y.; Wu, D.; Sokaras, D.; Mu, L.; Spence, S.; Nordlund, D.; Lin, F.; Du, X.-W., Fully Oxidized Ni–Fe Layered Double Hydroxide with 100% Exposed Active Sites for Catalyzing Oxygen Evolution Reaction. *ACS Catalysis* **2019,** *9* (7), 6027-6032.

57. Rosa, M.; Costa Bassetto, V.; Girault, H. H.; Lesch, A.; Esposito, V., Assembling Ni–Fe Layered Double Hydroxide 2D Thin Films for Oxygen Evolution Electrodes. *ACS Applied Energy Materials* **2019**.

58. Li, P.; Wang, M.; Duan, X.; Zheng, L.; Cheng, X.; Zhang, Y.; Kuang, Y.; Li, Y.; Ma, Q.; Feng, Z., Boosting oxygen evolution of single-atomic ruthenium through electronic coupling with cobalt-iron layered double hydroxides. *Nature communications* **2019,** *10* (1), 1-11.

59. Bhowmik, T.; Kundu, M. K.; Barman, S., CoFe layered double hydroxide supported on graphitic carbon nitrides: an efficient and durable bifunctional electrocatalyst for oxygen evolution and hydrogen evolution reactions. *ACS Applied Energy Materials* **2018,** *1* (3), 1200-1209.

60. Cheng, N.; Stambula, S.; Wang, D.; Banis, M. N.; Liu, J.; Riese, A.; Xiao, B.; Li, R.; Sham, T.-K.; Liu, L.-M., Platinum single-atom and cluster catalysis of the hydrogen evolution reaction. *Nature communications* **2016,** *7* (1), 1-9.

61. Tyo, E. C.; Vajda, S., Catalysis by clusters with precise numbers of atoms. *Nature nanotechnology* **2015,** *10* (7), 577-588.

62. Lu, Y.; Chen, W., Sub-nanometre sized metal clusters: from synthetic challenges to the unique property discoveries. *Chemical Society Reviews* **2012,** *41* (9), 3594-3623.

63. Jiao, F.; Frei, H., Nanostructured Cobalt Oxide Clusters in Mesoporous Silica as Efficient Oxygen-Evolving Catalysts. *Angewandte Chemie International Edition* **2009,** *48* (10), 1841-1844.

64. Fernando, A.; Weerawardene, K. D. M.; Karimova, N. V.; Aikens, C. M., Quantum mechanical studies of large metal, metal oxide, and metal chalcogenide nanoparticles and clusters. *Chemical reviews* **2015,** *115* (12), 6112-6216.

65. Marcano, D. C.; Kosynkin, D. V.; Berlin, J. M.; Sinitskii, A.; Sun, Z.; Slesarev, A.; Alemany, L. B.; Lu, W.; Tour, J. M., Improved synthesis of graphene oxide. *ACS nano* **2010,** *4* (8), 4806-4814.

66. Hwang, S.-G.; Kim, G.-O.; Yun, S.-R.; Ryu, K.-S., NiO nanoparticles with plate structure grown on graphene as fast charge–discharge anode material for lithium ion batteries. *Electrochimica Acta* **2012,** *78*, 406-411.

67. Pollitt, S.; Pittenauer, E.; Rameshan, C.; Schachinger, T.; Safonova, O. V.; Truttmann, V.; Bera, A.; Allmaier, G. n.; Barrabés, N.; Rupprechter, G. n., Synthesis and Properties of Monolayer-Protected Co x (SC2H4Ph) m Nanoclusters. *The Journal of Physical Chemistry C* **2017,** *121* (20), 10948-10956.

68. Zheng, Y.; Zhang, Z.; Li, C., A comparison of graphitic carbon nitrides synthesized from different precursors through pyrolysis. *Journal of Photochemistry and Photobiology A: Chemistry* **2017,** *332*, 32-44.

69. Ferrari, A. C.; Basko, D. M. J. N. n., Raman spectroscopy as a versatile tool for studying the properties of graphene. **2013,** *8* (4), 235.

70. Jones, R. R.; Hooper, D. C.; Zhang, L.; Wolverson, D.; Valev, V. K. J. N. r. l., Raman Techniques: Fundamentals and Frontiers. **2019,** *14* (1), 1-34.

71. Vlasov, A. V.; Maliar, N. L.; Bazhenov, S. V.; Nikelshparg, E. I.; Brazhe, N. A.; Vlasova, A. D.; Osipov, S. D.; Sudarev, V. V.; Ryzhykau, Y. L.; Bogorodskiy, A. O. J. C., Raman Scattering: From Structural Biology to Medical Applications. **2020,** *10* (1), 38.

72. Munir, A.; ul Haq, T.; Hussain, I.; Qurashi, A.; Ullah, U.; Iqbal, M. J.; Hussain, I. J. C., Ultrasmall Co@ Co (OH) 2 Nanoclusters Embedded in N-Enriched Mesoporous Carbon Network as Efficient Electrocatalysts for Durable Water Oxidation. **2019**.

73. Skoog, D. A.; Holler, F. J.; Crouch, S. R., *Principles of instrumental analysis*. Cengage learning: 2017.

74. Stanjek, H.; Häusler, W., Basics of X-ray Diffraction. *Hyperfine Interactions* **2004,** *154* (1), 107-119.

75. Hieulle, J. Structures and Electronic Properties of Organic Self-Assembled Monolayers Characterized by STM and XPS. 2014.

76. Morgan, D. J. J. C. C. I., School of Chemistry, Cardiff University, Cardiff, X-Ray Photoelectron Spectroscopy (XPS): An Introduction.

77. Trotochaud, L.; Young, S. L.; Ranney, J. K.; Boettcher, S. W., Nickel–iron oxyhydroxide oxygen-evolution electrocatalysts: the role of intentional and incidental iron incorporation. *Journal of the American Chemical Society* **2014,** *136* (18), 6744-6753.

78. Chauhan, M.; Reddy, K. P.; Gopinath, C. S.; Deka, S., Copper Cobalt Sulfide Nanosheets Realizing a Promising Electrocatalytic Oxygen Evolution Reaction. *ACS Catalysis* **2017,** *7* (9), 5871-5879.

79. Anantharaj, S.; Karthik, P.; Kundu, S., Petal-like hierarchical array of ultrathin Ni (OH) 2 nanosheets decorated with Ni (OH) 2 nanoburls: a highly efficient OER electrocatalyst. *Catalysis Science & Technology* **2017,** *7* (4), 882-893.

80. Men, Y.; Li, P.; Zhou, J.; Cheng, G.; Chen, S.; Luo, W., Tailoring the electronic structure of Co2P by N doping for boosting hydrogen evolution reaction at all pH values. *ACS Catalysis* **2019**.

81. Detsi, E.; Cook, J. B.; Lesel, B. K.; Turner, C. L.; Liang, Y.-L.; Robbennolt, S.; Tolbert, S. H., Mesoporous Ni 60 Fe 30 Mn 10-alloy based metal/metal oxide composite thick films as highly active and robust oxygen evolution catalysts. *Energy & environmental science* **2016,** *9* (2), 540-549.

82. Leitner, W.; Quadrelli, E. A.; Schlögl, R., Harvesting renewable energy with chemistry. *Green Chemistry* **2017,** *19* (10), 2307-2308.

83. Wang, D.; Li, Q.; Han, C.; Xing, Z.; Yang, X., When NiO@Ni Meets WS2 Nanosheet Array: A Highly Efficient and Ultrastable Electrocatalyst for Overall Water Splitting. *ACS Central Science* **2018,** *4* (1), 112-119.

84. Jiao, Y.; Zheng, Y.; Jaroniec, M.; Qiao, S. Z., Design of electrocatalysts for oxygen-and hydrogen-involving energy conversion reactions. *Chemical Society Reviews* **2015,** *44* (8), 2060-2086.

85. Lee, Y.; Suntivich, J.; May, K. J.; Perry, E. E.; Shao-Horn, Y., Synthesis and activities of rutile IrO2 and RuO2 nanoparticles for oxygen evolution in acid and alkaline solutions. *The journal of physical chemistry letters* **2012,** *3* (3), 399-404.

86. Gao, R.; Li, G.-D.; Hu, J.; Wu, Y.; Lian, X.; Wang, D.; Zou, X., In situ electrochemical formation of NiSe/NiO x core/shell nano-electrocatalysts for superior oxygen evolution activity. *Catalysis Science & Technology* **2016,** *6* (23), 8268-8275.

87. Li, Y.; Yan, D.; Zou, Y.; Xie, C.; Wang, Y.; Zhang, Y.; Wang, S., Rapidly engineering the electronic properties and morphological structure of NiSe nanowires for the oxygen evolution reaction. *Journal of Materials Chemistry A* **2017,** *5* (48), 25494-25500.

88. Wang, Y.; Yan, D.; El Hankari, S.; Zou, Y.; Wang, S., Recent Progress on Layered Double Hydroxides and Their Derivatives for Electrocatalytic Water Splitting. *Advanced Science* **2018**, 1800064.

89. Jung, S.; McCrory, C. C.; Ferrer, I. M.; Peters, J. C.; Jaramillo, T. F., Benchmarking nanoparticulate metal oxide electrocatalysts for the alkaline water oxidation reaction. *Journal of Materials Chemistry A* **2016,** *4* (8), 3068-3076.

90. Song, F.; Bai, L.; Moysiadou, A.; Lee, S.; Hu, C.; Liardet, L.; Hu, X., Transition metal oxides as electrocatalysts for the oxygen evolution reaction in alkaline solutions: An application-inspired renaissance. *Journal of the American Chemical Society* **2018**.

91. Vij, V.; Sultan, S.; Harzandi, A. M.; Meena, A.; Tiwari, J. N.; Lee, W.-G.; Yoon, T.; Kim, K. S., Nickel-based electrocatalysts for energy-related applications: oxygen reduction, oxygen evolution, and hydrogen evolution reactions. *ACS Catalysis* **2017,** *7* (10), 7196-7225.

92. Panapitiya, G.; Wang, H.; Chen, Y.; Hussain, E.; Jin, R.; Lewis, J. P., Structural and catalytic properties of the Au 25− x Ag x (SCH 3) 18 (x= 6, 7, 8) nanocluster. *Physical Chemistry Chemical Physics* **2018,** *20* (20), 13747-13756.

93. Tong, L.; Wu, W.; Kuepper, K.; Scheurer, A.; Meyer, K., Electrochemically Deposited Nickel Oxide from Molecular Complexes for Efficient Water Oxidation Catalysis. *ChemSusChem* **2018,** *11* (16), 2752-2757.

94. Liu, L.; Corma, A., Metal Catalysts for Heterogeneous Catalysis: From Single Atoms to Nanoclusters and Nanoparticles. *Chemical reviews* **2018,** *118* (10), 4981-5079.

95. AbdulHalim, L. G.; Ashraf, S.; Katsiev, K.; Kirmani, A. R.; Kothalawala, N.; Anjum, D. H.; Abbas, S.; Amassian, A.; Stellacci, F.; Dass, A., A scalable synthesis of highly stable and water dispersible Ag 44 (SR) 30 nanoclusters. *Journal of Materials Chemistry A* **2013,** *1* (35), 10148-10154.

96. Kauffman, D. R.; Alfonso, D.; Tafen, D. N.; Lekse, J.; Wang, C.; Deng, X.; Lee, J.; Jang, H.; Lee, J.-s.; Kumar, S., Electrocatalytic oxygen evolution with an atomically precise nickel catalyst. *ACS Catalysis* **2016,** *6* (2), 1225-1234.

97. Fominykh, K.; Feckl, J. M.; Sicklinger, J.; Döblinger, M.; Böcklein, S.; Ziegler, J.; Peter, L.; Rathousky, J.; Scheidt, E. W.; Bein, T., Ultrasmall dispersible crystalline nickel oxide nanoparticles as high-performance catalysts for electrochemical water splitting. *Advanced Functional Materials* **2014,** *24* (21), 3123-3129.

98. Gong, M.; Zhou, W.; Kenney, M. J.; Kapusta, R.; Cowley, S.; Wu, Y.; Lu, B.; Lin, M. C.; Wang, D. Y.; Yang, J., Blending Cr2O3 into a NiO–Ni electrocatalyst for

sustained water splitting. *Angewandte Chemie International Edition* **2015,** *54* (41), 11989-11993.

99. Joya, K. S.; Sinatra, L.; AbdulHalim, L. G.; Joshi, C. P.; Hedhili, M. N.; Bakr, O. M.; Hussain, I., Atomically monodisperse nickel nanoclusters as highly active electrocatalysts for water oxidation. *Nanoscale* **2016,** *8* (18), 9695-9703.

100. Thomas, H. R.; Marsden, A. J.; Walker, M.; Wilson, N. R.; Rourke, J. P., Sulfur-Functionalized Graphene Oxide by Epoxide Ring-Opening. *Angewandte Chemie International Edition* **2014,** *53* (29), 7613-7618.

101. Chua, C. K.; Pumera, M., Monothiolation and reduction of graphene oxide via one-pot synthesis: Hybrid catalyst for oxygen reduction. *ACS nano* **2015,** *9* (4), 4193-4199.

102. Chua, C. K.; Pumera, M., Renewal of sp 2 bonds in graphene oxides via dehydrobromination. *Journal of Materials Chemistry* **2012,** *22* (43), 23227-23231.

103. Huang, C.; Li, C.; Shi, G., Graphene based catalysts. *Energy & Environmental Science* **2012,** *5* (10), 8848-8868.

104. Jiang, Z.; Jiang, Z.-j.; Tian, X.; Chen, W., Amine-functionalized holey graphene as a highly active metal-free catalyst for the oxygen reduction reaction. *Journal of Materials Chemistry A* **2014,** *2* (2), 441-450.

105. Blanita, G.; Lazar, M. D., Review of graphene-supported metal nanoparticles as new and efficient heterogeneous catalysts. *Micro and Nanosystems* **2013,** *5* (2), 138-146.

106. Premi, C.; Jain, N., A nitrogen and sulphur functionalized graphene oxide–palladium nanoparticle hybrid catalyst for an efficient Heck coupling. *RSC Advances* **2016,** *6* (78), 74961-74967.

107. Song, X.-R.; Goswami, N.; Yang, H.-H.; Xie, J., Functionalization of metal nanoclusters for biomedical applications. *Analyst* **2016,** *141* (11), 3126-3140.

108. Dresselhaus, M.; Jorio, A.; Saito, R., Characterizing graphene, graphite, and carbon nanotubes by Raman spectroscopy. *Annu. Rev. Condens. Matter Phys.* **2010,** *1* (1), 89-108.

109. Ferrari, A. C.; Basko, D. M., Raman spectroscopy as a versatile tool for studying the properties of graphene. *Nature nanotechnology* **2013,** *8* (4), 235.

110. Dresselhaus, M. S.; Jorio, A.; Hofmann, M.; Dresselhaus, G.; Saito, R., Perspectives on carbon nanotubes and graphene Raman spectroscopy. *Nano letters* **2010,** *10* (3), 751-758.

111. Wang, J.; Xie, Y.; Yao, Y.; Huang, X.; Willinger, M.; Shao, L., Ni/NiO nanoparticles on a phosphorous oxide/graphene hybrid for efficient electrocatalytic water splitting. *Journal of Materials Chemistry A* **2017,** *5* (28), 14758-14762.

112. Ding, M.; Tang, Y.; Star, A., Understanding interfaces in metal–graphitic hybrid nanostructures. *The journal of physical chemistry letters* **2012,** *4* (1), 147-160.

113. Gao, X.; Chen, W., Highly stable and efficient Pd6(SR)12 cluster catalysts for the hydrogen and oxygen evolution reactions. *Chemical Communications* **2017,** *53* (70), 9733-9736.

114. Cheng, N.; Stambula, S.; Wang, D.; Banis, M. N.; Liu, J.; Riese, A.; Xiao, B.; Li, R.; Sham, T.-K.; Liu, L.-M., Platinum single-atom and cluster catalysis of the hydrogen evolution reaction. *Nature communications* **2016,** *7,* 13638.

115. Wang, J.; Mao, S.; Liu, Z.; Wei, Z.; Wang, H.; Chen, Y.; Wang, Y., Dominating role of Ni0 on the interface of Ni/NiO for enhanced hydrogen evolution reaction. *ACS applied materials & interfaces* **2017,** *9* (8), 7139-7147.

116. Chen, D.; Qiao, M.; Lu, Y. R.; Hao, L.; Liu, D.; Dong, C. L.; Li, Y.; Wang, S., Preferential Cation Vacancies in Perovskite Hydroxide for the Oxygen Evolution Reaction. *Angewandte Chemie International Edition* **2018,** *57* (28), 8691-8696.

117. Suntivich, J.; May, K. J.; Gasteiger, H. A.; Goodenough, J. B.; Shao-Horn, Y., A perovskite oxide optimized for oxygen evolution catalysis from molecular orbital principles. *Science* **2011,** *334* (6061), 1383-1385.

118. Man, I. C.; Su, H. Y.; Calle-Vallejo, F.; Hansen, H. A.; Martínez, J. I.; Inoglu, N. G.; Kitchin, J.; Jaramillo, T. F.; Nørskov, J. K.; Rossmeisl, J., Universality in oxygen evolution electrocatalysis on oxide surfaces. *ChemCatChem* **2011,** *3* (7), 1159-1165.

119. Huang, Z.; Chen, Z.; Chen, Z.; Lv, C.; Meng, H.; Zhang, C., Ni12P5 nanoparticles as an efficient catalyst for hydrogen generation via electrolysis and photoelectrolysis. *ACS nano* **2014,** *8* (8), 8121-8129.

120. Audichon, T.; Napporn, T. W.; Canaff, C.; Morais, C. u.; Comminges, C. m.; Kokoh, K. B., IrO2 coated on RuO2 as efficient and stable electroactive nanocatalysts for electrochemical water splitting. *The Journal of Physical Chemistry C* **2016,** *120* (5), 2562-2573.

121. Corrigan, D. A., The catalysis of the oxygen evolution reaction by iron impurities in thin film nickel oxide electrodes. *Journal of The Electrochemical Society* **1987,** *134* (2), 377-384.

122. Gao, M.; Sheng, W.; Zhuang, Z.; Fang, Q.; Gu, S.; Jiang, J.; Yan, Y., Efficient water oxidation using nanostructured α-nickel-hydroxide as an electrocatalyst. *Journal of the American Chemical Society* **2014,** *136* (19), 7077-7084.

123. Zhao, S.; Jin, R.; Abroshan, H.; Zeng, C.; Zhang, H.; House, S. D.; Gottlieb, E.; Kim, H. J.; Yang, J. C.; Jin, R., Gold Nanoclusters Promote Electrocatalytic Water Oxidation at the Nanocluster/CoSe2 Interface. *Journal of the American Chemical Society* **2017,** *139* (3), 1077-1080.

124. Tyo, E. C.; Vajda, S., Catalysis by clusters with precise numbers of atoms. *Nature nanotechnology* **2015,** *10* (7), 577.

125. Gao, X.; Chen, W., Highly stable and efficient Pd 6 (SR) 12 cluster catalysts for the hydrogen and oxygen evolution reactions. *Chemical Communications* **2017,** *53* (70), 9733-9736.

126. Chu, S.; Majumdar, A., Opportunities and challenges for a sustainable energy future. *nature* **2012,** *488* (7411), 294.

127. Lewis, N. S.; Nocera, D. G., Powering the planet: Chemical challenges in solar energy utilization. *Proceedings of the National Academy of Sciences* **2006,** *103* (43), 15729-15735.

128. Song, F.; Bai, L.; Moysiadou, A.; Lee, S.; Hu, C.; Liardet, L.; Hu, X., Transition metal oxides as electrocatalysts for the oxygen evolution reaction in alkaline solutions: an application-inspired renaissance. *Journal of the American Chemical Society* **2018,** *140* (25), 7748-7759.

129. Wang, H. F.; Tang, C.; Zhang, Q., A Review of Precious-Metal-Free Bifunctional Oxygen Electrocatalysts: Rational Design and Applications in Zn− Air Batteries. *Advanced Functional Materials* **2018,** *28* (46), 1803329.

130. Nørskov, J. K.; Rossmeisl, J.; Logadottir, A.; Lindqvist, L.; Kitchin, J. R.; Bligaard, T.; Jónsson, H., Origin of the Overpotential for Oxygen Reduction at a Fuel-Cell Cathode. *The Journal of Physical Chemistry B* **2004,** *108* (46), 17886-17892.

131. Wang, Y.; Yan, D.; El Hankari, S.; Zou, Y.; Wang, S., Recent progress on layered double hydroxides and their derivatives for electrocatalytic water splitting. *Advanced Science* **2018,** *5* (8), 1800064.

132. Anantharaj, S.; Ede, S. R.; Sakthikumar, K.; Karthick, K.; Mishra, S.; Kundu, S., Recent trends and perspectives in electrochemical water splitting with an emphasis on sulfide, selenide, and phosphide catalysts of Fe, Co, and Ni: a review. *ACS Catalysis* **2016,** *6* (12), 8069-8097.

133. Feng, C.; Faheem, M. B.; Fu, J.; Xiao, Y.; Li, C.; Li, Y., Fe-based Electrocatalysts for Oxygen Evolution Reaction: Progress and Perspectives. *ACS Catalysis* **2020**.

134. Zhang, J.; Zhang, Q.; Feng, X., Support and Interface Effects in Water-Splitting Electrocatalysts. *Advanced Materials* **2019**, 1808167.

135. Morales, D. M.; Kazakova, M. A.; Dieckhöfer, S.; Selyutin, A. G.; Golubtsov, G. V.; Schuhmann, W.; Masa, J., Trimetallic Mn-Fe-Ni Oxide Nanoparticles Supported on Multi-Walled Carbon Nanotubes as High-Performance Bifunctional ORR/OER Electrocatalyst in Alkaline Media. *Advanced Functional Materials* **2019**.

136. Munir, A.; Joya, K. S.; Ul Haq, T.; Babar, N. U. A.; Hussain, S. Z.; Qurashi, A.; Ullah, N.; Hussain, I., Metal nanoclusters: new paradigm in catalysis for water splitting, solar and chemical energy conversion. *ChemSusChem* **2019,** *12* (8), 1517-1548.

137. Munir, A.; ul Haq, T.; Hussain, I.; Qurashi, A.; Ullah, U.; Iqbal, M. J.; Hussain, I., Ultrasmall Co@Co(OH)2 Nanoclusters Embedded in N-Enriched Mesoporous

Carbon Networks as Efficient Electrocatalysts for Water Oxidation. *ChemSusChem n/a* (n/a).

138. Ye, R.; Tour, J. M., Graphene at fifteen. *ACS nano* **2019,** *13* (10), 10872-10878.

139. Chia, X.; Pumera, M., Characteristics and performance of two-dimensional materials for electrocatalysis. *Nature Catalysis* **2018,** *1* (12), 909-921.

140. van Deelen, T. W.; Mejía, C. H.; de Jong, K. P., Control of metal-support interactions in heterogeneous catalysts to enhance activity and selectivity. *Nature Catalysis* **2019**, 1-16.

141. Lu, C.; Wang, J.; Czioska, S.; Dong, H.; Chen, Z., Hierarchically structured Cu-based electrocatalysts with nanowires array for water splitting. *The Journal of Physical Chemistry C* **2017,** *121* (46), 25875-25881.

142. Guo, S.; Zhang, S.; Wu, L.; Sun, S., Co/CoO nanoparticles assembled on graphene for electrochemical reduction of oxygen. *Angewandte chemie international edition* **2012,** *51* (47), 11770-11773.

143. Thanh, T. D.; Chuong, N. D.; Hien, H. V.; Kim, N. H.; Lee, J. H., CuAg@ Ag core–shell nanostructure encapsulated by N-doped graphene as a high-performance catalyst for oxygen reduction reaction. *ACS applied materials & interfaces* **2018,** *10* (5), 4672-4681.

144. Wang, L.; Nitopi, S.; Wong, A. B.; Snider, J. L.; Nielander, A. C.; Morales-Guio, C. G.; Orazov, M.; Higgins, D. C.; Hahn, C.; Jaramillo, T. F., Electrochemically converting carbon monoxide to liquid fuels by directing selectivity with electrode surface area. *Nature Catalysis* **2019**, 1.

145. Jia, Q.; Iwase, A.; Kudo, A., BiVO4–Ru/SrTiO3:Rh composite Z-scheme photocatalyst for solar water splitting. *Chemical Science* **2014,** *5* (4), 1513-1519.

146. Stevens, M. B.; Enman, L. J.; Batchellor, A. S.; Cosby, M. R.; Vise, A. E.; Trang, C. D.; Boettcher, S. W., Measurement techniques for the study of thin film heterogeneous water oxidation electrocatalysts. *Chemistry of Materials* **2016,** *29* (1), 120-140.

147. Li, Z.; Zhang, Y.; Feng, Y.; Cheng, C. Q.; Qiu, K. W.; Dong, C. K.; Liu, H.; Du, X. W., Co3O4 Nanoparticles with Ultrasmall Size and Abundant Oxygen Vacancies for Boosting Oxygen Involved Reactions. *Advanced Functional Materials* **2019**.

148. Zhuang, Z.; Wang, Y.; Xu, C.-Q.; Liu, S.; Chen, C.; Peng, Q.; Zhuang, Z.; Xiao, H.; Pan, Y.; Lu, S., Three-dimensional open nano-netcage electrocatalysts for efficient pH-universal overall water splitting. *Nature communications* **2019,** *10* (1), 1-10.

149. Yin, B.; Cao, X.; Pan, A.; Luo, Z.; Dinesh, S.; Lin, J.; Tang, Y.; Liang, S.; Cao, G., Encapsulation of CoSx Nanocrystals into N/S Co-Doped Honeycomb-Like 3D Porous Carbon for High-Performance Lithium Storage. *Advanced Science* **2018,** *5* (9), 1800829.

150. Li, Y.; Du, X.; Huang, J.; Wu, C.; Sun, Y.; Zou, G.; Yang, C.; Xiong, J., Recent Progress on Surface Reconstruction of Earth-Abundant Electrocatalysts for Water Oxidation. *Small* **2019,** *15* (35), 1901980.

151. Zhang, B.; Zheng, X.; Voznyy, O.; Comin, R.; Bajdich, M.; García-Melchor, M.; Han, L.; Xu, J.; Liu, M.; Zheng, L., Homogeneously dispersed multimetal oxygen-evolving catalysts. *Science* **2016,** *352* (6283), 333-337.

152. Dresp, S. r.; Dionigi, F.; Klingenhof, M.; Strasser, P., Direct Electrolytic Splitting of Seawater: Opportunities and Challenges. *ACS Energy Letters* **2019,** *4* (4), 933-942.

153. Liu, Y.; Zhang, M.; Hu, D.; Li, R.; Hu, K.; Yan, K., Ar Plasma-Exfoliated Ultrathin NiCo-Layered Double Hydroxide Nanosheets for Enhanced Oxygen Evolution. *ACS Applied Energy Materials* **2019,** *2* (2), 1162-1168.

154. Li, R.; Liu, Y.; Li, H.; Zhang, M.; Lu, Y.; Zhang, L.; Xiao, J.; Boehm, F.; Yan, K., One-Step Synthesis of NiMn-Layered Double Hydroxide Nanosheets Efficient for Water Oxidation. *Small Methods* **2019,** *3* (1), 1800344.

155. Seh, Z. W.; Kibsgaard, J.; Dickens, C. F.; Chorkendorff, I.; Nørskov, J. K.; Jaramillo, T. F., Combining theory and experiment in electrocatalysis: Insights into materials design. *Science* **2017,** *355* (6321), eaad4998.

156. Hossain, M. D.; Liu, Z.; Zhuang, M.; Yan, X.; Xu, G. L.; Gadre, C. A.; Tyagi, A.; Abidi, I. H.; Sun, C. J.; Wong, H., Rational Design of Graphene-Supported Single Atom Catalysts for Hydrogen Evolution Reaction. *Advanced Energy Materials* **2019,** *9* (10), 1803689.

157. Kwon, G.; Ferguson, G. A.; Heard, C. J.; Tyo, E. C.; Yin, C.; DeBartolo, J.; Seifert, S. n.; Winans, R. E.; Kropf, A. J.; Greeley, J., Size-dependent subnanometer Pd cluster (Pd4, Pd6, and Pd17) water oxidation electrocatalysis. *ACS nano* **2013,** *7* (7), 5808-5817.

158. Han, X.-B.; Tang, X.-Y.; Lin, Y.; Gracia-Espino, E.; Liu, S.-G.; Liang, H.-W.; Hu, G.-Z.; Zhao, X.-J.; Liao, H.-G.; Tan, Y.-Z., Ultrasmall Abundant Metal-Based Clusters as Oxygen-Evolving Catalysts. *Journal of the American Chemical Society* **2018,** *141* (1), 232-239.

159. Guo, P.; Wu, J.; Li, X.-B.; Luo, J.; Lau, W.-M.; Liu, H.; Sun, X.-L.; Liu, L.-M., A highly stable bifunctional catalyst based on 3D Co (OH) 2@ NCNTs@ NF towards overall water-splitting. *Nano energy* **2018,** *47*, 96-104.

160. Liu, H.; Chang, L.; Bai, C.; Chen, L.; Luque, R.; Li, Y., Controllable encapsulation of “clean” metal clusters within MOFs through kinetic modulation: towards advanced heterogeneous nanocatalysts. *Angewandte Chemie International Edition* **2016,** *55* (16), 5019-5023.

161. Ong, W.-J.; Tan, L.-L.; Ng, Y. H.; Yong, S.-T.; Chai, S.-P., Graphitic carbon nitride (g-C3N4)-based photocatalysts for artificial photosynthesis and environmental

remediation: are we a step closer to achieving sustainability? *Chemical reviews* **2016,** *116* (12), 7159-7329.

162. Ao, X.; Zhang, W.; Li, Z.; Li, J.-G.; Soule, L.; Huang, X.; Chiang, W.-H.; Chen, H. M.; Wang, C.; Liu, M., Markedly Enhanced Oxygen Reduction Activity of Single-Atom Fe Catalysts via Integration with Fe Nanoclusters. *ACS Nano* **2019**.

163. Liu, Z.; Ouyang, T.; Ye, Y.; Wu, C.; Xiao, K., Heterostructures Comprised of Co/β-Mo2C-encapsulated N-doped carbon nanotubes as bifunctional electrodes for water splitting. *Angew. Chem., Int. Ed* **2019,** *58* (15), 4923-4928.

164. Liu, G.; Zhao, G.; Zhou, W.; Liu, Y.; Pang, H.; Zhang, H.; Hao, D.; Meng, X.; Li, P.; Kako, T., In situ bond modulation of graphitic carbon nitride to construct p–n homojunctions for enhanced photocatalytic hydrogen production. *Advanced Functional Materials* **2016,** *26* (37), 6822-6829.

165. Chen, Z.-J.; Cao, G.-X.; Gan, L.-Y.; Dai, H.; Xu, N.; Zang, M.-J.; Dai, H.-B.; Wu, H.; Wang, P., Highly Dispersed Platinum on Honeycomb-like NiO@ Ni Film as a Synergistic Electrocatalyst for the Hydrogen Evolution Reaction. *ACS Catalysis* **2018,** *8* (9), 8866-8872.

166. Shen, X.; Dai, S.; Zhang, C.; Zhang, S.; Sharkey, S. M.; Graham, G. W.; Pan, X.; Peng, Z., In situ atomic-scale observation of the two-dimensional Co (OH) 2 transition at atmospheric pressure. *Chemistry of Materials* **2017,** *29* (10), 4572-4579.

167. Yang, S.; Gong, Y.; Zhang, J.; Zhan, L.; Ma, L.; Fang, Z.; Vajtai, R.; Wang, X.; Ajayan, P. M., Exfoliated graphitic carbon nitride nanosheets as efficient catalysts for hydrogen evolution under visible light. *Advanced materials* **2013,** *25* (17), 2452-2456.

168. Zhang, H.; Tian, W.; Guo, X.; Zhou, L.; Sun, H.; Tadé, M. O.; Wang, S., Flower-like cobalt hydroxide/oxide on graphitic carbon nitride for visible-light-driven water oxidation. *ACS applied materials & interfaces* **2016,** *8* (51), 35203-35212.

169. Munir, A.; Haq, T. u.; Qurashi, A.; Rehman, H. u.; Ul-Hamid, A.; Hussain, I., Ultrasmall Ni/NiO Nanoclusters on Thiol-Functionalized and-Exfoliated Graphene Oxide Nanosheets for Durable Oxygen Evolution Reaction. *ACS Applied Energy Materials* **2018**.

170. Liu, Y.; Liang, X.; Gu, L.; Zhang, Y.; Li, G.-D.; Zou, X.; Chen, J.-S., Corrosion engineering towards efficient oxygen evolution electrodes with stable catalytic activity for over 6000 hours. *Nature communications* **2018,** *9* (1), 2609.

171. Cheng, W.; Zhao, X.; Su, H.; Tang, F.; Che, W.; Zhang, H.; Liu, Q., Lattice-strained metal–organic-framework arrays for bifunctional oxygen electrocatalysis. *Nature Energy* **2019,** *4* (2), 115.

172. McCrory, C. C.; Jung, S.; Peters, J. C.; Jaramillo, T. F., Benchmarking heterogeneous electrocatalysts for the oxygen evolution reaction. *Journal of the American Chemical Society* **2013,** *135* (45), 16977-16987.

173. Shao, Y.; Jiang, Z.; Zhang, Q.; Guan, J., Progress in Nonmetal-Doped Graphene Electrocatalysts for the Oxygen Reduction Reaction. *ChemSusChem* **2019,** *12* (10), 2133-2146.

174. Bergmann, A.; Jones, T. E.; Moreno, E. M.; Teschner, D.; Chernev, P.; Gliech, M.; Reier, T.; Dau, H.; Strasser, P., Unified structural motifs of the catalytically active state of Co (oxyhydr) oxides during the electrochemical oxygen evolution reaction. *Nature Catalysis* **2018,** *1* (9), 711.

175. Yang, J.; Liu, H.; Martens, W. N.; Frost, R. L., Synthesis and characterization of cobalt hydroxide, cobalt oxyhydroxide, and cobalt oxide nanodiscs. *The Journal of Physical Chemistry C* **2009,** *114* (1), 111-119.

176. Huang, Z.-F.; Song, J.; Du, Y.; Xi, S.; Dou, S.; Nsanzimana, J. M. V.; Wang, C.; Xu, Z. J.; Wang, X., Chemical and structural origin of lattice oxygen oxidation in Co–Zn oxyhydroxide oxygen evolution electrocatalysts. *Nature Energy* **2019,** *4* (4), 329.

177. Crabtree, G. W.; Dresselhaus, M. S.; Buchanan, M. V., The hydrogen economy. *Physics Today* **2004,** *57* (12), 39-44.

178. Dalle, K. E.; Warnan, J.; Leung, J. J.; Reuillard, B.; Karmel, I. S.; Reisner, E., Electro-and Solar-Driven Fuel Synthesis with First Row Transition Metal Complexes. *Chemical reviews* **2019**.

179. Zou, X.; Huang, X.; Goswami, A.; Silva, R.; Sathe, B. R.; Mikmeková, E.; Asefa, T., Cobalt-Embedded Nitrogen-Rich Carbon Nanotubes Efficiently Catalyze Hydrogen Evolution Reaction at All pH Values. *Angewandte Chemie International Edition* **2014,** *53* (17), 4372-4376.

180. Fabbri, E.; Schmidt, T. J., Oxygen Evolution Reaction—The Enigma in Water Electrolysis. **2018,** *8 (10)*, 9765–9774.

181. Li, J.; Zheng, G., One-Dimensional Earth-Abundant Nanomaterials for Water-Splitting Electrocatalysts. *Advanced Science* **2017,** *4* (3), 1600380.

182. Seitz, L. C.; Dickens, C. F.; Nishio, K.; Hikita, Y.; Montoya, J.; Doyle, A.; Kirk, C.; Vojvodic, A.; Hwang, H. Y.; Norskov, J. K., A highly active and stable IrOx/SrIrO3 catalyst for the oxygen evolution reaction. *Science* **2016,** *353* (6303), 1011-1014.

183. Sun, K.; Moreno-Hernandez, I. A.; Schmidt, W. C.; Zhou, X.; Crompton, J. C.; Liu, R.; Saadi, F. H.; Chen, Y.; Papadantonakis, K. M.; Lewis, N. S., A comparison of the chemical, optical and electrocatalytic properties of water-oxidation catalysts for use in integrated solar-fuel generators. *Energy & Environmental Science* **2017,** *10* (4), 987-1002.

184. Joya, K.; Munir, A.; Hussain, S. Z.; Ullah, N.; Qureshi, A.; Hussain, I.; Babar, N.-U.-A., Metal Nanoclusters: New Paradigm in Catalysis for Water Splitting, Solar and Chemical Energy Conversion. *ChemSusChem* **2018**.

185. Meng, T.; Cao, M., Transition Metal Carbide Complex Architectures for Energy-Related Applications. *Chemistry–A European Journal* **2018,** *24* (63), 16716-16736.

186. Kibsgaard, J.; Tsai, C.; Chan, K.; Benck, J. D.; Nørskov, J. K.; Abild-Pedersen, F.; Jaramillo, T. F., Designing an improved transition metal phosphide catalyst for hydrogen evolution using experimental and theoretical trends. *Energy & Environmental Science* **2015,** *8* (10), 3022-3029.

187. Zhu, C.; Shi, Q.; Feng, S.; Du, D.; Lin, Y., Single-atom catalysts for electrochemical water splitting. *ACS Energy Letters* **2018,** *3* (7), 1713-1721.

188. Li, H.; Li, Q.; Wen, P.; Williams, T. B.; Adhikari, S.; Dun, C.; Lu, C.; Itanze, D.; Jiang, L.; Carroll, D. L., Colloidal Cobalt Phosphide Nanocrystals as Trifunctional Electrocatalysts for Overall Water Splitting Powered by a Zinc–Air Battery. *Advanced Materials* **2018,** *30* (9), 1705796.

189. Yu, L.; Zhou, H.; Sun, J.; Qin, F.; Yu, F.; Bao, J.; Yu, Y.; Chen, S.; Ren, Z., Cu nanowires shelled with NiFe layered double hydroxide nanosheets as bifunctional electrocatalysts for overall water splitting. *Energy & Environmental Science* **2017,** *10* (8), 1820-1827.

190. Jia, Y.; Zhang, L.; Gao, G.; Chen, H.; Wang, B.; Zhou, J.; Soo, M. T.; Hong, M.; Yan, X.; Qian, G., A heterostructure coupling of exfoliated Ni–Fe hydroxide nanosheet and defective graphene as a bifunctional electrocatalyst for overall water splitting. *Advanced Materials* **2017,** *29* (17), 1700017.

191. Neri, G.; Walsh, J. J.; Teobaldi, G.; Donaldson, P. M.; Cowan, A. J., Detection of catalytic intermediates at an electrode surface during carbon dioxide reduction by an earth-abundant catalyst. *Nature Catalysis* **2018,** *1* (12), 952-959.

192. Li, X.; Lei, H.; Liu, J.; Zhao, X.; Ding, S.; Zhang, Z.; Tao, X.; Zhang, W.; Wang, W.; Zheng, X., Carbon Nanotubes with Cobalt Corroles for Hydrogen and Oxygen Evolution in pH 0–14 Solutions. *Angewandte Chemie International Edition* **2018,** *57* (46), 15070-15075.

193. Yin, Z.; Wang, Z.; Du, Y.; Qi, X.; Huang, Y.; Xue, C.; Zhang, H., Full solution-processed synthesis of all metal oxide-based tree-like heterostructures on fluorine-doped tin oxide for water splitting. *Advanced materials* **2012,** *24* (39), 5374-5378.

194. Meng, T.; Cao, M., Transition Metal Carbide Complex Architectures for Energy-Related Applications. *Chemistry–A European Journal* **2018**.

195. Han, N.; Yang, K. R.; Lu, Z.; Li, Y.; Xu, W.; Gao, T.; Cai, Z.; Zhang, Y.; Batista, V. S.; Liu, W.; Sun, X., Nitrogen-doped tungsten carbide nanoarray as an efficient bifunctional electrocatalyst for water splitting in acid. *Nature Communications* **2018,** *9* (1), 924.

196. Gao, Q.; Zhang, W.; Shi, Z.; Yang, L.; Tang, Y., Structural Design and Electronic Modulation of Transition-Metal-Carbide Electrocatalysts toward Efficient Hydrogen Evolution. *Advanced Materials* **2018**, 1802880.

197. Fan, X.; Peng, Z.; Ye, R.; Zhou, H.; Guo, X., M3C (M: Fe, Co, Ni) nanocrystals encased in graphene nanoribbons: An active and stable bifunctional electrocatalyst for oxygen reduction and hydrogen evolution reactions. *ACS nano* **2015,** *9* (7), 7407-7418.

198. Vrubel, H.; Hu, X., Molybdenum boride and carbide catalyze hydrogen evolution in both acidic and basic solutions. *Angewandte Chemie* **2012,** *124* (51), 12875-12878.

199. Ai, L.; Su, J.; Wang, M.; Jiang, J., Bamboo-structured Nitrogen-doped Carbon Nanotube Co-encapsulating Cobalt and Molybdenum Carbide Nanoparticles: An Efficient Bifunctional Electrocatalyst for Overall Water Splitting. *ACS Sustainable Chemistry & Engineering* **2018**.

200. Liu, Z.-Q.; Ouyang, T.; Ye, Y.-Q.; Wu, C.-Y.; Xiao, K., Heterostructures Comprised of Co/β-Mo2C-Encapsulated N-Doped Carbon Nanotubes as Bifunctional Electrodes for Water Splitting. *Angewandte Chemie International Edition* **2019**.

201. Yao, Y.; Zhang, B.; Shi, J.; Yang, Q., Preparation of nitrogen-doped carbon nanotubes with different morphologies from melamine-formaldehyde resin. *ACS applied materials & interfaces* **2015,** *7* (13), 7413-7420.

202. Wu, Q.; Yang, L.; Wang, X.; Hu, Z., From carbon-based nanotubes to nanocages for advanced energy conversion and storage. *Accounts of chemical research* **2017,** *50* (2), 435-444.

203. Dresp, S.; Dionigi, F.; Klingenhof, M.; Strasser, P., Direct Electrolytic Splitting of Seawater–Opportunities and Challenges. *ACS Energy Letters* **2019**.

204. Segawa, Y.; Yagi, A.; Matsui, K.; Itami, K., Design and synthesis of carbon nanotube segments. *Angewandte Chemie International Edition* **2016,** *55* (17), 5136-5158.

205. Zhao, Y.; Jia, X.; Chen, G.; Shang, L.; Waterhouse, G. I. N.; Wu, L.-Z.; Tung, C.-H.; O’Hare, D.; Zhang, T., Ultrafine NiO Nanosheets Stabilized by TiO2 from Monolayer NiTi-LDH Precursors: An Active Water Oxidation Electrocatalyst. *Journal of the American Chemical Society* **2016,** *138* (20), 6517-6524.

206. Zhang, S.; Kang, L.; Wang, X.; Tong, L.; Yang, L.; Wang, Z.; Qi, K.; Deng, S.; Li, Q.; Bai, X.; Ding, F.; Zhang, J., Arrays of horizontal carbon nanotubes of controlled chirality grown using designed catalysts. *Nature* **2017,** *543*, 234.

207. Bayer, B. C.; Bosworth, D. A.; Michaelis, F. B.; Blume, R.; Habler, G.; Abart, R.; Weatherup, R. S.; Kidambi, P. R.; Baumberg, J. J.; Knop-Gericke, A., In situ observations of phase transitions in metastable nickel (carbide)/carbon nanocomposites. *The Journal of Physical Chemistry C* **2016,** *120* (39), 22571-22584.

208. Das, D.; Santra, S.; Nanda, K. K., In Situ Fabrication of a Nickel/Molybdenum Carbide-Anchored N-Doped Graphene/CNT Hybrid: An Efficient (Pre) catalyst for OER and HER. *ACS applied materials & interfaces* **2018,** *10* (41), 35025-35038.

209. Qin, Q.; Hao, J.; Zheng, W., Ni/Ni3C Core/Shell Hierarchical Nanospheres with Enhanced Electrocatalytic Activity for Water Oxidation. *ACS Applied Materials & Interfaces* **2018,** *10* (21), 17827-17834.

210. He, K.; Xie, J.; Liu, Z.-Q.; Li, N.; Chen, X.; Hu, J.; Li, X., Multi-functional Ni 3 C cocatalyst/gC 3 N 4 nanoheterojunctions for robust photocatalytic H 2 evolution under visible light. *Journal of Materials Chemistry A* **2018,** *6* (27), 13110-13122.

211. Kitchin, J. R.; Nørskov, J. K.; Barteau, M. A.; Chen, J. G., Trends in the chemical properties of early transition metal carbide surfaces: a density functional study. *Catalysis Today* **2005,** *105* (1), 66-73.

212. Furlan, A.; Lu, J.; Hultman, L.; Jansson, U.; Magnuson, M., Crystallization characteristics and chemical bonding properties of nickel carbide thin film nanocomposites. *Journal of Physics: Condensed Matter* **2014,** *26* (41), 415501.

213. Xiong, W.; Guo, Q.; Guo, Z.; Li, H.; Zhao, R.; Chen, Q.; Liu, Z.; Wang, X., Atomic layer deposition of nickel carbide for supercapacitors and electrocatalytic hydrogen evolution. *Journal of Materials Chemistry A* **2018,** *6* (10), 4297-4304.

214. Yu, Y.; Peng, Z.; Asif, M.; Wang, H.; Wang, W.; Wu, Z.; Wang, Z.; Qiu, X.; Tan, H.; Liu, H., FeP Nanocrystals Embedded in N-Doped Carbon Nanosheets for Efficient Electrocatalytic Hydrogen Generation over a Broad pH Range. *ACS Sustainable Chemistry & Engineering* **2018,** *6* (9), 11587-11594.

215. An, L.; Jiang, N.; Li, B.; Hua, S.; Fu, Y.; Liu, J.; Hao, W.; Xia, D.; Sun, Z., A highly active and durable iron/cobalt alloy catalyst encapsulated in N-doped graphitic carbon nanotubes for oxygen reduction reaction by a nanofibrous dicyandiamide template. *Journal of Materials Chemistry A* **2018,** *6* (14), 5962-5970.

216. Rao, R.; Pint, C. L.; Islam, A. E.; Weatherup, R. S.; Hofmann, S.; Meshot, E. R.; Wu, F.; Zhou, C.; Dee, N.; Amama, P. B., Carbon Nanotubes and Related Nanomaterials: Critical Advances and Challenges for Synthesis toward Mainstream Commercial Applications. *ACS nano* **2018,** *12* (12), 11756-11784.

217. Pigos, E.; Penev, E. S.; Ribas, M. A.; Sharma, R.; Yakobson, B. I.; Harutyunyan, A. R., Carbon nanotube nucleation driven by catalyst morphology dynamics. *ACS nano* **2011,** *5* (12), 10096-10101.

218. Kang, J. X.; Zhang, D. F.; Guo, G. C.; Yu, H. J.; Wang, L. H.; Huang, W. F.; Wang, R. Z.; Guo, L.; Han, X. D., Au Catalyzed Carbon Diffusion in Ni: A Case of Lattice Compatibility Stabilized Metastable Intermediates. *Advanced Functional Materials* **2018,** *28* (21), 1706434.

219. Hansen, T. W.; DeLaRiva, A. T.; Challa, S. R.; Datye, A. K., Sintering of Catalytic Nanoparticles: Particle Migration or Ostwald Ripening? *Accounts of Chemical Research* **2013,** *46* (8), 1720-1730.

220. Liang, Q.; Zhong, L.; Du, C.; Zheng, Y.; Luo, Y.; Xu, J.; Li, S.; Yan, Q., Mosaic-Structured Cobalt Nickel Thiophosphate Nanosheets Incorporated N-doped

Carbon for Efficient and Stable Electrocatalytic Water Splitting. *Advanced Functional Materials* **2018,** *28* (43), 1805075.

221. Zhao, Y.; Nakamura, R.; Kamiya, K.; Nakanishi, S.; Hashimoto, K., Nitrogen-doped carbon nanomaterials as non-metal electrocatalysts for water oxidation. *Nature communications* **2013,** *4*, 2390.

222. Xia, B. Y.; Yan, Y.; Li, N.; Wu, H. B.; Lou, X. W.; Wang, X., A metal–organic framework-derived bifunctional oxygen electrocatalyst. *Nature Energy* **2016,** *1*, 15006.

223. Montoya, J. H.; Seitz, L. C.; Chakthranont, P.; Vojvodic, A.; Jaramillo, T. F.; Nørskov, J. K., Materials for solar fuels and chemicals. *Nature materials* **2017,** *16* (1), 70.

224. Gong, M.; Zhou, W.; Tsai, M.-C.; Zhou, J.; Guan, M.; Lin, M.-C.; Zhang, B.; Hu, Y.; Wang, D.-Y.; Yang, J., Nanoscale nickel oxide/nickel heterostructures for active hydrogen evolution electrocatalysis. *Nature communications* **2014,** *5*, 4695.

225. Zhao, L.; Guo, S.; Liu, H.; Zhu, H.; Yuan, S.; Guo, W., Density Functional Study of Hydrogen Evolution on Cobalt-Embedded Carbon Nanotubes: Effects of Doping and Surface Curvature. *ACS Applied Nano Materials* **2018,** *1* (11), 6258-6268.

226. Deng, J.; Ren, P.; Deng, D.; Yu, L.; Yang, F.; Bao, X., Highly active and durable non-precious-metal catalysts encapsulated in carbon nanotubes for hydrogen evolution reaction. *Energy & Environmental Science* **2014,** *7* (6), 1919-1923.

227. Zhang, X.; Zhou, F.; Pan, W.; Liang, Y.; Wang, R., General Construction of Molybdenum-Based Nanowire Arrays for pH-Universal Hydrogen Evolution Electrocatalysis. *Advanced Functional Materials* **2018,** *28* (43), 1804600.

228. Wygant, B. R.; Kawashima, K.; Mullins, C. B., Catalyst or Pre-Catalyst? The Effect of Oxidation on Transition Metal Carbide, Pnictide, and Chalcogenide Oxygen Evolution Catalysts. *ACS Energy Letters* **2018**.

229. Lai, L.; Potts, J. R.; Zhan, D.; Wang, L.; Poh, C. K.; Tang, C.; Gong, H.; Shen, Z.; Lin, J.; Ruoff, R. S., Exploration of the active center structure of nitrogen-doped graphene-based catalysts for oxygen reduction reaction. *Energy & Environmental Science* **2012,** *5* (7), 7936-7942.

230. Zhao, L.; Wang, Q.; Zhang, X.; Deng, C.; Li, Z.; Lei, Y.; Zhu, M., Combined Electron and Structure Manipulation on Fe-Containing N-Doped Carbon Nanotubes To Boost Bifunctional Oxygen Electrocatalysis. *ACS applied materials & interfaces* **2018,** *10* (42), 35888-35895.

231. Li, G.; Jin, R., Atomically precise gold nanoclusters as new model catalysts. *Accounts of chemical research* **2013,** *46* (8), 1749-1758.

232. Desireddy, A.; Conn, B. E.; Guo, J.; Yoon, B.; Barnett, R. N.; Monahan, B. M.; Kirschbaum, K.; Griffith, W. P.; Whetten, R. L.; Landman, U., Ultrastable silver nanoparticles. *Nature* **2013,** *501* (7467), 399-402.

233. Chen, Y.; Zeng, C.; Kauffman, D. R.; Jin, R., Tuning the magic size of atomically precise gold nanoclusters via isomeric methylbenzenethiols. *Nano letters* **2015,** *15* (5), 3603-3609.